Nouvelles perspectives dans les traitements classique et semiclassique de la dynamique réactionnelle

Wilmer Arbelo Gonzalez

N° d'ordre : 4668

THÈSE

PRÉSENTÉE À

L'UNIVERSITÉ BORDEAUX 1

ECOLE DOCTORALE DES SCIENCES CHIMIQUES

Wilmer, ARBELO GONZÁLEZ

POUR OBTENIR LE GRADE DE

DOCTEUR

SPÉCIALITÉ : Chimie-Physique

NOUVELLES PERSPECTIVES DANS LES TRAITEMENTS CLASSIQUE ET SEMICLASSIQUE DE LA DYNAMIQUE RÉACTIONNELLE

Directeurs de recherche :
Dr. Laurent BONNET
Prof. Dr. Jesús RUBAYO SONEIRA

Soutenance prévue le 15 Novembre 2013

Après avis de :

M. RONCERO, Octavio	Directeur de Recherche au CSIC (Madrid, Espagne)	*Rapporteur*
M. LEPETIT, Bruno	Chargé de Recherche au CNRS, HDR (Toulouse, France)	*Rapporteur*

Devant la commission d'examen formée de :

M. RAYEZ, Jean-Claude	Professeur Emérite à l'Université Bordeaux 1 (Talence, France)	*Président du Jury*
M. MONNERVILLE, Maurice	Professeur à l'Université Lille 1 (Villeneuve d'Ascq, France)	
M. BONNET, Laurent	Directeur de Recherche au CNRS (Talence, France)	
M. RUBAYO SONEIRA, Jesús	Professeur à l'InSTEC (C. Habana, CUBA)	

A mis padres
y mi hermano

Abstract

The goal of chemical reaction dynamics theory is the quantitative description of reactive molecular collisions at the atomic scale. Since nuclear motions are difficult to study quantum mechanically, nuclei are often considered as classical objects. However, quantum effects may play a major role in some situation, and the standard classical description does not take them into account. This thesis brings new perspectives on the inclusion into the classical treatment of one of the strongest quantum effects, the quantization of reagents and products.

Keywords: Chemical Reaction Dynamics, Semi-classical Approach, Photodissociation, Wigner Distribution Function.

Résumé

La théorie de la dynamique des processus chimiques élémentaires cherche a décrire quantitativement les collisions réactives à l'échelle atomique. Les mouvements des noyaux étant extrêmement difficiles à traiter dans le formalisme quantique, les atomes sont souvent considérés comme des objets classiques. Cependant, les effets pûrement quantiques jouent un rôle majeur dans certaines situations, alors que la description classique les néglige. Cette thèse apporte de nouvelles perspectives sur l'inclusion, dans le formalisme classique, de forts effets quantiques, à savoir la quantification des mouvements internes des réactifs et produits.

Mots clés: dynamique réactionnelle, approche semi-classique, Photodissociation, Distribution de Wigner.

Agradecimientos

Deseo expresar mis más sinceros agradecimientos a varias personas, sin cuya ayuda, esta Tesis no hubiera sido posible. En particular:

- A Laurent Bonnet, mi tutor en la Universidad de Burdeos, por acogerme como su estudiante y enseñarme un mundo de conocimientos a lo largo de estos tres años. Por su constancia y motivación en el trabajo, decisivos en estos últimos meses. Pero también por sus buenos consejos, que indudablemente van mucho más allá de estas páginas. Por su paciencia. Por su apoyo en los momentos difíciles que inevitablemente acompañan a la distancia. En pocas palabras, por ser más que un tutor un verdadero amigo. Muchas gracias.

- A Pascal Larrégaray, mi otro 'tutor no oficial' en la Universidad de Burdeos. Por su ayuda y preocupación constantes. Por encargarse de mis problemas de una manera casi paternal. Porque además es una de las personas mas honestas, amables y sencillas que uno puede conocer, y tener su amistad es un preciado regalo. Muchas gracias por todo amigo mío.

- A Jesús Rubayo Soneira, mi tutor en el InSTEC. Por ser un ejemplo como educador. Por dedicar tanto tiempo y esfuerzo a lograr que nosotros, los jóvenes que hacemos ciencia hoy en Cuba, nos superemos y podamos seguir en este duro camino. Este agradecimiento viene de parte de todos nosotros, los que siempre te estaremos agradecidos.

- A Maykel Leonardo González Martínez, mi tutor y guía durante mis años en la universidad. Mi buen amigo además. Una de las personas a las que le debo en gran medida que hoy sea Doctor. Muchas gracias.

✘ A Jean-Claude Rayez y Marie-Thérèse Rayez, por esas deliciosas cenas de navidad. A Cédric Crespo y todos los colegas del ISM.

✘ A los buenos amigos que se han preocupado durante todo este tiempo. A los que me acompãron durante la defensa, Carlitos y Oto. Muchas gracias a todos.

Résumé de la thèse de
Mr. W. Arbelo-Gonzalez

Talence, 31 Janvier 2014

NOUVELLES PERSPECTIVES DANS LES TRAITEMENTS CLASSIQUE ET SEMICLASSIQUE DE LA DYNAMIQUE RÉACTIONNELLE

L'objectif principal de la dynamique réactionnelle est de mesurer, décrire théoriquement et analyser les mouvements atomiques se produisants au cours de processus chimiques tels que les collisions bimoléculaires réactives et les photodissociations.

Product pair correlation in CH_3OH photodissociation at 157 nm: the OH + CH_3 channel

Zhichao Chen,[ab] Andre T. J. B. Eppink,[b] Bo Jiang,[a] Gerrit C. Groenenboom,[c] Xueming Yang*[a] and David H. Parker*[b]

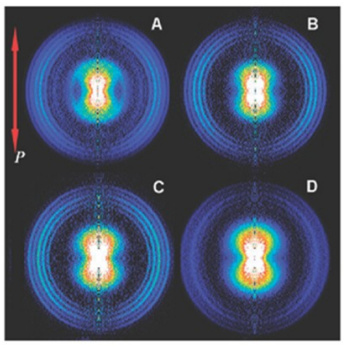

Inverted images of CH_3 (v_2 = 0) (A), CH_3 (v_2 = 1) (B), CH_3 (v_2 = 2) (C) and CH_3 (v_2 = 3) (D) products from the photodissociation of methanol at 157 nm. The double arrow indicates the polarization both of the pump and probe lasers. The ring features correspond to the vibrational states of the coincident OH (v) product.

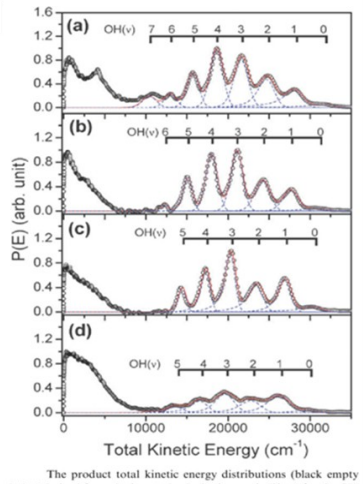

The product total kinetic energy distributions (black empty circles) derived from the inverted velocity images in Fig. 4 for the OH (v) + CH_3 (v_2) channels. The red lines are the fitting results and the blue dash lines are the individual OH vibrational components.

Phys. Chem. Chem. Phys., 2011, **13**, 2350–2355

ISM - Université Bordeaux 1 - CNRS UMR 5255 - F33405 Talence cedex
Tél. : 33(0)5 4000 6282 - Fax : 33(0)5 4000 6994 - e-mail : secretariat@ism.u-bordeaux1.fr –
www.ism.u-bordeaux1.fr

Les expériences modernes de jets moléculaires supersoniques couplées aux techniques spectroscopiques les plus en pointes permettent de mesurer avec une précision spectaculaire la distribution de l'énergie de translation entre produits formés. De plus, ces distributions sont bien souvent corrélées en états, cad, pour un états quantique donné d'un des fragments. C'est le cas des quatre distributions présentées à droite de la figure de la page précédente.

Des approches théoriques précises sont donc nécessaires pour reproduire et rationnaliser ces distributions (ou les prédires lorsque les expériences ne peuvent être réalisées). Par ailleurs, si les expériences évoquées ne nous donnent des informations que sur les mouvements finals des molécules produites, la théorie nous renseigne sur la totalité de la réaction ; il est même possible de visualiser les mouvements atomiques sur l'écran d'un ordinateur dans le cadre de la description classique des noyaux, ou celle quantique dépendante du temps.

Au-delà de son intérêt sur le plan fondamental, la dynamique réactionnelle fourni des données très utiles aux spécialistes des atmosphères planétaires ainsi que ceux des nuages interstellaires, et forme une branche de la physique moléculaire, source continuelle de progrès technologiques depuis plus d'un siècle (lasers, techniques de jets, spectroscopiques, d'ultra vide, etc...).

Pendant plus de trois décennies, les études expérimentales précises furent réservées aux réactions triatomiques. Aujourd'hui, cependant, de nouvelles techniques telles que celle baptisée “velocity imaging” permettent d'étendre ces études précises aux processus polyatomiques, mettant en jeu de 4 à quelques

dizaines d'atomes. Idéalement, il conviendrait de décrire les distributions par des approches quantiques exactes. Cependant, de telles approches conduisent à des calculs d'une telle lourdeur sur le plan numérique, qu'elles sont inenvisageables en pratique pour la majorité des processus polyatomiques.

L'alternative consiste à décrire classiquement les mouvement nucléaires, les equations de Hamilton étants beaucoup plus simples à résoudre numériquement que l'équation de Schrödinger. Bien souvent, néamoins, des effets quantiques majeurs influencent fortement la dynamique, de sorte qu'il faut trouver le moyen de tenir compte de ces effets en incluant des corrections semiclassiques dans le traitement classique, à la lumière des travaux fondateurs de Miller, Marcus, Heller et d'autres au début des années soixante dix [1].

Il existe trois principaux effets: l'effet tunnel au travers de barrières de potentiel, les transitions non adiabatiques entre états electroniques couplés, et la quantification des mouvements internes des produits formés. Si les deux premiers effets on été très étudiés et qu'il existe des méthodes pour en tenir compte dans les calculs de trajectoires classiques, cela n'a pas été le cas du troisième jusqu'au début des années 2000.

L'idée de tenir compte du principe de quantification de Bohr dans les calculs classiques fut alors proposée [1]. Cette idée débouche sur une technique très simple, appellée Gaussian Binning (GB), qui consiste à donner aux trajectoires des poids statistiques d'autant plus forts que les actions vibrationnelles finales sont proches de

valeurs entières. De façon générale, les mouvements de rotation n'ont pas besoin d'être quantifiés de la même façon.

Cette technique GB s'est avérée améliorer fortement l'accord entre prédictions classiques et quantiques dans le cas des réactions à trois atomes. Cependant, l'application de la procédure GB pose de sérieux problèmes pour les réactions polyatomiques, pour des raisons techniques qu'il n'est pas utile d'aborder ici.

Le travail de thèse de Mr. W. Arbelo-Gonzalez a consisté à développer l'approche dite “Backward”, permettant de palier les problèmes précédents. Il a effectué ce travail dans le cadre des réactions de photodissociation, extensible en principe aux collisions bimoléculaires.

Il a de plus étendu l'approche Semi-Classical Wigner (SCW)) de Heller, initialement limitée aux processus colinéaires, à ceux réalistes mettant en jeu des mouvements de rotation. Cette approche est plus performante que la procédure GB pour des processus directs, cad, se déroulants en quelques dizaines de femtosecondes. Elle est basée sur le formalisme de Wigner de la mécanique quantique. L'application de cette extension originale de l'approche SCW à la photodissociation de CH_3I a conduit à un accord spectaculaire entre les prédictions semiclassique et quantique [2].

En conclusion, les travaux de Mr. W. Arbelo-Gonzalez renforcent l'espoir de pouvoir étudier avec précision la dynamique des processus polyatomiques par des approches classiques dans un esprit quantique.

1. L. Bonnet, Classical dynamics of chemical reactions in a quantum spirit, Int. Rev. Phys. Chem., 2013, 32, 171, ainsi que les références mentionnées dans cet article.

2. W. Arbelo-Gonzalez, L. Bonnet and A. Garcia-Vela, New insights into the semiclassical Wigner treatment of photodissociation dynamics, Phys. Chem. Chem. Phys., 2013, 15, 9994.

ISM - Université Bordeaux 1 - CNRS UMR 5255 - F33405 Talence cedex
Tél. : 33(0)5 4000 6282 - Fax : 33(0)5 4000 6994 - e-mail : secretariat@ism.u-bordeaux1.fr –
www.ism.u-bordeaux1.fr

Contents

List of Figures

General introduction

The goal of chemical reaction dynamics is to arrive at a clear understanding of how chemical reactions take place at the atomic scale, and to provide theoretical tools to predict their outcomes [1]. Beyond their fundamental interest, reaction dynamics studies are paving the way to the control of chemical reactions by lasers [2], are providing specialists of planetary atmospheres or interstellar clouds with crucial data [3, 4], and they form a branch of molecular physics which has continuously generated technological progress for more than a century.

Most experiments in this field are energy resolved [5–20], *i.e.*, the quantum state of the reagent species is controlled. In these experiments, the usual observables are the relative velocity/translational energy between final products, their quantum states (i.e. scalar observables; we concentrate on them in this work), the scattering angle between reagent and product velocity vectors for bimolecular reactions, and the angle between the pump laser field and the product velocity vector for photodissociations (vector observables). Although these data only provide information on initial and final atomic motions, they allow one to check the validity of theoretical models describing the whole fate of chemical reactions. We note, however, that femtosecond time-resolved experiments on photofragmentations are increasing, and more and more data on the full-time evolution of these processes are available [21–23].

State-of-the-art descriptions of the previous observables are performed by means of exact quantum scattering calculations [16, 24–33]. The prerequisite for these calculations is that the electronic problem has been solved by the usual methods of quantum chemistry [34, 35] and potential energy surfaces (PES) are available. However, quantum scattering methods lead to very heavy calculations and they are mostly inapplicable to polyatomic processes.

On the other hand, the classical simulation of the dynamics, well-known as the quasi-classical trajectory (QCT) method [36–39], can easily be applied to polyatomic processes [40–43]. Moreover, it is a very powerful interpretative tool which, for instance, allowed John Polanyi to establish his famous rules linking the location of the barrier along the reaction path and the energy partitioning for direct bimolecular reactions [44]. Obviously, the QCT method inherently ignores any quantum effect, except the fact that the vibrational energy of the reagent(s) is kept at the quantized value corresponding to the experimental conditions (see further below in this introduction).

Mostly important quantum effects are tunneling, non adiabatic transitions, and the quantization of internal motions of reagent and product molecules, in particular vibrational ones. How the first two effects may be taken into account in the classical approach has been largely treated before (see, for example, Refs. [45–53] for the first effect, Refs. [37, 54–63] for the second, and references therein). Hence, we shall concentrate on the last effect in this work.

In order to introduce it as clearly as possible, we consider the triatomic collinear inelastic collision between atom A and diatom BC at the classically available energy E with respect to the separated fragments. BC is supposed to be a harmonic oscillator, initially in the vibrational state n_1, and the question we wish to answer here is: what is the probability $P_{n_2 n_1}$ for the final vibrational state of BC to be n_2? The translational energy distribution is then straightforwardly deduced from the previous quantity by invoking the conservation of energy.

The standard way of answering this question, dating back to the early sixties, is as follows. The usual Jacobi coordinates of the problem are R, the distance between A and the center-of-mass of BC and r, the BC bond length. Their conjugate momenta are P_R and P_r, respectively. The usual form of the classical Hamiltonian in the separated fragments is given by

$$\mathcal{H} = \frac{P_R^2}{2\mu} + \mathcal{H}_{\rm v}, \tag{1}$$

with

$$\mathcal{H}_{\rm v} = \frac{P_r^2}{2m} + \frac{1}{2} m\omega^2 (r - r_e)^2. \tag{2}$$

$\mathcal{H}_{\rm v}$ is the vibrational Hamiltonian. μ is the reduced mass of A with respect to BC, m is the reduced mass of BC, r_e its equilibrium bond length and ω is 2π times its vibrational frequency.

Instead of r and P_r, it is quite convenient to consider the angle-action variables

q and n, respectively defined by

$$r = r_e + \left[\frac{\hbar(2n+1)}{m\omega}\right]^{1/2} \sin q \tag{3}$$

and

$$P_r = [m\hbar\omega(2n+1)]^{1/2} \cos q, \tag{4}$$

where $\hbar$ is Planck constant h over 2π (see Appendix A in Ref. [64], and references therein). q belongs to the range $[0,\, 2\pi]$. In terms of these new coordinates, the vibrational Hamiltonian reads

$$\mathcal{H}_{\rm v} = \hbar\omega\Big(n + \frac{1}{2}\Big), \tag{5}$$

i.e., its form is exactly the same as in quantum mechanics. Hence, the vibrational action n appears to be the classical analogue of the vibrational quantum number.

At time zero, corresponding to a large value R_i of R such that BC vibrates freely, n is thus kept at the value n_1 and q at a given value $\bar{q}$. The reaction function provides the final value $n(\bar{q})$ of n in terms of the initial angle $\bar{q}$. The standard expression of $P_{n_2 n_1}$ is then given by

$$P_{n_2 n_1} = \frac{1}{2\pi}\int_0^{2\pi} d\bar{q}\; \Delta[n(\bar{q}); n_2], \tag{6}$$

where $\Delta[x; x^*]$ is a square barrier function of unitary width and height, formally defined as

$$\begin{aligned} \Delta(x; x^*) &= \Theta\left(x^* + 1/2 - x\right)\Theta\left(x - x^* + 1/2\right), \\ &= \begin{cases} 1, & \text{if} \quad x \in [x^* - 1/2, x^* + 1/2] \\ 0, & \text{if} \quad x \notin [x^* - 1/2, x^* + 1/2]. \end{cases} \end{aligned} \tag{7}$$

$\Theta(x)$ is the well-known Heaviside function. In other words, trajectories contribute to the state n_2 closest to the final action $n(\bar{q})$. Such a procedure is called *standard binning* (SB), or *histogram binning* (HB) [36–39, 64].

Using the fact that within the Monte-Carlo approximation

$$\int_0^1 f(x)dx \simeq \frac{1}{N}\sum_{i=1}^{N} f(x_i), \tag{8}$$

where the x_i are randomly selected and $f(x)$ is an arbitrary function, Eq. (6) is readily found to be

$$P_{n_2 n_1} = \frac{N_{n_2}}{N}. \tag{9}$$

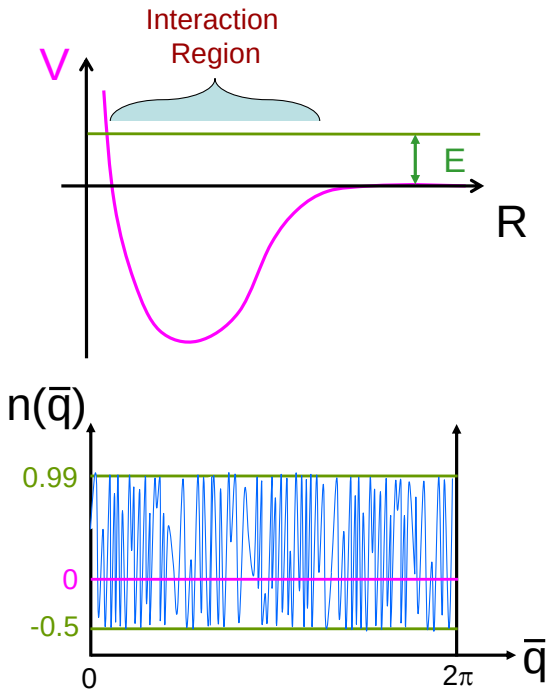

Figure 1: Upper panel: energy profile along the steepest descent path on $V(R, r)$. The energy available to the separated fragments is denoted E. Inside the well, A and BC strongly interact, thus forming a long-lived complex the dynamics of which are chaotic. Lower panel: as a consequence, the final action $n(\bar{q})$ varies in terms of $\bar{q}$ on an apparently erratic way, between -0.5 and an upper bound, equal to 0.99 if $E = 1.49\hbar\omega$.

In Eq. (9), N is the total number of trajectories run (with $\bar{q}$ randomly selected) while N_{n_2} is the number of trajectories ending with $|n(\bar{q}) - n_2| \leq 1/2$.

This convenient *ad-hoc* SB procedure leads, however, to inconsistencies in the limit where the energy E and consequently, the number of available states is small. Assume, for instance, that the collision involves a deep well within the interaction region, as illustrated in Fig. 1, with no barrier between the well and the separated fragments. The dynamics are thus expected to be chaotic, and $n(\bar{q})$ should be randomly distributed between -0.5 and its maximum value consistent with E. If $E = 1.49\hbar\omega$, for instance, the previous range is [-0.5, 0.99]. Moreover, both n_1 and n_2 are necessarily equal to 0 and therefore, P_{00} is equal to 1. Nevertheless, the SB procedure leads to $P_{00} \simeq 2/3$ and $P_{10} \simeq 1/3$, since [-0.5, 0.5] and [0.5, 0.99] represent approximately 2/3 and 1/3 of [-0.5, 0.99], respectively. Consequently, P_{10} is non zero though $n_2 = 1$ is a closed channel.

To go round this difficulty, the Gaussian binning (GB) procedure was proposed [64], which amounts to replace the standard bin in Eq. (6) by a Gaussian

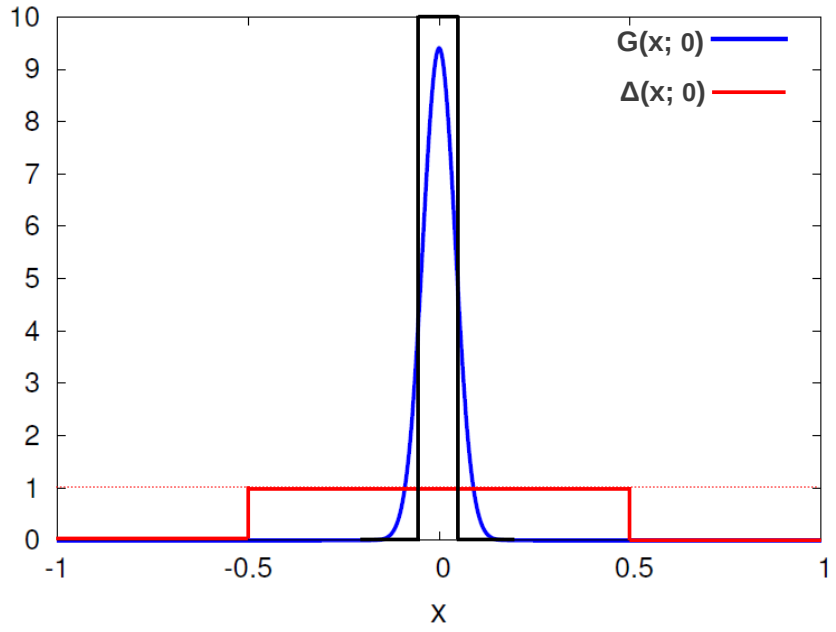

Figure 2: The Gaussian function $G[x,0]$ with $\epsilon \backsimeq 0.06$ and the standard bin $\Delta(x;0)$, are represented by the blue and red curves, respectively. Using $G(x;0)$ roughly amounts to use the 10 % wide black bin.

much narrower than 1. The resulting expression is

$$P_{n_2 n_1} = \frac{\int_0^{2\pi} d\bar{q}\; G[n(\bar{q}); n_2]}{\sum_{n_2} \int_0^{2\pi} d\bar{q}\; G[n(\bar{q}); n_2]} \tag{10}$$

with

$$G(x; x^*) = \frac{\exp[-(x-x^*)^2/\epsilon^2]}{\pi^{1/2}\epsilon}. \tag{11}$$

In practice, ϵ is usually kept at ~ 0.06 in order to get a full width at half maximum of the Gaussian of ~ 10 %. The $G(x;0)$ and $\Delta(x;0)$ functions are represented in Fig. 2. We note that using $G(x;0)$ roughly amounts to use the 10 % wide black bin in the same figure, for out of the range [-0.05, 0.05], $G(x;0)$ takes small or negligible values. The denominator 2π in Eq. (6), has been replaced by the denominator in Eq. (10) in order to ensure that the final state distribution is normalized to unity.

Going back to the previous numerical example, $n_2 = 0$ is the only value for which $n_2 = n(\bar{q})$ has roots (see the lower panel in Fig. 1), thus making $G[n(\bar{q}); n_2]$ negligible for $n_2 \geq 1$ (and ϵ sufficiently small). It is thus clear that the correct expectations $P_{00} = 1$ and $P_{10} = 0$ are recovered within the GB procedure.

The MC estimation of Eq. (10) is

$$P_{n_2 n_1} = \frac{\sum_{i=1}^{N} G[n(\bar{q}_i); n_2]}{\sum_{n_2} \sum_{i=1}^{N} G[n(\bar{q}_i); n_2]}. \tag{12}$$

At the difference with Eq. (6), Eq. (10) with ϵ tending to 0, *i.e.*, with the Gaussian tending to a delta function, is shown to derive from exact quantum mechanical expressions in the semiclassical limit [64], *i.e.*, when making $\hbar$ tend to 0 in the previous expressions [65–67]. In this limit, only those trajectories starting from integer actions and ending with integer actions are contributing to the collision. The GB procedure is thus a practical way to deal with Bohr quantization principle. More details on the QCT-GB method can be found in Ref. [64].

QCT-GB has been successfully applied to many reactions over the last decade [64], and one of the best improvements of GB over SB is shown in Fig. 3 in the case of the reaction between O(^{3}P) and HCl. The process under scrutiny is described in a realistic way, *i.e.*, rotation motions are taken into account. As a matter of fact, using the GB procedure shifts the vibrationally resolved rotational state distributions towards the right and makes them narrower, improving thereby the agreement between the QCT predictions and the exact quantum scattering results.

The GB procedure, however, has some drawbacks, and the goal of this thesis is to reveal some of them and possibly, propose some approaches in order to correct them. Two families of processes will be considered in this work, photodissociations and reactions involving *strongly bound species*, either molecules, or radicals. Within the first type of process, we consider direct photodissociation and a particular kind of indirect photodissociation called *vibrational predissociation* (VP), frequent in *van de Waals* (vdW) complexes. The VP of vdW clusters have been the object of deep studies at the 'Instituto Superior de Tecnologías y Ciencias Aplicadas', in La Havana, while intense research on reaction dynamics has been carried out at the 'Institut des Sciences Moléculaires de l'Université' in Bordeaux. Checking the ability of QCT-GB to describe these two different types of processes fully justified completing the present joint-doctorate in the two previous institutions.

The thesis is divided in four parts, the common denominator of which is the development of accurate trajectory-based methods to avoid solving Schrödinger equation for the nuclei:

Chapter I: Most QCT-GB calculations published so far used the following MC

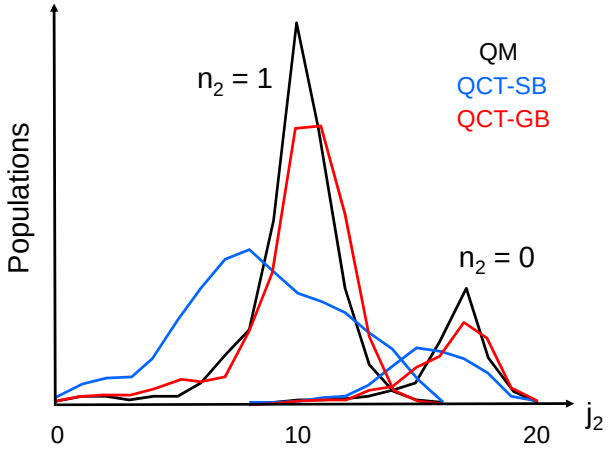

Figure 3: Quantum mechanical (QM), QCT-SB and QCT-GB state-resolved distributions for the direct reaction $O(^3P) + HCl(n_1 = 2,\ j_1 = 1) \longrightarrow OH(n_2 = 0,\ 1,\ j_2) + Cl$.

expression

$$P_{n_2 n_1} = \frac{\sum_{i=1}^{N} G[n(\bar{q}_i); n_2]}{N}, \tag{13}$$

instead of Eq. (12). The above equation is obtained from Eq. (9) by replacing N_{n_2} by the sum of Gaussian statistical weights associated with n_2. This expression turns out to be the one obtained from classical S matrix theory (CSMT), *i.e.*, from the simplest (yet quite complex) semiclassical approach of molecular collisions pioneered by Miller and Marcus in the early seventies [65–67]. However, CSMT suffers from not being strictly unitary, in particular when only a few quantum states are available to the final fragments. This makes Eq. (13) non unitary itself, i.e., the sum over n_2 of $P_{n_2 n_1}$ is not exactly equal to 1. Eq. (12) obviously eliminates this problem. This issue is discussed at length in this first part.

Chapter II: Van der Waals complexes composed of a rare gas atom and a halogen molecule (Rg-X_2) have been studied intensely during the past three decades. One of the main reasons is that, despite their relative simplicity, these complexes have been shown to exhibit a wide variety of dynamical behaviors, *e.g.*, intramolecular vibrational relaxation (IVR), electronic predissociation, VP, etc.; and therefore have become important prototypes for rationalizing inter- and intramolecular energy transfer mechanisms at the state-to-state level. In this second part, we check

the ability of QCT-GB, and more generally, the classical description, to describe the VP of tetratomic complexes of the type Rg_2-X_2. If many studies of this type have been performed for triatomic complexes, they have been very sparse for tetratomic ones. We shall see that fundamental limitations seem to prevent the QCT method from being quantitative for the VP, whatever the binning procedure adopted. Genuine quantum effects have to be understood and adequate semiclassical approaches developed before being able to properly account for vibrational predissociation.

Chapter III: A known drawback of the GB procedure is its numerical inefficiency for polyatomic processes. As previously seen, the GB procedure, for triatomic reactions, involves one Gaussian for pseudo-quantizing the vibration motion of the final diatom. It is thus clear from Fig. 2 that only $\sim 10\%$ of the trajectories contributing to SB populations do actually contribute to GB populations. These trajectories reach the products with a vibrational action within (or close to) the thin black bin, where Gaussian weights are large, while the remaining paths carry small, or negligible weights. As a consequence, it is necessary to run ~ 10 times more trajectories with GB than with SB to get the same level of convergence of the final results (or signal-to-noise ratio). For tetratomic reactions leading to two diatomic molecules, the whole Gaussian weight is the product of two Gaussians, one for each vibrational degree-of-freedom. The first weight puts emphasis on $\sim 10\%$ of the trajectories contributing to SB populations and the second weight puts emphasis on $\sim 10\%$ of the previous $\sim 10\%$, i.e. $\sim 1\%$ on the whole. Therefore, it is necessary to run ~ 100 times more trajectories with GB than with SB in the present case. The same reasoning shows that this number scales in general as 10^N where N is the number of product vibrational modes. For a polyatomic reaction such as $F + CH_4 \longrightarrow FH + CH_3$, and its isotopic variants, much studied experimentally in the recent years [68], the previous number is 10^7. Since one needs at least a few hundreds of thousands of trajectories within the SB procedure, one should run a few trillion of trajectories within the GB procedure, which is mostly unfeasible. In practice, GB turns out to be only applicable to three and four atom reactions. In order to circumvent this difficulty, Czakó and Bowman proposed a few years ago to pseudo-quantize, with one Gaussian only, the total vibrational energy instead of the vibrational actions [69]. Consequently, this procedure, called 1GB [70], allows for a huge amount of computational savings for large systems. The strict equivalence between the 1GB and GB procedures was subsequently proved in the limiting situation where the distribution in the product vibrational action space consistent with the available energy is uniform [70]. It can also be shown that for a sufficiently smooth distribution in the action space, the 1GB procedure makes sense, but in the general case, it cannot be justified on the basis of solid semiclassical arguments.

However, it was recently shown for photodissociation processes how the so-called *backward picture of molecular collisions* allows to account for the Bohr quantization principle in a much more powerful way than QCT-GB [71]. This method, which allows the analytical removal of the Gaussians in the analogue of Eq. (10) for photodissociations (see chapter III) and hence, ignores the convergence issue of the GB procedure, had only been applied to a collinear triatomic model of fragmentation when I began my thesis. In the present chapter, the method is tested on the realistic three-dimensional photodissociation of the van der Waals complex $NeBr_2(B)$.

Chapter IV: We recenty applied the previous backward approach to Guo's triatomic-like model of methyl iodide photodissociation [72], for which rigorous quantum final state populations are available. However, we did not observe the close agreement between the classical and the quantum predictions we were expecting. In our attempt to explain the origin of this disagreement, we finally realized that one may actually go beyond QCT calculations based on Bohr quantization by using a more refined method in the hierarchy of semiclassical approaches, called the *semiclassical Wigner method*. This method was pioneered by Heller in the late 70's [73, 74], but was initially restricted to collinear processes. However, we have recently made it applicable to realistic three-dimensional processes by including rotational motions. This method, based on the Wigner picture of quantum mechanics [75, 76], follows the exact quantum phase space formulation of state-resolved absorption cross sections as far as possible, before introducing classical mechanics in a very natural way. The method, as proposed by Heller, is not numerically powerful. However, implementing it within the backward picture of the dynamics strongly speeds up the calculations. The predictions of the method mostly appear to be in quantitative agreement with the exact quantum mechanical results.

We now enter into the details of these four works.

CHAPTER I

Normalization of the QCT-GB method for indirect reactions

Summary

We focus in this chapter on the description of indirect reactions by means of the QCT+GB method and the phase space theory (PST). The normalization issue of the GB procedure is discussed and a simple way to solved it is proposed. This new procedure, called normalized Gaussian binning, is rationalized on the basis of statistical arguments and tested for the reaction $D^+ + H_2$.

I.1 Theoretical introduction

Let us consider the following indirect reaction at collision energy E_c,

$$\mathrm{A} + \mathrm{BC}(n_1{=}0, j_1{=}0) \rightarrow \mathrm{ABC}^* \rightarrow \begin{cases} \mathrm{A} + \mathrm{BC}(n_2, j_2), & \text{channel} \quad \gamma \\ \mathrm{B} + \mathrm{AC}(n_2', j_2'), & \text{channel} \quad \beta_1 \\ \mathrm{C} + \mathrm{AB}(n_2', j_2'), & \text{channel} \quad \beta_2, \end{cases} \tag{I.1}$$

where γ denotes the non-reactive channel and β_i the reactive ones. For consistency with the next section, we only focus on the particular case B≡C, which makes both β_i channels strictly equivalent. Indexes (n_1, j_1) denote the rovibra-

tional quantum number of the diatomic constituent in the reagents, while (n_2, j_2) and (n_2', j_2') have and analogous meaning in the products of the α and β_i channels, respectively.

For process I.1, the exact expression of the state-resolved integral cross section (ICS) for reaction (β_i channels) is given by [77, 78]

$$\begin{aligned}\sigma_{n_2'j_2'} &= \frac{\pi}{k_c^2(2j_1+1)} \sum_{Jl_2'l_1} (2J+1) P^J_{n_2'j_2'l_2'} \\ &= \frac{\pi}{k_c^2} \sum_{Jl_2'} (2J+1) P^J_{n_2'j_2'l_2'},\end{aligned} \tag{I.2}$$

which results from the fact that $j_1 = 0$ and therefore the initial orbital quantum number l_1 is equal the total angular momentum quantum number J. l_2' represents the product orbital quantum number. k_c is the linear momentum related to E_c by $k_c = (2\mu E_c)^{1/2}/\hbar$, where μ is the reduced mass of A with respect to BC. $P^J_{n_2'j_2'l_2'}$ is the probability to go from (n_1, j_1, l_1) to (n_2', j_2', l_2') at J and E_c. With Eq. (I.2), the total ICS is

$$\sigma = \sum_{n_2'j_2'} \sigma_{n_2'j_2'}. \tag{I.3}$$

By just setting $(n_2', j_2', l_2') = (n_2, j_2, l_2)$ in Eqs. (I.2) and (I.3), analogous expressions of the state-resolved and total ICS's are obtained for the non-reactive channel.

Normalization of the QCT+GB method

According to the classical S matrix theory (CSMT) in the random phase approximation, it is possible to show that [64]

$$P^J_{n_2'j_2'l_2'} = \frac{1}{(2\pi)^3} \int_{D_\mathrm{R}} \boldsymbol{d\bar{q}}\, \delta[n'(\bar{\boldsymbol{q}}) - n_2']\, \delta[j'(\bar{\boldsymbol{q}}) - j_2']\, \delta[l'(\bar{\boldsymbol{q}}) - l_2'], \tag{I.4}$$

with $\bar{\boldsymbol{q}} = (\bar{q}_n, \bar{q}_j, \bar{q}_l)$, and

$$P^J_{n_2j_2l_2} = \frac{1}{(2\pi)^3} \int_{D_\mathrm{NR}} \boldsymbol{d\bar{q}}\, \delta[n(\bar{\boldsymbol{q}}) - n_2]\, \delta[j(\bar{\boldsymbol{q}}) - j_2]\, \delta[l(\bar{\boldsymbol{q}}) - l_2]. \tag{I.5}$$

The variables involved in these equations have the following meaning. Let us define as R the distance between A and the center of mass of BC and r the BC bond length; and set the origin of time, $t = 0$, by a large value $\bar{R}$ of R, so that A and BC do not interact each other. $\bar{q}_n$, $\bar{q}_j$ and $\bar{q}_l$ denote the angles conjugated to the vibrational action $\bar{n}$ of BC, its rotational angular momentum $\bar{j}$ and the orbital angular momentum $\bar{l}$, respectively, at R=$\bar{R}$. They all belong to

the range $[0, 2\pi]$. The set of initial actions $(\bar{n}, \bar{j}, \bar{l})$, with the angular momentums expressed in units of $\hbar$, are kept at (n_1, j_1, l_1) at $t = 0$. Far in the products of the β_i channels, $n'(\bar{\boldsymbol{q}})$, $j'(\bar{\boldsymbol{q}})$ and $l'(\bar{\boldsymbol{q}})$ represents the final vibrational action of the diatom, its rotational angular momentum and the orbital angular momentum, respectively. $n(\bar{\boldsymbol{q}})$, $j(\bar{\boldsymbol{q}})$ and $l(\bar{\boldsymbol{q}})$ have an analogous meaning in the γ channel. In order to avoid heavy notations, only the dependence on $\bar{\boldsymbol{q}}$ of the final actions have been explicitly represented, though they actually depend on $\bar{n}$, $\bar{j}$, $\bar{l}$, J and E_c. Integration in Eqs. (I.4) and (I.5) is over initial angles leading to reactive and non-reactive trajectories, respectively.

When rotational motions are considered in process I.3, the GB procedure amounts to approximate

$$P^J_{n'_2 j'_2 l'_2} \simeq \frac{1}{(2\pi)^3} \int_{D_\mathrm{R}} \boldsymbol{d\bar{q}}\; G[n'(\bar{\boldsymbol{q}}); n'_2]\; \Delta[j'(\bar{\boldsymbol{q}}); j'_2]\; \Delta[l'(\bar{\boldsymbol{q}}); l'_2], \tag{I.6}$$

with $G(x; x^*)$ and $\Delta(x; x^*)$ given by Eqs. (11) and (7), respectively. A similar expression stands for the γ channel. Rotational motions of the products are treated classically while Bohr quantization of vibrational motion is taken into account by inserting the Gaussian function on the final vibrational action.

Inserting Eq. (I.6) into Eq. (I.2), the GB expression of the state-resolved ICS becomes

$$\begin{aligned}\sigma^{\mathrm{GB}}_{n'_2 j'_2} &= \frac{\pi}{k_c^2} \sum_J (2J+1) \frac{1}{(2\pi)^3} \int_{D_\mathrm{R}} \boldsymbol{d\bar{q}}\; G[n'(\bar{\boldsymbol{q}}); n'_2]\; \Delta[j'(\bar{\boldsymbol{q}}); j'_2] \sum_{l'_2} \Delta[l'(\bar{\boldsymbol{q}}); l'_2] \\ &= \frac{\pi}{k_c^2} \sum_J (2J+1) \frac{1}{(2\pi)^3} \int_{D_\mathrm{R}} \boldsymbol{d\bar{q}}\; G[n'(\bar{\boldsymbol{q}}); n'_2]\; \Delta[j'(\bar{\boldsymbol{q}}); j'_2],\end{aligned}$$

which results from the fact that once $l'(\bar{\boldsymbol{q}})$ is fixed, $\sum_{l'_2} \Delta[l'(\bar{\boldsymbol{q}}); l'_2] = 1$. For a similar reason, the total ICS can read

$$\sigma_{\mathrm{GB}} = \frac{\pi}{k_c^2} \sum_J (2J+1) \frac{1}{(2\pi)^3} \int_{D_\mathrm{R}} \boldsymbol{d\bar{q}} \sum_{n'_2} G[n'(\bar{\boldsymbol{q}}); n'_2]. \tag{I.7}$$

As we stated before, rotational motions are treated classically, so we replace the $2J + 1$ factor by its classical analogue $2J$, and transform the sum over J by an integral. We obtain then that

$$\sigma_{\mathrm{GB}} = \pi \left(\frac{J_M}{k_c}\right)^2 \frac{1}{J_M^2} \int_0^{J_M^2} dJ^2\; \eta_{GB}(J), \tag{I.8}$$

with

$$\eta_{\mathrm{GB}}(J) = \frac{1}{(2\pi)^3} \int_{D_{\mathrm{R}}} \boldsymbol{d\bar{q}} \sum_{n_2'} G[n'(\bar{\boldsymbol{q}}); n_2']. \tag{I.9}$$

J_M is the maximum value of J consistent with reaction. The sum over n_2' is from $n_2' = 0$ to the maximum value consistent with the available energy. Let us keep in mind that the dependence on J in Eq. (I.9) is implicit in $n'(\bar{\boldsymbol{q}})$.

Using Eq. (8), the MC expression of Eq. (I.8) can be written as

$$\sigma_{\mathrm{GB}} = \pi \left(\frac{J_M}{k_c}\right)^2 \frac{1}{N} \sum_{i=1}^{N_{\mathrm{R}}} \sum_{n_2'} G[n'(\bar{\boldsymbol{q}}_i); n_2'], \tag{I.10}$$

where N is the total number of trajectories run and N_{R} the number of reactive ones. $\bar{\boldsymbol{q}}_i$ compacts the initial angles for the ith trajectory, which are randomly selected.

Within the SB procedure, $G[n'(\bar{\boldsymbol{q}}); n_2']$ is replaced by $\Delta[n'(\bar{\boldsymbol{q}}); n_2']$ in Eq. (I.6). Following the same reasonings as before, the MC expression of the total ICS is given by the simple expression

$$\sigma_{\mathrm{SB}} = \pi \left(\frac{J_M}{k_c}\right)^2 \frac{N_{\mathrm{R}}}{N}. \tag{I.11}$$

Naturally, replacing $n'(\bar{\boldsymbol{q}}_i)$ by $n(\bar{\boldsymbol{q}}_i)$ and n_2' by n_2; and summing over non-reactive trajectories N_{NR} (which results from integrating over the domain of initial angles leading to non-reactive trajectories, D_{NR}), analogous expressions to Eqs. (I.10) and (I.11) for the γ channel are readily found.

Now, let us calculate the probability for the system to end in any final state of any product channel, at J and E_c, i.e. the quantity

$$Q(J, E_c) = \sum_{n_2' j_2' l_2'} P^J_{n_2' j_2' l_2'} + \sum_{n_2 j_2 l_2} P^J_{n_2 j_2 l_2}. \tag{I.12}$$

Substituting $P^J_{n_2' j_2' l_2'}$ and $P^J_{n_2 j_2 l_2}$ by their corresponding SB expressions, and using the fact that $\sum_{x_i} \Delta[x(\bar{\boldsymbol{q}}); x_i] = 1$, it is relatively easy to show that $Q(J, E_c) = 1$, as it should be expected from a probability function normalized to unity. Replacing $P^J_{n_2' j_2' l_2'}$ and $P^J_{n_2 j_2 l_2}$ by their corresponding GB expressions, however, we find that

$$Q(J, E_c) = \frac{1}{(2\pi)^3} \left\{ \int_{D_{\mathrm{R}}} \boldsymbol{d\bar{q}} \sum_{n_2'} G[n'(\bar{\boldsymbol{q}}); n_2'] + \int_{D_{\mathrm{NR}}} \boldsymbol{d\bar{q}} \sum_{n_2} G[n(\bar{\boldsymbol{q}}); n_2] \right\}. \tag{I.13}$$

which, in general, is not necessary equal to 1. This means that the resulting

GB population are not normalized to unity. As was already mentioned in the introduction, that is one of the issues of the GB procedure, which seems to be consequence of the fact that the CSMT is not necessary normalized to unity, specially in the quantum regime, where only a few vibrational states are available to the final fragments.

A straightforward solution to get normalized final populations, called in the following normalized Gaussian binning (NGB), is simply to replace $P^J_{n_2'j_2'l_2'}$ by $P^J_{n_2'j_2'l_2'}/Q(J,E_c)$ and $P^J_{n_2j_2l_2}$ by $P^J_{n_2j_2l_2}/Q(J,E_c)$. By doing so, Eq. (I.9) takes the form

$$\eta_{\mathrm{NGB}}(J) = \frac{\int_{D_\mathrm{R}} \boldsymbol{d\bar{q}} \sum_{n_2'} G[n'(\bar{\boldsymbol{q}}); n_2']}{\int_{D_\mathrm{R}} \boldsymbol{d\bar{q}} \sum_{n_2'} G[n'(\bar{\boldsymbol{q}}); n_2'] + \int_{D_\mathrm{NR}} \boldsymbol{d\bar{q}} \sum_{n_2} G[n(\bar{\boldsymbol{q}}); n_2]}. \tag{I.14}$$

The total ICS, now normalized, reads

$$\sigma_{\mathrm{NGB}} = \pi \left(\frac{J_M}{k_c}\right)^2 \frac{1}{J_M^2} \int_0^{J_M^2} dJ^2 \; \eta_{\mathrm{NGB}}(J). \tag{I.15}$$

The MC expressions of Eqs. (I.14) and (I.15) can be written as

$$\eta_{\mathrm{NGB}}(J_k) = \frac{\sum_{i=1}^{N_r} \sum_{n_2'} G[n'(\bar{\boldsymbol{q}}_i); n_2']}{\sum_{i=1}^{N_r} \sum_{n_2'} G[n'(\bar{\boldsymbol{q}}_i); n_2'] + \sum_{i=N_r+1}^{N} \sum_{n_2} G[n(\bar{\boldsymbol{q}}_i); n_2]} \tag{I.16}$$

and

$$\sigma_{\mathrm{NGB}} = \pi \left(\frac{J_M}{k_c}\right)^2 \frac{1}{N_J} \sum_{k=1}^{N_J} \eta_{\mathrm{NGB}}(J_k), \tag{I.17}$$

respectively. N_J is the number J^2 values randomly selected and N the number of trajectories run for each of them. Trajectories from $i = N_r + 1$ to N are the non-reactive ones. Analogous expressions of $\eta_{\mathrm{NGB}}(J_k)$ and σ_{NGB} for the non-reactive channel are readily obtained in the same way than before.

In practice, no matters which procedure we use, initial conditions are generated in angle-action coordinates, with the classical actions exactly matching the initial rovibrational quantum numbers and phases randomly selected. Since the integration of classical equations of motion in angle-action may lead to numerical instabilities, a transformation to Cartesian coordinates needs to be done. Appendix A from next section presents in great details such a transformation for triatomic molecules. Trajectories are then run until they reach the product region, usually defined by a large value R'_{diss} of R' (R_{diss} in the γ channel). Total ICS's are computed simply counting trajectories (Eq. I.11) in the case of SB, summing the statistical Gaussian weights of each trajectory (Eq. I.10) in the case of GB, or normalizing the GB ICS's in the sense of Eqs. (I.16)-(I.17).

Elements of PST

Let us assume now that the interaction between the fragments in process I.1 is governed by isotropic long-range attractive forces of the form $-C/R^6$. Let us also assume that a deep well is present along the reaction coordinate, and the intermediate complex lives enough (a few ps) for complete energy randomization of the available energy among the internal degrees-of-freedom. In other words, we assume that the phase space distribution inside the well becomes microcanonical.

Under these assumptions, the PST [79–84] states that the reaction probability for reaction I.1 can be written as

$$P^J = P_{\rm cap}(E_c)\frac{2F_\beta}{F_\gamma + 2F_\beta}, \tag{I.18}$$

where F_γ and F_β are the fluxes towards the reagents and one of the two equivalent product channels, respectively. $P_{\rm cap}(E_c)$ is the intermediate complex formation probability at E_c and J, estimated by the classical Langevin capture model [79–84]. Within the framework of this model, $P_{\rm cap}(E_c) = 1$ for $\bar{l} \leq \bar{l}_M$, and zero otherwise, with

$$\bar{l}_M = (3\mu)^{1/3}(2C)^{1/6}(E_c)^{1/6}. \tag{I.19}$$

$\bar{l}_M$ is the maximum possible value of initial orbital quantum momentum $\bar{l}$, consistent with a translational energy E_c. Note that we keep using the same notation than before.

Since in our particular case $\bar{j} = 0$, then $J = \bar{l}$ and therefore $J_M = \bar{l}_M$. We can formally write that

$$P_{\rm cap}(E_c) = \begin{cases} 1, & \text{if} \quad J \leq J_M \\ 0, & \text{if} \quad J > J_M, \end{cases} \tag{I.20}$$

with J_M given by Eq. (I.19). Consequently, the total ICS is

$$\sigma_{\rm PST} = \frac{\pi}{k_c^2}\int_0^{J_M^2} dJ^2 \frac{2F_\beta}{F_\gamma + 2F_\beta}. \tag{I.21}$$

For processes governed by long-range forces, as our case here, it is a fair approximation to calculate the flux of trajectories F_γ and F_β through a phase space surface called the transition state (TS). This surface is the frontier between the SCR and the separated fragments, i.e., once a trajectory crosses the TS, it cannot cross back and the subsequent movement only leads to fragmentation. The TS can be defined as a phase space surface perpendicular to R, located at $R = R^\ddagger(E_T)$. Given a value E_T of translational energy, $R^\ddagger(E_T)$ cor-

responds with the value of R for which the orbital angular momentum l takes its maximum possible value l_M, i.e., the one given by an analogous expression to Eq. (I.19). Moreover, for $R = R^{\ddagger}(E_T)$ the system describes circular periodic orbits and therefore $l_M = kR^{\ddagger}(E_T)$, where $k = (2\mu E_T)^{1/2}$. Thus,

$$R^{\ddagger}(E_T) = \left(\frac{3}{2}\right)^{1/3} \left(\frac{6C}{E_T}\right)^{1/6}. \tag{I.22}$$

Now we can calculate the different fluxes. For the γ channel, for instance, the phase space flux of trajectories at total energy E and total angular momentum J, through the reagent TS defined by $R = R^{\ddagger}$, reads

$$F_\gamma = \int \boldsymbol{d\Gamma} \delta(R - R^{\ddagger}) \frac{P_R}{\mu} \Theta(P_R) \delta(E - \mathcal{H}) \delta(J - J'), \tag{I.23}$$

with

$$\boldsymbol{d\Gamma} = dR\, dP_R\, dq_n\, dn\, dJ'\, dM\, dj\, dl\, dq_J\, dq_M\, dq_j\, dq_l. \tag{I.24}$$

In this set coordinates, the actions (n, j, l) have the same meaning than before and (q_n, q_j, q_l) are their conjugated angles. P_R is the momentum conjugated to R. J' is the total angular momentum and M its space-fixed component, which is rigorously equal to J since $\bar{j} = 0$. q_J and q_M are the conjugated angles to J' and M, respectively. Moreover, $\mathcal{H}$ is the Hamilton function corresponding to the γ channel.

It is not difficult to show that Eq. (I.23) reduces to

$$F_\gamma^C = (2\pi)^5 J \int dn \int djdl\, \Theta(E - E_{nj}), \tag{I.25}$$

where E_{nj} is the rovibrational energy of the diatomic fragment in terms of n and j. Integration in the (j, l) plane can be easily performed, for instance, by a MC procedure, subject to the constrain

$$|j - J| \leq l \leq j + J, \tag{I.26}$$

i.e., the triangular inequality. Also, once n and j are selected in Eq. (I.25), that implicitly fixed the available energy to the translation, $E - E_{nj}$, and therefore the maximum possible value l_M of l (see Eq. I.19). We also have to keep in mind that once n is fixed, the maximum possible value of j is for $l = 0$.

In a pure classical description, the final vibrational motion is not quantized and therefore we integrate over n in Eq. (I.25). Within a semi-classical treatment,

quantization of n is taken into account and Eq. (I.25) transforms into

$$F_{\gamma}^{SC} = (2\pi)^5 J \sum_{n=1}^{n_{\max}} \int djdl\ \Theta(E - E_{nj}), \tag{I.27}$$

where $n_{\max}$ is the maximum value of n consistent with E. Using in Eqs. (I.25) and Eq. (I.27) parameters from the product channel, analogous expressions for F_{β}^{C} and F_{β}^{SC} are straightforwardly obtained.

Next section continues now with the application of the methods presented in this section to the reaction $D^+ + H_2$.

I.2 Publication

Computational and Theoretical Chemistry 990 (2012) 30–38

Contents lists available at SciVerse ScienceDirect

Computational and Theoretical Chemistry

journal homepage: www.elsevier.com/locate/comptc

Normalization of the Gaussian binning trajectory method for indirect reactions

L. Bonnet [a,*], P. Larrégaray [a], W. Arbelo-González [a,b], M. de Castro-Vítores [c]

[a] Institut des Sciences Moléculaires, Université Bordeaux 1, 351 Cours de la Libration, 33405 Talence Cedex, France
[b] Departamento de Física General, Instituto Superior de Tecnologías y Ciencias Aplicadas, Habana 6163, Cuba
[c] Donostia International Physics Center DIPC, Paseo Manuel de Lardizabal 4, 20018 San Sebastián, Spain

ARTICLE INFO

Article history:
Received 26 June 2011
Received in revised form 11 October 2011
Accepted 1 November 2011
Available online 15 November 2011

Keywords:
Reaction dynamics
Indirect processes
Classical trajectories
Gaussian binning
Normalization issue

ABSTRACT

The method of Gaussian weighted trajectories combines the classical description of gas-phase chemical reactions and Bohr quantization of final fragment vibrations. In practice, trajectories are assigned Gaussian statistical weights such that the closer the final vibrational actions to integer values, the larger the weights. This approach, called classical trajectory method with Gaussian binning (CT-GB) in the following, is a practical implementation of classical *S* matrix theory (CSMT) in the random phase approximation. However, CSMT is non unitary and consequently, the most utilized version of CT-GB is not strictly normalized to unity. In other words, the sum of product and re-formed reagent state populations is not exactly equal to one. The purpose of this work is to show that normalizing these populations to unity should significantly improve the quality of the predictions for indirect reactions. This finding is illustrated from calculations on the $D^+ + H_2$ reaction.

1. Introduction

In recent years, many gas-phase chemical reactions [1–19] have been studied by means of the method of Gaussian weighted trajectories, a particular implementation of the classical trajectory (CT) method within the Gaussian binning (GB) procedure [20–24]. This approach is an alternative to the classic quasi-classical trajectory (QCT) method with standard binning (SB), used since the sixties [25,26].

In QCT-SB, all the trajectories contribute equally likely to the dynamics, while in CT-GB, trajectories are assigned Gaussian statistical weights such that the closer the final vibrational actions to integer values, the larger the weights. This is actually a natural trick for taking into account Bohr quantization of product vibrations in the classical description of the dynamics.

CT-GB often appears to be much more realistic than QCT-SB in the quantum regime where only a few vibrational states are available to the products [1–19]. In addition to that, CT-GB solves to a large extent the zero point energy (ZPE) problem since all the trajectories reaching the products with a vibrational energy less than the ZPE have a negligible contribution.

Initially proposed on the basis of intuitive arguments [20], CT-GB was later shown to be a practical implementation of classical *S* matrix theory (CSMT) within the random phase approximation [21]. CSMT was the first semi-classical description of molecular collisions pioneered by Miller and Marcus in the early seventies [27–33]. By expressing *S* matrix elements in terms of classical paths, this approach led to a profound modification of our understanding of molecular collisions and chemical reactivity.

Nevertheless, CSMT suffers one major drawback: it is not strictly unitary. As a consequence, the most frequently utilized version of CT-GB, which strictly derives from CSMT, is not normalized to unity. In other words, the sum of product and re-formed reagent state populations found from the previous approach is not strictly equal to one.

The main goal of the present paper is to show that normalizing to unity the final state populations obtained by means of the usual GB procedure should generally improve the quality of the predictions for an important class of bimolecular processes: *indirect reactions* [34].

By opposition to direct reactions involving stripping or rebound mechanisms, indirect reactions are defined here as the bimolecular collisions proceeding through an intermediate complex experiencing at least a few vibration motions before its eventual fragmentation towards products, or back to reagents. Complex formation is due to the presence of a deep well along the reaction path [7]. Statistical processes for which intramolecular vibrational redistribution (IVR) is complete are typically indirect. However, indirect reactions are not necessarily statistical, for a few vibration motions in the strong coupling region (SCR) does not ensure full IVR.

Reactions like $H^+ + H_2$ and $H^+ + D_2$ are only partially indirect according to our definition, at least for collision energies of a few tenth of eV. Although they involve a deep well along the reaction path, a large amount of non reactive trajectories turn out to be very short-lived and therefore direct for large impact parameters (the

* Corresponding author.
E-mail address: l.bonnet@ism.u-bordeaux1.fr (L. Bonnet).

2210-271X/$ - see front matter © 2011 Elsevier B.V. All rights reserved.
doi:10.1016/j.comptc.2011.11.001

incoming ion undergoes a single rebound against the diatom for these paths). This is due to mass combinations unfavorable to energy transfer between radial and vibrational coordinates, a requirement for capture in the SCR for at least a few vibration motions. For these processes, it was noted that removing vibrationally adiabatic non reactive trajectories makes the CT-GB cross sections in much better agreement with exact quantum ones than when taking these paths into account [22]. Up to the present, however, this correction lacks for convincing theoretical justification and the connection between quantum and classical dynamics for these reactions remains a puzzling issue. Therefore, we do not consider them in this work.

On the other hand, the recently studied $D^+ + H_2$ reaction [17] appears to be truly indirect, as the mass combination is more favorable to energy transfer from translation to vibration motion than previously, leading therefore to capture with a much larger probability. Moreover, benchmark quantum results are available for this process over a large range of collision energies. We thus focus our attention on it in order to highlight the efficiency and rationalize the effect of normalizing to unity final state populations for indirect processes.

The paper is organized as follows. The normalization issue is considered within the framework of statistical collinear inelastic processes in Section 2. Realistic classical trajectory calculations on the $D^+ + H_2$ reaction are presented in Section 3. SB, GB and normalized GB (NGB) integral cross sections (ICS) are compared with benchmark quantum results in a large interval of collision energies. The NGB ICS appears to be in much better agreement with the quantum one than the GB ICS which strongly underestimates it. Simplified and accurate statistical phase space theory (PST) calculations [35–40] are then performed in Section 4 in order to rationalize the increase of ICS due to normalization. Section 5 concludes.

2. Statistical collinear inelastic collisions

Consider the collinear inelastic collision between atom A and the diatomic molecule BC in the vibrational state n_1 at the classically available energy E with respect to the free fragments. BC is supposed to be a harmonic oscillator. The usual Jacobi coordinates of the problem are R, the distance between A and the center-of-mass of BC and r, the BC bond length. Their conjugate momenta are P and p, respectively. The usual form of the classical Hamiltonian in the separated fragments is given by:

$$H = \frac{P^2}{2\mu} + H_V \tag{1}$$

with

$$H_V = \frac{p^2}{2m} + \frac{1}{2}m\omega^2(r - r_e)^2. \tag{2}$$

H_V is the vibrational Hamiltonian. μ is the reduced mass of A with respect to BC, m is the reduced mass of BC, r_e is its equilibrium bond length and ω is 2π times its vibrational frequency.

Instead of r and p, it is convenient to consider the angle-action variables q and n defined by:

$$r = r_e + \left(\frac{\hbar(2n+1)}{m\omega}\right)^{1/2} sinq \tag{3}$$

and

$$p = (m\hbar\omega(2n+1))^{1/2} cosq \tag{4}$$

where ħis Planck constant h over 2π. q belongs to the range $[0, 2\pi]$. In term of these new coordinates, the vibrational Hamiltonian reads

$$H_V = \hbar\omega\left(n + \frac{1}{2}\right). \tag{5}$$

At time zero, corresponding to a large value R_i of R, n and q are equal to n_1 and $\bar{q}$, respectively. The reaction function provides the final value $n(\bar{q})$ of n in terms of $\bar{q}$.

According to CSMT in the random phase approximation, the probability $P_{n_2 n_1}$ that the final vibrational state of BC is n_2 is given by the classical density of probability:

$$P_{n_2 n_1} = \frac{1}{2\pi}\int_0^{2\pi} d\bar{q}\ \delta(n_2 - n(\bar{q})) \tag{6}$$

that the final action $n(\bar{q})$ is equal to n_2 [21,22,33]. In CT-GB, the δ function in the above equation is replaced by the Gaussian function G defined by:

$$G(u) = \frac{e^{-u^2/\epsilon^2}}{\pi^{1/2}\epsilon} \tag{7}$$

where ϵ is usually kept at $\sim$0.05 in order to get a full width at half maximum of $\sim$10%.

The SB probability is formally given by:

$$P^{SB}_{n_2 n_1} = \int_{n_2 - 1/2}^{n_2 + 1/2} dn\ P_{nn_1}. \tag{8}$$

Let us now assume that the collision is statistical, i.e., $n(\bar{q})$ is a random function of $\bar{q}$ between $-1/2$, corresponding to $H_V = 0$ (see Eq. (5)), and the maximum value

$$n_M = \frac{E}{\hbar\omega} - \frac{1}{2}, \tag{9}$$

corresponding to $H_V = E$. As a density of probability, $P_{n_2 n_1}$ is then immediately given by:

$$P_{n_2 n_1} = \frac{1}{n_M + 1/2}. \tag{10}$$

The quantum counterpart of this assumption is that the final states are equally likely (this is precisely the basic assumption of Phase Space Theory [35–40]). Since n_2 can take any one of the integer values $(0, \ldots, Int(n_M))$, the quantum population $P^Q_{n_2 n_1}$ is given by:

$$P^Q_{n_2 n_1} = \frac{1}{Int(n_M) + 1}. \tag{11}$$

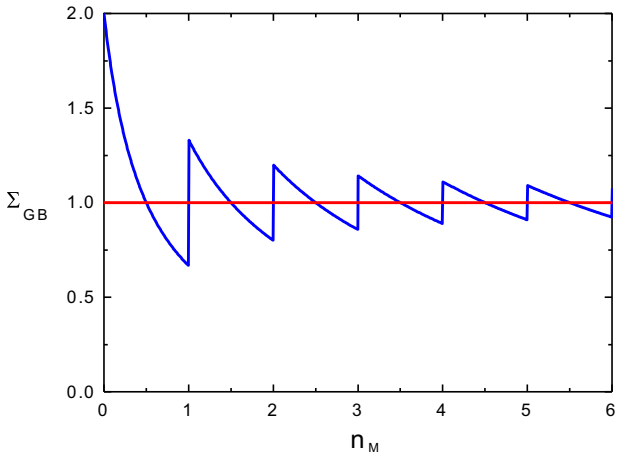

Fig. 1. Norm Σ_{GB} (see Eq. (12)) in terms of the maximum vibrational action n_M (blue curve). Σ_{GB} is generally different from 1. (For interpretation of the references to colour in this figure legend, the reader is referred to the web version of this article.)

Since $P^{GB}_{n_2 n_1}$ is expected to be an excellent approximation of Eq. (10), one immediately sees that $P^{GB}_{n_2 n_1}$ is a satisfying approximation of $P^{Q}_{n_2 n_1}$ only for sufficiently large values of n_M. Consequently, the GB norm

$$\Sigma_{GB} = \sum_{n_2=0}^{n_M} P^{GB}_{n_2 n_1} \approx \frac{Int(n_M)+1}{n_M+1/2}, \tag{12}$$

represented in Fig. 1, is in general quite different from the expected unit value, especially for the low values of n_M typical of the quantum regime.

From Eq. (8),

$$P^{SB}_{n_2 n_1} = \frac{1}{n_M+1/2} \tag{13}$$

for all the values of n_2 but the largest one. If $n_M - Int(n_M) < 1/2$, the maximum value of n_2 is $Int(n_M)$ and

$$P^{SB}_{Int(n_M)\ n_1} = \frac{n_M - Int(n_M) + 1/2}{n_M+1/2}. \tag{14}$$

If on the other hand, $n_M - Int(n_M) \geqslant 1/2$, this value is $Int(n_M)+1$ and

$$P^{SB}_{Int(n_M)+1\ n_1} = \frac{n_M - Int(n_M) - 1/2}{n_M+1/2}. \tag{15}$$

Note that $n_2 = Int(n_M)+1$ is a forbidden state in quantum mechanics. One may check that in both cases, the sum of the populations is strictly equal to 1.

The conclusions of the present section are the followings: (i) the quantum populations are all equal and normalized to unity; (ii) the GB populations are all equal, like the quantum ones, but they are generally not normalized to unity. Obviously, re-normalizing them to unity makes them "exact", in the statistical sense adopted in this work; (iii) at the opposite, the SB populations are rigorously normalized to unity, but the population of the most excited state is in general different from (lower than) the other ones. If 10 levels or more are available, the agreement with quantum populations is quite satisfying, but if only 2 levels are available, as is the case in sufficiently cold collisions, the agreement is in general very poor.

3. Trajectory calculations for the $D^+ + H_2$ reaction

We now apply the previous normalization procedure to the calculation of the ICS for the $D^+ + H_2$ reaction, assuming that the initial H_2 molecule is in the ro-vibrational ground state ($n_1 = 0, j_1 = 0$). The potential energy surface used is the one proposed by Aguado et al. [41].

The exact expression of the ICS is:

$$\sigma = \sum_{n'_2 j'_2} \sigma_{n'_2 j'_2} \tag{16}$$

with

$$\sigma_{n'_2 j'_2} = \frac{\pi}{k^2} \sum_{J l'_2} (2J+1)\ P^{J}_{n'_2 j'_2 l'_2}. \tag{17}$$

n'_2 is the vibrational quantum number of the HD product and j'_2 is its rotational quantum number. k is the linear momentum related to the collision energy E_c by:

$$k = (2\mu E_c)^{1/2}/\hbar. \tag{18}$$

J is the total angular momentum quantum number and l'_2 is the product orbital quantum number. $P^{J}_{n'_2 j'_2 l'_2}$ is the probability that the products are formed in the state (n'_2, j'_2, l'_2). According to CSMT in the random phase approximation, this quantity is given by:

$$P^{J}_{n'_2 j'_2 l'_2} = \frac{1}{(2\pi)^3} \int d\bar{\mathbf{q}}\ \delta_{n'}\ \delta_{j'}\ \delta_{l'} \tag{19}$$

with

$$\bar{\mathbf{q}} = (\bar{q}, \bar{\alpha}_j, \bar{\alpha}_l), \tag{20}$$

$$\delta_{n'} = \delta\left(n'(\bar{\mathbf{q}}, J) - n'_2\right), \tag{21}$$

$$\delta_{j'} = \delta\left(j'(\bar{\mathbf{q}}, J) - j'_2\right) \tag{22}$$

and

$$\delta_{l'} = \delta\left(l'(\bar{\mathbf{q}}, J) - l'_2\right) \tag{23}$$

[23]. If R is the distance between D^+ and the center-of-mass of H_2, $\bar{q}, \bar{\alpha}_j$ and $\bar{\alpha}_l$ are, at time zero corresponding to a large value R_i of R, the values of the angles q, α_j and α_l conjugate to the vibrational action n_1 of H_2, its rotational angular momentum j_1, and the orbital angular momentum l_1, respectively. The three angles belong to the range $[0, 2\pi]$. All the angular momenta are expressed in units of $\hbar$ in the following. $n'(\bar{\mathbf{q}}, J)$ is the product vibrational action and $j'(\bar{\mathbf{q}}, J)$ and $l'(\bar{\mathbf{q}}, J)$ are the product rotational and orbital angular momenta, respectively. It is implicitly assumed that one only integrates over the initial angles leading to reactive trajectories in Eq. (19).

In practice, trajectories are run in Jacobi coordinates which allow a very stable numerical integration of Hamilton equations. Their initial values are deduced from the previous action-angle variables and some other ones according to the transformation detailed in Appendix A. For clarity's sake, the calculation of the final vibrational action is recalled in Appendix A.

We performed GB, SB and normalized GB (NGB) calculations. In CT-GB, the product vibration motion is the only "quantized" final quantity. Consequently, we may replace the quantum degeneracy factor $2J+1$ by its classical analog $2J$, transform the sum over J, j'_2 and l'_2 in Eqs. (16) and (17) by an integral, replace $\delta_{j'}$ and $\delta_{l'}$ by standard bins of unit width and height and $\delta_{n'}$ by $G(n'(\bar{\mathbf{q}}, J) - n'_2)$ (see Eq. (7)). The sum over j'_2 and l'_2 disappears and we arrive at:

$$\sigma_{GB} = \pi \left(\frac{J_M}{k}\right)^2 \frac{1}{J_M^2} \int_0^{J_M^2} dJ^2\ \eta_{GB}(J) \tag{24}$$

with

$$\eta_{GB}(J) = \frac{1}{(2\pi)^3} \int d\bar{\mathbf{q}} \sum_{n'_2} G\left(n'(\bar{\mathbf{q}}, J) - n'_2\right). \tag{25}$$

J_M is the maximum value of J consistent with reaction. The sum over n'_2 is from $n'_2 = 0$ to the maximum value consistent with the available energy.

$\eta_{GB}(J)$ is the reaction probability at J. If one analogously defines the inelastic reaction probability, one arrives at the conclusion that the sum of the latter and $\eta_{GB}(J)$ is not necessarily equal to 1.

The MC expression of σ_{GB} is readily found to be:

$$\sigma_{GB} = \pi \left(\frac{J_M}{k}\right)^2 \frac{1}{N} \sum_{i=1}^{N_r} \sum_{n'_2} G\left(n'(\bar{\mathbf{q}}_i, J_i) - n'_2\right). \tag{26}$$

N is the total number of trajectories run while N_r is the number of reactive trajectories. $\bar{\mathbf{q}}_i$ gathers the initial angles, randomly distributed between 0 and 2π, for the ith trajectory. J_i is the total angular momentum for the same path. Note that J^2 is randomly selected, not J.

The MC expression of the SB ICS is simply given by:

$$\sigma_{SB} = \pi \left(\frac{J_M}{k}\right)^2 \frac{N_r}{N}. \tag{27}$$

The NGB cross section reads:

$$\sigma_{NGB} = \pi\left(\frac{J_M}{k}\right)^2 \frac{1}{J_M^2}\int_0^{J_M^2} dJ^2\,\eta_{NGB}(J) \tag{28}$$

with

$$\eta_{NGB}(J) = \frac{\int d\bar{\mathbf{q}} \sum_{n_2'} G(n'(\bar{\mathbf{q}},J) - v')}{\int d\bar{\mathbf{q}} \sum_{n_2} G(n(\bar{\mathbf{q}},J) - n_2) + \int d\bar{\mathbf{q}} \sum_{n_2'} G(n'(\bar{\mathbf{q}},J) - n_2')}. \tag{29}$$

$\eta_{NGB}(J)$ is again the reaction probability at J. Defining the inelastic reaction probability in an analogous way implies that the sum of the latter and $\eta_{NGB}(J)$ is now exactly equal to 1.

The MC expression of σ_{NGB} is given by:

$$\sigma_{NGB} = \pi\left(\frac{J_M}{k}\right)^2 \frac{1}{N_J}\sum_{k=1}^{N_J} \eta(J_k) \tag{30}$$

and

$$\eta(J_k) = \frac{\sum_{i=1}^{N_r}\sum_{n_2'} G(n'(\bar{\mathbf{q}}_i,J_k) - n_2')}{\sum_{i=1}^{N_r}\sum_{n_2'} G(n'(\bar{\mathbf{q}}_i,J_k) - n_2') + \sum_{i=N_r+1}^{N}\sum_{n_2} G(n(\bar{\mathbf{q}}_i,J_k) - n_2)} \tag{31}$$

where N_J values of J^2 are randomly selected and N trajectories are run for each one of these values. Note that $i > N_r$ defines the non reactive trajectories.

σ_{GB}, σ_{SB} and σ_{NGB} are represented in terms of E_c in Fig. 2, together with the benchmark quantum ICS σ_Q [17,42]. σ_{GB} and σ_{SB} are found to be in excellent agreement with the similar ICSs reported in Ref. [17], which validates our calculations. In line with the conclusions of Section 2, NGB predictions turn out to be in much better agreement with quantum ones than GB predictions, at least in the first half of collision energy range.

The failure of the CT-GB method to account for the accurate quantum mechanical excitation function for the $D^+ + H_2$ reaction was recently invoked in Ref. [17]. The previous results clearly moderate this conclusion; rather than the GB procedure itself, it is more the lack of normalization to unity of the reaction and inelastic probabilities which appears to be responsible for the failure.

At last, one notes that QCT-SB results are also in good agreement with quantum ones in the present case (see Fig. 2). However, this is generally not true, especially for endothermic processes, as shown for instance in Ref. [17]. In addition to that, the QCT-SB rotationally resolved reaction cross section turns out to be in poor agreement with the quantum one, as illustrated in Fig. 6 of Ref. [17]. QCT-SB should thus not be used in the quantum regime where very few vibrational states are available in the asymptotic channels.

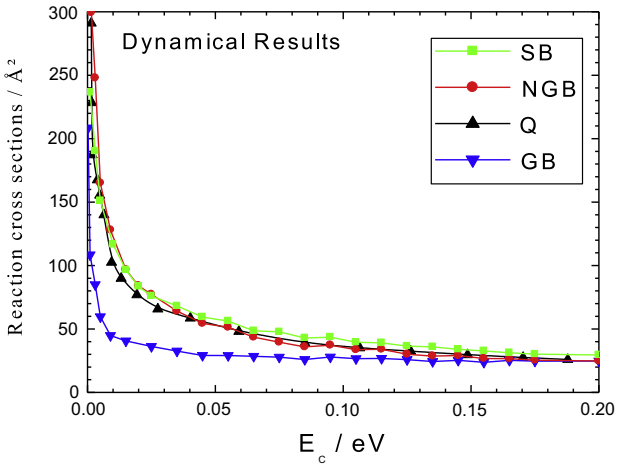

Fig. 2. σ_{GB}, σ_{SB} and σ_{NGB} for the $D^+ + H_2$ reaction are represented in terms of the collision energy and are compared with the benchmark quantum cross section σ_Q.

4. Rationalizing from statistical arguments the enhancement of the GB ICS through normalization

The goal of the present section is to rationalize the enhancement of the GB ICS through normalization within the framework of phase space theory (PST) [35–39]. PST is a theory for processes governed by long-range attractive forces supposed to be isotropic. In the reagent channel, for instance, the potential energy is usually approximated by an expression of the type:

$$V = v(r) - C/R^n \tag{32}$$

where $v(r)$ is the internal potential of H_2 and $-C/R^n$ is the long-range attractive potential between D^+ and H_2. For an ion–molecule reaction, n is generally equal to 4, but it turns out that with n kept at 6 and C at 80 eV Å^6, Eq. (32) fits very well the mean potential obtained from averaging over the Jacobi angle the accurate potential energy of Aguado et al. [41]. The details of the averaging are given in Ref. [40]. The radial part of the mean potential and its approximation $-C/R^6$ are represented in Fig. 3. Expressions analogous to Eq. (32) are considered in product channels.

PST also assumes that reaction proceeds through an intermediate complex living a sufficiently long period of time (a few ps) for complete energy randomization of the available energy among internal degrees-of-freedom. Soon after its formation, the distribution of the phase space states of the complex is then supposed to be micro-canonical. As a consequence, the reaction probability is simply given by $2F_C'/(F_C + 2F_C')$ where F_C is the flux towards the reagent channel and F_C' is the flux towards one of the two equivalent product channels. The classical PST reaction cross section is therefore given by:

$$\sigma_C^{PST} = \frac{\pi}{k^2}\int_0^{J_M^2} dJ^2\,\frac{2F_C'}{F_C + 2F_C'}. \tag{33}$$

The initial rotational angular momentum being zero, J_M is equal to the initial orbital angular momentum, related to the maximum impact parameter $b_M(E_c)$ by the relation:

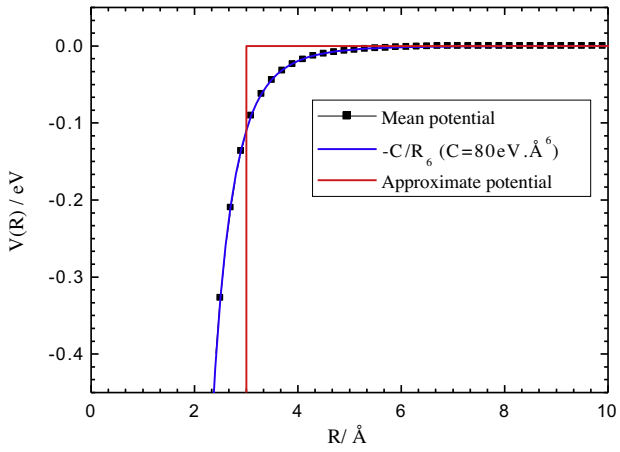

Fig. 3. Comparison between the radial term $-C/R^6$ with $C = 80$ eV Å^6 (blue solid line), and the radial part of the mean potential obtained from averaging over the Jacobi angle the accurate potential energy of Aguado et al. [41] (black solid line with squares). In the approximate PST treatment, the radial part is represented by a step (red solid line). (For interpretation of the references to colour in this figure legend, the reader is referred to the web version of this article.)

$$J_M = kb_M(E_c). \tag{34}$$

Moreover, for the radial interaction considered, it can be shown within the framework of Langevin capture model [35–39] that:

$$b_M(E_c) = \left(\frac{3}{2}\right)^{1/3}\left(\frac{3C}{E_c}\right)^{1/6}. \tag{35}$$

We are now in a position to solve Eq. (33). We shall first do it approximately, by means of an analytical approach in order to pinpoint the key factors governing the reaction cross section, and then accurately, from exact numerical calculations.

We shall also consider two alternative semi-classical expressions of the cross section, called σ_{SC}^{PST} and σ_{NSC}^{PST}. σ_C^{PST} is the PST analog of σ_{SB} and σ_{SC}^{PST} and σ_{NSC}^{PST} will appear to be the PST analogs of σ_{GB} and σ_{NGB}.

4.1. Approximate PST

For the sake of both simplicity and clarity, we first consider a simple model where, as far as the estimation of the reaction probability $2F'_C/(F_C + 2F'_C)$ is concerned, the radial interaction $-C/R^6$ is replaced by a step at $R = R^{\ddagger} = 3$ Å. This step is represented in Fig. 3.

The phase space flux of trajectories at total energy E and total angular momentum J through the reagent phase space surface defined by a large value R_i of R reads:

$$F_C = \int d\Gamma\,\delta(R - R_i)\frac{P}{\mu}\Theta(P)\delta(E - H)\delta(J - J') \tag{36}$$

with

$$d\Gamma = dR\ dP\ dq\ dn\ dJ'\ dM\ dj\ dl\ d\alpha\ d\beta\ d\alpha_j d\alpha_l. \tag{37}$$

The above variables have been defined previously and in Appendix A. Save for an unimportant constant, F_C is found after some steps of algebra to be given by:

$$F_C = J\int dn\ dj\ dl\ \Theta\left[E - \hbar\omega\left(n + \frac{1}{2}\right) - \frac{\hbar^2 j^2}{2I}\right] \tag{38}$$

where H_2 is considered as a rigid rotor harmonic oscillator with moment of inertia I and vibrational frequency $\omega/2\pi$.

Integration in the plane (j,l) is in principle limited by the triangular inequality:

$$|j - l| \leqslant J \leqslant j + l \tag{39}$$

and the fact that the upper bound of l is given by:

$$l_M(E_t) = \hbar^{-1}R^{\ddagger}(2\mu E_t)^{1/2} \tag{40}$$

with

$$E_t = E - \hbar\omega\left(n + \frac{1}{2}\right) - \frac{\hbar^2 j^2}{2I}. \tag{41}$$

E_t is the translational energy. The phase space flux F'_C towards one of the two equivalent product channel $DH + H^+$ is obtained in exactly the same way using product parameters.

From the two previous equations, the energetic constraint on j and l turns out to be:

$$\frac{\hbar^2 l^2}{2\mu R^{\ddagger 2}} + \frac{\hbar^2 j^2}{2I} \leqslant E - \hbar\omega\left(n + \frac{1}{2}\right). \tag{42}$$

The available area in the planes (j,l) and (j',l') are represented in Fig. 4 for n and n' kept at 0 and $J = 8$. A reasonable assumption is that inequality (39) affects both F_C and F'_C in roughly the same way. Hence, it is not necessary to take it into account in the developments. From Eqs. (33) and (34), we thus obtain:

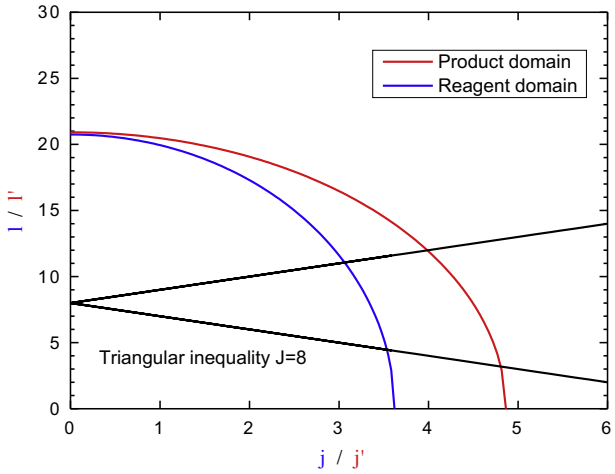

Fig. 4. Available areas in the planes (j,l) and (j',l') for $J = 8$. The red and blue elliptic boundaries are relative to products and reagents, respectively. The areas below these boundaries correspond to Eq. (42). The one inside the triangle corresponds to triangular inequality (39). The available areas are the intersections of the two previous areas.

$$\sigma_C^{PST} \approx \pi b_M(E_c)^2\frac{2F'_C}{F_C + 2F'_C} \tag{43}$$

where F_C is still found from Eq. (38), forgetting however inequality (39), and F'_C is given by the same expression using product parameters. These fluxes are hence given by the integrals over the vibrational actions of the areas below the elliptic boundaries in Fig. 4. For F_C, we arrive at:

$$F_C = \frac{\pi R^{\ddagger}(\mu I)^{1/2}JE^2}{4\hbar\omega}. \tag{44}$$

(if J is larger than its maximum value consistent with E, F_C is of course equal to zero). In addition to that, $I = mr_e^2$ where m is the reduced mass of H_2 and r_e is its equilibrium geometry. Since both $R^{\ddagger}$ and r_e are the same in all channels, it is a simple matter to show that:

$$\sigma_C^{PST} \approx \pi b_M(E_c)^2\frac{2\omega}{2\omega + \omega'}. \tag{45}$$

As previously outlined, this cross section is the statistical analog of σ_{SB} in the previous section.

The first alternative to σ_C^{PST} is:

$$\sigma_{SC}^{PST} \approx \pi b_M(E_c)^2\frac{2F'_{SC}}{F_C + 2F'_C} \tag{46}$$

with

$$F'_{SC} = J\int dn'dj'dl'\Theta\left[E - \hbar\omega'\left(n' + \frac{1}{2}\right) - \frac{\hbar^2 j'^2}{2I'}\right]\delta(n'). \tag{47}$$

In this semi-classical (SC) treatment, only the vibration motion of the product diatom HD is quantized. σ_{SC}^{PST} is the statistical analog of σ_{GB} in the previous section (see Eq. (26)). Replacing the delta-function by a Gaussian in Eq. (47) and performing an MC calculation of Eq. (46) would indeed correspond to Eq. (26). Just as for σ_{GB}, the sum of the reaction and inelastic probabilities is not equal to 1. After some mathematical steps, we arrive at:

$$F'_{SC} = \frac{\pi}{2}R^{\ddagger}(\mu' I')^{1/2}J\left(E - \frac{\hbar\omega'}{2}\right) \tag{48}$$

and

$$\sigma_{SC}^{PST} \approx \pi b_M(E_c)^2 \frac{2\hbar\omega\omega'(2E_c+\hbar(\omega-\omega'))}{(2\omega+\omega')(E_c+\hbar\omega/2)^2}. \quad (49)$$

A second alternative to σ_C^{PST} is:

$$\sigma_{NSC}^{PST} \approx \pi b_M(E_c)^2 \frac{2F'_{SC}}{F_{SC}+2F'_{SC}}, \quad (50)$$

leading to:

$$\sigma_{NSC}^{PST} \approx \pi b_M(E_c)^2 \frac{2(E_c+\hbar(\omega-\omega')/2)}{E_c+2(E_c+\hbar(\omega-\omega')/2)} \quad (51)$$

This cross section is the statistical analog of σ_{NGB} in the previous section (see Eqs. (30) and (31)). Both the (re-formed) reagent and product vibration motions are indeed quantized and the sum of the reaction and inelastic probabilities is now equal to 1.

σ_C^{PST}, σ_{SC}^{PST} and σ_{NSC}^{PST} are represented in terms of E_c in Fig. 5. ω was kept at 4400 cm^{-1} and ω' at 3810 cm^{-1}. The similarity with σ_{SB},σ_{GB} and σ_{NGB}, respectively, is striking (see Fig. 2); σ_C^{PST} and σ_{NSC}^{PST} are indeed close to each other and well above σ_{SC}^{PST} . Hence, the present analytical version of PST provides a good description of the $D^+ + H_2$ reaction dynamics and confirms the fact recently outlined by Jambrina et al. that the dynamics of the $D^+ + H_2$ reaction involves a strong statistical component [17].

We shall now take advantage of the simplicity of our approximate PST description to understand the gross features of the previous cross sections. For instance, why is σ_{SC}^{PST} always lower than σ_C^{PST} over the energy range considered? The reason turns out to be very simple: F'_{SC}, proportional to $(E-\hbar\omega'/2)$ (see Eq. (48)), is always lower than or equal to F'_C, proportional to $E^2/2\hbar\omega'$ (see Eq. (44)). Equality occurs only at $E=\hbar\omega'$. Since $E=E_c+\hbar\omega/2$, $E=\hbar\omega'$ corresponds to $E_c=\hbar\omega'-\hbar\omega/2\approx$ 0.2 eV. This is why over the energy range of Fig. 5, σ_{SC}^{PST} (see Eq. (46)) is always lower than σ_C^{PST} (see Eq. (43)) but gets closer and closer to the latter as the collision energy increases. Since PST appears to be a satisfying description of the dynamics, the same remark holds for σ_{GB} and σ_{SB} in Fig. 2. The fact that σ_{GB} and σ_{SB} become roughly equal for a product energy larger than $\hbar\omega'$ has been recently outlined in Ref. [17]. Our statistical model allows for clearly formalizing this finding. One may also show that for energies larger than $\hbar\omega'$, σ_{GB} and σ_{SB} keeps close to each other despite the fact that F'_{SC} becomes lower than F'_C. This is actually due to the opening of new product vibrational states.

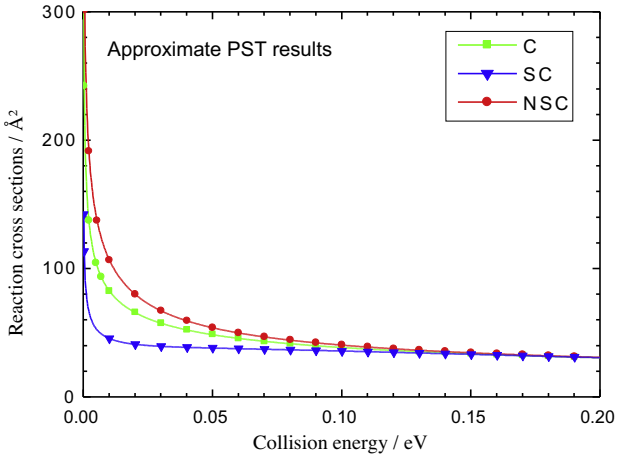

Fig. 5. Representation in terms of the collision energy of the approximate σ_C^{PST}, σ_{SC}^{PST} and σ_{NSC}^{PST} of Section 4.1 for the $D^+ + H_2$ reaction.

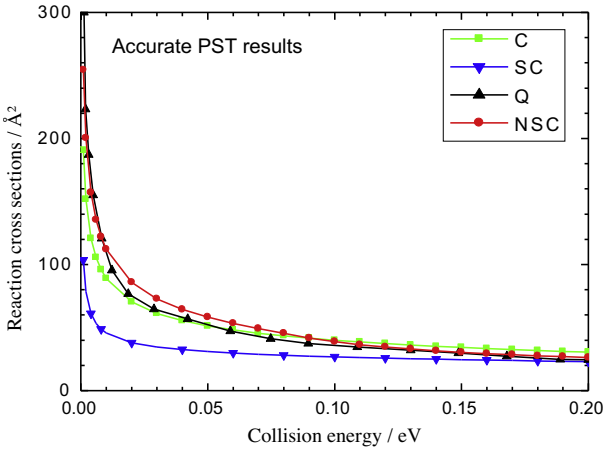

Fig. 6. Representation in terms of the collision energy of the accurate σ_C^{PST}, σ_{SC}^{PST} and σ_{NSC}^{PST} of Section 4.2 for the $D^+ + H_2$ reaction.

Moreover, σ_{SC}^{PST} is always lower than σ_{NSC}^{PST} since the numerator of the former (see Eq. (46)) is systematically larger than the one of the latter (see Eq. (50)). This is also what one observes for σ_{GB} and σ_{NGB}.

On the other hand, the order relation between σ_C^{PST} and σ_{NSC}^{PST} is less obvious since both the numerator and the denominator of σ_C^{PST} (see Eq. (43)) are larger than those of σ_{NSC}^{PST} (see Eq. (50)).

4.2. Accurate PST

The accurate PST expression of σ_C^{PST} is given by Eq. (33) with F_C obtained from Eqs. (38)–(41) and $R^{\ddagger}$ replaced by $b_M(E_t)$ (see Eq. (35)). F'_C is given by similar expressions where product parameters are substituted to reagent ones. Triangular inequality (39) is now taken into account. The accurate PST expression of σ_{SC}^{PST} is given by Eq. (33) with F'_C replaced by F'_{SC} (see Eq. (47)) in the numerator of the integrand. The one of σ_{NSC}^{PST} is also given by Eq. (33) with both F_C and F'_C replaced by F_{SC} and F'_{SC}.

σ_C^{PST}, σ_{SC}^{PST} and σ_{NSC}^{PST} are represented in terms of E_c in Fig. 6. r_e was kept at 0.743 Å for the calculation of the moment of inertia I. As a matter of fact, accurate PST cross sections are in good agreement with approximate ones (see Fig. 5), giving therefore credit to the discussion of the previous subsection.

Note that accurate PST cross sections are in even better agreement with dynamical ones (compare Figs. 2 and 6) than approximate PST cross sections.

5. Conclusion

The GB procedure most frequently utilized in classical trajectory (CT) calculations does not lead to final state populations rigorously normalized to unity. In other words, the sum of product and re-formed reagent state populations found from the previous approach is not strictly equal to one.

We have shown in this paper that for triatomic collinear inelastic collisions involving statistical dynamics, re-normalizing to unity GB state populations makes them equal to quantum ones.

Moreover, we have found that applying the same normalized GB (NGB) procedure in CT calculations for the realistic $D^+ + H_2$ indirect reaction significantly enhances the reaction cross section and makes it in much better accordance with its exact quantum value than the usual GB procedure.

Last but not least, we have analyzed why normalization enhances the reaction cross section within the framework of

simplified phase space theory calculations corroborated by accurate ones.

Overall, the present study tends to show that CT-NGB should provide quite accurate predictions for indirect reactions, except in the particular situation where vibrationally elastic paths play an important role in the dynamics, as may for instance be the case for the $H^+ + H_2$ and $H^+ + D_2$ reactions [22]. When it is so, an adiabaticity correction proposal can be applied [22], but its clear justification from first principles remains to be done.

In a near future, we plan to perform CT-NGB calculations for gas-phase triatomic chemical reactions in the quantum regime and check whether the improvement observed for the $D^+ + H_2$ reaction as compared to CT-GB predictions is systematic or not.

Appendix A

The Jacobi vectors **R** and **r** go from the center-of-mass of H_2 to D^+, and from one H atom to the other one, respectively.

The goal of this appendix is to give the transformation from (a) the set composed of R, its conjugate momentum P, and the ten remaining action-angle coordinates J, M, l, j, n, α, β, α_l, α_j, q to (b) the twelve Cartesian projections R_x, R_y, R_z, r_x, r_y, r_z, P_x, P_y, P_z, p_x, p_y, p_z of **R** and **r** and their conjugate momentum vectors **P** and **p** on the laboratory axis x, y and z. M is the projection of **J** on the z axis.

Note that, as previously stated, angular momenta are in units of ħ.

The previous transformation can for instance be found in Ref. [43] where it is deduced from a generator given in Ref. [44]. For clarity's sake, however, we recall it here in close details, following a pedestrian geometrical approach. The conventions of the more general transformation given in Ref. [45] are used. All the figures referred to in this appendix are from Ref. [45]. That paper should thus be within reach for a clear understanding of the transformation.

We now decompose it in seven steps.

A.1. Step 1: Passage from (q,n) to (r,p)

For sufficiently small values of the vibrational energy, the Morse function

$$v(r) = D(1 + exp(-2a(r - r_e)) - 2exp(-a(r - r_e))) \tag{A.1}$$

with D = 4.49 eV, a = 2.02 Å^{-1} and r_e = 0.743 Å, is a good approximation of the potential energy $v(r)$ of H_2 obtained from the potential energy surface of Aguado et al. [41] for D^+ far away from H_2.

In such a case, it can be shown that:

$$r = r_e - \frac{1}{a} ln\left(\frac{b^2}{1 + (1 - b^2)^{1/2} cosq}\right) \tag{A.2}$$

with

$$b = 1 - \frac{2n + 1}{2c} \tag{A.3}$$

and

$$c = \frac{(2mD)^{1/2}}{\hbar a}. \tag{A.4}$$

p is then deduced from r by the relation:

$$p = (2m(D(1 - b^2) - v(r)))^{1/2} \tag{A.5}$$

if q belongs to the range $[0,\pi]$ and the opposite value if q belongs to the range $[\pi,2\pi]$.

A.2. Step 2: Cartesian components of **l**

Substituting **j** for **k** in Fig. 2 of Ref. [45], the three vectors **J**, **l** and **j** are represented in the laboratory frame (G,x,y,z) centered on the center-of-mass G of the triatomic system. Note that M is called J_z in Fig. 2 of Ref. [45]. **J**, **l** and **j** lie in the plane (G,y',z') represented in Fig. 7 of Ref. [45]. The relation of total angular momentum conservation can be written as:

$$\mathbf{J} - \mathbf{l} = \mathbf{j}. \tag{A.6}$$

Squaring each side of the previous equality and rearranging leads to:

$$cos\theta_{Jl} = \frac{J^2 + l^2 - j^2}{2Jl}. \tag{A.7}$$

The projection l'_z of **l** along the z' axis, equal to $l\ cos\theta_{Jl}$, is thus given by:

$$l'_z = \frac{J^2 + l^2 - j^2}{2J}. \tag{A.8}$$

l'_y, equal to $l\ sin\theta_{Jl}$, i.e., to $l(1 - cos^2\theta_{Jl})^{1/2}$ (given the convention adopted, l'_y is necessarily positive), is therefore given by:

$$l'_y = \left(l^2 - \left(\frac{J^2 + l^2 - j^2}{2J}\right)^2\right)^{1/2}. \tag{A.9}$$

At last, l'_x is zero.

l is deduced from **l**′ by the standard Euler rotation:

$$\mathbf{l} = \mathbf{M_3}(-\beta)\mathbf{M_1}(-\theta_J)\mathbf{M_3}(-\alpha)\mathbf{l}' \tag{A.10}$$

where for a given angle χ,

$$\mathbf{M_1}(-\chi) = \begin{pmatrix} 1 & 0 & 0 \\ 0 & cos\chi & -sin\chi \\ 0 & sin\chi & cos\chi \end{pmatrix} \tag{A.11}$$

and

$$\mathbf{M_3}(-\chi) = \begin{pmatrix} cos\chi & -sin\chi & 0 \\ sin\chi & cos\chi & 0 \\ 0 & 0 & 1 \end{pmatrix}. \tag{A.12}$$

Fig. 2 of Ref. [45] shows indeed that one goes from (G,x',y',z') to (G,x,y,z) by a rotation of $(-\alpha)$ around the z' axis, then a rotation of $(-\theta_J)$ around the "new" x' axis, and finally a rotation of $(-\beta)$ around the "new" z' axis. One may check that these transformations are achieved by the above matrices.

$cos\theta_J$ is given by:

$$cos\theta_J = \frac{M}{J} \tag{A.13}$$

and $sin\theta_J$, necessarily positive (θ_J belongs to the range $[0,\pi]$), is given by

$$sin\theta_J = \left(1 - \left(\frac{M}{J}\right)^2\right)^{1/2}. \tag{A.14}$$

One notes that angular momenta often appear at the denominator of the ratios involved in the developments. Consequently, they cannot be exactly zero. One should always check that this constraint is satisfied when performing QCT calculations.

A.3. Step 3: Cartesian components of **R**

From Fig. 3 of Ref. [45] and following the same reasoning as above, **R** can be shown to satisfy:

$$\mathbf{R} = \mathbf{M_3}(-\beta_l)\mathbf{M_1}(-\theta_l)\mathbf{M_3}(-\alpha_l)\mathbf{R}' \tag{A.15}$$

where $\mathbf{R}'$ represents the vector $(R,0,0)$. Fig. 8 of Ref. [45] shows how the angles β_l and θ_l are related to $\mathbf{l}$. $cos\theta_l$ is given by:

$$cos\theta_l = \frac{l_z}{l} \tag{A.16}$$

and $sin\theta_l$, necessarily positive, by:

$$sin\theta_l = \left(1 - \left(\frac{l_z}{l}\right)^2\right)^{1/2}. \tag{A.17}$$

$cos\beta_l$ is given by:

$$cos\beta_l = -\frac{l_y}{l_{xy}} \tag{A.18}$$

and $sin\beta_l$ by:

$$sin\beta_l = \frac{l_x}{l_{xy}} \tag{A.19}$$

where

$$l_{xy} = (l^2 - l_z^2)^{1/2} \tag{A.20}$$

is the modulous of the projection of $\mathbf{l}$ on the (G,x,y) plane (see Fig. 8 of Ref. [45]).

A.4. Step 4: Cartesian components of **P**

Since **l = RxP**, **P** lies in the plane (G,x',y'), as shown in Fig. 3 of Ref. [45]. P'_x has already been denoted P, P'_y is equal to l/R and P'_z is zero. **P** satisfies:

$$\mathbf{P} = \mathbf{M_3}(-\beta_l)\mathbf{M_1}(-\theta_l)\mathbf{M_3}(-\alpha_l)\mathbf{P}' \tag{A.21}$$

where $\mathbf{P}'$ represents the vector $(P,l/R,0)$.

A.5. Step 5: Cartesian components of **j**

Replacing again **k** with **j** in Fig. 2 of Ref. [45], we may follow a reasoning analogous to the one for **l**. The relation of total angular momentum conservation can be written as:

$$\mathbf{J} - \mathbf{j} = \mathbf{l}. \tag{A.22}$$

Squaring each side of the previous equality and rearranging leads to:

$$cos\theta_{lj} = \frac{J^2 + j^2 - l^2}{2Jj}. \tag{A.23}$$

j'_z, equal to $j\ cos\theta_{lj}$, is thus given by:

$$j'_z = \frac{J^2 + j^2 - l^2}{2J}. \tag{A.24}$$

j'_y, equal to $(-j\ sin\theta_{lj})$, i.e., to $(-j(1 - cos^2\theta_{lj})^{1/2})$ (given the convention adopted, j'_y is necessarily negative), is therefore given by:

$$j'_y = -\left(j^2 - \left(\frac{J^2 + j^2 - l^2}{2J}\right)^2\right)^{1/2} \tag{A.25}$$

(one may check that j'_y is the just the opposite of l'_y). At last, j'_x is zero. **j** is then obtained from $\mathbf{j}'$ by the same transformation as the one relating **l** and $\mathbf{l}'$ (see Eq. (A.10)):

$$\mathbf{j} = \mathbf{M_3}(-\beta)\mathbf{M_1}(-\theta_J)\mathbf{M_3}(-\alpha)\mathbf{j}'. \tag{A.26}$$

A.6. Step 6: Cartesian components of **r**

Following the same reasoning as for **R**, **r** can be shown to satisfy:

$$\mathbf{r} = \mathbf{M_3}(-\beta_j)\mathbf{M_1}(-\theta_j)\mathbf{M_3}(-\alpha_j)\mathbf{r}' \tag{A.27}$$

where $\mathbf{r}'$ represents the vector $(r,0,0)$.

$cos\theta_j$ is given by:

$$cos\theta_j = \frac{j_z}{j} \tag{A.28}$$

and $sin\theta_j$, necessarily positive, by:

$$sin\theta_j = \left(1 - \left(\frac{j_z}{j}\right)^2\right)^{1/2}. \tag{A.29}$$

$cos\beta_j$ is given by:

$$cos\beta_j = -\frac{j_y}{j_{xy}} \tag{A.30}$$

and $sin\beta_j$ by:

$$sin\beta_j = \frac{j_x}{j_{xy}} \tag{A.31}$$

where

$$j_{xy} = (j^2 - j_z^2)^{1/2} \tag{A.32}$$

is the modulous of the projection of $\mathbf{j}$ on the (G,x,y) plane.

A.7. Step 7: Cartesian components of **p**

Following the same reasoning as for **P**, **p** satisfies

$$\mathbf{p} = \mathbf{M_3}(-\beta_j)\mathbf{M_1}(-\theta_j)\mathbf{M_3}(-\alpha_j)\mathbf{p}' \tag{A.33}$$

where $\mathbf{p}'$ represents the vector $(p,j/r,0)$. This relation achieves the expected transformation.

A.8. Step 8: Vibrational action n' of the product diatom

n' is defined by [31]:

$$n' = \frac{2}{h}\int_{r'_{in}}^{r'_{out}} p'dr' - \frac{1}{2}, \tag{A.34}$$

where r' is the bond length of HD, r'_{in} and r'_{out} correspond to the inner and outer turning points and p' is the conjugate momentum of r', given by:

$$p' = \left[2m'\left(E'_{vj} - \frac{j'^2}{2m'r'^2} - v'(r')\right)\right]^{1/2}. \tag{A.35}$$

m' is the reduced mass of HD, E'_{vj} is its ro-vibrational energy at the end of a given trajectory and $v'(r')$ is its potential energy, obtained from the potential energy surface of Aguado et al. [41] for H^+ far away from HD.

References

[1] L. Bañares, F.J. Aoiz, P. Honvault, B. Bussery-Honvault, J.-M. Launay, J. Chem. Phys. 118 (2003) 565.
[2] N. Balucani, G. Capozza, L. Cartechini, A. Bergeat, R. Boddenkamp, P. Casavecchia, F.J. Aoiz, L. Bañares, P. Honvault, B. Bussery-Honvault, J.-M. Launay, Phys. Chem. Chem. Phys. 6 (2004) 4957.
[3] T. Xie, J. Bowman, J.W. Duff, M. Braunstein, B. Ramachandran, J. Chem. Phys. 122 (2005) 014301.
[4] N. Balucani, G. Capozza, E. Segoloni, A. Russo, R. Bobbenkamp, P. Casavecchia, T. Gonzalez-Lezana, E.J. Rackham, L. Bañares, F.J. Aoiz, Phys. Chem. Chem. Phys. 122 (2005) 234309.

[5] L. Bañares, J.F. Castillo, P. Honvault, J.-M. Launay, J. Chem. Phys. 7 (2005) 627.
[6] N. Balucani, P. Casavecchia, L. Bañares, F.J. Aoiz, T. González-Lezana, P. Honvault, J.-M. Launay, J. Phys. Chem. A 110 (2006) 817.
[7] F.J. Aoiz, L. Bañares, V.J. Herrero, J. Phys. Chem. A 110 (2006) 12546.
[8] T. González-Lezana, O. Roncero, P. Honvault, J.-M. Launay, N. Bulut, F.J. Aoiz, L. Banares, J. Chem. Phys. 125 (2006) 094314.
[9] M.L. González-Martínez, L. Bonnet, P. Larrégaray, J.-C. Rayez, J. Chem. Phys. 126 (2007) 041102.
[10] P. Halvick, T. Stoecklin, P. Larrégaray, L. Bonnet, Phys. Chem. Chem. Phys. 9 (2007) 582.
[11] Z. Sun, D.H. Zhang, C. Xu, S. Zhou, D. Xie, G. Lendvay, S-Y. Lee, S.Y. Lin, H. Guo, J. Am. Chem. Soc. 130 (2008) 14962.
[12] G. Lendvay, D. Xie, H. Guo, Chem. Phys. 349 (2008) 181.
[13] M.L. González-Martínez, W. Arbelo-González, J. Rubayo-Soneira, L. Bonnet, J.-C. Rayez, Chem. Phys. Lett. 463 (2008) 65.
[14] G. Czakó, J.M. Bowman, J. Chem. Phys. 131 (2009) 244302.
[15] Z. Sun, L. Liu, S.Y. Lin, R. Schinke, H. Guo, D.H. Zhang, Proc. Nat. Acad. Sci. 107 (2010) 555.
[16] J. Espinosa-Garcia, L. Bonnet, J.C. Corchado, Phys. Chem. Chem. Phys. 12 (2010) 3873.
[17] P.G. Jambrina, J.M. Alvariño, F.J. Aoiz, V.J. Herrero, V. Sãez-Rábanos, Phys. Chem. Chem. Phys. 12 (2010) 12591.
[18] Z. Li, C. Xie, B. Jiang, D. Xie, L. Liu, Z. Sun, D.H. Zhang, H. Guo, J. Chem. Phys. 134 (2011) 134303.
[19] J.D. Sierra, L. Bonnet and M. Gonzalez, J. Phys. Chem. A, doi:10.1021/jp202022p.
[20] L. Bonnet, J.-C. Rayez, Chem. Phys. Lett. 277 (1997) 183.
[21] L. Bonnet, J.-C. Rayez, Chem. Phys. Lett. 397 (2004) 106.
[22] L. Bonnet, J. Chem. Phys. 128 (2008) 044109.
[23] L. Bonnet, Chin. J. Chem. Phys. 22 (2009) 210.
[24] L. Bonnet, J. Espinosa-Garcia, J. Chem. Phys. 133 (2010) 164108.
[25] R.N. Porter, L.M. Raff, in: W.H. Miller (Ed.), Dynamics of Molecular Collisions, Part B, Plenum, New York, 1976.
[26] T.D. Sewell, D.L. Thomson, Int. J. Mod. Phys. B 11 (1997) 1067.
[27] W.H. Miller, J. Chem. Phys. 53 (1970) 1949.
[28] R.A. Marcus, Chem. Phys. Lett. 7 (1970) 252.
[29] W.H. Miller, Adv. Chem. Phys. 25 (1974) 69.
[30] W.H. Miller, J. Phys. Chem. A 105 (2001) 2942.
[31] M.S. Child, Molecular Collision Theory, Academic Press, 1974.
[32] J.N.L. Connor, Chem. Soc. Rev. 5 (1976) 125.
[33] L. Bonnet, C. Crespos, Phys. Rev. A 78 (2008) 062713.
[34] We note the existence of a paper by R.W. Anderson on binning [46], based on the correspondence of continuous classical and discrete quantum distributions [47], which naturally enforces unitarity and does address relationship with Gaussian binning.
[35] P. Pechukas, J.C. Light, J. Chem. Phys. 42 (1965) 3281.
[36] E.E. Nikitin, Theory of Elementary Atomic and Molecular Process in Gases, Clarendon Press, Oxford, USA, 1974 (sections 28-31, 50, and references of this author therein).
[37] L. Bonnet, J.-C. Rayez, Chem. Phys. 201 (1995) 203.
[38] L. Bonnet, J.-C. Rayez, J. Phys. Chem. A 101 (1997) 9318.
[39] P. Larrégaray, L. Bonnet, J.-C. Rayez, J. Phys. Chem. A 110 (2006) 1552.
[40] P. Larrégaray, L. Bonnet, J.-C. Rayez, J. Chem. Phys. 127 (2007) 084308.
[41] A. Aguado, O. Roncero, C. Tablero, C. Sanz, M. Paniagua, J. Phys. Chem. 112 (2000) 1240.
[42] The σ_Q cross section presented here is a smooth fit of the exact results given in Ref. [17].
[43] W.H. Miller, J. Chem. Phys. 54 (1971) 5386.
[44] E.T. Whittaker, Treatise on the Analytical Dynamics, 4th ed., Cambridge University Press, Cambridge, UK, 1989.
[45] M.L. González-Martínez, L. Bonnet, P. Larrégaray, J.-C. Rayez, J. Rubayo-Soneira, J. Chem. Phys. 130 (2009) 114103.
[46] R.W. Anderson, Mol. Phys. 106 (2008) 977.
[47] R.W. Anderson, V. Aquilanti, J. Chem. Phys. 124 (2006) 214104.

CHAPTER II

Vibrational predissociation of weakly bound van der Waals clusters

Summary

The vibrational predissociation (VP) of the $Ne_2Br_2(B)$ van der Waals (vdW) complex is investigated in the range of vibrational levels v'=16–23, by means of the QCT-SB and QCT-GB methods. Section II.1 presents a short summary on the characteristics of VP and the quasi-classical approach for its description for triatomic vdW molecules. Section II.2 extends the method to the tetratomic aggregates and applies it to a concrete system, *i.e.*, the $Ne_2Br_2(B)$ complex.

II.1 Theoretical introduction

Photodissociation of RgBC complexes in the $B \leftarrow X$ band

Triatomic vdW molecules RgBC, formed by a chemically bound diatom BC and a rare gas atom Rg, may exhibit different dissociation mechanisms upon laser-induced excitation in the $B \leftarrow X$ band of RgBC. As it is represented in panel a) of Fig. II.1, the molecule can be excited either to a completely repulsive elec-

tronic state in the dissociation coordinate [1] or a 'partially' repulsive state with a very shallow well. In both cases, excitation leads to the rapid formation of BC and Rg products. This process is called direct photodissociation (DP). For several RgBC complexes, there are experimental and theoretical evidence of the existence of both linear and T-shaped isomers in the ground electronic state X. Excitation from the linear isomer usually leads to DP [85, 86]. Another dissociation mechanism is shown in panel b) of the same figure. It is possible for the diatom to be excited to a bound electronic state and the rare gas atom to induce a nonadiabatic coupling with a different electronic state of BC whose potential is repulsive, so that dissociation finally takes place in the latter, yielding free B and C atoms in the products. This process is known as electronic predissociation (EP) [87–90].

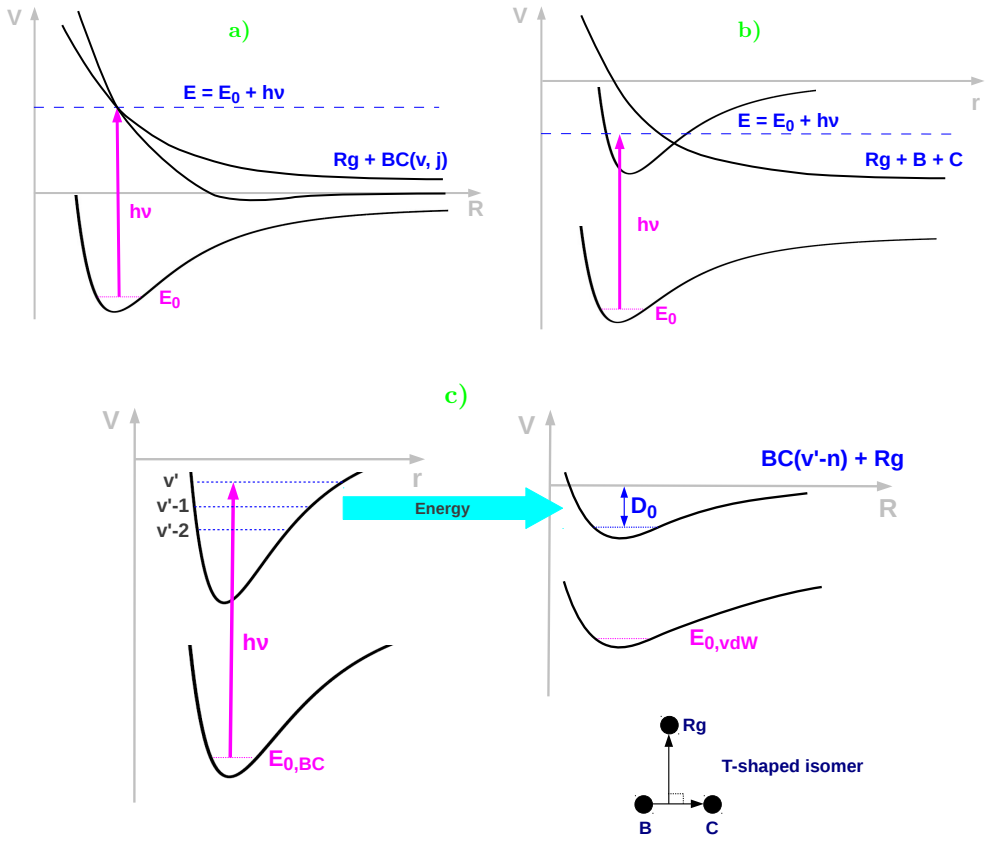

Figure II.1: Schematic representation of the different photodissociation pathways in RgBC(B) vdW molecules. Direct photodissociation in panel a), electronic predissociation in b), and vibrational predissociation in panel c).

A different fragmentation pathway arises when the laser induces a vibrational excitation of BC in the upper electronic state. The subsequent transfer of such

[1] Assuming that the photo-excitation does not provide enough energy to break the BC bond, the dissociation coordinate coincides with the distance R from the center of mass of BC to Rg

excess of (vibrational) energy into the vdW modes eventually dissociates the molecule, leading to Rg+BC products after a given time. This is called vibrational predissociation, usually observed following excitation from the T-shaped isomer. An schematic representation of VP is shown in panel c) of Fig. II.1. Other dissociation mechanisms can also be mentioned involving, for instance, rotational predissociation, tunneling through a centrifugal barrier, etc., but the ones depicted in Fig. II.1 seem to be the most frequently observed.

In general, all these decay mechanisms can be simultaneously present upon excitation and detected experimentally. VP from the T-shaped isomer gives a discrete spectrum, usually much more intense than the one from the linear isomer, which is a broad continuum more difficult to detect. In the case of EP, no signal is received as BC brakes and its presence has to be inferred indirectly. Despite all of these processes compete each other, the VP seems to be most predominant for a wide variety of rare gas-diatom species and, naturally, most of the attention has been focused on this process. We concentrate in this chapter in the quasi-classical study of the VP following excitation from the T-shaped isomer.

VP of RgBC(*B,v'*) complexes

To study the VP of RgBC(B), the diatom is excited within the complex from the electronic and vibrational ground states to a very specific vibrational level v' of the B-electronic state of BC. The resulting quasistable state of the complex completely decays together with the loss of n vibrational quanta of BC after certain time, that is,

$$\mathrm{RgBC}(X, v_1 = 0, j_1) \xrightarrow{h\nu} \left[\mathrm{RgBC}(B, v', j')\right]^* \xrightarrow{\mathrm{VP}} \mathrm{Rg} + \mathrm{BC}(B, v, j), \qquad \text{(II.1)}$$

where $v = v' - n$, and the system is said to dissociate through channel $\Delta v = v - v' = -n$. It is frequent to report in this kind of processes the survival probabilities curves, from which the lifetimes τ of the intermediate complex can be extracted, and the final rovibrational distributions of BC. All these observables together can give a complete picture of the dynamics of the process, which, however, may result in a much more complicated decay mechanism than represented in scheme II.1.

The experiment shows that, when the energy associated with $n = 1$ is sufficient to break the vdW bond, the initial state usually couples directly with the $\Delta v = -1$ continuum and VP is direct. In that case, only the $(v' - 1)$ product channel would be populated. However, as v' approaches the closing of the $\Delta v = -1$ channel, population in the $(v' - 2)$ product channel appears and progressively increases, even when the loss of one quantum of vibrational energy is enough to dissociate the system. Clearly, a different decay mechanism starts

becoming significantly more important. It is possible for the initial state to couple with one or more highly excited vdW states of the $\Delta v = -1$ channel before dissociating to the $\Delta v = -2$ continuum. In other words, BC losses a vibrational quantum, excites nondissociative vdW modes so that no dissociation is observed. The subsequent loss of another vibrational quantum is what ultimately dissociates the molecule. This mechanism is know as intramolecular vibrational energy redistribution (IVR).

For each particular system, depending on v', IVR may have a dominant role in the dissociation over the other dissociation mechanisms. In $ArCl_2$ [91,92], for instance, for v'=6 and 7, VP is direct while for v'=10 and 11, for which $\Delta v = -1$ channel is closed, IVR dominates the dynamics. For $HeBr_2$ [93] and $NeBr_2$ [94] about the closing of their corresponding $\Delta v = -1$ channels, something similar occurs. A direct evidence of IVR are highly structured rotational distributions that strongly depend on the initial vibrational level v'. Using time- and frequency-resolved pump-probe spectroscopy, experimentalists have been able to monitor in real-time the VP. One may also infer that IVR is present in the $\Delta v = -n$ channel, if the signal coming from RgBC(B,v') complex disappears and no signal from BC(B,$v'-n$) is received until some time interval later. As mentioned before, it is also possible for direct VP and EP to be in competition depending on v', as was recently observed for $HeBr_2$ and $NeBr_2$ [89]. This is reflected in strong oscillations of τ with v', as opposed to the monotonic decreasing dependence observed for direct VP.

In the light of exact quantum mechanical calculations, complex processes such as EP and the IVR dynamics of triatomic vdW molecules have been clarified in detail [90, 93, 95–100]. As far as tetratomic vdW complexes involving VP are concerned, very few exact full dimensional quantum mechanical calculations are reported in the literature [101–103]. For larger systems, it seems that non can be found, being the most used tools (i) an hybrid full dimensional quantum-classical method called 'molecular dynamics with quantum transitions' (MDQT) [104], developed and applied to the study of the VP of Ne_nBr_2 with n=$\overline{1,9}$ [105], Ne_nI_2 with n=$\overline{2,6}$ [106, 107] and Ne_nCl_2 with n=$\overline{2,3}$ [108], and (ii) the quasi-classical approach used in this work.

The QCT method for the VP of RgBC(B,v') complexes

In the description of the photofragmentation of triatomic vdW molecules is particularly convenient to use *Jacobi coordinates* ($\boldsymbol{r}$, $\boldsymbol{R}$), where $\boldsymbol{r}$ is a vector from B to C and $\boldsymbol{R}$ goes from the center of mass of BC to Rg. Under the assumption of zero total angular momentum, $\boldsymbol{J} = \boldsymbol{0}$, a fair constraint when modeling photodissocia-

tion process [39], the set of coordinates reduces to (r, R, θ), where $r = |\boldsymbol{r}|$, $R = |\boldsymbol{R}|$ and θ is the angle between vectors $\boldsymbol{r}$ and $\boldsymbol{R}$. Being (P_r, P_R, P_θ) the conjugated momenta to (r, R, θ), a phase space point is given by $\boldsymbol{\Gamma}$=$(r, R, \theta, P_r, P_R, P_\theta)$. In these coordinates, the Hamilton function can read [109]

$$\mathcal{H} = \mathcal{H}_{\mathrm{BC}} + \frac{1}{2\mu}\left(P_R^2 + \frac{P_\theta^2}{R^2}\right) + V_{\mathrm{Rg,BC}}(r, R, \theta), \tag{II.2}$$

where

$$\mathcal{H}_{\mathrm{BC}} = \frac{1}{2m}\left(P_r^2 + \frac{P_\theta^2}{r^2}\right) + V_{\mathrm{BC}}(r) \tag{II.3}$$

and

$$V_{\mathrm{Rg,BC}}(r, R, \theta) \overset{\mathrm{def}}{=} V(r, R, \theta) - V_{\mathrm{BC}}(r). \tag{II.4}$$

Here

$$m = \frac{m_{\mathrm{B}} m_{\mathrm{C}}}{m_{\mathrm{B}} + m_{\mathrm{C}}} \qquad \text{and} \qquad \mu = \frac{m_{\mathrm{Rg}}(m_{\mathrm{B}} + m_{\mathrm{C}})}{m_{\mathrm{Rg}} + m_{\mathrm{B}} + m_{\mathrm{C}}}$$

are the reduced masses of B-C and Rg-BC, respectively, and $V_{\mathrm{BC}}(r)$ is the interaction potential of the isolated BC molecule. Details on the global potential energy surface (PES) are given in the next section.

In general, quasi-classical methods mix the assumption that the movement of the atoms within the molecule is well described by classical mechanics with the inclusion of some elements from the quantum formalism, which are introduced *ad hoc*. In particular, the QCT method we adopt in this chapter states that the partial cross section for absorbing a photon of energy $E_f = h\nu$ and producing the BC fragment in the rovibrational state (v, j) is, assuming a constant transition dipole moment and excluding an unimportant factor, given by [39]

$$\sigma(E, v, j) \propto \int d\boldsymbol{\Gamma}_0 \rho(\boldsymbol{\Gamma}_0) \delta[\mathcal{H}(\boldsymbol{\Gamma}_0) - E] \delta[v_f(\boldsymbol{\Gamma}_0) - v] \delta[j_f(\boldsymbol{\Gamma}_0) - j]. \tag{II.5}$$

In this last equation E is the total energy of the molecule in the upper electronic state and $\rho(\boldsymbol{\Gamma}_0)$ is the phase-space distribution at time $t = 0$ (just after the electronic transition), which means that integration is over the initial phase-space states, $\boldsymbol{\Gamma}_0$. (v_f, j_f) are the semi-classical rovibrational actions of BC in the free products, given by [39]

$$\begin{aligned} v_f &= \frac{1}{2\pi\hbar} \oint P_r dr - \frac{1}{2} \\ &= \frac{\sqrt{2m}}{\pi\hbar} \int_{r_{\min}}^{r_{\max}} \sqrt{E_{\mathrm{BC}} - V_{\mathrm{BC}}(r) - \frac{P_\theta^2}{2mr^2}}\ dr - \frac{1}{2} \end{aligned} \tag{II.6}$$

and

$$j_f = \frac{1}{2}\left[\sqrt{1+4\left(\frac{P_\theta}{\hbar}\right)^2}-1\right], \tag{II.7}$$

respectively. In Eq. (II.6), $r_{\rm min}$ and $r_{\rm max}$ are the classical turning points (of BC) for an energy $E_{\rm BC} \equiv \mathcal{H}_{\rm BC}$ and an effective potential $V_{\rm eff} = V_{\rm BC} + P_\theta^2/2mr^2$.

In practice, the last two $\delta[x(\boldsymbol{\Gamma}_0) - x^*]$ functions in Eq. (II.5) need to be replaced by some approximated functions for their evaluation. A common procedure has been to replace them by simple bin (or box) functions (Eq. 7) [36–39,64]. We did something similar in the previous chapter for collisions. The $\delta[x(\boldsymbol{\Gamma}_0)-x^*]$ function on energy can also be replaced or, alternatively, a procedure such as the one explained in Chapter IV can be employed for higher numerical efficiency. In any case, its purpose is to limit the integration to those initial phase-space states, $\boldsymbol{\Gamma}_0^E$, whose corresponding total energy is within a narrow window about E. Inserting Eq. (7) into Eq. (II.5) and solving the integral by a MC procedure, results in the QCT-SB working expression

$$\sigma_{\rm SB}(E,v,j) \propto \frac{1}{N_{\rm diss}} \sum_{i=1}^{N_{\rm diss}} \rho(\boldsymbol{\Gamma}_{0,i}^E)\; \Delta[v_f(\boldsymbol{\Gamma}_{0,i}); v]\; \Delta[j_f(\boldsymbol{\Gamma}_{0,i}); j], \tag{II.8}$$

where $N_{\rm diss}$ are the number of points—dissociated trajectories—used in the evaluation of Eq. (II.5).

Application of Eq. (II.8) to a concrete problem requires (i) generating an *ensemble* of initial phase-space points according to $\rho(\boldsymbol{\Gamma}_0)$ and compatible with a total energy E, (ii) propagating classical trajectories starting from all those points until they reach the product region, usually defined by a large value $R_{\rm diss}$ of R, and (iii) assigning a weight to each trajectory given by the product of the last two box functions in Eq. (II.8). Now, given the usual relatively high density of rotational states, the use of Eq. (7) to weight the final rotation of BC is a fair approximation. For the vibration, however, where just a few states can be populated—say 1-3, as in $HeBr_2(B)$—, that may lead to unphysical results [110]. As was illustrated in the introduction and the previous chapter, more realistic observables can be obtained if vibration of the products is weighted by normalized Gaussian functions (Eq. 11) [111–113]. Replacing Eq. (11) (with $\epsilon \simeq 0.06$) by its analogue in Eq. (II.8), one gets the QCT-GB expression for the partial cross section,

$$\sigma_{\rm GB}(E,v,j) \propto \frac{1}{N_{\rm diss}} \sum_{i=1}^{N_{\rm diss}} \rho(\boldsymbol{\Gamma}_{0,i}^E)\; G[v_f(\boldsymbol{\Gamma}_{0,i}); v]\; \Delta[j_f(\boldsymbol{\Gamma}_{0,i}); j]. \tag{II.9}$$

Eqs. (14) and (16) of the next section are slight variations of Eq. (II.8) and

Eq. (II.9) to get the vibrationally resolved distribution of any observable. They also implicitly take into account the total energy constraint.

The quasi-classical approach presented so far is quite general in the photodissociation of triatomic molecules, being the main distinct feature of each implementation of the QCT method the definition of the initial phase-space distribution $\rho(\boldsymbol{\Gamma}_0)$. Regarding that, the intuitive idea we followed is that the best (classical) representation of the initial state is the one that most closely parallels the experimental conditions. With that in mind, initial coordinates are generated from the initial quantum distributions, while momenta—with their respective signs—are randomly selected, both subject to the constraint of constant total energy and angular momentum. Details on this procedure are given in ref. [114] for the triatomic case and in next section an algorithm is outlined for tetratomic complexes. In the VP of vdW molecules, moreover, as BC is excited to a specific v', the total energy E has to be consistent with the energy corresponding to the vibrational level v' of BC, $E_{\mathrm{BC}}^{v'}$.

The current formulation of the QCT method, however, is able to reproduce only 'partially' the VP observables [110]. While the kinetic of the process is reasonably well described with the method, the agreement of final vibrational distributions with the experiment and quantum calculations is only qualitative for the same accuracy level of the PES. At least three reasons are responsible for that: (i) the markedly non-statistic behavior of the dynamics, given by the large difference between the B-C and Rg-BC vibrational frequencies, which makes the energy transfer from the diatom to the vdW modes very inefficient, (ii) the dominant role of IVR in the dynamics, which is a purely quantum effect, impossible to reproduce within the current QCT formulation and (iii) an intrinsically classical correlation between τ and v', which seems to be a consequence of the phase-space structure of the system (next section clarifies this). A similar behavior should be expected in larger vdW complexes as the same arguments hold.

Next section continues with the extension of the QCT method presented here to the tetratomic case and, in particular, to the description of the VP of the $Ne_2Br_2(B,v')$ complex.

II.2 Publication

THE JOURNAL OF CHEMICAL PHYSICS **136**, 144303 (2012)

Quasi-classical trajectories study of $Ne_2Br_2(B)$ vibrational predissociation: Kinetics and product distributions

Wilmer Arbelo-González,[1] Maykel L. González-Martínez,[1,a)] Stewart K. Reed,[2] Jesús Rubayo-Soneira,[1] and Dmitrii V. Shalashilin[2]
[1]*Departamento de Física General, Instituto Superior de Tecnologías y Ciencias Aplicadas, Habana 10600, Cuba*
[2]*School of Chemistry, University of Leeds, Leeds LS2 9JT, United Kingdom*

(Received 1 December 2011; accepted 19 March 2012; published online 9 April 2012)

The vibrational predissociation of the $Ne_2Br_2(B)$ van der Waals complex has been investigated using the quasi-classical trajectory method (QCT), in the range of vibrational levels $v' = 16$–23. Extensive comparison is made with the most recent experimental observations [Pio *et al.*, J. Chem. Phys. **133**, 014305 (2010)], molecular dynamics with quantum transitions simulations [Miguel *et al.*, Faraday Discuss. **118**, 257 (2001)], and preliminary results from 24-dimensional Cartesian coupled coherent state (CCCS) calculations. A sequential mechanism is found to accurately describe the theoretical dynamical evolution of intermediate and final product populations, and both QCT and CCCS provide very good estimates for the dissociation lifetimes. The capabilities of QCT in the description of the fragmentation kinetics are analyzed in detail by using reduced-dimensionality models of the complexes and concepts from phase-space transport theory. The problem of fast decoupling of the different coherent states in CCCS simulations, resulting from the high dimensionality of phase space, is tackled using a re-expansion scheme. QCT ro-vibrational product state distributions are reported. Due to the weakness of the van der Waals couplings and the low density of vibrational states, QCT predicts a larger than observed propensity for $\Delta v' = -1$ and -2 channels for the respective dissociation of the first and second Ne atoms. © *2012 American Institute of Physics*. [http://dx.doi.org/10.1063/1.3700156]

I. INTRODUCTION

Studying the influence of size-selected solvents on the structure and dynamics of molecular systems is essential in understanding both molecular energy transfers and the transition from the gas to condensed phase.

In this regard, clusters of rare gas (Rg) atoms doped with a diatomic halogen (BC) are particularly convenient for at least two reasons: (1) the weakness of the van der Waals (vdW) interactions provides a means to effectively "separate" the diatom from the environment, which in turn allows a relatively simple identification of the different energy transfer mechanisms at the state-to-state level; and (2) the number n of Rg atoms can be spectroscopically selected for their addition induces a known blueshift in the vibronic transition $B(v') \leftarrow X(v = 0)$.[1–3]

These weakly bound complexes have been the subject of intense scrutiny since the pioneering experiments of Levy and co-workers[1,2,4–6] and the theoretical work of Beswick *et al.*[7,8] in the late seventies. In their experiments, Levy and co-workers used laser-induced fluorescence to study Rg_nI_2 molecules based on He, Ne, and Ar with up $n = 7$ I atoms.

Following the laser-induced vibrational excitation of BC, the energy is usually redistributed within the molecule leading to the breaking of the vdW bonds. This process is known as vibrational predissociation (VP) and provides significant information, for instance, on the dynamics of intramolecular vibrational energy redistribution (IVR). Rotational, electronic, and other predissociation processes are possible. In the former, rotational de-excitation of the BC molecule directly provides enough energy for fragmentation. In electronic predissociation, non-adiabatic transitions to repulsive electronic states of BC may instead lead to dissociation of the chemically bonded molecule. This was first observed in Ar_nI_2 (Refs. 5 and 6) and recently studied in $HeBr_2$ and $NeBr_2$.[9] In general, the dependence of the transitions on the details of the potential energy surfaces (PESs) as well as on the available energy makes it possible to extract useful information on binding energies and electronic couplings.

The VP of vdW complexes is by far the predominant dissociation process and as such has been the most extensively studied. Depending on the vibrational state excited, vdW systems fragment following one or several elementary steps, which usually include direct dissociation, different IVR regimes, evaporative cooling (EC), etc. For example, the VP of Ne_nBr_2 clusters is described in Refs. 10 and 11. Each step may have different accessible final states and characteristic kinetics which manifest themselves in experiments through distinctively structured product state distributions as in the case of $ArCl_2$,[12] $HeBr_2$, and $NeBr_2$.[13,14]

All of the above work (and considerably more) has proved through the years that, despite their apparent simplicity, even small vdW aggregates with $n = 1, 2$ undergo

a)Present address: Department of Chemistry, Durham University, Durham DH1 3LE, United Kingdom. Electronic mail: m.l.gonzalez-martinez@durham.ac.uk.

a wide variety of processes that are representative of most of the dynamical pathways observed in more complex, and conventionally bonded, molecules.[15] Hence, vdW systems have become valuable prototypes in the analysis of both intermolecular and intramolecular energy transfers.

For small molecules, exact quantum mechanical calculations (EQM) can be performed with modern computers and algorithms. Being essentially exact, at least to the accuracy of the PESs, these calculations have provided a rigorous picture of the VP process. More recently, they have also addressed in detail the problem of IVR dynamics and the role played by continuum resonances in triatomic systems.[16–22] Quantum calculations on larger complexes almost inevitably use various approximate methods and there are just a few EQM studies in the literature. In 2001, Meier and Manthe studied the VP of Ne_2I_2 using the multiconfiguration time-dependent Hartree method[23] and although vibrational branching ratios were compared with the experiment,[2] the main aim of their work was to provide a benchmark for future developments in the methodology. In 2005, García-Vela proposed a full-dimensional, fully coupled wave packet method and used it to study the VP of He_2Cl_2,[24] obtaining good agreement with experimental lifetimes and rotational distributions thus providing a test for the accuracy of the PES employed.

Yet, time-dependent, fully detailed investigations of energy transfers in vdW molecules containing more than one or two Rg atoms still pose a considerable challenge for both experiments and EQM calculations. In the former, researchers should be able to identify and characterize all intermediate complexes as well as address their dynamical evolution. In the latter they have to cope with the increasing number of degrees of freedom (DOF) and large basis sets that eventually make the computational cost prohibitive. Thus, in the investigation of larger systems hybrid quantum-classical, e.g., molecular dynamics with quantum transitions (MDQT) simulations,[10,11,25–27] and quasi-classical trajectory (QCT) methods have been to date the most widely used practical alternatives.

In fact, most QCT applications have successfully reproduced the fragmentation kinetics for at least several tri- and tetra-atomic complexes. This is the case for molecules such as Ne_nI_2 ($n = 1, 2$),[19,28,29] HeICl,[30] and $NeBr_2$[14,31] in which many classical predictions were later confirmed by EQM.[32] More recently, some of us have explored the extent to which the Gaussian weighted (GW) trajectory method[33,34] adds to the applicability of QCT in the study of $RgBr_2$ (Rg = He, Ne, Ar) molecules.[35] We found that GW may enhance the QCT description of product state distributions both quantitatively and qualitatively, especially if only a few vibrational states are populated or calculations are performed very close to a channel closing. However, in cases such as the VP of $NeCl_2$ (Ref. 36) and generally, when IVR takes place in the sparse regime and plays a significant role, it seems that only quantum mechanical calculations can be compatible with the experimental observations. Hence, despite the success of many previous implementations of QCT, the validity of classical concepts in the context of the VP of vdW aggregates is yet to be clarified. At last, complementary studies addressing the dynamical (in)stability of these systems exist in the literature. The analysis of phase-space bottlenecks in the predissociation of HeI_2 was used as a benchmark in the foundation of phase-space transport theory (PSTT).[37–41] More recently, irregular variations of decay rates as well as details of the absorption spectra have been studied through the analysis of the phase-space structure and its evolution with increasing excitation energy.[42–45]

In general, testing the accuracy and reliability of theoretical methods largely depends on detailed experimental data becoming available. In particular, as stated above, realistic kinetic mechanisms can only be obtained if the dynamics of all intermediate species is recorded in the experiment. This has traditionally proved to be quite challenging. For instance, in 1992, Gutmann *et al.*[46] used picosecond pump-probe spectroscopy to study the VP of Ne_nI_2 with $n = 2$–4 but only registered the formation of I_2. They therefore inferred the evolution of intermediates by fitting the product dihalogen formation to a sequential first-order kinetic mechanism. In 2010, Pio *et al.*[47] reported the characterization of the VP of $Ne_2Br_2(B)$ at an unprecedented level of detail. Using time- and frequency-resolved pump-probe spectroscopy they were able to record the real time evolution of all complexes involved, propose a kinetic mechanism, and determine time constants and product vibrational state distributions.

In this paper, we report QCT and preliminary Cartesian coupled coherent states (CCCS) (Refs. 48 and 49) calculations on the VP of $Ne_2Br_2(B, v' = 16$–$23)$. We compare both theoretical methods as well as their ability to reproduce the experimental observations[47] and previous MDQT predictions.[11] Our main goal is to build upon the current understanding of the capabilities of QCT in the simulation of VP processes involving larger vdW clusters, and to distinguish whenever possible the results which are intrinsic to the methodology from those that are characteristic to the systems under consideration. Complementary analysis of full-dimensional and simplified models for the VP of the $NeBr_2$ triatomic complex have been very useful in the interpretation of QCT results and are conveniently discussed.

II. THEORY

A. Vibrational predissociation of a tetra-atomic van der Waals cluster

Assuming that the photo-excitation does not provide enough energy to break the BC bond, the VP of a tetra-atomic vdW aggregate is represented in Scheme 1 where the i and f superscripts denote intermediate and final states, respectively. Two main fragmentation paths are possible, which we refer to as the *sequential* (*S*) and *concerted* (*C*) mechanisms, comprising two channels each. The former is associated with two well-defined dissociation steps and usually dominates as long as direct dissociation prevails over IVR. It leads to the loss of two vibrational quanta and has relatively simple implications in the VP kinetics.[11,29] The latter becomes increasingly important as IVR dominates, and is very often linked to the loss of more than two vibrational quanta and

$$\mathrm{Rg_1Rg_2BC}(X,v,j) \xrightarrow{h\nu} \left[\mathrm{Rg_1Rg_2BC}(B,v',j')\right]^* \xrightarrow{\mathrm{VP}_{(1)}} \begin{cases} (S_{1(2)})\ \mathrm{Rg}_{1(2)} + \mathrm{Rg}_{2(1)}\mathrm{BC}(B,v^{\mathrm{i}},j^{\mathrm{i}}) \xrightarrow{\mathrm{VP}_{(2)}} \mathrm{Rg_1} + \mathrm{Rg_2} + \mathrm{BC}(B,v^{\mathrm{f}},j^{\mathrm{f}}) \\ (C_1)\ \mathrm{Rg_1} + \mathrm{Rg_2} + \mathrm{BC}(B,v^{\mathrm{f}},j^{\mathrm{f}}) \\ (C_2)\ \mathrm{Rg_1Rg_2}(v_{12}^{\mathrm{f}},j_{12}^{\mathrm{f}}) + \mathrm{BC}(B,v^{\mathrm{f}},j^{\mathrm{f}}) \end{cases}$$

SCHEME 1. Representation of the VP of a generic Rg_1Rg_2BC vdW molecule, showing the $(S_{1(2)})$ sequential, as well as concerted (C_1) *without* and (C_2) *with* molecular formation mechanisms.

highly-structured product state distributions. All these features help in distinguishing between the concerted and sequential mechanisms for in the vast majority of cases they lead to the same final products (compare $S_{1(2)}$ and C_1). Finally, when the interaction between the Rg atoms is sufficiently strong and the dynamical evolution allows for favorable configurations, there is a non-negligible probability of formation of a Rg_1Rg_2 molecule.

B. Potential energy surfaces

As seen in Scheme 1 both the ground X and excited B electronic states are, at least in principle, involved in the VP process. Recent studies on the structure of He_2Br_2 and He-ICl complexes[50,51] and EQM calculations on He_2Cl_2[24] have shown that the global PES for these systems is accurately approximated by

$$V = V_{\mathrm{Rg_1,BC}} + V_{\mathrm{Rg_2,BC}} + V_{\mathrm{Rg_1Rg_2}} + V_{\mathrm{BC}}, \qquad (1)$$

where V_{BC} is the interaction potential of the isolated BC molecule, $V_{\mathrm{Rg_i,BC}}$ $(i = 1, 2)$ is the vdW PES of the ith triatomic aggregate, and $V_{\mathrm{Rg_1Rg_2}}$ is the potential describing the Rg_1–Rg_2 interaction.

Here, we extrapolate these results and in a first step, we express the global PESs for the Ne_2Br_2 complex in form (1). It is important to note that, even if this proves to be a good approximation for Rg = He and Ne due to the weakness of the vdW bonds, neglecting 4-body contributions in the global PES of clusters containing heavier Rg atoms could eventually fail. Second, by using pairwise additive potentials for the terms $V_{\mathrm{Rg_i,BC}}$, we neglect 3-body contributions to the triatomic vdW PES. Although this is known to be a good approximation for the B electronic state, which is where the VP process takes place, it is only partially adequate for the ground state.[54,55] In particular, there is theoretical[56] and experimental[57] evidence for an additional minimum at linear configurations in the PES of the X state, which cannot be reproduced by pairwise interactions. The topology of the two electronic states is in fact similar but the linear minimum for the B state moves to a longer distance and becomes much shallower compared to the X state, which makes a pairwise additive description adequate for the former and not the latter. Nevertheless, the calculations presented here refer to the fragmentation induced by the photo-excitation of the T-shaped isomer which can be correctly reproduced in the pairwise additive approximation. All pair interactions are analytically modeled by Morse functions, the parameters for which have been taken from the literature and are summarized in Table I.

C. Quasi-classical trajectories

1. System model

A particular Jacobi association diagram yields the most convenient set of coordinates to describe the unimolecular dissociation of a triatomic RgBC vdW complex. Two Jacobi vectors are involved, $\boldsymbol{r}$ which conventionally runs from the heaviest to the lightest of atoms B or C, and $\boldsymbol{R}$, from the diatom's center of mass towards the Rg atom. Among its main advantages are the symmetrical decomposition of the molecular PES, the explicit use of a dissociation coordinate, and an associated diagonal kinetic operator. It is therefore common when studying larger vdW aggregates, i.e., $Rg_1\ldots\underline{Rg_n}BC$, to choose a "generalized" set of vectors $\boldsymbol{r}$, $\boldsymbol{R}_i$ $(i = \overline{1,n})$ which inherits most of the aforementioned advantages. These are not actually Jacobi coordinates but are referred to as satellite or bond coordinates, their main drawback being a non-diagonal kinetic operator.

The total angular momentum of a tetra-atomic vdW system is given by $\boldsymbol{J} = \boldsymbol{l}_1 + \boldsymbol{l}_2 + \boldsymbol{j}$, where $\boldsymbol{l}_i$ is the end-over-end orbital angular momentum of atom Rg_i with respect to BC, and $\boldsymbol{j}$ is the rotational angular momentum of BC. Using satellite coordinates and keeping $\boldsymbol{J}$ at zero, the set of coordinates reduces to $\{r, R_1, R_2, \theta_1, \theta_2, \phi\}$. These have been depicted in Fig. 1. Choosing $\boldsymbol{J}$ to be zero is a well-justified constraint when studying the photo-dissociation of rotationally cold species[58] as produced in the experiment through a supersonic free jet expansion.[47] The complete set of variables in classical phase space $\boldsymbol{\Gamma}$ is finally obtained by adjusting the respective conjugate momenta so that the Hamilton

TABLE I. Morse parameters for the various pair interactions in Ne_2Br_2.

	Br_2 state	D (cm^{-1})	α (Å^{-1})	r_{eq} (Å)	Reference
Br–Br	X	24 557.674	1.588	2.281	16
	B	3 788.0	2.045	2.667	52
Br–Ne	X	45.0	1.67	3.7	20
	B	42.0	1.67	3.9	53
Ne–Ne	X, B	29.36	2.088	3.091	29

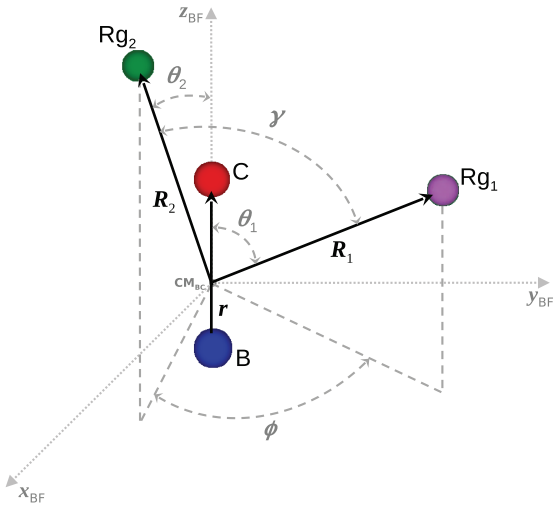

FIG. 1. Coordinate set for a prototypical Rg_1Rg_2BC vdW molecule in its body-fixed reference frame.

function reads[59]

$$\mathcal{H}^{J=0} = \mathcal{H}_{BC} + \sum_{i=1}^{2} \frac{1}{2\mu_{Rg_i,BC}} \left(P_{R_i}^2 + \frac{l_i^2}{R_i^2} \right) + \frac{\boldsymbol{P}_1 \cdot \boldsymbol{P}_2}{m_B + m_C} + V_{vdW}(\boldsymbol{r}, \boldsymbol{R}_1, \boldsymbol{R}_2), \tag{2}$$

where

$$\mathcal{H}_{BC} \stackrel{\text{def}}{=} \frac{1}{2\mu_{BC}} \left(P_r^2 + \frac{\boldsymbol{j}^2}{r^2} \right) + V_{BC}(r) \tag{3}$$

and

$$V_{vdW}(\boldsymbol{r}, \boldsymbol{R}_1, \boldsymbol{R}_2) \stackrel{\text{def}}{=} V(\boldsymbol{r}, \boldsymbol{R}_1, \boldsymbol{R}_2) - V_{BC}(r). \tag{4}$$

Here, $\mu_{Rg_i,BC}^{-1} = m_{Rg_i}^{-1} + (m_B + m_C)^{-1}$ and $\mu_{BC}^{-1} = m_B^{-1} + m_C^{-1}$ are the inverse of the appropriate reduced masses, while the angular momenta

$$\boldsymbol{l}_i^2 = P_{\theta_i}^2 + \frac{P_\phi^2}{\sin^2\theta_i}; \quad i = 1, 2 \tag{5}$$

and

$$\begin{aligned} \boldsymbol{j}^2 = \boldsymbol{l}_1^2 + \boldsymbol{l}_2^2 + 2\boldsymbol{l}_1 \cdot \boldsymbol{l}_2 = P_{\theta_1}^2 + P_{\theta_2}^2 + 2P_{\theta_1}P_{\theta_2}\cos\phi \\ - 2\sin\phi \left(\frac{\cos\theta_2}{\sin\theta_2} P_{\theta_1} + \frac{\cos\theta_1}{\sin\theta_1} P_{\theta_2} \right) P_\phi \\ + \left(\frac{1}{\sin^2\theta_1} + \frac{1}{\sin^2\theta_2} - 2\cos\phi \frac{\cos\theta_1\cos\theta_2}{\sin\theta_1\sin\theta_2} - 2 \right) P_\phi^2. \end{aligned} \tag{6}$$

The non-diagonal coupling term, $\boldsymbol{P}_1 \cdot \boldsymbol{P}_2$, can be expressed as

$$\begin{aligned} \boldsymbol{P}_1 \cdot \boldsymbol{P}_2 = P_{R_1}P_{R_2}\cos\gamma - \frac{\cos\phi}{R_1R_2\sin\theta_1\sin\theta_2} P_\phi^2 \\ + \frac{\cos\theta_1\cos\theta_2\cos\phi + \sin\theta_1\sin\theta_2}{R_1R_2} P_{\theta_1}P_{\theta_2} \\ + \frac{\sin\theta_1\cos\theta_2\cos\phi - \cos\theta_1\sin\theta_2}{R_2} P_{R_1}P_{\theta_2} \\ + \frac{\cos\theta_1\sin\theta_2\cos\phi - \sin\theta_1\cos\theta_2}{R_1} P_{R_2}P_{\theta_1} \\ - \frac{\sin\theta_1\sin\phi}{R_2\sin\theta_2} P_{R_1}P_\phi - \frac{\sin\theta_2\sin\phi}{R_1\sin\theta_1} P_{R_2}P_\phi \\ - \frac{\cos\theta_1\sin\phi}{R_1R_2\sin\theta_2} P_{\theta_1}P_\phi - \frac{\cos\theta_2\sin\phi}{R_1R_2\sin\theta_1} P_{\theta_2}P_\phi \end{aligned} \tag{7}$$

with

$$\cos\gamma = \sin\theta_1\sin\theta_2\cos\phi + \cos\theta_1\cos\theta_2. \tag{8}$$

Finally, in the interpretation of our results, models with two and three DOF (2/3-DOF) are used for the intermediate RgBC complex. The 3-DOF model is a full-dimensional $\boldsymbol{J} = \boldsymbol{0}$ approximation of RgBC. The phase-space variables span a subspace of $\boldsymbol{\Gamma}$, i.e., $\boldsymbol{\Gamma}_3 = \{r, R, \theta, P_r, P_R, P_\theta\}$, and all relevant formulae can be easily obtained from Eqs. (2)–(4) or the literature, e.g., Ref. 35. The 2-DOF is constructed by additionally fixing $\theta = \pi/2$, corresponding to the equilibrium configuration of $NeBr_2$ in the B electronic state. The phase state is thus $\boldsymbol{\Gamma}_2 = \{r, R, P_r, P_R\}$ and all necessary formulae can be obtained by simplification of the 3-DOF. In particular, several results can be better understood by analyzing the structure of classical phase space for the 2-DOF model. To this end, we have used Poincaré surfaces of section (SOS), which are powerful visual tools when considering systems with two DOF.[60] All SOS employed here were constructed from trajectory intersections with the hypersurface ($r = r_{eq}$, R, $P_r \geq 0$, P_R), where r_{eq} is the equilibrium bond length of BC.

2. Initial conditions

In general, the QCT simulation of photo-induced processes requires the initial conditions to closely match those recreated in the experiment.[58] The latter are however quantum in nature, and are often quite difficult to determine and reproduce classically, especially for polyatomic systems. Obviously, the workarounds commonly used in systems with strong intermolecular/intramolecular interactions[61] are not applicable here and quantum distributions need to be calculated from the molecular wave function.

Although the rigorous form of the initial wave function is known to depend on the particular shape of the laser pulse, cf. Ref. 20, we assume that the pump laser acts during an extremely short time and the system undergoes a perfect vertical transition. The Schrödinger equation for the tetra-atomic system in both the ground and excited states is solved using the variational method proposed in Ref. 62. Then, the X-state wave function is used to calculate the probability distributions (statistical weights) for all relevant variables, while the eigenvalues from the B-state determine the VP energetics, as in our previous work.[31,35] Once the X- and B-state quantum problems are solved, QCT initial conditions are calculated following the algorithm proposed in Ref. 63 (with only a few minor modifications):

1. a set of "quantum" numbers $\{l_1, l_2, j\}$ is selected using their respective distributions—checking it satisfies the triangle condition $\triangle(l_1, l_2, j)$ to ensure compatibility with $\boldsymbol{J} = \boldsymbol{0}$;

2. the angles θ_1, θ_2, γ are generated following the appropriate distributions, and ϕ calculated from Eq. (8);
3. the system of nonlinear equations (5) and (6) is solved for the angular momenta P_{θ_1}, P_{θ_2} and P_ϕ;
4. r is generated from the calculated distribution, and the value of j used to calculate P_r from Eq. (3). Here, $\mathcal{H}_{\rm BC}$ is conveniently replaced with $\mathcal{E}_{\rm BC}^{B,v'}$, i.e., the eigenvalue corresponding to the $(B, v', j' = 0)$ state of BC,[62] and the sign of P_r randomly chosen;
5. R_1 and R_2 are generated with the corresponding distribution, and approximate conjugate momenta calculated using

$$P_{R_i}^{\rm app} = \pm\sqrt{2\mu_{{\rm Rg_i,BC}}\left(\mathcal{E}_{\rm Rg_i,BC}^{B,v'} - \frac{l_i^2}{2\mu_{\rm Rg_i,BC}R_i^2} - V_{\rm Rg_i,BC}\right)}, \tag{9}$$

where $\mathcal{E}_{\rm Rg_i,BC}^{B,v'}$ is the eigenvalue corresponding to the $\rm Rg_i BC$ triatomic aggregate with BC in its (B, v') state,[62] and the sign of the momentum is once again randomly chosen;
6. finally, the energy associated to the non-diagonal kinetic term $\boldsymbol{P}_1 \cdot \boldsymbol{P}_2$ and $V_{\rm Rg_1Rg_2}$ is redistributed within the vdW modes by writing $P_{R_{1(2)}} = P_{R_{1(2)}}^{\rm app} + \Delta_{1(2)}$, where Δ_1 and Δ_2 are quantities to be determined. Their calculation requires evaluating $\mathcal{H}^{J=0} = \mathcal{E}^{B,v'}$, the energy of the tetra-atomic complex with Br_2 in the (B, v') state, using the set of values $\{r, R_1, R_2, \theta_1, \theta_2, \phi, P_r, P_{R_1}^{\rm app}, P_{R_2}^{\rm app}, P_{\theta_1}, P_{\theta_2}, P_\phi\}$, as well as the additional constrain $P_{R_1}^{\rm app}/P_{R_2}^{\rm app} = \Delta_1/\Delta_2$.

Steps 1–6 are repeated until $N_{\rm tot}$ initial conditions are obtained.

3. From classical magnitudes to observables

We have recently discussed the statistical handling of QCT results for comparison with experimental observables in the specific case of the VP of triatomic vdW systems.[35] There is however one fundamental difference between the process in tri- and tetra-atomic molecules, namely, the possible formation in the latter of an intermediate complex. For consistency, the general methodology is only summarized here with emphasis on the changes made in order to analyze the QCT results in our specific case.

When the molecule completely dissociates, $V_{\rm vdW} \to 0$ and both $\boldsymbol{j}$ and $\mathcal{H}_{\rm BC}$ become integrals of motion with the latter corresponding to the classical energy of the BC fragment, $E_{\rm BC}$. The final semi-classical ro-vibrational quantum numbers for the ith dissociated trajectory, i.e., $v_{c,i}^{\rm f}$ and $j_{c,i}^{\rm f}$, are then rigorously constant and are given by

$$\begin{aligned} v_{c,i}^{\rm f} &= \frac{1}{2\pi\hbar}\oint P_r dr - \frac{1}{2} \\ &= \frac{\sqrt{2\mu_{\rm BC}}}{\pi\hbar}\int_{r_{\rm min}}^{r_{\rm max}}\sqrt{E_{{\rm BC},i} - V_{\rm eff}}\, dr - \frac{1}{2}, \end{aligned} \tag{10}$$

where $V_{\rm eff}$ is the effective interaction potential of BC (includes the centrifugal term) and the closed integral is evaluated over one BC vibrational period[64] ($r_{\rm min}$ and $r_{\rm max}$ are the classical turning points), while

$$j_{c,i}^{\rm f} = \frac{1}{2}\left[\sqrt{1 + 4\left(\frac{\boldsymbol{j}_i}{\hbar}\right)^2} - 1\right], \tag{11}$$

which results from $\boldsymbol{j}_i^2 = j_{c,i}^{\rm f}(j_{c,i}^{\rm f} + 1)\hbar^2$.[65] Due to the weakness of the vdW interaction, the BC vibrational state in the intermediate complex, $v_{c,i}^{\rm i}$, can be estimated using Eq. (10). This requires replacing the final state magnitudes with approximate values for the intermediate state, despite these not being rigorously defined.

In what follows, we neglect the quantized nature of the rotational DOF as it has a very high density of states and refer simply to channel $\Delta v' = v^{\rm f} - v'$ by the associated final vibrational quantum number, $v^{\rm f}$.

In the procedure known as *histogram* or *standard* binning (SB), the probability density $P(M, v^{\rm f})$ that a given observable has the value M and the final BC vibrational state is $v^{\rm f}$, can be formally written as

$$P_{\rm SB}(M, v^{\rm f}) = \int d\boldsymbol{\Gamma}\,\rho(\boldsymbol{\Gamma})\delta\left[M(\boldsymbol{\Gamma}) - M\right]\Xi[v^{\rm f}(\boldsymbol{\Gamma}); v^{\rm f}, 1], \tag{12}$$

where $\rho(\boldsymbol{\Gamma})$ is the probability distribution of the initial phase-space state, $\boldsymbol{\Gamma}$, and

$$\Xi(x; x^*, \Delta) = \frac{1}{\Delta}\Theta(x^* + \Delta/2 - x)\Theta(x - x^* + \Delta/2). \tag{13}$$

$\delta(x)$ and $\Theta(x)$ are, respectively, the Dirac and Heaviside functions. $M(\boldsymbol{\Gamma})$ and $v^{\rm f}(\boldsymbol{\Gamma})$ are the final values of the observable and the vibrational action in terms of $\boldsymbol{\Gamma}$. It is relatively easy to see from Eq. (13) that Ξ defines a square barrier function of x, which equals $1/\Delta$ on $[x^* - \Delta/2, x^* + \Delta/2]$ and 0 everywhere else. Also, $P_{\rm SB}$ in Eq. (12) is normalized to 1.

In practice, $P_{\rm SB}$ is estimated by means of the Monte-Carlo expression

$$\begin{aligned} P_{\rm SB}(M_k, v^{\rm f}) \approx \frac{1}{N_{\rm diss}}\sum_{i=1}^{N_{\rm diss}}\Xi\left[M(\boldsymbol{\Gamma}_i); M_k, \alpha_k\right] \\ \times\Xi[v^{\rm f}(\boldsymbol{\Gamma}_i); v^{\rm f}, 1], \end{aligned} \tag{14}$$

where M_k is the kth midpoint in the $\{M\}_{k=1}^K$ set partition of the interval $[M_{\rm min}, M_{\rm max}]$, $\alpha_k = M_{k+1} - M_k$, and $N_{\rm diss}$ is the total number of dissociated trajectories, which is assumed to be large.

In the GW procedure one simply replaces the square barrier function $\Xi[v^{\rm f}(\boldsymbol{\Gamma}); v^{\rm f}, 1]$ in Eq. (14) with the Gaussian

$$g[v^{\rm f}(\boldsymbol{\Gamma}); v^{\rm f}, \epsilon] = \frac{\exp\{-[v^{\rm f}(\boldsymbol{\Gamma}) - v^{\rm f}]^2/\epsilon^2\}}{\pi^{1/2}\epsilon}, \tag{15}$$

in which ϵ is usually kept at 0.05. Hence, $P_{\rm GW}$ is simply

$$\begin{aligned} P_{\rm GW}(M_k, v^{\rm f}) \approx \frac{1}{N_{\rm diss}}\sum_{i=1}^{N_{\rm diss}}\Xi\left[M(\boldsymbol{\Gamma}_i); M_k, \alpha_k\right] \\ \times g[v^{\rm f}(\boldsymbol{\Gamma}_i); v^{\rm f}, \epsilon]. \end{aligned} \tag{16}$$

In the tetra-atomic case, variations of these general expressions can describe either the intermediate or final states. To do this, it is sufficient to use the appropriate weight

function for the desired state for the second Ξ function in Eq. (14) and the Gaussian function in Eq. (15), respectively. We must note that the weight for the intermediate state is calculated as the product of the weights corresponding to the semi-classical vibrational level of BC and that of the intermediate vdW complex: $w^{\mathrm{i}} = w_1^{\mathrm{i}}(v_c^{\mathrm{i}})w_2^{\mathrm{i}}(n_c^{\mathrm{i}})$, where w refers to either Ξ or g. This could dramatically increase the number of trajectories necessary for convergence. Moreover, although Eq. (10) provides a simple means to estimate the semi-classical analogue for the vibrational state of BC, that of the vdW complex is much more difficult to evaluate. A simpler approach, known as the 1GB procedure, uses the total ro-vibrational energy rather than that of the individual states to calculate the corresponding weight: $w^{\mathrm{i}} = w^{\mathrm{i}}(E^{B,v_c^{\mathrm{i}}}_{\mathrm{Rg_i BC}})$. Both the $\mathcal{E}^{B,v'}_{\mathrm{BC}}$ and $\mathcal{E}^{B,v'}_{\mathrm{Rg_i,BC}}$ eigenvalues are involved in this calculation, see Sec. II C 2. The method was proposed by Czakó and Bowman[66] on the basis of rather intuitive arguments and was later theoretically validated by Bonnet and Espinosa-García.[67] In the particular case when the first and second dissociation steps are statistically independent, the total weight can be calculated as the product $w = w^{\mathrm{i}}w^{\mathrm{f}}$. In addition, mixed strategies may be tested by simply using $w = w^{\mathrm{i(f)}}$, hence calculating the desired state distributions independent of the final/intermediate vibrational state.

The time evolution of the populations of the various complexes can be obtained by small modifications to the formulae determining survival probabilities, i.e., the probability that a given complex has not dissociated at time t, which read[35]

$$P_{\mathrm{SB}}(t) = 1 - \frac{1}{N_{\mathrm{diss}}}\sum_{i=1}^{N_{\mathrm{diss}}}\Theta(t - t_i),$$

$$P_{\mathrm{GW}}(t) = 1 - \frac{1}{\sum_{i=1}^{N_{\mathrm{diss}}} g_i}\sum_{i=1}^{N_{\mathrm{diss}}} g_i\Theta(t - t_i), \qquad (17)$$

with $g_i = \sum_{\forall v} g(v(\mathbf{\Gamma}_i); v, \epsilon)$ and t_i being the dissociation time for the ith trajectory. In the particular case of a Rg_2BC cluster, for which t_1 and t_2 are the dissociation times for the first and second Rg atoms, the different populations are explicitly obtained as: (1) $P_4(t) = P(t_1)$, the decay of the parent molecule; (2) $P_3(t) = P(t_2) - P(t_1)$, time evolution of the intermediate RgBC population; and (3) $P_2(t) = 1 - P(t_2)$, formation of the BC fragment. Moreover, (4) $P_3'(t) = P(t_2 - t_1)$ directly represents the decay of the RgBC complex. The reasons for the subscripts will become apparent in Sec. III A.

4. Simulation details

Batches of $N_{\mathrm{tot}} = 5 \times 10^5$ trajectories were propagated using an adaptive-stepsize Bulirsch-Stoer method.[68] Each trajectory was followed until one of two conditions was fulfilled: (1) the two Ne atoms dissociated, i.e., $R_{1(2)} \geq R^{\mathrm{QCT}}_{\mathrm{diss}} = 14$ Å or (2) the propagation time $t = T_{\mathrm{max}} = 1200$ ps. Dissociation is said to occur when $R_{1(2)} = 14$ Å, the distance at which the vdW interactions become negligible. The integration parameters were adjusted so that the maximum error in total energy did not exceed $\Delta E = 10^{-5}$ cm^{-1}, i.e., less than $10^{-8}\,E$. With this choice of parameters all trajectories dissociated at least one Ne atom while over 88–99%, depending on v', completely fragmented. A typical trajectory requires less than 1 s of central processing unit time on an Intel®Core™I7 Q720 (6M Cache, 1.60 GHz) processor.

D. Cartesian coupled coherent states

The CCCS method is a trajectory-based quantum dynamics technique designed to be similar to classical trajectory simulations. The main focus of this paper is the QCT predictions and thus CCCS results are mainly presented to corroborate the conclusions and the quality of the QCT results. Consequently, we will only give a brief outline of CCCS in order to aid comprehension of the results that are included. The interested reader is referred to Ref. 49 which not only describes in detail our previous work on the VP of $NeBr_2$ but also outlines the extension to larger clusters. A more detailed CCCS study of Ne_2Br_2 will be published in due course.[69]

The QCT method described hitherto is concerned with the point-like nuclei that make up the Ne_2Br_2 cluster whereas the CCCS method allows us to study the time evolution of the associated quantum mechanical wave function. The CCCS method expands the wave function using a basis of coherent states (CS). In CCCS, the CS are Gaussian-shaped wave packets that describe both the position and momentum for each Cartesian DOF of each atom. Thus for Ne_2Br_2, each CS has 24 dimensions. The CS move on the same PES, and according to the same equations as the nuclei in QCT. However, the potential energy for the CS is the convolution of the CS and the PES. In contrast, within the QCT method, the potential energy of a given configuration is simply the value of the PES at that point in configuration space. In CCCS, the convolution may be done in advance of the simulations and it gives the so-called *averaged* or *re-ordered* PES (or equivalently, Hamiltonian) upon which the centers of the CS move.

The amplitudes evolve with time according to an expression derived from Schrödinger's equation and which depends upon the fact that the basis functions overlap. This overlap couples the amplitudes of the basis functions together. If the basis functions are separated by a sufficiently large distance in the 24-dimensional phase space, they cease to overlap and become decoupled. Once all the basis functions have decoupled, the CCCS method is essentially a semi-classical method. However, even in its semi-classical limit, the CCCS technique takes into account the majority of zero point energy effects.

1. Simulation details

The initial coordinates for the basis functions are determined from a set of bond lengths and momenta so that the total linear and angular momenta of the cluster are zero. For Br–Br, these were chosen from the phase-space trajectory at the energy expectation value of the isolated molecule. In the case of Br–Ne and Ne–Ne, they were chosen randomly from the ground state wave functions of the bonds. Initially, each basis consisted of 400 basis functions and the results have been averaged over 10 different basis sets per Br_2 vibrational level.

As CCCS simulations are considerably more expensive than QCT calculations, a Ne atom is said to have dissociated once the mean distance between it and the Br_2 molecule exceeds $R_{\text{diss}}^{\text{CCCS}} = 10$ Å. Similarly, the second stage dissociation is said to occur when the distance between Br_2 and the remaining Ne exceeds the same cutoff.

In our previous work,[49] we found that the basis functions in the simulations of the VP of $NeBr_2$ remained coupled until the clusters completely dissociate. In the current work, however, the basis functions decouple much more quickly due to the increased dimension of phase space. Obviously, the time at which each basis function decouples varies greatly but it is typically less than 10 ps: the mean time in one simulation was about 6 ps. As will be discussed later, this leaves comparatively few independent basis functions to describe the dissociating wave function and leads to increased lifetimes.

The calculated lifetimes can be improved by spawning a secondary simulation each time a basis function permanently decouples in which the decoupled basis function is expanded on a new basis of 50 CS. The calculation of the lifetimes is thus a two-part process: first we perform a simulation of the whole wave function expanded on the basis of 400 CS; and then we perform 400 secondary simulations each with 50 basis functions describing one of the basis functions of the original simulation, starting from when that basis function decoupled. We found that decoupling invariably occurs before dissociation, which makes the combination of the dissociation curves from 400 secondary simulations easier.

The time required to perform the CCCS calculations depends upon the length of time for which the basis functions remain coupled and increases nonlinearly with the number of basis functions. As an example, the mean time for $v = 17$ for 100 ps (10^5 steps), using 400 basis functions was 3.2 days. The mean time for the re-expansions however was 1.3 h/simulation on Intel®Xeon® "Woodcrest" processors.

III. RESULTS AND DISCUSSION

A. Kinetics and lifetimes

1. QCT

PSTT establishes that certain structures in classical phase space (resonant islands, tori, cantori…) act as intermolecular and intramolecular bottlenecks to the diffusion of trajectories from regions defining "reactants" and "products."[37–39] A rigorous (classical) kinetic mechanism must therefore reflect the details of these partial obstacles. In addition, a complete rationalization of the energy-dependence of decay rates requires the stability of periodic orbits and the evolution of bifurcations in the phase-space portrait to be addressed in depth. While this is possible and has already been carried out for simple 2-DOF models of molecular systems, including vdW complexes,[42,43,70–72] its extension to more DOF introduces serious technical difficulties[39] and constitutes in itself an active field of research. In fact, further below we use some of these results and a 2-DOF model of $NeBr_2$ to better understand the relation between product states and dissociation lifetimes, as well as certain features in the time-evolution of the intermediate complex.

Analyzing the phase-space structure of Ne_2Br_2, or even $NeBr_2$, is however far from our objective here and, at this point, we take advantage of one important experimental conclusion: At least for low v' levels, a simple sequential kinetic mechanism (Sec. II A) provides an excellent fit to the delay scans (Figs. 7 and 8 in Ref. 47). This is consistent with several results from our QCT calculations: (1) once the Ne_2Br_2 complex decayed into $NeBr_2$, the only process observed was the fragmentation of the resulting triatomic into Ne and Br_2 products; (2) less than about 0.05% of all trajectories dissociated via the concerted mechanism (taken as the subset of all trajectories for which both Ne atoms dissociated within one Br_2 vibrational period, excluding those predicted by the sequential mechanism to dissociate within that time interval[73]); and (3) no significant statistical correlation was found between the variables defining the intermediate complex and $t_2 - t_1$. The latter confirms, at least from the kinetics viewpoint, that the second dissociation step is nearly statistically independent on the first.[74] All of these observations agree with the fact that: (4) EQM calculations on the VP of $NeBr_2$ show that direct predissociation dominates within the vibrational range explored here.[20]

The proposed kinetic mechanism is schematically

$$N_4 \xrightarrow{\tau_1} N_3 \xrightarrow{\tau_2} N_2, \tag{18}$$

where N_4, N_3, and N_2 stand for the Ne_2Br_2, $NeBr_2$, and Br_2 populations, respectively, while τ_1 and τ_2 are the corresponding lifetimes. Mathematically, Eq. (18) can be written as

$$\begin{aligned} dN_4/dt &= -k_1 N_4, \\ dN_3/dt &= k_1 N_4 - k_2 N_3, \\ dN_2/dt &= k_2 N_3, \end{aligned} \tag{19}$$

with $k_i = \tau_i^{-1}$, and its solution

$$\begin{aligned} N_4(t) &= N_4(0)\exp(-k_1 t), \\ N_3(t) &= \left[N_3(0) - \frac{k_1 N_4(0)}{k_2 - k_1}\right]\exp(-k_2 t) + \frac{k_1 N_4(t)}{k_2 - k_1}, \\ N_2(t) &= N_{\text{tot}} - N_4(t) - N_3(t), \end{aligned} \tag{20}$$

where $N_4(0) = N_{\text{tot}}$ and $N_3(0) = N_2(0) = 0$. Given the dependence on τ_1 and τ_2 of Eqs. (20), various schemes to extract the lifetimes from survival probability curves become possible. One can: (1, 2) first obtain τ_1 from fits to Ne_2Br_2 decay curves and use this value to get τ_2 from the time dependence of $NeBr_2$, or alternatively, Br_2 populations; or (3, 4) directly infer both values from the evolution of $NeBr_2$ or Br_2 populations. Alternatively, taking into account that the individual dissociation times t_1 and t_2 are nearly uncorrelated, one may: (5) directly extract the value of τ_2 by fitting the probability of complete dissociation after a time $t_{21} = t_2 - t_1$ (fragmentation of the triatomic once it is formed) to a single exponential decay. This is implicit in our kinetic mechanism and readily seen by adding the first two equations in (19). Schemes (1)–(4) are somewhat similar to the experimental freedom of determining the lifetimes by measuring the time dependence of the $Ne_2Br_2/NeBr_2$ signal in a given Br_2 vibrational state, referred to as "disappearance" of the parent complex, and that of the $NeBr_2/Br_2$ signal in the vibrational states resulting from

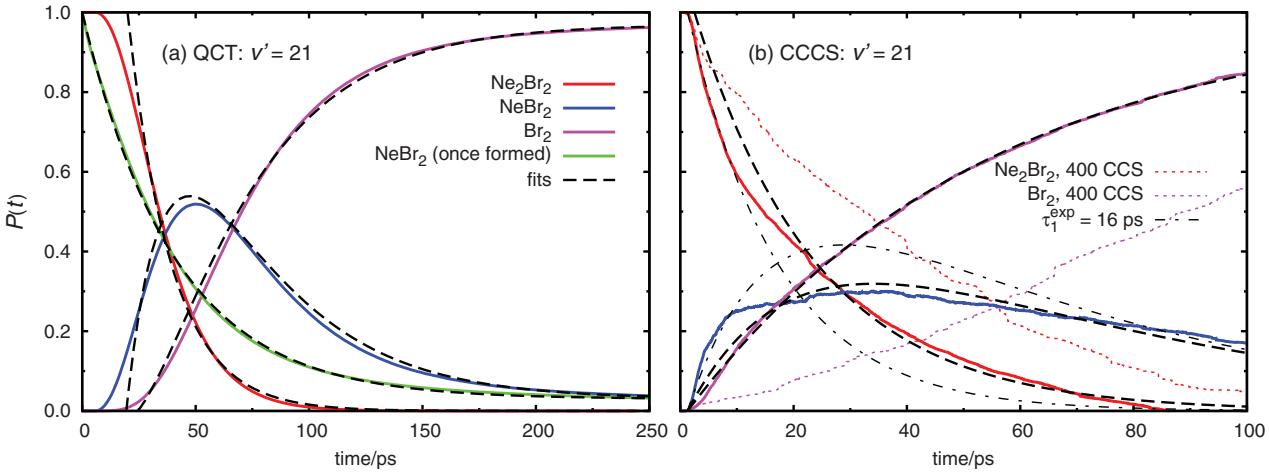

FIG. 2. Time evolution of the population of all complexes involved in the vibrational predissociation of $Ne_2Br_2(B, v' = 21)$: (a) QCT and (b) CCCS calculations.

dissociation, the "appearance" of the daughter molecule, etc. Depending on the signal monitored, different values are obtained in the experiments (and EQM), which provide a measure of IVR.[20,47,75] However, QCT will yield the same lifetimes no matter what scheme is used (though numerical fitting and convergence will in practice result in small differences). This is easily understood for according to our criteria, the disappearance of Ne_2Br_2 exactly matches the appearance of $NeBr_2$, etc. As an example, the relevant probability curves, i.e., $P_i(t) = N_i(t)/N_{tot}$, $i = 4$–2, and $P'_3(t)$, corresponding to $v' = 21$ are shown in panel (a) of Fig. 2, together with the respective fits. We have verified that the various schemes yield similar results, and experimental and theoretical lifetimes are summarized in Table II. In the latter, column "v'" corresponds to the vibrational level in the B electronic state to which the Ne_2Br_2 molecule is excited by the laser pulse. Column "Species(v)" then corresponds to the molecular product (in the specific vibrational state v) that is monitored in the experiment. "τ_1" and "τ_2" are the lifetimes of Ne_2Br_2 and $NeBr_2$. In particular, as seen in Eqs. (20), the fragmentation of Ne_2Br_2 depends only on k_1, which is why no τ_2 is reported in the experiment for this molecule. As discussed above, the theoretical methods yield nearly identical results independently on the probability curve used for the fitting, and a single pair of values τ_1, τ_2 is thus reported for the system (note that no τ_2 value was reported in Ref. 11).

TABLE II. Experimental[47] and theoretical—this work and MDQT[11]—lifetimes (in ps) in the vibrational predissociation of $Ne_2Br_2(B, v' = 16$–$23)$.

		Experiment		QCT		CCCS		MDQT
v'	Species(v)	τ_1	τ_2	τ_1	τ_2	τ_1	τ_2	τ_1
16	$Ne_2Br_2(16)$			62.1	134.0			
17	$Ne_2Br_2(17)$	32 ± 3		48.5	115.9	44.0	98.9	29
	$NeBr_2(16)$	30 ± 3	88 ± 3					
	$Br_2(15)$	31 ± 2	82 ± 3					
18	$Ne_2Br_2(18)$	28 ± 3		33.8	89.6			
	$NeBr_2(17)$	27 ± 5	58 ± 5					
	$Br_2(16)$	28 ± 3	55 ± 4					
19	$Ne_2Br_2(19)$			28.0	66.5			24
20	$Ne_2Br_2(20)$			23.9	51.1			19
21	$Ne_2Br_2(21)$	16 ± 3		19.3	40.5	21.7	53.1	16
	$NeBr_2(20)$	14 ± 5	30 ± 2					
	$NeBr_2(19)$	17 ± 4	54 ± 3					
	$Br_2(19)$	16 ± 2	29 ± 2					
	$Br_2(18)$	16 ± 2	47 ± 2					
22	$Ne_2Br_2(22)$			16.2	34.5			13
23	$Ne_2Br_2(23)$			14.1	28.9	15.3	39.4	

Simple inspection of panel (a) in Fig. 2 shows that the agreement between our fits and QCT calculations is very good, which confirms the accuracy of the kinetic mechanism proposed. This is the general trend for all vibrational levels explored here. Even so, in most cases, small discrepancies occur at short and large times. From the comparison of the classical survival probability curves corresponding to the decay of the Ne_2Br_2 (red curve) and the fragmentation of the intermediate $NeBr_2$ (green curve) the nature of the plateau usually observed at short times becomes rather clear. It is simply an artifact resulting from both the classical description of the process and the way initial conditions are sampled. More explicitly: there is a minimum time for the gradual classical energy transfer from the Br_2 vibrational mode to dissociate one Ne atom which, in the case of the first decay, has been located close to the vdW minima at the belt-like configuration. In contrast, a quantum vibrational transition may immediately release enough energy for dissociation to occur, as readily seen in CCCS curves from panel (b). The fact that no such feature is observed in the second QCT step further confirms this reasoning for once the first atom is lost, the dynamics would sample more evenly the available phase space and have placed the second Ne atom arbitrarily close to R_{diss}. One may say that this apparent non-exponential behavior (in the fragmentation kinetics) mainly arises from initial state selection.[76]

The reasons for the discrepancies at larger times are more complex and better understood using a 2-DOF model for the VP of $NeBr_2$ (with $\theta = \pi/2$). Analysis of the SOS shows a 1:10 nonlinear resonance (for $v' = 21$) surrounding the

stable central region around the point ($R = R_{eq}$, $P_R = 0$). This resonance occupies a significant proportion of the available phase space. The extent to which such intramolecular bottlenecks affect the overall time evolution of the classical ensemble depends on the proportion of initial conditions lying inside or relatively close to their boundaries. Actually, early work on PSTT showed that kinetic mechanisms can be conveniently modified to account for such behavior.[37] In our case, only a relatively low percent of trajectories, about 0.3% for $v' = 21$ in Fig. 2, show a strong non-exponential behavior, *always* after the dissociation of the first Ne atom. This is most likely due to remaining lower-dimensionality tori, which have been recently demonstrated to play a significant role as bottlenecks between diffusive and statistical behavior in systems with more than two DOF.[77]

Given all of the above, the actual equations used to produce the fits shown in Fig. 2 are in fact slightly modified versions of Eqs. (20) which account for both sources of non-exponential behavior. That at low times is "avoided" by fitting from $t_0^{v'} > 0$, while the long-time behavior is modeled by adding a given constant (which equals the asymptotic proportion of non-dissociated trajectories at each v'). We should note that, after adding this constant, all coefficients need to be adequately modified to recover the correct behavior at $t = 0$.

2. CCCS

The survival probabilities for the different complexes for $v' = 21$, as calculated using CCCS, are shown in panel (b) of Fig. 2. In contrast to panel (a): (1) dotted lines (labeled "400 CCS") correspond to the initial CCS simulations with 400 basis functions, the re-expansion of which gives the main curves; (2) the survival probability of $NeBr_2$ once it is formed from the Ne_2Br_2 cluster is not presented, as this time is ill-defined in the CCCS calculations; and (3) dotted-dashed lines (labeled "$\tau_1^{exp} = 16$ ps") use the experimental value[47] to model the time evolution at short times. The fits are obtained using the same sequential kinetic mechanism as for QCT, and the lifetimes given in Table II are from fitting the modified versions of Eqs. (20) to the CCCS data, also necessary here, mainly to account for those basis functions that do not dissociate.

Theoretically, CCCS will provide a quantum mechanical description as long as the basis functions remain coupled, which ideally should be for a time comparable to the process of interest. As in our previous study of the $NeBr_2$ system,[49] CCCS removes the nonphysical plateau shown by QCT at short times, thus accurately reproducing the initial quantum dynamics. However, it becomes harder to fit the results of CCCS to a simple model of sequential dissociation at longer times. This could be because quantum mechanics makes non-sequential dissociation more likely. Previously, non-sequential IVR-EC contributions to dissociation were found to be important in MDQT simulations for $v' > 14$ where they account for one fifth of all dissociative trajectories.[11] Also, the experiment[47] seem to indicate that complicated non-sequential mechanisms are important for $v' > 19$. However, it would be premature to claim that the current CCCS simulations prove the pertinence of non-sequential mechanisms. Although our re-expansion technique (Sec. II D 1) greatly increases the time scale at which CCCS works, it is still below the range of hundreds of picoseconds required for the description of the whole fragmentation process. At such long time scales, CCCS works as a semi-classical technique running largely uncoupled CS on the averaged potential. It accounts for zero point energy effects but not for the full quantum coupling in phase space. We are currently working on strategies to further extend the coupling time between the CS in the quantum simulations. More detailed (and costly) investigations are necessary and the results will be published in Ref. 69.

In general, both QCT and CCCS predictions are in very good agreement with each other, thus CCCS confirming the good quality of much simpler and less expensive QCT results. Both methods are also in good agreement with the experimental lifetimes, over the whole range of initial vibrational states. However, although providing a near-quantitative description of the kinetics, they seem to consistently yield larger than observed values. In the case of QCT, this may be intrinsic to the methodology and the existence of low-dimensional tori in classical phase space. Additional CCCS calculations are needed in order to verify whether this is inherent to the method or due to, e.g., an inadequate representation of the PES or the wave function.

B. PSTT, SB, GW, and QCT dissociation times

Based on PSTT, it seems reasonable to expect that trajectories with the highest Gaussian weights, which contribute the most to the GW curves and correspond to vibrational actions the closest to integer values, do not necessarily explore the same regions in phase space than the whole ensemble and could therefore undergo different kinetics. Hence, at least in principle, applying the SB or GW methods can produce different time evolution probability curves (Sec. II C 3) and correspondingly, result in different lifetimes. In turn, GW results should be the closest to the experimental values for this method effectively eliminates trajectories which finish in nonphysical vibrational channels. Quite surprisingly, no significant differences between SB and GW lifetimes were found in our previous calculations on the VP of $RgBr_2$ (Rg = He, Ne, Ar) molecules (see Fig. 1 in Ref. 35), where several possible reasons were proposed.

In the VP of Ne_2Br_2 studied here, the predictive capabilities of GW can be additionally tested for the experiment provided detailed information on the kinetics associated to different vibrational channels for $v' = 21$ (see Table II). Unfortunately, once again, our calculations seem to corroborate that both the SB and GW methods result in nearly identical lifetimes, with no significant variation between the various vibrational channels. In other words: the GW procedure was found to be unable to provide vibrational resolution in the dissociation lifetimes. In the rest of this section, we will show that 2- and 3-DOF models for the VP of $NeBr_2$ are very helpful in the detailed analysis of this issue.

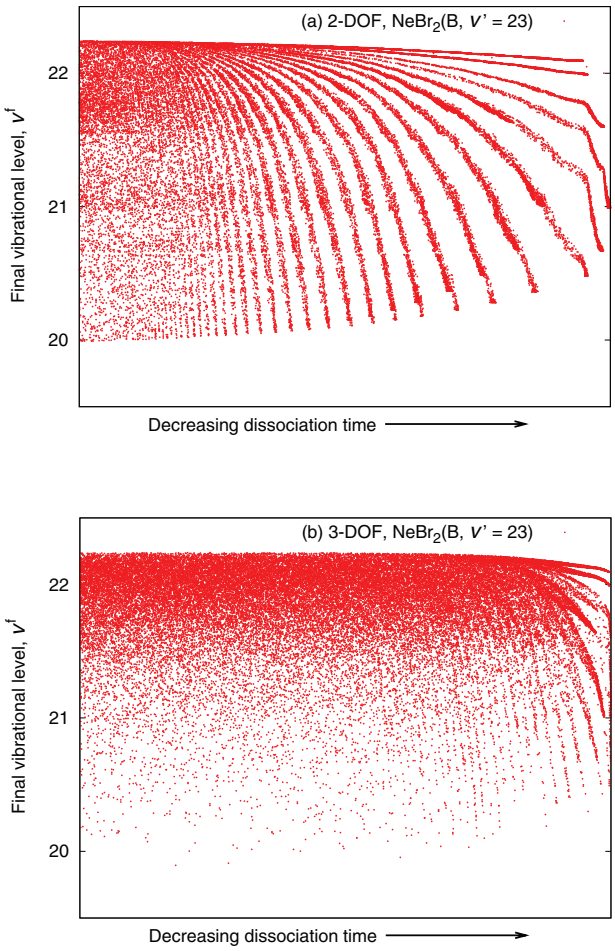

FIG. 3. Dependence between dissociation lifetimes and final vibrational states in the vibrational predissociation of $NeBr_2$ from $v' = 23$: (a) 2-DOF and (b) 3-DOF model.

The relation between trajectory lifetimes and final states is rather intricate, as is apparent from Fig. 3. Panel (a) shows how final vibrational states relate to the individual dissociation times for an ensemble of 5×10^4 trajectories in the 2-DOF model. As readily seen, there is a relative insensitivity between these magnitudes for trajectories with longer to medium lifetimes, while a specific pattern arises for shorter dissociation times. These finger-like structures can be understood by analyzing the VP process in phase space, in the spirit of PSTT. For simplicity we will only introduce here the essential elements of the methodology that are required by our interpretation. Further information can be found in the seminal work of Davis *et al.*, most notably in Ref. 37.

Figure 4 depicts the main structures in the SOS of a 2-DOF model for a generic triatomic. The SOS is constructed by the procedure described in Sec. II C and the molecule is assumed to dissociate if $R \geq R_{\text{diss}}$. The *separatrix* (continuous red line) encloses the interaction region and constitutes the intramolecular bottleneck to dissociation. The fingers (green/blue dashed lines) limit the region available to the outgoing/incoming flux. All dissociating trajectories will intersect the region enclosed by the outgoing fingers (dashed, green) and the separatrix, once only. Thus, after leaving the

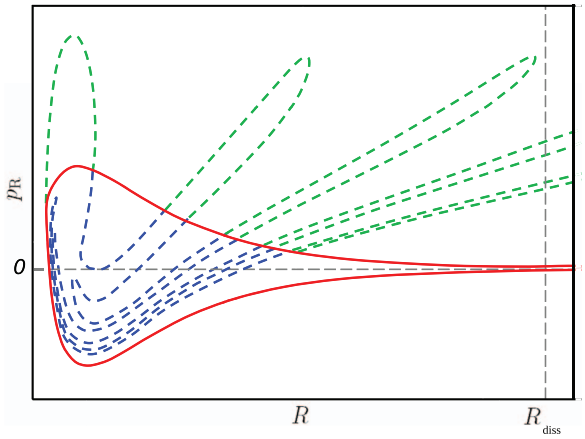

FIG. 4. Schematic view of the main structures in the SOS of a 2-DOF model for the VP of a generic triatomic: separatrix (red, continuous line), outgoing (green, dashed line), and incoming (blue, dashed line) fluxes.

interaction region, any given trajectory will inevitably dissociate and consecutive intersections will lie in different fingers as $R(t)$ increases monotonically. All that rests now is to notice that trajectories closer to the fingers' "tips," i.e., those with the largest P_R, correspond to the smallest v available (and vice versa). The previous follows from the fact that the total energy E is fixed in the ensemble. At last, the existence of finger-like structures like those in Fig. 3 will strongly depend on the characteristics of the dynamics within the interaction region. If completely stochastic, initial conditions will be effectively "forgotten" and trajectories will access the outgoing fingers after exploring the interaction region during a random propagation time. No correlation between dissociation times and final vibrational states will be observed. On the other hand, if intermolecular couplings are not strong enough, a subset of trajectories whose initial conditions lie within a specific region inside the separatrix will directly access the outgoing fingers. These trajectories will therefore dissociate rapidly and a pattern will arise. Following this line of reasoning, it is not difficult to see why the structures in panel (a) of Fig. 3 have precisely their shape. Panel (b) in the same figure shows results for the 3-DOF model of $NeBr_2$. The similarities between the 2- and 3-DOF models are evident, although the finger-like structures get increasingly blurred the larger the number of DOF. The number of such finger-like structures depends on the kinetic energy available to dissociation, hence decreasing with increasing vibrational excitation. Additional calculations show that all structures completely disappear for energies above the linearization threshold (Br–Ne–Br configuration barrier).

C. Product state distributions

Ro-vibrational product state distributions were calculated from the ensemble of quasi-classical trajectories as described in Sec. II C 3. As many relevant features of these observables strongly depend on the energetics of the VP process, details of the latter are summarized in Table III: (1) the vibrational energy gap associated to the $\Delta v' = -1$ channel, $\Delta\mathcal{E}^{B,v'-1}_{Br_2}$

TABLE III. Energies (in cm^{-1}) in the vibrational predissociation of $Ne_2Br_2(B, v')$ (see text for full details).

v'	$\Delta\mathcal{E}_{Br_2}^{B,v'-1}$	$D_0^{NeBr_2(B,v')}$	$D_0^{B,v'}$	$E_{avail}^{v'-1}$	$E_{avail}^{v'-2}$
16	107.4	63.3	137	33	81
17	103.8	63.1	137	29	74
18	100.2	62.8	137	26	67
19	96.6	62.6	137	22	60
20	93.1	62.3	136	19	54
21	89.5	62.0	136	15	47
22	85.9	62.5	135	13	40
23	82.3	62.4	135	9	33

$= \mathcal{E}_{Br_2}^{B,v'} - \mathcal{E}_{Br_2}^{B,v'-1}$; (2, 3) $NeBr_2$ (Ref. 14) and Ne_2Br_2 binding energies, $D_0^{NeBr_2(B,v')} = -\mathcal{E}_{NeBr_2}^{B,v'}$ and $D_0^{B,v'} = -\mathcal{E}^{B,v'}$; and (4, 5) the energies available after dissociation of the first and second Ne atoms via, respectively, the $\Delta v' = -1, -2$ channels, i.e., $E_{avail}^{v'-1}$ and $E_{avail}^{v'-2}$.

Tests on basis-set convergence yield an estimate for the accuracy of our $D_0^{B,v'}$ values of about 1 cm^{-1} (any further improvement was considered unnecessary for our purposes here). These theoretical values are just slightly different from the 141 cm^{-1} estimate of Pio *et al.*,[47] and suggest an interaction energy for the Ne–Ne bond of about 10–12 cm^{-1}, which is to be compared with the 17 cm^{-1} of isolated Ne_2 used in Ref. 47. Our predictions are, however, consistent with the value of 12.81 cm^{-1} in Ref. 11 for the effective Ne–Ne bond. Moreover, our calculations predict an average Ne–Ne interatomic distance at the minimum energy structure of about 3.2 Å (within 3.8% of the value for Ne_2, see Table I), also in good agreement with the estimate in Ref. 11. It is important to note that all values in Table III, except for $D_0^{NeBr_2(B,v')}$, are theoretical predictions based on the B-state PES used in this work. This is the reason for small discrepancies with some experimental predictions.[47] For instance, we estimate the closing of the $\Delta v' = -1$ channel for the dissociation of the first Ne atom to occur at $v' = 25$, as opposed to the experimental $v' = 23$. Also, complete dissociation via the $\Delta v' = -2$ channel would be energetically accessible up to $v' = 27$ (instead of $v' = 25$).

1. Vibrational branching ratios

Experimental and QCT vibrational branching ratios after the dissociation of one Ne atom, $NeBr_2(v' - n)$:$NeBr_2(v' - 1)$, and two Ne atoms, $Br_2(v' - n)$:$Br_2(v' - 2)$, are given in Table IV. It is readily apparent that QCT fails to capture the physics behind the vibrational distributions in the VP process, irrespectively of the statistical procedure (SB or GW) employed. This is a general effect of the large mismatch in the strengths of the different DOF involved in the VP of vdW clusters, at least for moderate vibrational excitations of the chemically bounded diatom. The same behavior may therefore be expected in similar systems. In the absence of resonances, such a mismatch causes the energy transfer from the vibrational to the vdW dissociation modes to be very inefficient. This is remarkably different from the unimolecular dissociation of more conventional, i.e., chemically bounded, molecules, where statistical arguments are usually applicable at least for the DOF directly involved in the fragmentation. In the classical description of the VP of Ne_2Br_2, the Br_2 vibrational energy gradually "flows" into the vdW modes and eventually becomes large enough for dissociation to occur. A very limited number of the accessible final vibrational states is hence populated, the distributions being highly nonstatistical (Fig. 3). In addition, due to the very low density of vibrational states, the classical picture dramatically differs from the quantum-mechanical description and hence the

TABLE IV. Experimental[47] and theoretical (this work) branching ratios in the vibrational predissociation of $Ne_2Br_2(B, v')$.

		$NeBr_2(v' - n)$:$NeBr_2(v' - 1)$			$Br_2(v' - n)$:$Br_2(v' - 2)$			
v'		$(v' - 2)$	$(v' - 3)$	$(v' - 4)$	$(v' - 1)$	$(v' - 3)$	$(v' - 4)$	$(v' - 5)$
16	Experiment					0.16		
	QCT: SB/GW	0.04/0.27			0.98/0.0			
17	Experiment					0.31	0.05	
	QCT: SB/GW	0.08/0.29			0.48/0.0			
18	Experiment					0.33	0.08	
	QCT: SB/GW	0.16/0.35			0.20/0.0	0.01/0.0		
19	Experiment					0.45	0.09	
	QCT: SB/GW	0.28/0.45			0.07/0.0	0.02/0.01		
20	Experiment					0.65	0.13	0.03
	QCT: SB/GW	0.47/0.56	0.01/0.01		0.02/0.0	0.05/0.03		
21	Experiment					0.97	0.29	
	QCT: SB/GW	0.71/0.73	0.02/0.02		0.01/0.0	0.10/0.06		
22	Experiment					1.58	0.51	0.17
	QCT: SB/GW	1.04/0.92	0.06/0.04		0.01/0.0	0.18/0.10	0.01/0.0	
23	Experiment					3.28	1.37	0.49
	QCT: SB/GW	1.52/1.22	0.15/0.09	0.01/0.0		0.29/0.15	0.02/0.01	

experimental observations. This is particularly clear from SB product branching ratios. In this case, the loss of 1.5 "quanta" provides enough energy to eject both Ne atoms up to $v' = 22$ (Table III), which is reflected in nonphysical trajectories dissociating via the $\Delta v' = -1$ channel (Table IV). The main advantage of GW over SB results in this case is to populate the qualitatively correct vibrational channels. However, as discussed above, the classical description is intrinsically inadequate and GW predicts a larger than observed propensity for $\Delta v' = -1$ and -2 channels for the respective dissociation of the first and second Ne atoms. Also, the increasing importance of highly state-specific IVR (sparse regime) predicted in the experiment for states above $v' = 19$ cannot be adequately reproduced within QCT. Some additional discrepancies, e.g., in channels closings, are due to the PES employed and have been already discussed at the end of Sec. III C.

2. Rotational distributions

Together with vibrational distributions, product rotational state distributions provide a more detailed picture of the VP process than dissociation lifetimes. In particular, they contain important information on the anisotropy of the PES, the vibrational level spacings, and the effects of IVR and resonances on the fragmentation dynamics.[58] Rotational distributions corresponding to various initial v' levels for the $NeBr_2$ intermediate triatomic complex and the Br_2 diatomic product are depicted in panels (a) and (b) of Fig. 5, respectively. Only the GW results are shown because even if just a few vibrational states are populated, the SB and GW curves are only slightly different. This is not particularly surprising; although the available energy more than halves in the range of v' is considered (Table III), the tail of QCT distributions rapidly tends to zero before this effect becomes important.

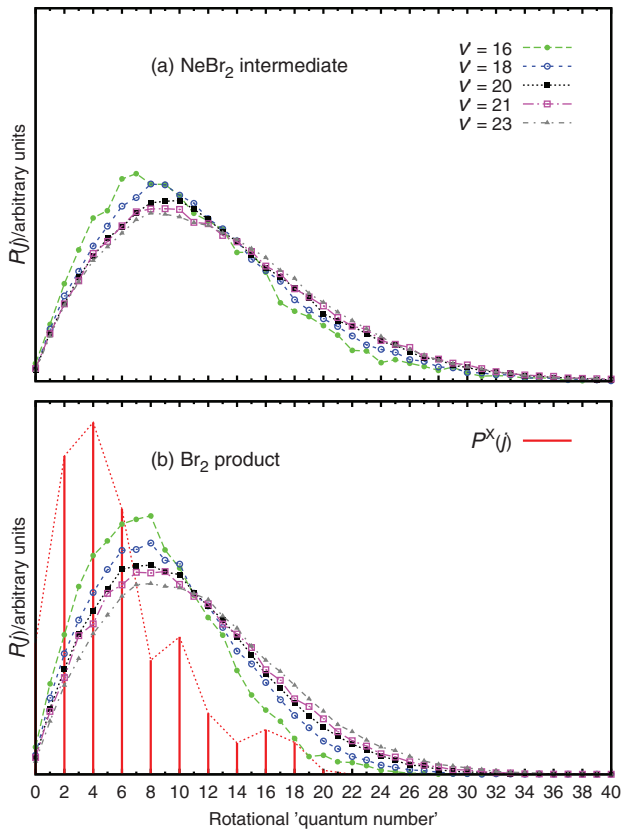

FIG. 5. Rotational distributions in the vibrational predissociation of $Ne_2Br_2(B)$, for (a) $NeBr_2$ intermediate complex and (b) Br_2 diatomic product. $P^X(j)$ is the quantum distribution used to generate the quasi-classical initial conditions.

The rotational state of the $NeBr_2$ intermediate complex was calculated from $\boldsymbol{j} + \boldsymbol{l}_{1(2)} = -\boldsymbol{l}_{2(1)}$, which is valid only for $\boldsymbol{J} = \boldsymbol{0}$. As seen in panel (a), the dissociation of the first Ne atom leaves the resultant triatomic complex in a highly excited rotational state. The corresponding distribution extends over more than 30 rotational levels and peaks around 8–10. Such rotational excitation, together with the additional excitation of the vdW vibrations, is expected to be the cause for the lifetime of the intermediate molecule being larger than that of the directly excited triatomic complex. This effect has been observed in the experiment[47] and is reproduced by our QCT calculations, as seen by comparing the corresponding lifetimes in Table II with the QCT predictions in Table 1 of Ref. 31.

The GW rotational distributions for the Br_2 product, shown in panel (b), extend over the full range of accessible states determined by the maximum available energy in Table III. For the sake of comparison, the initial distribution $P^X(j)$ has also been included in this panel. In the particular case of $\boldsymbol{J} = \boldsymbol{0}$, symmetry considerations for the ground state are responsible for only even j values contributing in $P^X(j)$.[62] In general, the calculated rotational distributions are considerably hotter for the products, with a maximum at about $j^f = 6$–8 almost independently of v'. The initial and final distributions have, nevertheless, similar shapes. Although experimental rotational distributions were not reported in the experiment,[47] a few points can be made with respect to QCT predictions: (a) the Boltzmann-like shape seems to be consistent with experimental measurements for the directly excited $NeBr_2$ molecule,[14] and previous QCT calculations[31,35] and (b) the Br_2 product is more rotationally excited than in the photo-dissociation of $NeBr_2$,[14,31,35] for which the distributions peak about $j^f = 4$–6. The extent of the QCT distributions may be expected to differ from future experimental measurements due to the PES employed (see discussion at the end of Sec. III C), particularly close to a channel closing.

IV. SUMMARY AND CONCLUSIONS

We have studied the VP of the $Ne_2Br_2(B,\ v' = 16$–$23)$ vdW cluster using the QCT and the (Cartesian) CCS methods.

A sequential mechanism was used to fit the dynamical evolution of the different complexes involved. Both QCT and CCS are shown to provide very good estimates for the different dissociation lifetimes reported in the experiment[47] and previous MDQT simulations.[11] QCT predictions are, however, obtained at a much lower computational expense. Various sources of non-exponential behavior have been identified and their implications are extensively discussed. In particular, the initial shape of the QCT curves at short

times arises from the "non-democratic" selection of classical initial conditions and the classical description of the process. Meanwhile, the quantum CCS simulations give curves whose initial shape is in much better agreement with the experimental observations.[47] However, the basis functions used to describe the wave function follow dissociative trajectories. The high dimensionality of the phase space therefore results in the basis functions decoupling and thus a semi-classical description of the cluster. This change is as least partially responsible for the departure at longer times of the curves from their initial exponential shape. An intrinsic multi-step dissociation mechanism, as observed in the experiment[47] and predicted by MDQT calculations,[11] may also be responsible for such non-exponential behavior at long times. Additional calculations are needed in order to clarify this issue. The time scale over which the CCS gives a good description was increased significantly to around 15 ps by re-expanding the dissociated basis functions. Despite this improvement, the QCT simulations give curves that agree much more closely with the experimental results at longer times. The behavior of the QCT curves at longer times is, however, affected by low-dimensional tori in classical phase space. These tori are mainly in the form of quasi-periodic trajectories and are partially due to the weakness of vdW interactions. In both QCT and CCS calculations, the percentage of trajectories which correspond to the concerted mechanism is practically negligible, below 0.1% for QCT and about 2% for CCCS. In this regard, it is important to note that trajectory-based approaches like CCS may become more effective than "standard" quantum methods, mainly because they allow analyzing the different mechanisms by simply inspecting the trajectories.

As in our previous work with QCT on triatomic vdW molecules,[35] we found that application of the GW procedure yields survival probability curves, and consequently lifetimes, which are not significantly different from those calculated using the SB procedure. In addition, the capabilities of QCT in the description of the fragmentation kinetics were analyzed in detail by using reduced-dimensionality models of the complexes and concepts from phase-space transport theory.

We have reported QCT ro-vibrational product state distributions for the intermediate and final states of the VP process, and compared the vibrational distributions with the experimental results of Pio *et al.*[47] As in previous studies, e.g., Ref. 35, the SB was found to populate nonphysical dissociation channels ($\Delta v' = -1$ in this case). This is due to energetic issues and can be easily solved by using the GW method. The latter, however, predicts a larger than observed propensity for dissociation of the first (second) Ne atom via the $\Delta v' = -1$ (-2) channel. We argued that this is a general problem in the classical description of the VP of vdW clusters, which may be attributed to the weakness of vdW interactions. Due to the latter, the characteristic frequencies for the diatomic subunit are usually one or more orders of magnitude larger than those of the bending mode within the vdW well. The energy transfer leading to dissociation is inefficient and slow. To complicate matters further, as energy flows from the vibrational to the transitional modes, the vdW bending modes evolve from bounded, through hindered, to free type of motion and the role of many nonlinear resonances becomes increasingly important.[42] This fact additionally worsens the quality of any classical description of the VP process, since quantum state-selectivity cannot be adequately described. As expected, the quantum-classical discrepancies will be more pronounced for relatively low v', given the very low density of vibrational states.

Dissociation of the first Ne atom leaves the $NeBr_2$ in a highly excited rotational state. This rotational excitation, and the additional excitation of the vdW vibration, are responsible for an increased dissociation lifetime of the intermediate complex, as compared to the lifetime of the directly excited $NeBr_2$. This effect was observed in the experiment[47] and is correctly predicted by our calculations. Product Br_2 rotational distributions are found to be significantly hotter in the products, extending over the full range of available energies.

ACKNOWLEDGMENTS

W.A.G., M.L.G.M., and J.R.S. wish to thank Professor Gerardo Delgado-Barrio, from the Consejo Superior de Investigaciones Científicas, España, for his contribution in the calculation of quasi-classical initial distributions. These authors wish also to acknowledge the support from the PNCB/2/9 project of the Departamento de Física General in the Instituto Superior de Tecnologías y Ciencias Aplicadas, Cuba. S.K.R. would like to thank the Engineering and Physical Sciences Research Council (United Kingdom) (EPSRC) for funding through Grant No. EP/E009824/1 and more recently the University of Leeds for a Visiting Research Fellowship. S.K.R. would also like to acknowledge the use of the UK National Grid Service (NGS) and the University of Leeds central HPC system in performing the CCCS simulations. The collaboration between the Cuban and British groups was possible thanks to an International Joint Project grant from the Royal Society.

[1] W. Sharfin, K. E. Johnson, L. Wharton, and D. H. Levy, J. Chem. Phys. **71**, 1292 (1979).
[2] J. E. Kenny, K. E. Johnson, W. Sharfin, and D. H. Levy, J. Chem. Phys. **72**, 1109 (1980).
[3] B. A. Swartz, D. E. Brinza, C. M. Western, and K. C. Janda, J. Phys. Chem. **88**, 6272 (1984).
[4] R. E. Smalley, D. H. Levy, and L. Wharton, J. Chem. Phys. **64**, 3266 (1976).
[5] G. Kubiak, P. S.H. Fitch, L. Wharton, and D. H. Levy, J. Chem. Phys. **68**, 4477 (1978).
[6] K. E. Johnson, W. Sharfin, and D. H. Levy, J. Chem. Phys. **74**, 163 (1981).
[7] J. A. Beswick and J. Jortner, J. Chem. Phys. **69**, 512 (1979).
[8] J. A. Beswick, J. Jortner, and G. Delgado-Barrio, J. Chem. Phys. **70**, 3895 (1979).
[9] M. A. Taylor, J. M. Pio, W. E. van der Veer, and K. C. Janda, J. Chem. Phys. **132**, 104309 (2010).
[10] B. Miguel, A. Bastida, J. Zúñiga, A. Requena, and N. Halberstadt, J. Chem. Phys. **113**, 10130 (2000).
[11] B. Miguel, A. Bastida, J. Zúñiga, A. Requena, and N. Halberstadt, Faraday Discuss. **118**, 257 (2001).
[12] D. D. Evard, C. R. Bieler, J. I. Cline, N. Sivakumar, and K. C. Janda, J. Chem. Phys. **89**, 2829 (1988).
[13] A. Rohrbacher, T. Ruchti, K. C. Janda, A. A. Buchachenko, M. I. Hernández, T. González-Lezana, P. Villarreal, and G. Delgado-Barrio, J. Chem. Phys. **110**, 256 (1999).
[14] M. Nejad-Sattari and T. A. Stephenson, J. Chem. Phys. **106**, 5454 (1997).
[15] A. Rohrbacher, N. Halberstadt, and K. C. Janda, Annu. Rev. Phys. Chem. **51**, 405 (2000).
[16] T. González-Lezana, M. I. Hernández, G. Delgado-Barrio, A. A. Buchachenko, and P. Villarreal, J. Chem. Phys. **105**, 7454 (1996).

[17]T. González-Lezana, M. I. Hernández, G. Delgado-Barrio, and P. Villarreal, J. Chem. Phys. **106**, 3216 (1997).
[18]T. A. Stephenson and N. Halberstadt, J. Chem. Phys. **112**, 2265 (2000).
[19]O. Roncero, J. Campos-Martínez, M. I. Hernández, G. Delgado-Barrio, P. Villarreal, and J. Rubayo-Soneira, J. Chem. Phys. **115**, 2566 (2001).
[20]A. García-Vela and K. C. Janda, J. Chem. Phys. **124**, 034305 (2006).
[21]A. García-Vela, J. Chem. Phys. **126**, 124306 (2007).
[22]A. García-Vela, J. Chem. Phys. **129**, 094307 (2008).
[23]C. Meier and U. Manthe, J. Chem. Phys. **115**, 5477 (2001).
[24]A. García-Vela, J. Chem. Phys. **122**, 014312 (2005).
[25]A. Bastida, J. Zúñiga, A. Requena, N. Halberstadt, and J. A. Beswick, J. Chem. Phys. **109**, 6320 (1998).
[26]S. Fernández-Alberti, N. Halberstadt, J. A. Beswick, A. Bastida, J. Zúñiga, and A. Requena, J. Chem. Phys. **111**, 239 (1999).
[27]A. Bastida, B. Miguel, J. Zúñiga, A. Requena, N. Halberstadt, and K. C. Janda, J. Chem. Phys. **111**, 4577 (1999).
[28]J. Rubayo-Soneira, A. García-Vela, G. Delgado-Barrio, and P. Villarreal, Chem. Phys. Lett. **243**, 236 (1995).
[29]A. García-Vela, J. Rubayo-Soneira, G. Delgado-Barrio, and P. Villarreal, J. Chem. Phys. **104**, 8405 (1996).
[30]R. L. Waterland, J. M. Skene, and M. I. Lester, J. Chem. Phys. **89**, 7277 (1988).
[31]M. L. González-Martínez, J. Rubayo-Soneira, and K. Janda, Phys. Chem. Chem. Phys. **8**, 4550 (2006).
[32]R. L. Waterland, M. I. Lester, and N. Halberstadt, J. Chem. Phys. **92**, 4261 (1990).
[33]L. Bonnet and J.-C. Rayez, Chem. Phys. Lett. **277**, 183 (1997).
[34]L. Bonnet and J.-C. Rayez, Chem. Phys. Lett. **397**, 106 (2004).
[35]M. L. González-Martínez, W. Arbelo-González, J. Rubayo-Soneira, L. Bonnet, and J.-C. Rayez, Chem. Phys. Lett. **463**, 65 (2008).
[36]J. I. Cline, N. Sivakumar, D. D. Evard, C. R. Bieler, B. P. Reid, N. Halberstadt, S. R. Hair, and K. C. Janda, J. Chem. Phys. **90**, 2605 (1989).
[37]M. J. Davis and S. K. Gray, J. Chem. Phys. **84**, 5389 (1986).
[38]S. K. Gray, J. Chem. Phys. **87**, 2051 (1987).
[39]R. E. Gillilan and G. S. Ezra, J. Chem. Phys. **94**, 2648 (1991).
[40]M. Zhao and S. A. Rice, J. Chem. Phys. **96**, 3542 (1992).
[41]M. Zhao and S. A. Rice, J. Chem. Phys. **96**, 6654 (1992).
[42]A. A. Granovsky, A. V. Medvedev, A. A. Buchachenko, and N. F. Stepanov, J. Chem. Phys. **108**, 6282 (1998).
[43]R. Prosmiti, P. Villarreal, G. Delgado-Barrio, and O. Roncero, Chem. Phys. Lett. **359**, 229 (2002).
[44]R. Sospedra-Alfonso, L. Velázquez, and J. Rubayo-Soneira, Chem. Phys. Lett. **375**, 261 (2003).
[45]M. L. González Martínez and J. Rubayo Soneira, Rev. Cub. Física **22**, 48 (2005) (in Spanish), online at URL: http://www.fisica.uh.cu/biblioteca/revcubfi/2006/vol23-No1/RCF2312006-54.pdf.
[46]M. Gutmann, D. M. Willberg, and A. H. Zewail, J. Chem. Phys. **97**, 8048 (1992).
[47]J. M. Pio, M. A. Taylor, W. E. van der Veer, C. R. Bieler, J. A. Cabrera, and K. C. Janda, J. Chem. Phys. **133**, 014305 (2010).
[48]S. K. Reed, D. R. Glowacki, and D. V. Shalashilin, Chem. Phys. **370**, 223 (2010).
[49]S. K. Reed, M. L. González-Martínez, J. Rubayo-Soneira, and D. V. Shalashilin, J. Chem. Phys. **134**, 054110 (2011).
[50]A. Valdés, R. Prosmiti, P. Villarreal, and G. Delgado-Barrio, J. Chem. Phys. **122**, 044305 (2005).
[51]A. Valdés, R. Prosmiti, P. Villarreal, and G. Delgado-Barrio, J. Chem. Phys. **125**, 014313 (2006).
[52]R. F. Barrow, T. C. Clark, J. A. Coxon, and K. K. Lee, J. Mol. Spectrosc. **51**, 428 (1974).
[53]A. A. Buchachenko, A. Y. Baisogolov, and N. F. Stepanov, J. Chem. Soc., Faraday Trans. **90**, 3229 (1994).
[54]F. Y. Naumkin and P. J. Knowles, J. Chem. Phys. **103**, 3392 (1995).
[55]A. Rohrbacher, J. Williams, and K. C. Janda, Phys. Chem. Chem. Phys. **1**, 5263 (1999).
[56]R. Prosmiti, C. Cunha, A. A. Buchachenko, G. Delgado-Barrio, and P. Villarreal, J. Chem. Phys. **117**, 10019 (2002).
[57]J. M. Pio, W. E. van der Veer, C. R. Bieler, and K. C. Janda, J. Chem. Phys. **128**, 134311 (2008).
[58]R. Schinke, *Photodissociation Dynamics* (Cambridge University Press, Cambridge, England, 1993).
[59]J. Rubayo-Soneira, "Estudio de la predisociación de sistemas triatómicos y tetraatómicos de van der Waals," Ph.D. dissertation (Consejo Superior de Investigaciones Científicas, Madrid, España, 1995) (in Spanish).
[60]A. J. Lichtenberg and M. A. Lieberman, *Regular and Stochastic Motion* (Springler-Verlag, New York, 1993).
[61]After assuming that strong IVR makes all available configurations equally populated within an induction time relatively short compared to the time scale of the process of interest, classical initial conditions are computed using microcanonical distributions.
[62]P. Villarreal, O. Roncero, and G. Delgado-Barrio, J. Chem. Phys. **101**, 2217 (1994).
[63]G. Delgado-Barrio, A. García-Vela, C. García-Rizo, M. I. Hernández, and P. Villarreal, Mol. Eng. **7**, 219 (1997).
[64]W. H. Miller, Adv. Chem. Phys. **25**, 69 (1974).
[65]R. N. Porter and L. M. Raff, in *Dynamics of Molecular Collisions, Part B*, edited by W. H. Miller (Plenum, New York, 1976).
[66]G. Czakó and J. M. Bowman, J. Chem. Phys. **131**, 244302 (2009).
[67]L. Bonnet and J. Espinosa-García, J. Chem. Phys. **133**, 164108 (2010).
[68]W. H. Press, S. A. Teukolsky, W. T. Vetterling, and B. T. Flannery, *Numerical Recipes. The Art of Scientific Computing.*, 3rd ed. (Cambridge University Press, Cambridge, England, 2007).
[69]S. K. Reed, M. L. González-Martínez, W. Arbelo-González, J. Rubayo-Soneira, and D. V. Shalashilin, "Quantum dynamical study of $Ne_2Br_2(B)$ vibrational predissociation using the Cartesian coupled coherent states method" (unpublished).
[70]M. J. Davis, J. Chem. Phys. **83**, 1016 (1985).
[71]S. K. Gray, S. A. Rice, and M. J. Davis, J. Phys. Chem. **90**, 3470 (1986).
[72]M. Zhao and S. A. Rice, J. Chem. Phys. **96**, 7483 (1992).
[73]In order to further distinguish between C_1 and C_2 events in Scheme 1, the Ne–Ne energy was checked for compatibility with formation of a Ne_2 molecule.
[74]One may consider the case where the initial dissociation step leads—for a significant part of the ensemble—to states "trapped" behind large centrifugal barriers, i.e., orbiting resonances. These would act as effective bottlenecks to the dissociation of the triatomic intermediate complex and result in a slightly more complicated kinetic mechanism, as in Ref. 29. In such cases, the rotational angular momentum of the intermediate complex would result statistically correlated with $t_2^i - t_1^i$.
[75]J. A. Cabrera, C. R. Bieler, B. C. Olbricht, W. E. van der Veer, and K. C. Janda, J. Chem. Phys. **123**, 054311 (2005).
[76]D. L. Bunker and W. L. Hase, J. Chem. Phys. **59**, 4621 (1973).
[77]R. Paškauskas, C. Chandre, and T. Uzer, Phys. Rev. Lett. **100**, 083001 (2008).

CHAPTER III

The backward method

Summary

The Wigner distribution function is inserted into the QCT-SB and QCT-GB methods as a more accurate representation of the initial state. An alternative backward approach for direct photodissociation, rigorously equivalent to the standard forward one, is presented. This equivalence is tested in Section III.2 for a realistic process, the photodissociation of $NeBr_2(B)$ linear isomer, showing the numerical advantages of the new method.

III.1 Theoretical introduction

The standard forward picture of direct photodissociation

In Chapter II, the quasi-classical formalism was oriented to the description of the VP of vdW complexes. Here, we focus the attention on direct photodissociation process, such as the one represented in Fig. III.1. The ABC molecule in its ground electronic and rovibrational state is pumped with a laser of energy $\hbar\omega$ to a repulsive PES where dissociation rapidly takes place. We assume that A + BC is only open channel at the excitation energies considered. As most of the theory presented in Chapter II is general for the photofragmentation, it can be directly applied to this case by simply setting Rg≡A. As usual, Jacobi coordinates are employed to describe the system. The (v,j) state-resolved absorption cross

section of the process, for a constant transition dipole moment $\boldsymbol{d}$, is given by Eq. (II.5). If the $\boldsymbol{d}$ is allowed to depend on (r, R, θ), according to Ref. [39] this equation takes the form

$$\sigma(E, v, j) \propto \int d\boldsymbol{\Gamma}_0 \, d_e^2 \rho(\boldsymbol{\Gamma}_0) \, \delta[\mathcal{H}(\boldsymbol{\Gamma}_0) - E] \, \delta[v_f(\boldsymbol{\Gamma}_0) - v] \, \delta[j_f(\boldsymbol{\Gamma}_0) - j], \quad \text{(III.1)}$$

where d_e is component of $\boldsymbol{d}$ in the direction of the polarization of the electric field of the incident photon.

The only difference between Eq. (III.1) and Eq. (5.23) of Schinke's book (Ref. [39]) is the factor $\sin\theta_0$ multiplying the integrand, which seems to result from including the rotational degree of freedom (see Chapter IV). That factor was omitted in the developments of Chapter II and the next section. However, as the purpose of the present chapter is to show the equivalence and numerical advantages of the backward approach with respect to the forward one in a realistic process, it introduces no inconsistency.

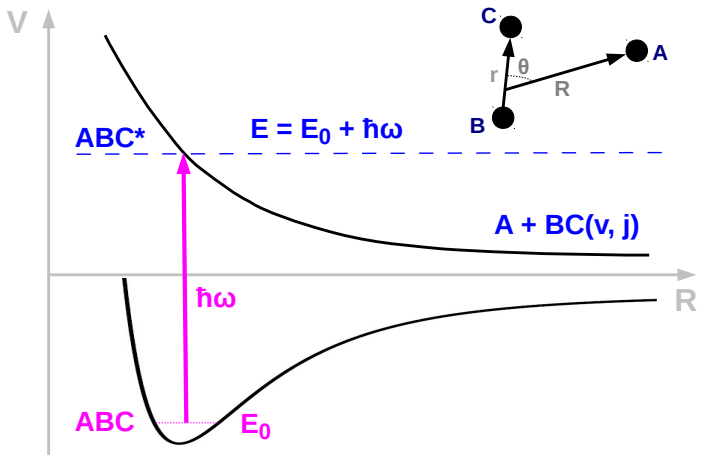

Figure III.1: Schematic representation of a direct photodissociation process in an ABC molecule.

As before, $\rho(\boldsymbol{\Gamma}_0)$ in Eq. (III.1) represents the distribution function of the initial phase-space states, $\boldsymbol{\Gamma}_0$. A definition of $\rho(\boldsymbol{\Gamma}_0)$ basically intuitive and therefore without a theoretical justification was already introduced in Chapter II. Here, let us consider instead that $\rho(\boldsymbol{\Gamma}_0)$ is given by the so-called *Wigner distribution function* [75], *i.e.*,

$$\rho(\boldsymbol{\Gamma}_0) = \frac{1}{(\hbar\pi)^3} \int d\boldsymbol{s} \, \mathrm{e}^{2i\boldsymbol{p}_0\cdot\boldsymbol{s}/\hbar} \, \Psi_0^*(\boldsymbol{x}_0 + \boldsymbol{s})\Psi_0(\boldsymbol{x}_0 - \boldsymbol{s}), \quad \text{(III.2)}$$

where Ψ_0 is the wavefunction corresponding to the electronic ground state of the

system; $\boldsymbol{x}_0$ and $\boldsymbol{p}_0$ compact all the initial coordinates and conjugate momenta, respectively; and $\boldsymbol{s} = (s_r, s_R, s_\theta)$. This function is particularly interesting as a phase-space distribution for several reasons. It is not difficult to show that integrating it over $\boldsymbol{p}_0$ leads to $|\Psi(\boldsymbol{x}_0)|^2$, integrating it over $\boldsymbol{p}_0$ leads to $|\Psi(\boldsymbol{p}_0)|^2$ and integrating it over $\boldsymbol{\Gamma}_0$ gives 1. Moreover, calling $\hat{H}$ the quantum Hamiltonian, integration of $\mathcal{H}(\boldsymbol{\Gamma}_0)\rho(\boldsymbol{\Gamma}_0)$ over $\boldsymbol{\Gamma}_0$ leads to $\langle\Psi_0|\hat{H}|\Psi_0\rangle$. All those properties are expected from an appropriate phase-space distribution corresponding to the quantum state Ψ_0. The Wigner function, however, can take negative values in some regions of the phase-space and that is inconsistent with a probability distribution. Nevertheless, one can formally use this non-conventional density of probability as an usual one. Additionally, it is shown in Ref. [39] that under the harmonic approximation and for the ground rovibronic state, Eq. (III.2) transforms into a simple positive-defined analytical expression. That makes it also particularly efficient from the numerical point of view.

Using Eq. (III.2) as the initial phase-space distribution, the working equations for the QCT-SB and QCT-GB partial cross sections, given by Eq. (II.8) and Eq. (II.9) in Chapter II, remain valid by only including the d_e^2 factor into their expressions. It is worth noting that all the developments in this chapter are based on Eq. (5.23) of Ref. [39], where the component of the transition dipole moment appears explicitly in the equations. In the next chapter we show that this is not rigorously correct, although this has no relevance for our purposes here.

The classical 'Backward' picture of direct photodissociation

In order to introduce the backward approach, consider the projection on (R,P_R) of the phase-space path followed by a generic trajectory in the repulsive PES, represented in Fig. III.1. Point P, which defines the origin of time, $t = 0$, is located in the products at $\boldsymbol{\Gamma}_f = (r_f, \theta_f, P_{rf}, P_{\theta f}, R_f, P_{Rf})$, with R_f sufficiently large for $V_{\mathrm{A,BC}} \simeq 0$ and for P_{Rf} to be given by the positive value

$$P_{Rf} = \sqrt{2\mu_{\mathrm{A,BC}}(\mathcal{H} - E_{\mathrm{BC}})}. \tag{III.3}$$

E_{BC} is the rovibrational energy of BC at point Q, given by Eq. (II.3). The dynamical state of the system at an arbitrary point B, defined by a value $t < 0$, is completely specified by $\boldsymbol{\Gamma}(t)$. Now, it is possible to show that an alternative set of coordinates to $\boldsymbol{\Gamma}(t)$ is given by $(t, \mathcal{H}, r_f, \theta_f, P_{rf}, P_{\theta f})$ [64, 71, 115–117]. That is, given the value of R at $t = 0$, R_f, the quadruplet $(r_f, \theta_f, P_{rf}, P_{\theta f})$ specifies the internal state of BC at $t = 0$ and therefore E_{BC}, while Eq. (III.3) specifies P_{Rf}. The resulting $\boldsymbol{\Gamma}_f$, then, defines a given classical path, any point of which corresponds to a given time t.

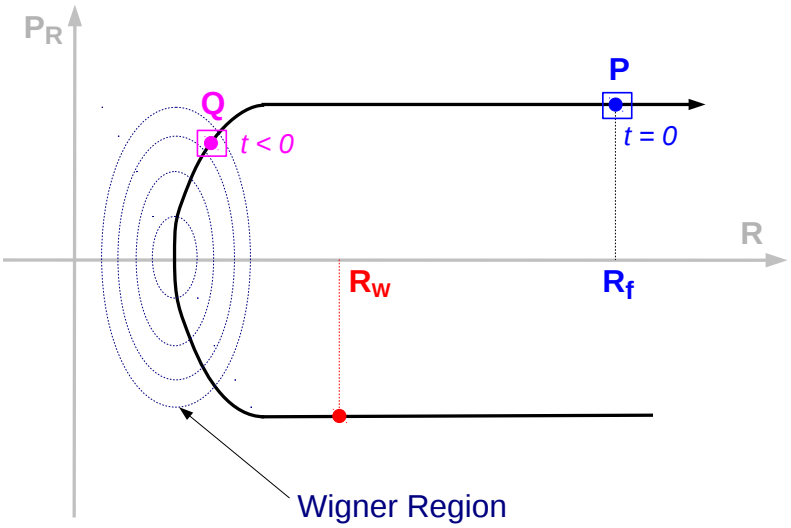

Figure III.2: Projection on (R,P_R) of the phase-space path followed by a generic trajectory in the repulsive PES.

In addition, it is possible to prove following the reasoning from Appendix C of Ref. [64], that the Jacobian of the transformation $\boldsymbol{\Gamma}_f \rightarrow (t, \mathcal{H}, r_f, \theta_f, P_{rf}, P_{\theta f})$ is equal to 1 at $t = 0$. As $\mathcal{H}$ is a constant of motion, so is the volume element in the phase-space from the Liouville theorem, which means that at any time $\boldsymbol{d\Gamma}(t) = dtd\mathcal{H}dr_f d\theta_f dP_{rf} dP_{\theta f}$. Consequently, the volume element $\boldsymbol{d\Gamma}_0$ in Eq (III.1) satisfies that

$$\boldsymbol{d\Gamma}_0 = dtd\mathcal{H}dr_f d\theta_f dP_{rf} dP_{\theta f}. \tag{III.4}$$

Moreover, we can represent BC in the products ($t = 0$) in angle-action coordinates $(q_v, \hbar v_f, q_j, \hbar j_f)$, where v_f is given by Eq. (II.6); j_f is now $P_\theta/\hbar$ (this is rigorously a result of the condition $\boldsymbol{J} = 0$); and (q_v, q_j) are the conjugate angles associates with (v_f, j_f). The corresponding transformation $(r_f, \theta_f, P_{rf}, P_{\theta f}) \rightarrow (q_v, \hbar v_f, q_j, \hbar j_f)$ being volume-preserved, *i.e.*, $dr_f d\theta_f dP_{rf} dP_{\theta f} = \hbar^2 dq_v dq_j dv_f dj_f$, Eq. (III.4) can be rewritten as

$$\boldsymbol{d\Gamma}_0 = \hbar^2 dtd\mathcal{H}dq_v dq_j dv_f dj_f. \tag{III.5}$$

Inserting this expression into Eq. (III.1),

$$\sigma(E, v, j) \propto \int dtd\mathcal{H}dq_v dq_j dv_f dj_f d_e^2\rho \; \delta(\mathcal{H} - E)\delta(v_f - v)\delta(j_f - j), \tag{III.6}$$

where the constant factors has been absorbed into the proportional sign and the dependence on the new coordinates is implicit. Integration over $\mathcal{H}$, v_f and j_f in

Eq. (III.6) leads directly to the simple expression of the *Backward method* [71]

$$P(E,v,j) \propto \int dt dq_v dq_j d_e^2 \rho. \tag{III.7}$$

Solving the integrals over (q_v, q_j) by a Monte-Carlo procedure, Eq. (III.7) can be rewritten as

$$\sigma(E,v,j) \propto \frac{1}{N_{\text{traj}}} \sum_{i=1}^{N_{\text{traj}}} \int dt d_e^2 \rho, \tag{III.8}$$

where N_{traj} is the number of trajectories run for each rovibrational state (v,j).

Application of Eq. (III.8) to a concrete problem is more subtle than applying the forward method. Trajectories have to be started in the products ($t = 0$) with integer values of the rovibrational actions of BC, exactly matching (v,j), while phases (q_v, q_j) are randomly sampled. Each trajectory is propagated backward in time until it is completely out of the region where the Wigner function has significant values. This *Wigner region*, represented in Fig. III.1, can be easily delimited for each trajectory by a value of R, say $R = R_W$, with $P_R < 0$. The integral of $d_e^2\rho$ along the path defined by the trajectory needs to be calculated. This value gives the statistical weight of the trajectory, which has to be multiplied by -1 as integration is in the domain $t < 0$. The population of a particular (v,j)-state is computed then simply summing the weights corresponding to the N_{traj} trajectories ran for that state.

The backward method offers the great advantages over the standard forward QCT method of taking into account exactly the Bohr quantization of final fragments, without the use of any binning technique. As a consequence, the same convergence level of $\sigma(E,v,j)$ is expected to be achieved with a considerable lower number of trajectories. In addition, it has the property of being state-selective, *i.e.*, each rovibrational state can be converged independently, running for each just the "right" number of trajectories. The numerical efficiency of the backward method, however, has one main limitation. Only trajectories started within some particular boundaries of (q_v, q_j), actually reach the Wigner region, the rest being completely useless to converge Eq. (III.7). As one cannot guess in advance the limits of these intervals, a practical solution is to run a few hundred trajectories with the forward method and determine where these 'important' regions in q_v and q_j are. Then, initial conditions for the backward method are selected inside them. By doing so, the number of trajectories required by the backward approach can be dramatically decreased.

Next section continues with the application of the QCT-GB and backward methods to a realistic process, the photodissociation of $NeBr_2(B)$ linear isomer.

III.2 Publication

Chemical Physics 399 (2012) 117–121

Contents lists available at ScienceDirect

Chemical Physics

journal homepage: www.elsevier.com/locate/chemphys

Classical photodissociation dynamics with Bohr quantization: Application to the fragmentation of a van der Waals cluster

W. Arbelo-González [a,b,*], L. Bonnet [a,*], P. Larrégaray [a], J.-C. Rayez [a], J. Rubayo-Soneira [b]

[a] Institut des Sciences Moléculaires, Université Bordeaux 1, 351 Cours de la Libération, 33405 Talence Cedex, France
[b] Departamento de Física General, Instituto Superior de Tecnologías y Ciencias Aplicadas, Habana 10600, Cuba

ARTICLE INFO

Article history:
Available online 28 July 2011

Keywords:
Photodissociation dynamics
Classical description
Standard forward approach
Gaussian binning
New backward approach

ABSTRACT

The recent classical dynamical approach of photodissociations with Bohr quantization [L. Bonnet, J. Chem. Phys. 133 (2010) 174108] is applied for the first time to a realistic process, the photofragmentation of the van der Waals cluster $NeBr_2$. We illustrate the fact that this approach, formally equivalent to the standard one, may be numerically much more efficient.

1. Introduction

Modern experiments on polyatomic photodissociations allow spectacular measurements of their dynamics at an unprecedent level of details [1]. In most cases, the measured quantities are the state correlated distributions of the translational energy between the two nascent product molecules [2]. To be more precise, the distribution of their relative recoil energy is measured, often by means of the ion-imaging technics [1], for a given quantum state of one of the two products. For such a reason, the distribution involves well defined structures due to quantization of the internal energy of the remaining partner. From these structures, the populations of the corresponding states may be deduced.

Unfortunately, accurate theoretical predictions of state correlated distributions remain difficult, and this limitation is detrimental to the crucial synergy between experiment and theory; on the one hand, exact quantum approaches can hardly be applied to more than three or four atom processes to date [3], and on the other hand, the classical description in its standard implementation [3–5] ignores quantum effects which may play a key role.

Among the strongest quantum effects is the quantization of product internal energies previously evoked. In the standard classical approach, this effect can be dealt with by means of the Gaussian binning (GB) procedure which emphasizes the classical paths satisfying Bohr quantization of product internal motions (supposed to be separable) [6–10]. In practice, however, this approach turns out to be only efficient for reactions involving three or four atoms [9,10]. Being based on trajectories going from the optically excited reagent molecule to the products, this method is referred to as *forward* in the following.

To go round this difficulty, an alternative though rigorously equivalent method was recently proposed [11] which avoids the numerically demanding GB procedure while allowing for exact Bohr quantization of product internal motions. At the opposite of the previous approach, the present method is based on reverse trajectories initially going from the products to the optically excited reagent molecule. For such a reason, we refer to it as *backward* further below.

Up to now, this method has only been tested against the forward one on a model photodissociation. The goal of the present work is to repeat this test on a realistic process, the fragmentation of the van der Waals cluster $NeBr_2$ [12–22]. We wish to emphasize here that our scope is not to discuss the validity of the classical approach itself.

The paper is organized as follows: we recall the forward and backward methodologies in Section 2. Their predictions are compared in Section 3. Section 4 concludes.

2. Theoretical methods

2.1. System

The following photodissociation process is considered:

$$NeBr_2(X, v = 0, j = 0) + \hbar\omega \rightarrow NeBr_2(B, v')^* \rightarrow Ne + Br_2(B, v'', j''). \quad (1)$$

* Corresponding authors. Address: Institut des Sciences Moléculaires, Université Bordeaux 1, 351 Cours de la Libération, 33405 Talence Cedex, France.
E-mail addresses: wilmer@instec.cu (W. Arbelo-González), l.bonnet@ism.u-bordeaux1.fr (L. Bonnet).

0301-0104/$ - see front matter © 2011 Elsevier B.V. All rights reserved.
doi:10.1016/j.chemphys.2011.07.022

$NeBr_2$ is optically excited from the linear isomer of the electronic ground state X to the excited state B. The $NeBr_2$ clusters are supposed to be prepared in a cold beam so their rotation motion is roughly frozen. For simplicity's sake, we keep their total angular momentum $\boldsymbol{J}$ at zero. Jacobi coordinates (r,R,θ) are employed to describe the complex, where r is the Br–Br distance, R is the distance between Ne and the center of mass of Br_2 and θ is the angle between vectors $\boldsymbol{r}$ and $\boldsymbol{R}$. In this coordinate system, the Hamilton function can be written as:

$$\mathcal{H}(\boldsymbol{q},\boldsymbol{p}) = \frac{p_r^2}{2\mu_{Br_2}} + \frac{P^2}{2\mu_{Ne,Br_2}} + \frac{p_\theta^2}{2I} + V(r,R,\theta), \tag{2}$$

with

$$\frac{1}{I} = \frac{1}{\mu_{Br_2} r^2} + \frac{1}{\mu_{Ne,Br_2} R^2}. \tag{3}$$

$\mu_{Br_2} = m_{Br}/2$ and $\mu_{Ne,Br_2} = 2m_{Ne}m_{Br}/(m_{Ne}+2m_{Br})$ are the reduced masses of Br–Br and Ne–Br_2, respectively. p_r, P and p_θ are the momenta conjugate to r, R, and θ, respectively. In Eq. 2 and in the rest of the paper, the notation $\boldsymbol{q} = (r,R,\theta)$ and $\boldsymbol{p} = (p_r,P,p_\theta)$ will be used.

The total PES's for both electronic states X and B are expressed as the sum $V(r,R,\theta) = V_{Br_2}(r) + V_{vdW}(r,R,\theta)$ where $V_{Br_2}(r)$ is the potential of an isolated Br_2 molecule and $V_{vdW}(r,R,\theta)$ describes the van der Waals (vdW) interaction Ne–Br_2. The Br–Br potential is analytically expressed by a Morse function with parameters $D^X = 24557.674\ cm^{-1}$, $r_{eq}^X = 2.281$ Å, $\alpha^X = 1.588$ Å^{-1} [23] and $D^B = 3788.0\ cm^{-1}$, $r_{eq}^B = 2.667$ Å, $\alpha^B = 2.045$ Å^{-1} [24] for electronic states X and B, respectively.

The vdW potential in the electronic state X was constructed using the recent *ab initio* calculations reported in Ref. [19]. In that work, *Morse-vdW* functions depending on R were employed to fit the *ab initio* points for five different values of θ and r. The global PES was computed by interpolation with first, a collocation method in θ using only even Legendre polynomials $P_n(\cos\theta)$ (n = 0,2,4,6,8), due to the symmetry with respect to $\theta = 90°$, and second, a standard Lagrange interpolation in r. In the electronic state B, a pairwise sum was assumed, *i.e.* $V_{vdW}^B(r,R,\theta) = V_{Mrs}(R_1) + V_{Mrs}(R_2)$, where $V_{Mrs}(R_i)$ is a Morse function with parameters $D^{vdW} = 42.0\ \text{cm}^{-1}$, $R_{eq}^{vdW} = 3.9$ Å, $\alpha^{vdW} = 1.67$ Å^{-1} [20] and R_1 and R_2 are the distances between the Ne atom and each Br atoms, easily calculated by means of the cosine law, for instance.

2.2. Forward method

In the case of a triatomic molecule ABC, the standard expression of the cross section for absorbing a photon of frequency ω and producing the diatom BC in a given vibro-rotational state (v'',j'') is [3,25,26]

$$\sigma(\omega, v'', j'') \propto \omega \int d\boldsymbol{q}d\boldsymbol{p}\rho_W \mu_{(e)}^2 \delta[\mathcal{H}(\boldsymbol{q},\boldsymbol{p}) - E_{tot}]\delta[x(\boldsymbol{q},\boldsymbol{p}) - v'']\delta[j(\boldsymbol{q},\boldsymbol{p}) - j'']. \tag{4}$$

$\boldsymbol{q}$ and $\boldsymbol{p}$ are the coordinates of ABC at time zero. $\mathcal{H}(\boldsymbol{q},\boldsymbol{p})$ and E_{tot} are the Hamilton function and total energy in the upper electronic state, respectively. The zero of energy corresponds to the three atoms infinitely separated. $x(\boldsymbol{q},\boldsymbol{p})$ and $j(\boldsymbol{q},\boldsymbol{p})$ are the vibrational and rotational actions (see further below) of the final BC diatom (Br_2 in this case). ρ_W is the *Wigner distribution function* before the optical transition and $\mu_{(e)}$ is the component of the transition dipole function in the direction of the electric field vector. These two quantities depend on $\boldsymbol{q}$ and $\boldsymbol{p}$, but for convenience's sake, we do not specify it explicitly. ω is 2π times the frequency of the photon.

The usual *Monte Carlo* (MC) technique may then be applied in order to solve the integral of Eq. (4) with the Dirac's delta functions approximated by

$$\delta[\mathcal{H}(\boldsymbol{q},\boldsymbol{p}) - E_{tot}] \approx \Xi[\mathcal{H}(\boldsymbol{q},\boldsymbol{p}); E_{tot}, \Delta E_{tot}], \tag{5}$$

$$\delta[j(\boldsymbol{q},\boldsymbol{p}) - j''] \approx \Xi[j(\boldsymbol{q},\boldsymbol{p}); j'', 1], \tag{6}$$

$$\delta[x(\boldsymbol{q},\boldsymbol{p}) - v''] \approx G[x(\boldsymbol{q},\boldsymbol{p}); v'', \epsilon]. \tag{7}$$

$\Xi[x(\boldsymbol{q},\boldsymbol{p}); x, \Delta x]$ is the square barrier function of width Δx and height $1/\Delta x$, formally defined as:

$$\Xi[x(\boldsymbol{q},\boldsymbol{p}); x, \Delta x] = \Theta[x(\boldsymbol{q},\boldsymbol{p}) + \Delta x/2 - x]\Theta[x - x(\boldsymbol{q},\boldsymbol{p}) + \Delta x/2]/\Delta, \tag{8}$$

$\Theta(x)$ being the Heaviside function. $G[x(\boldsymbol{q},\boldsymbol{p}); x, \epsilon]$ is the Gaussian function

$$G[x(\boldsymbol{q},\boldsymbol{p}); x, \epsilon] = \frac{e^{-(x(\boldsymbol{q},\boldsymbol{p})-x)^2/\epsilon^2}}{\pi^{1/2}\epsilon} \tag{9}$$

where ϵ is supposed to be much lower than 1. Note that we only quantized (in Bohr spirit) the vibration motion of Br_2, not its rotation motion for which the classical description is in general more reasonable (using Eq. 8 with $\Delta x = 1$ (standard binning) or Eq. 9 leads in general to the same predictions for the rotation motion).

Assuming for simplicity's sake that $\mu_{(e)}$ does not depend on the configuration of the system, the MC expression of Eq. 4 finally used in practice reads:

$$\sigma(\omega, v'', j'') \propto \sum_{k=1}^{N_{diss}} \Xi[\mathcal{H}(\boldsymbol{q}_k,\boldsymbol{p}_k); E_{tot}, \Delta E_{tot}] G[x(\boldsymbol{q}_k,\boldsymbol{p}_k); v'', \epsilon]\Xi[j(\boldsymbol{q}_k,\boldsymbol{p}_k); j'', 1], \tag{10}$$

where index k runs over the N_{diss} dissociated trajectories whose initial conditions are chosen according to ρ_W. Note that all constant factors have been included into the proportionality sign.

The rotational action $j(\boldsymbol{q},\boldsymbol{p})$ of BC is given by the final value of p_θ divided by $\hbar$ (this is a consequence of the condition $\boldsymbol{J} = \boldsymbol{0}$), and the vibrational action is computed by the usual expression:

$$x(\boldsymbol{q},\boldsymbol{p}) = \frac{1}{2\pi\hbar}\oint p_r dr = \frac{\sqrt{2\mu_{Br_2}}}{\pi\hbar}\int_{r_{in}}^{r_{out}} \sqrt{E_{xj} - V_{Br_2} - \frac{\hbar^2 j(\boldsymbol{q},\boldsymbol{p})^2}{2\mu_{Br_2} r^2}}\, dr \tag{11}$$

where E_{xj} is the final internal energy of BC. r_{in} and r_{out} define the inner and outer turning points, respectively. The vibro-rotational distributions are easily computed by using Eq. 10.

2.3. Wigner distribution function

A second order Taylor expansion of $V(r,R,\theta)$ around its minimum position $\boldsymbol{q}_{eq} = (2.281\text{ Å}, 4.48\text{ Å}, 0)$, corresponding to the linear isomer of the ground electronic state X, may be done. Under this approximation, the total PES is expressed as a sum of harmonic potential functions depending on one variable only and the problem, therefore, becomes separable. It can be shown that, for the vibro-rotational ground state, Wigner density of states ρ_W is expressed as the product of six Gaussians [3]

$$\rho_W(\boldsymbol{q},\boldsymbol{p}) = \frac{1}{(\hbar\pi)^3}\exp\left[-\frac{2\boldsymbol{\alpha}(\boldsymbol{q}-\boldsymbol{q}_{eq})^2}{\hbar}\right]\exp\left(-\frac{\boldsymbol{p}^2}{2\boldsymbol{\alpha}\hbar}\right), \tag{12}$$

with

$$\boldsymbol{\alpha} = (\alpha_r, \alpha_R, \alpha_\theta) = \left(\frac{\mu_{Br_2}\omega_r}{2}, \frac{\mu_{NeBr_2}\omega_R}{2}, \frac{\widetilde{I}\omega_\theta}{2}\right). \tag{13}$$

$\widetilde{I}$ is given by Eq. 3, evaluated at the minimum of the electronic ground state.

Angular frequencies are expressed as

$$\omega_\xi = \left(\frac{k_\xi}{M_\xi}\right)^{1/2}, \tag{14}$$

with $\xi \equiv \{r,R,\theta\}$ and $M_\xi \equiv \{\mu_{Br_2}, \mu_{NeBr_2}, \widetilde{I}\}$. The force constants for each mode are

$$k_\xi = \left|\frac{\partial^2 V(\boldsymbol{q})}{\partial \xi^2}\right|_{\boldsymbol{q}=\boldsymbol{q}_{eq}}, \tag{15}$$

where the second derivatives of the total PES are carried out numerically.

2.4. Backward method

This alternative method recently proposed in Ref. [11] is based on the transformation $(t,\mathcal{H},\phi_i,\hbar x_i,\theta_i,\hbar j_i) \rightarrow (r,p_r,R,P,\theta,\hbar j)$ (we now use $\hbar j$ instead of p_θ). The left-hand-side coordinates are defined as follows. We consider a classical path starting at time 0 from a large distance R_i of R in the free products with a negative value P_i of P. A and BC are thus approaching each other. The initial values of x and j are denoted x_i and j_i and their conjugate angles are ϕ_i and θ_i, respectively. The value of P_i is deduced from x_i, j_i and the fact that $\mathcal{H} = E_{tot}$. At time t along the previous path, the system is supposed to be at the phase space point $(r,p_r,R,P,\theta,\hbar j)$. Now, it can be shown [11,27] that the above transformation is volume preserving, i.e.,

$$dr dp_r dR dP d\theta dj = \hbar dt d\mathcal{H} d\phi_i dx_i d\theta_i dj_i. \tag{16}$$

From this identity, Eq. (4) can be rewritten as:

$$\sigma(\omega, v'', j'') \propto \omega \int dt d\mathcal{H} d\phi_i dx_i d\theta_i dj_i \rho_W \mu^2_{(e)} \delta[\mathcal{H} - E_{tot}] \delta[x_i - v''] \delta[j_i - j'']. \tag{17}$$

Integrating over $\mathcal{H}$, x_i and j_i, Eq. (17) takes the form

$$\sigma(\omega, v'', j'') \propto \hbar\omega \int dt d\phi_i d\theta_i \rho_W \cdot \mu^2_{(e)}. \tag{18}$$

An equation equivalent to Eq. (16) has already been used in semiclassical mechanics to improve the calculation of the Herman–Kluck propagator [28].

The MC expression of Eq. (18), which is the final working equation of the backward method, can be written as

$$\sigma(\omega, v'', j'') \propto \sum_{l=1}^{N_{traj}} \sum_{k=1}^{N_l} \rho_W^{lk} \tag{19}$$

where, again, all constant factors have been included into the proportionality sign ($\mu_{(e)}$ is supposed to be constant). $N_{traj} = N_\phi \times N_\theta$ is the number of trajectories for a given vibro-rotational state (v'',j''), N_ϕ and N_θ are the number of sampled points in ϕ_i and θ_i, respectively, N_l is the total number of time steps along the lth trajectory, τ is the time step of integration and ρ_W^{lk} is the value of $\rho_W(\boldsymbol{q},\boldsymbol{p})$ for the lth trajectory and kth time step.

In other words, applying Eq. (19) requires to start trajectories in the products with $x = v''$ and $j = j''$, i.e., such as exactly satisfying Bohr quantization conditions, and propagate them toward the interaction region until they come back to the products. Each trajectory is then assigned a weight, given by the time integral of ρ_W along it, multiplied by some constant factor.

In the present work, phases ϕ_i and θ_i were uniformly sampled. Two technical details may be given for clarity's sake. The first one has to do with the calculation of the vibro-rotational energy $E_{v''j''}$ of Br_2 in the products. $E_{v''j''}$ defines the energy available to the translation at $t = 0$, $E_{trans} = E_{tot} - E_{v''j''}$, and therefore the value of P_i, given by:

$$P_i = -\sqrt{2\mu_{NeBr_2} E_{trans}}. \tag{20}$$

$E_{v''j''}$ minimizes the function

$$\chi(E_{xj''}) = (x - v'')^2, \tag{21}$$

where the action x is given by Eq. (11) with $j = j''$. The minimization leading to $E_{v''j''}$ can be performed by means of any standard numerical procedure [29].

The second technical aspect is about the uniform sampling of ϕ_i and the transformation from $(\phi_i,\hbar x_i)$ to (r^i, p_r^i), the values of r and p_r at $t = 0$ (it is in the framework of these variables, together with R,P, θ and $p_\theta = \hbar j$ that the numerical propagation of trajectories is performed). Since for sufficiently large values of R, both P and x are constants of motion, both R and ϕ are linear functions of time. Uniform samplings in ϕ and R are thus equivalent. Having found $E_{v''j''}$ as explained above and starting from an inner turning point, R was sampled in the interval $(R_{diss}, R_{diss} + \Delta R)$ where

$$\Delta R = -\frac{P_i}{\mu_{NeBr_2}} T_{v''j''}, \tag{22}$$

$R_{diss} = 10$ Å and $T_{v''j''}$ is the vibrational period in the state (v'',j'') computed integrating the classical equations of motion for Br_2 isolated.

3. Results and discussion

The *vdW* potential of the ground electronic state X has two minima, one in linear configuration, the deepest, and another in T-shaped configuration (see Ref. [19] for more details). The PES of the upper electronic state B, on the other hand, has only one minimum in T-shaped configuration, consequence of the additive pairwise scheme used. Thus, excitation from the linear isomer drives the system to a repulsive region of the *vdW* coordinate and dissociation is direct.

The application of the forward method requires first to generate initial conditions according to ρ_W, under the restriction that the total energy in the excited electronic state B is inside a close neighborhood of E_{tot}. The latter was selected as $E_{tot} = E_{v'} + D_0$ where $E_{v'}$ is the vibrational energy of Br_2 corresponding to the quantum vibrational level v', computed by solving the Schrödinger equation for the isolated Br_2, and D_0 is the dissociation energy in the *vdW* mode extracted from Ref. [30].

Although calculations were done for different values of E_{tot}, we will only show the results of a representative example, corresponding to $v' = 26$, for which $E_{tot} = -744.542$ cm^{-1}. An energy window $\Delta E_{tot} = 2$ cm^{-1} was employed and a set of 10^6 initial conditions were generated. Trajectories were propagated using a standard four-order predictor–corrector algorithm with stepsize $\tau = 10^{-4}$ ps, which assures an error in conservation of total energy of 10^{-8} cm^{-1}.

The system was assumed dissociated when $R \geqslant 10$ Å, distance for which $V_{vdW}(r,R,\theta)$ is totally negligible. The values of ω_ξ obtained from Eq. (14) and needed for evaluating ρ_W are as follows: $\omega_r = 1.483 \times 10^{-3}$, $\omega_R = 1.572 \times 10^{-4}$ and $\omega_\theta = 4.760 \times 10^{-5}$, in atomic units.

As shown in Fig. 1, the values of θ for $R = 10$ Å obtained from the forward method are mainly distributed in the interval $(-\pi/4, \pi/4)$. This could be expected, considering the short interaction time of the process. In the backward method, trajectories were started from $R = 10$ Å in the direction of the reagent molecule with θ sampled only in the previously mentioned interval. Propagation was done in exactly the same manner as for the forward approach.

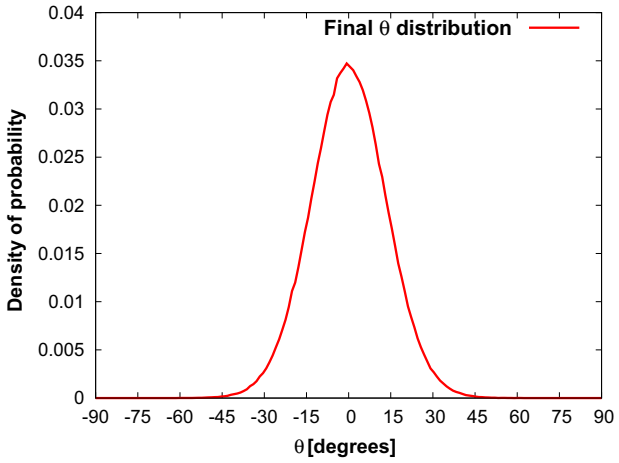

Fig. 1. Distribution of the θ angle at $R = 10$ Å.

The first observable we discuss is the final vibrational state distribution of Br_2. As far as the forward method is concerned, the usual value $\epsilon = 0.05$ was used in the GB procedure [6–10]. By running several million trajectories, we checked that the vibrational distribution obtained by means of one million trajectories was well converged and could be taken as a 'benchmark' distribution to compare with. This distribution is represented in Fig. 2 (blue dots). It is shown in the same figure that, for instance, half million trajectories are not sufficient to converge the distribution (green triangles).

For the backward method, we found after some test that taking (1) $N_\phi = 20$ and $N_\theta = 5$, which result in 100 trajectories per vibro-rotational state (v'',j''), (2) the first 30 rotational level for each v'' and (3) up to $v'' = 7$, whose population is negligible, the agreement with the forward distribution is excellent. The backward distribution requires a total of about 6×10^4 trajectories. This distribution is also represented in Fig. 2. As a matter of fact, the new method achieves the same level of convergence as the standard one with 94% less trajectories.

In the backward method, trajectories are run from the products towards the reagent molecule and back to the products whereas in the forward method, they are run from the reagent molecule up to the products. Therefore, the average numerical cost per trajectory with the backward method is roughly twice the one with the forward method. Consequently, the numerical efficiency of the former

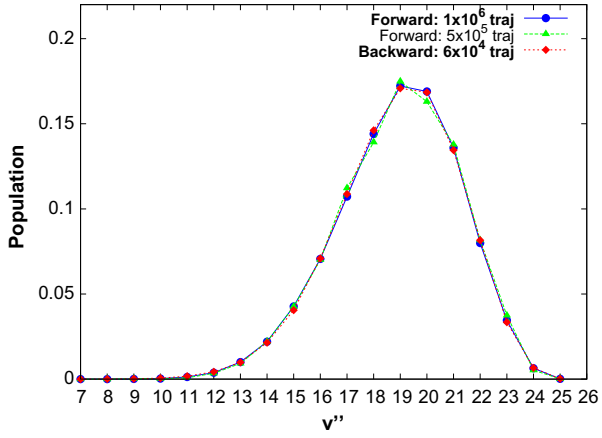

Fig. 2. Comparison of the final vibrational state distributions of Br_2 obtained by means of the forward and backward methods. Distributions are normalized to unity.

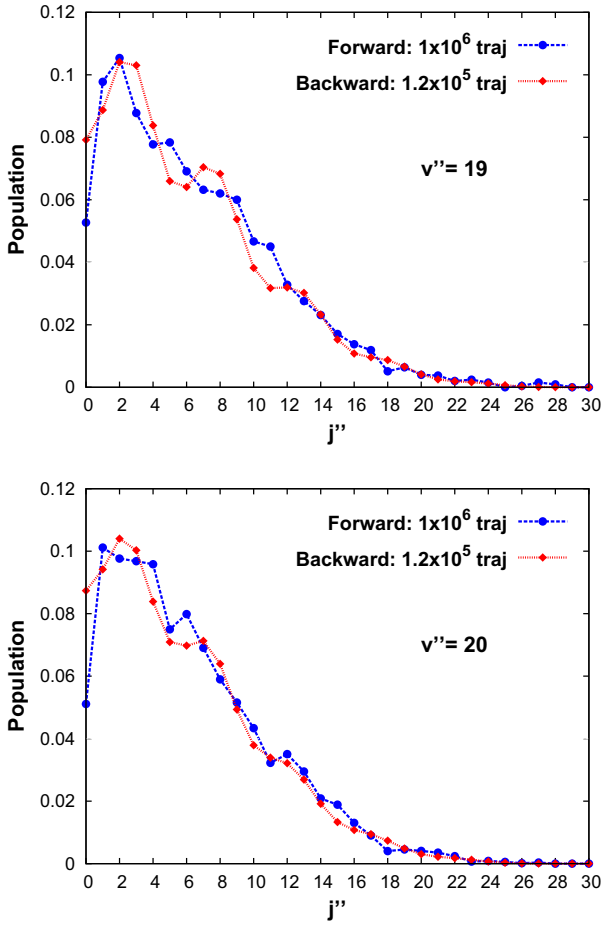

Fig. 3. Comparison of two vibrationally resolved rotational state distributions of Br_2 obtained by means of the forward and backward methods. Distributions are normalized to the populations of the corresponding vibrational states.

is ~8 times larger than the one of the latter. One may however still double the efficiency of the backward method by stopping the trajectories as soon as they leave the phase space region where the Wigner distribution takes non negligible values. This region is indeed roughly placed in the middle of the trajectories.

As for vibrationally resolved (VR) rotational distributions, the backward method demands more trajectories to be in good agreement with the forward method. N_θ has now to be kept at 10, the rest of the parameters being unchanged. Two examples are presented in Fig. 3, corresponding to $v'' = 19$ and $v'' = 20$. Although with twice the previous number of trajectories per vibro-rotational state (1.2×10^5), the method still gains in efficiency; only 12% of the trajectories are needed as compared to the forward approach.

Due to the fact that the distributions of Fig. 3 are more state-resolved than those of Fig. 2, the former appear to be significantly less converged than the latter. One should clearly increase the total number of trajectories run in both approaches to improve the level of convergence of the distributions. However, our goal was just to illustrate the fact that for VR rotational distributions, the backward method is still much more efficient than the forward one.

4. Summary and conclusions

In the standard classical description of photodissociation dynamics, one may deal with Bohr quantization of product internal motions (when separable) by using Gaussian weights such that the

closer the final actions to integer values, the larger the weights [6–10]. This procedure, usually called Gaussian binning (GB), makes the description more realistic than the usual standard binning (SB) procedure in the quantum regime where a relatively low number of quantum states are available to the products. Nevertheless, a major weakness of GB is that the number of trajectories necessary to converge the calculations scales like $\sim 10^N$ where N is the number of (pseudo) quantized modes, as compared to SB. Consequently, GB can only be applied to three or four atom processes where only product vibrations are quantized.

Recently, however, a new classical approach of photodissociation dynamics has been proposed [11] which is formally equivalent to the standard description with GB of zero width ("Dirac binning") while being in principle applicable whatever the number of quantized modes. The convergence of the calculations in terms of number of trajectories run is in principle the same as for the standard approach with SB.

Up to now, the equivalence between the new method and the standard approach with GB has only been illustrated from a model collinear dissociation [11]. Here, we have confirmed it for the first time in the case of a realistic process, the photodissociation of the van der Waals cluster $NeBr_2$. As expected from the fact that only one mode was quantized (the vibration motion of Br_2), the new approach led to results in excellent agreement with GB ones using $\sim$10 times less trajectories only.

We now plan to apply the backward method to the description of state-correlated distributions in polyatomic photodissociations, using theoretical tools already developed in our group [31,32].

Acknowledgment

The authors are grateful to Maykel L. González Martínez for suggesting the study of linear $NeBr_2$ and for stimulating discussions.

References

[1] D. Townsend, W. Li, S.K. Lee, R.L. Gross, A.G. Suits, J. Phys. Chem. A 109 (2005) 8661.
[2] Z. Chen Z, A.T. Eppink, B. Jiang, G.C. Groenenboom, X. Yang, D.H. Parker, Phys. Chem. Chem. Phys. 13 (2011) 2350.
[3] R. Schinke, Photodissociation Dynamics, Cambridge University Press, Cambridge, 1993.
[4] R.N. Porter, L.M. Raff, in: W.H. Miller (Ed.), Dynamics of Molecular Collisions, Part B, Plenum, New York, 1976.
[5] T.D. Sewell, D.L. Thomson, Int. J. Mod. Phys. B 11 (1997) 1067.
[6] L. Bonnet, J.-C. Rayez, Chem. Phys. Lett. 277 (1997) 183.
[7] L. Bañares, F.J. Aoiz, P. Honvault, B. Bussery-Honvault, J.-M. Launay, J. Chem. Phys. 118 (2003) 565.
[8] L. Bonnet, J.-C. Rayez, Chem. Phys. Lett. 397 (2004) 106.
[9] G. Czakó, J.M. Bowman, J. Chem. Phys. 131 (2009) 244302.
[10] L. Bonnet, J. Espinosa-García, J. Chem. Phys. 133 (2010) 164108.
[11] L. Bonnet, J. Chem. Phys. 133 (2010) 174108.
[12] M.A. Taylor, J.M. Pio, W.E. van der Veer, K.C. Janda, J. Chem. Phys. 132 (2010) 104309.
[13] C. Sanz-Sanz, O. Roncero, R. Hernández-Lamoneda, J.M. Pio, M.A. Taylor, K.C. Janda, J. Chem. Phys. 132 (2010) 221103.
[14] J.M. Pio, M.A. Taylor, W.E. van der Veer, C.R. Bieler, J.A. Cabrera, K.C. Janda, J. Chem. Phys. 133 (2010) 014305.
[15] T.A. Stephenson, N. Halberstadt, J. Chem. Phys. 112 (2000) 2265.
[16] B. Miguel, A. Bastida, J. Zúñiga, A. Requena, N. Halberstadt, J. Chem. Phys. 113 (2000) 10130.
[17] O. Roncero, J. Campos-Martínez, M.I. Hernández, G. Delgado-Barrio, P. Villarreal, J. Rubayo-Soneira, J. Chem. Phys. 115 (2001) 2566.
[18] R. Prosmiti, C. Cunha, P. Villarreal, G. Delgado-Barrio, J. Chem. Phys. 116 (2002) 9249.
[19] R. Prosmiti, C. Cunha, A.A. Buchachenko, G. Delgado-Barrio, P. Villarreal, J. Chem. Phys. 117 (2002) 10019.
[20] A. García-Vela, K.C. Janda, J. Chem. Phys. 124 (2006) 034305.
[21] M.L. González-Martínez, J. Rubayo-Soneira, K.C. Janda, Phys. Chem. Chem. Phys. 8 (2006) 4550.
[22] M.L. González-Martínez, W. Arbelo-González, J. Rubayo-Soneira, L. Bonnet, J.-C. Rayez, Chem. Phys. Lett. 463 (2008) 65.
[23] T. González-Lezana, M.I. Hernandez, G. Delgado-Barrio, A.A. Buchachenko, P. Villarreal, J. Chem. Phys. 105 (1996) 7494.
[24] R.F. Barrow, T.C. Clark, J.A. Coxon, K.K. Lee, J. Mol. Spectrosc. 51 (1974) 428.
[25] W.H. Miller, Adv. Chem. Phys. 25 (1974) 69.
[26] W.H. Miller, Adv. Chem. Phys. 30 (1975) 77.
[27] M. Gutzwiller, Chaos in classical and quantum mechanics, Springer, 1990 (Chapter 7.5).
[28] Y. Elran, K.G. Kay, J. Chem. Phys. 110 (1999) 8912.
[29] W.H. Press, S.A. Teukolsky, W.T. Vetterling, B.P. Flannery, Numerical Recipes in Fortran 90: The Art of Parallel Scientific Computing, Cambridge University Press, 1997.
[30] M. Nejad-Sattari, T.A. Stephenson, J. Chem. Phys. 106 (1997) 5454.
[31] M.L. González-Martínez, L. Bonnet, P. Larrégaray, J.-C. Rayez, J. Rubayo-Soneira, J. Chem. Phys. 130 (2009) 114103.
[32] M.L. González-Martínez, L. Bonnet, P. Larrégaray, J.-C. Rayez, Phys. Chem. Chem. Phys. 12 (2009) 115.

CHAPTER IV

The semiclassical Wigner method

Summary

The next section introduces the semiclassical Wigner treatment of photodissociations [74] of Brown and Heller, with the inclusion for the first time of rotational motions. An approximate version we called forward II, which is still accurate while numerically much more efficient, is also proposed. At the end of the section, the backward method that results from adding the backward approach introduced in Chapter III with the rigorous Wigner formulation, is presented. The application of all these methods to the triatomic-like model of methyl iodide (CH_3I) photodissociation [72], can be found in Section IV.2.

IV.1 Theoretical introduction

Partial cross section of photodissociation in terms of wavefunctions

In order to introduce the Wigner method, let us go back first to the quantum expression for the partial cross section of photodissociation. We keep considering direct processes and triatomic molecules, as represented in Fig. III.1. Usual Jacobi coordinates $(\boldsymbol{r}, \boldsymbol{R})$ are employed. From the microscopic theory of light-matter interaction, it can be shown that the (v, j) state-resolved absorption cross

section, within the electric dipole approximation, is given by [39]

$$\sigma(E,v,j) \propto \left|\langle \bar{\Psi}_E^{vj}(\boldsymbol{r},\boldsymbol{R})|\boldsymbol{d}\cdot\boldsymbol{e}|\bar{\phi}_0(\boldsymbol{r},\boldsymbol{R})\rangle\right|^2. \tag{IV.1}$$

$\bar{\Psi}_E^{vj}$ is the state of inelastic scattering between AB and C at energy E, in the electronic excited state, and with unit outgoing flux in channel (v,j). $\bar{\phi}_0$ is the rovibrational ground state in the electronic ground state, supposed to be known. Both $\bar{\Psi}_E^{vj}$ and $\bar{\phi}_0$ are defined in the laboratory reference frame. $\boldsymbol{d}$ is transition dipole moment, which in general depends on $\boldsymbol{r}$ and $\boldsymbol{R}$, and $\boldsymbol{e}$ is a unit vector in the direction of the polarization of the electric field of the incident photon.

Let us assume that $\boldsymbol{d}\cdot\boldsymbol{e}$ in Eq. (IV.1) can be replaced by $|\boldsymbol{d}| = d(r,R,\theta)$ at the instant of the laser-induced transition and define

$$\bar{\Phi}_0(\boldsymbol{r},\boldsymbol{R}) = d(r,R,\theta)\bar{\phi}_0(\boldsymbol{r},\boldsymbol{R}). \tag{IV.2}$$

By doing so,

$$\sigma(E,v,j) \propto \left|\int \boldsymbol{dr}\boldsymbol{dR}\, \bar{\Psi}_E^{vj*}(\boldsymbol{r},\boldsymbol{R})\bar{\Phi}_0(\boldsymbol{r},\boldsymbol{R})\right|^2. \tag{IV.3}$$

Let us consider now the following expression of the identity operator

$$\hat{1} = e^{i\hat{\bar{H}}t/\hbar}e^{-i\hat{\bar{H}}t/\hbar}, \tag{IV.4}$$

where $\hat{\bar{H}}$ is quantum Hamiltonian of the excited electronic state in the laboratory frame, given by Eqs. (A.9) and (A.11) from next section[1]. By inserting Eq. (IV.4) into Eq. IV.3,

$$\begin{aligned}\sigma(E,v,j) &\propto \left|\int \boldsymbol{dr}\boldsymbol{dR}\, \bar{\Psi}_E^{vj*}(\boldsymbol{r},\boldsymbol{R})e^{iEt/\hbar}\bar{\Phi}_t(\boldsymbol{r},\boldsymbol{R})\right|^2 \\ &= \left|\int \boldsymbol{dr}\boldsymbol{dR}\, \bar{\Psi}_E^{vj*}(\boldsymbol{r},\boldsymbol{R})\bar{\Phi}_t(\boldsymbol{r},\boldsymbol{R})\right|^2,\end{aligned} \tag{IV.5}$$

where $\bar{\Phi}_t$ is the wave-packet obtained by propagating $\bar{\Phi}_0$ in the electronic excited state during a time t. The unimportant phase factor $e^{iEt/\hbar}$ arises from the fact that $\hat{\bar{H}}\bar{\Psi}_E^{vj} = E\bar{\Psi}_E^{vj}$.

It is shown in Appendix A of the next section, that defining a body-fixed frame where $\boldsymbol{R}$ sets the direction of the Z-axis and expressing accordingly all wavefunctions and operators within that frame, it is possible to rewrite Eq. (IV.5),

[1]References to equations from the next section will be made along this introduction. This introduces no conflict as they are labeled by numbers or capital letters followed by numbers.

for the particular case when $\boldsymbol{J} = \mathbf{0}$, as

$$\sigma(E, v, j) \propto \left| \int dr dR d\theta \sin\theta \, \Psi_E^{vj*}(r, R, \theta) \Phi_t(r, R, \theta) \right|^2 . \tag{IV.6}$$

The wavefunctions of the new frame Ψ_E^{vj*} and Φ_t are related with $\bar{\Psi}_E^{vj*}$ and $\bar{\Phi}_t$ by means of Eqs. (A.3) and (A.4), and naturally have an analogous meaning, *e.g.*, Φ_t is the wave-packet obtained by propagating Φ_0 during t. In addition, Ψ_E^{vj*} satisfies that $\hat{H}\Psi_E^{vj*} = E\Psi_E^{vj*}$, with $\hat{H}$ given by Eqs. (9) and (11).

Assuming that vibrational and rotational motions of BC are uncoupled far in the asymptotic channel, Ψ_E^{vj*} is defined by Eq. (14). Moreover, for $t \to \infty$ the wave-packet Φ_t lies entirely in the product region and is moving outward. Consequently, the overlap in Eq. (IV.6) reduces to

$$\sigma(E, v, j) \propto \lim_{t \to +\infty} \left| \int dr dR d\theta \sin\theta \left[\frac{\mu}{2\pi\hbar^2 k_{vj}} \right]^2 \mathrm{e}^{-ik_{vj}R} \chi_v(r) Y_j^0(\theta) \Phi_t(r, R, \theta) \right|^2 , \tag{IV.7}$$

where χ_v represents the nth vibrational state of BC in the products and Y_j^0 is jth spherical harmonic, defined by Eq. (16). k_{vj} is the wave vector given by

$$k_{vj} = \frac{1}{\hbar} \left[2\mu \left(E - E_{vj} \right) \right]^{1/2} , \tag{IV.8}$$

where E_{vj} is the quantum rovibrational energy of BC in the free products. As χ_v and Y_j^0 are real functions, their complex conjugate superscript has been omitted. In principle, the partial cross section is thus straightforwardly deduced from the (infinite) time-evolved initial wavefunction.

Partial cross section of photodissociation in terms of Wigner functions

The inclusion of the Wigner distribution function into the quasi-classical formalism presented in Chapter III, as a more accurate phase space representation of the initial quantum state, was more than a simple matter of choice. It turns out that a complete equivalent formulation of quantum mechanics exits in terms of Wigner functions. The basic assumption is the existence of a phase space distribution function, $\rho(\boldsymbol{\Gamma})$, associated to each quantum state $\Psi(\boldsymbol{x})$, by means of Eq. (III.2). This classical density is used to find probabilities and expectation values of operators.

The Wigner function satisfies, besides all the properties mentioned in the previous chapter, two crucial additional properties. First, it is possible to show

that [75]

$$\begin{aligned}\frac{\partial \rho}{\partial t} = &- \frac{\partial \mathcal{H}}{\partial \boldsymbol{p}} \frac{\partial \rho}{\partial \boldsymbol{x}} + \frac{\partial \mathcal{H}}{\partial \boldsymbol{x}} \frac{\partial \rho}{\partial \boldsymbol{p}} \\ &- \frac{\hbar^2}{24} \frac{\partial^3 \mathcal{H}}{\partial \boldsymbol{x}^3} \frac{\partial^3 \rho}{\partial \boldsymbol{p}^3} + \frac{\hbar^4}{1920} \frac{\partial^5 \mathcal{H}}{\partial \boldsymbol{x}^5} \frac{\partial^5 \rho}{\partial \boldsymbol{p}^5} + O(\hbar^6) + \ldots ,\end{aligned} \tag{IV.9}$$

where as before $\boldsymbol{x}$ and $\boldsymbol{p}$ comprise respectively all the coordinates and momenta. In the semiclassical limit as $\hbar \to 0$, Eq. (IV.9) reduces to

$$\frac{\partial \rho}{\partial t} = -\frac{\partial \mathcal{H}}{\partial \boldsymbol{p}} \frac{\partial \rho}{\partial \boldsymbol{x}} + \frac{\partial \mathcal{H}}{\partial \boldsymbol{x}} \frac{\partial \rho}{\partial \boldsymbol{p}}, \tag{IV.10}$$

the well-known equation of Liouville's theorem. This means that the time evolution of $\rho(\boldsymbol{\Gamma})$, up to terms of first order in $\hbar$, is ruled by classical mechanics. Also in cases where $\partial^k \mathcal{H}/\partial \boldsymbol{x}^k \equiv \partial^k V/\partial \boldsymbol{x}^k = 0$ with $k \geq 3$, *e.g.*, for quadratic potentials, Eq. (IV.10) reduces to Eq. (IV.9) and the previous statement is rigorously true.

Second, following the same reasoning as in Appendix B from Ref. [64], it is not too difficult to show that a rigorously equivalent phase space integral expression of Eq. (IV.7) is

$$\sigma(E, v, j) \propto \lim_{t \to +\infty} (2\pi\hbar)^3 \int \boldsymbol{d\Gamma} \rho_t(\boldsymbol{\Gamma}) \rho_{tr}(R, P_R) \rho_v(r, P_r) \rho_j(\theta, P_\theta). \tag{IV.11}$$

$\rho_t(\boldsymbol{\Gamma})$ is the Wigner function associated with $\Phi_t(r, R, \theta)$ by Eq. (B.3). $\rho_v(r, P_r)$ and $\rho_j(\theta, P_\theta)$ are the *vibrational* and *rotational Wigner functions* related to $\chi_v(r)$ $Y_j^0(\theta) \sin\theta$, respectively, by means of Eqs. (20) and (21). The *translational Wigner function* can be analytically expressed as

$$\rho_{tr}(R, P_R) = \frac{1}{2\pi\hbar} \delta\left(E_{tr}^c - E_{tr}^q\right) \Theta(P_R) \tag{IV.12}$$

with

$$E_{tr}^c = \frac{P_R^2}{2\mu} \qquad \text{and} \qquad E_{tr}^q = \frac{\hbar^2 k_{vj}^2}{2\mu}, \tag{IV.13}$$

respectively.

In principle, if the Wigner function associated to the initial state, $\rho_0(\boldsymbol{\Gamma}_0)$, is propagated exactly up to $t \to \infty$ by means of Eq. (IV.9), partial cross sections given by Eq. (IV.11) and Eq. (IV.7) have to be strictly the same. Naturally, the practical problem is to find the solution of Eq. (IV.9). Here is when classical mechanics enters into the theory. We showed before that in the semiclassical

limit ($\hbar \to 0$), $\rho(\boldsymbol{\Gamma})$ satisfies Eq. (IV.10). Consequently, we can state that

$$\rho_t(\boldsymbol{\Gamma})\boldsymbol{d\Gamma} = \rho_0(\boldsymbol{\Gamma}_0)\boldsymbol{d\Gamma}_0. \tag{IV.14}$$

Here, $\boldsymbol{\Gamma}$ should be understood as the dynamical state of ABC reached at time t when starting from state $\boldsymbol{\Gamma}_0$ at $t = 0$. Inserting Eq. (IV.14) into Eq. (IV.11),

$$\sigma(E, v, j) \propto \lim_{t\to+\infty} (2\pi\hbar)^3 \int \boldsymbol{d\Gamma}_0 \rho_0(\boldsymbol{\Gamma}_0)\rho_{tr}(R, P_R)\rho_v(r, P_r)\rho_j(\theta, P_\theta). \tag{IV.15}$$

The fundamental drawback of Eq. (IV.15) is that classical mechanics does not propagate correctly the Wigner distribution for large times. This *degrading effect*, discussed to some extent in the next section, is due to the variations of $\rho_v(r, P_r)$ and $\rho_j(\theta, P_\theta)$ along classical orbits, specially the rotational Wigner distribution. To reduce this effect as much as possible, the classical propagation has to be stopped at the exact moment when j_f cease to vary, which corresponds to the instant where the system crosses the frontier separating the interaction region from the free products. This frontier can be defined by a given value R_f of R. Thus, Eq. (IV.7) can be modified as

$$\sigma(E, v, j) \propto (2\pi\hbar)^3 \int \boldsymbol{d\Gamma}_0 \rho_0(\boldsymbol{\Gamma}_0)\rho_{tr}(R_f, P_{Rf})\rho_v(r_f, P_{rf})\rho_j(\theta_f, P_{\theta f}), \tag{IV.16}$$

where $(r_f, \theta_f, P_{rf}, P_{Rf}, P_{\theta f})$ are the values of $(r, \theta, P_r, P_R, P_\theta)$ at $R = R_f$. Inserting the expression for $\rho_{tr}(R_f, P_{Rf})$ into Eq. (IV.16) and omitting the constant factors, finally gives the equation of what we called the *forward I method*,

$$\sigma(E, v, j) \propto \int \boldsymbol{d\Gamma}_0 \rho_0(\boldsymbol{\Gamma}_0)\, \delta\left(E^c_{tr} - E^q_{tr}\right) \Theta(P_{Rf})\rho_v(r_f, P_{rf})\rho_j(\theta_f, P_{\theta f}). \tag{IV.17}$$

In practice, the Dirac function in Eq. (IV.17) is replaced by a narrow bin, *i.e.*,

$$\delta\left(E^c_{tr} - E^q_{tr}\right) \simeq \begin{cases} 1/E^c_{tr}, & \text{if} \quad E^c_{tr} \in [E^q_{tr} - \Delta E_{tr}/2, E^q_{tr} + \Delta E_{tr}/2] \\ 0, & \text{if} \quad E^c_{tr} \notin [E^q_{tr} - \Delta E_{tr}/2, E^q_{tr} + \Delta E_{tr}/2], \end{cases} \tag{IV.18}$$

whose width, ΔE_{tr}, is selected conveniently; and a Monte-Carlo procedure is used to solved the integral, analogous to what has been done in previous chapters. Trajectories are generated according to $\rho_0(\boldsymbol{\Gamma}_0)$ but only those fulfilling Eq. (IV.18) will contribute to the state (v, j), with a weight given by the product of Eq. (IV.18) with the rovibrational Wigner functions $\rho_v(r_f, P_{rf})$ and $\rho_j(\theta_f, P_{\theta f})$. Since not all trajectories contribute to all rovibrational states, condition (IV.18) imposes a clear limitation to the efficiency of the method.

A reasonable approximation of Eq. (IV.17) arises from the fact that the trans-

lational Wigner may be rewritten as

$$\rho_{tr}(R_f, P_{Rf}) = \delta\left[\mathcal{H} - E + E_{vj} - E_{int}(r_f, P_{rf}, P_{\theta f})\right], \tag{IV.19}$$

where E_{vj} and $E_{int}(r_f, P_{rf}, P_{\theta f})$ are the quantum and classical rovibrational energy of BC in the products, respectively. For not too excited rovibrational states, the average difference of these two magnitudes should be negligible as compared to E (see next section), so using

$$\rho_{tr}(R_f, P_{Rf}) = \delta\left(\mathcal{H} - E\right), \tag{IV.20}$$

should not change appreciable the value of $\sigma(E, v, j)$. Replacing Eq. (IV.20) by Eq. (IV.19) in Eq. (IV.17), we have the expression of the *forward II method*

$$\sigma(E, v, j) \propto \int \boldsymbol{d\Gamma}_0 \rho_0(\boldsymbol{\Gamma}_0)\, \delta\left(\mathcal{H} - E\right) \rho_v(r_f, P_{rf}) \rho_j(\theta_f, P_{\theta f}). \tag{IV.21}$$

Trajectories are now selected according to $\rho_0(\boldsymbol{\Gamma}_0)$ but all having the same value of total energy, E. Next section presents an efficient way to do that. The weight of each trajectory to the state (v, j) is given by the product $\rho_v(r_f, P_{rf}) \times \rho_j(\theta_f, P_{\theta f})$; all trajectories contributing to all rovibrational states.

At last, a simple inspection of Eq. (IV.21) shows the similarity with its quasi-classical analogue (III.1). As far as we know, no derivation from first principle of the latter has been reported yet and a proper one by means of Eq. (IV.21) is a work in progress at the moment. From all the previous developments, however, what seems to be correct is to associate the Wigner distribution at $t = 0$ with the product of initial wavefunction multiplied by the transition dipole moment.

Adding the backward approach to the Forward I method

A very interesting result seems to come out by mixing the backward approach of photodissociation presented in Chapter III with the semiclassical expression (IV.17) for the partial cross section. If we keep in mind Eq. (III.4) and together with Eq. (IV.19) we insert them into Eq. (IV.17), then

$$\begin{aligned}\sigma(E, v, j) \propto \int dt d\mathcal{H} dr_f d\theta_f dP_{rf} dP_{\theta f}\ \rho_0\ \rho_v(r_f, P_{rf}) \rho_j(\theta_f, P_{\theta f}) \times \\ \times\ \delta\left[\mathcal{H} - E + E_{vj} - E_{int}(r_f, P_{rf}, P_{\theta f})\right].\end{aligned} \tag{IV.22}$$

Integration over $\mathcal{H}$ leads directly to the expression of the *backward method*

$$\sigma(E, v, j) \propto \int dr_f d\theta_f dP_{rf} dP_{\theta f} \rho_v(r_f, P_{rf}) \rho_j(\theta_f, P_{\theta f}) \int_{-\infty}^{0} dt \rho_0\left[\boldsymbol{\Gamma}(t)\right], \tag{IV.23}$$

where $\mathcal{H}$ is forced to be equal to $E - E_{vj} + E_{int}(r_f, P_{rf}, P_{\theta f})$. Given the fact that in the free products $\mathcal{H} - E_{int}(r_f, P_{rf}, P_{\theta f}) = P_{Rf}^2/2\mu$ and from Eq. (IV.8) $E - E_{vj} = \hbar^2 k_{vj}^2/2\mu$, the constrain on $\mathcal{H}$ is equivalent to set $P_{Rf} = \hbar k_{vj}$. As in the previous chapter, the meaning of $\boldsymbol{\Gamma}(t)$ in Eq. (IV.23) is the dynamical state reached by the system at time t when starting from $\boldsymbol{\Gamma}_f$ at time 0.

In practice, integrals over $(r_f, \theta_f, P_{rf}, P_{\theta f})$ in Eq. (IV.23) are solved by a Monte-Carlo technique, *i.e.*, values of $(r_f, \theta_f, P_{rf}, P_{\theta f})$ are randomly selected within proper boundaries and the integrand $\rho_v(r_f, P_{rf})\rho_j(\theta_f, P_{\theta f}) \int_{-\infty}^{0} dt \rho_0[\boldsymbol{\Gamma}(t)]$ is evaluated for each of them. Consequently, the integral over time needs to be evaluated for each trajectory. That does not present any problem as the quadruplet $(r_f, \theta_f, P_{rf}, P_{\theta f})$, plus R_f and $P_{Rf} = \hbar k_{vj}$, completely define the initial condition of the trajectory. However, the fact that only trajectories starting within some particular phase space regions of the products do actually reach the Wigner region represents a problem. With the help of the forward I method, a practical solution to this issue is explained in the next section, which seems to reduce appreciably the number of trajectories with respect to the forward methods.

The Chapter continues now with the application of the forward I, II and backward methods to the triatomic-like model of methyl iodide (CH_3I) photodissociation [72]. Analytical developments omitted in this introduction can also be found in the next section.

IV.2 Publication

PCCP

RSC Publishing

PERSPECTIVE

New insights into the semiclassical Wigner treatment of photodissociation dynamics

Cite this: *Phys. Chem. Chem. Phys.*, 2013, **15**, 9994

W. Arbelo-González,[ab] L. Bonnet*[a] and A. García-Vela[c]

The *semiclassical Wigner treatment* of Brown and Heller [*J. Chem. Phys.* 1981, **75**, 186] is applied to direct triatomic (or triatomic-like polyatomic) photodissociations with the aim of accurately predicting final state distributions at relatively low computational cost, and having available a powerful interpretative tool. For the first time, the treatment takes rotational motions into account. The proposed formulation closely parallels the quantum description as far as possible. An approximate version is proposed, which is still accurate while numerically much more efficient. In addition to being weighted by usual vibrational Wigner distributions, final phase space states appear to be weighted by new *rotational Wigner distributions*. These densities have remarkable structures clearly showing that classical trajectories most contributing to rotational state j are those reaching the products with a rotational angular momentum close to $[j(j+1)]^{1/2}$ (in $\hbar$ units). The previous methods involve running trajectories from the reagent molecule onto the products. The alternative *backward approach* [L. Bonnet, *J. Chem. Phys.*, 2010, **133**, 174108], in which trajectories are run in the reverse direction, is shown to strongly improve the numerical efficiency of the most rigorous method in addition to being *state-selective*, and thus, ideally suited to the description of state-correlated distributions measured in velocity imaging experiments. The results obtained by means of the previous methods are compared with rigorous quantum results in the case of Guo's triatomic-like model of methyl iodide photodissociation [*J. Chem. Phys.*, 1992, **96**, 6629] and close agreement is found. In comparison, the standard method of Goursaud *et al.* [*J. Chem. Phys.*, 1976, **65**, 5453] is only semi-quantitative.

Received 4th February 2013,
Accepted 2nd May 2013

DOI: 10.1039/c3cp50524c

www.rsc.org/pccp

[a] *CNRS, Univ. Bordeaux, ISM, UMR 5255, 33405, Talence, France. E-mail: l.bonnet@ism.u-bordeaux1.fr*
[b] *Departamento de Física General, Instituto Superior de Tecnologías y Ciencias Aplicadas, Habana 6163, Cuba*
[c] *Instituto de Física Fundamental, C.S.I.C., Serrano 123, 28006 Madrid, Spain*

I. Introduction

Modern molecular beam and spectroscopic techniques allow the measurement of quantum state distributions of photodissociation

W. Arbelo-González

Wilmer Arbelo-González received a MSc (2011) in Physics from the Instituto Superior de Tecnologías y Ciencias Aplicadas (InSTEC), Habana, Cuba. He is currently a PhD student under the supervision of Dr Laurent Bonnet and Prof. Jesus Rubayo-Soneira, sharing his time between Bordeaux University and the InSTEC. His research interests are the classical and semiclassical descriptions of the photodissociation dynamics of molecules and van der Waals clusters.

L. Bonnet

Laurent Bonnet obtained a MSc (1990) and a PhD (1994) in Physics from Bordeaux University, under the guidance of Prof. Jean-Claude Rayez, and was a postdoctoral fellow at Perugia University with Prof. Vincenzo Aquilanti (1995). Since 1996, he has been a CNRS Researcher at Bordeaux University, currently as Directeur de Recherche. He was also a Visiting Associate Professor at Osaka University, in the group of Prof. Toshio Kasai (2003). His research interests are mainly focused on the development of classical, semiclassical and statistical descriptions of molecular reaction dynamics.

products with a high level of precision.[1–5] Accurate theoretical descriptions of the mechanics of molecular fragmentation[6] are thus needed to reproduce and rationalize these data, or predict them when experiments cannot be performed. Beyond their fundamental interest, photodissociation dynamics studies provide very useful data to specialists of planetary atmospheres[7] or interstellar clouds,[8] and they form a branch of molecular physics which has continuously generated technological progress for more than a century.

The goal of the present perspective is to report some new insights into the *semiclassical Wigner treatment*[9,10] of the dynamics of direct triatomic (or triatomic-like polyatomic) photodissociations (see also ref. 6 and 11–18 for related works). In these very common processes, nascent products strongly repel each other after the optical excitation and are completely free in a few tenths of femtoseconds.[6] The practical interest of the semiclassical Wigner method, proposed about three decades ago by Brown and Heller,[9] is that it is found to be more accurate than the earlier and more classical approach of Goursaud *et al.*,[9,11] and leads to calculations much easier to perform than exact quantum calculations.[19–31] As far as polyatomic molecules are concerned, the latter are usually prohibitive and the semiclassical Wigner treatment might thus be an interesting alternative in the future. From the fundamental side, the interpretative power of this approach makes it a powerful tool for rationalizing the dynamics.

The semiclassical Wigner method is based on the notion of *Wigner distribution* associated with a given quantum state.[6,32–39] For a one-dimensional system of configuration coordinate x and conjugate momentum p_x in the state $|\Psi\rangle$, the Wigner distribution is defined as

$$\rho(x,p_x)=\frac{1}{\pi\hbar}\int \mathrm{d}s\, \mathrm{e}^{2ip_xs/\hbar}\langle\Psi|x+s\rangle\langle x-s|\Psi\rangle. \qquad (1)$$

This density was introduced by Wigner in 1932[32] as a convenient tool for quantum mechanically correcting the Gibbs–Boltzmann theory of thermodynamic equilibrium in the limit of small temperatures. Integration of $\rho(x,p_x)$ over p_x leads to $|\langle x|\Psi\rangle|^2$ while integration over x leads to $|\langle p_x|\Psi\rangle|^2$. In addition to that, calling, respectively, H and $\hat{H}$ the classical and quantum Hamiltonians of the system, integration of $\rho(x,p_x)H$ with respect to x and p_x leads to $\langle\Psi|\hat{H}|\Psi\rangle$. One might thus be tempted to call $\rho(x,p_x)$ the phase space distribution corresponding to $|\Psi\rangle$. *Stricto sensu*, however, one should not, for $\rho(x,p_x)$ takes negative values in some parts of the phase space when $\langle x|\Psi\rangle$ (or $\langle p_x|\Psi\rangle$) involves at least one node, and the uncertainty principle puts a shadow on the phase space concept. Nevertheless, one can formally use this non-conventional density of probability as an usual one.

An interesting feature of the semiclassical Wigner treatment is that it mixes the quantum and classical descriptions in a very natural way.[9,10] The underlying principle of the treatment is as follows. The population of a given product quantum state is shown to be proportional to the square modulus of the overlap between (i) the product state wave function, and (ii) the time-evolved wave packet resulting from the propagation of the initial reagent state (multiplied by the transition moment) over a period of time large enough for the whole wave packet to be located in the product channel.[6,9] This expression is then transformed into an overlap between the Wigner distribution corresponding to the product state, and the Wigner distribution associated with the time-evolved wave packet.[9] Everything has been rigorous up to now. What makes the Wigner treatment semiclassical is that the Wigner distribution of the time-evolved wave packet is obtained by propagating in time the Wigner density of the initial reagent state according to the laws of classical mechanics,[9] just as if this density was a solution of the Liouville equation.[40] To recap, initial and final dynamical states (phase space points) are assigned statistical weights according to quantum mechanics through Wigner distributions while nuclear dynamics are ruled by classical mechanics. The corresponding mathematical developments are given in Section IIA. In this approach, trajectories are run forward in time from the reagent molecule onto the separated products. We shall call it *forward I*.

In the only two applications of the semiclassical Wigner method that seem to have been published to date,[9,10] rotational motions were frozen. In the present work, however, we take into account the full-dimensionality of the triatomic system, making thereby the method applicable to processes taking place under realistic conditions.

In addition to the usual vibrational Wigner distributions,[6,9,10,12,13,35–38] the method involves *rotational Wigner distributions* which, to our knowledge, are introduced for the first time in the context of reaction dynamics. These quantities are, respectively, discussed in Sections IIB and IIC. Rotational Wigner distributions have remarkable structures clearly showing that the classical trajectories most contributing to rotational state j are those reaching the products with a rotational angular momentum close to $[j(j+1)]^{1/2}$ (in $\hbar$ units).

The study of a Franck–Condon model process in Section IID allows us to illustrate how the *degrading effect*, discussed by

A. García-Vela

Alberto García-Vela carried out his PhD thesis at Consejo Superior de Investigaciones Científicas (CSIC) in Madrid (Spain) in the field of theoretical Chemical Physics, receiving the PhD in 1989. Then he spent about three years working with R. B. Gerber at the Hebrew University of Jerusalem and at the University of California, Irvine. After that he got a senior researcher permanent position of Científico Titular at CSIC in Madrid in 1993, being promoted later in 2007 to the position of Investigador Científico. His research involves the study of photodissociation of small clusters and molecules, and the design of control methods.

Gray and Truhlar[13] and Schinke *et al.*,[10] alters state-resolved cross sections en route to products. This effect is related to the inability of classical mechanics to propagate Wigner densities for a long period of time when the potential energy is anharmonic. A slight formal modification of the forward I method is then suggested in order to greatly improve its accuracy.

Nevertheless, this method turns out to have a limited numerical efficiency. An approximation is thus proposed in Section IIE in order to strongly increase it. The resulting method will be called *forward II*.

The recent *backward approach*,[16–18] in which trajectories are run from the products onto the reagent molecule, is shown in Section III to be strictly equivalent to the forward I method while being numerically much more efficient. In addition to that, it is *state-selective*, and thus, ideally suited to the description of state-correlated distributions measured in velocity imaging experiments.[1–5]

Since we shall also apply the standard method of Goursaud *et al.*,[11] we briefly recall its main lines in Section IV.

The results obtained by means of the two forward methods and the backward one are compared in Section V with rigorous quantum results[26,30] in the case of the triatomic-like model of methyl iodide photodissociation of Guo,[41] and very good – often quantitative – agreement is found. In comparison, the method of Goursaud *et al.*[11] is only semi-quantitative, at least for one of the two excited electronic states involved in the process, within which the system has a more quantum-like behavior. In particular, this approach does not allow us to systematically reproduce inverted vibrational or rotational state populations, contrary to the semiclassical Wigner treatment. Section VI concludes.

II. Forward semiclassical Wigner approach

A. Accurate formulation

1. System. Let us consider a triatomic molecule ABC optically excited by a photon of energy $h\nu$ from its rovibronic ground state at energy E_0 up to a given repulsive excited electronic state. The future products, say AB and C, strongly repel each other immediately after the photon absorption and are formed in a few tenths of femtoseconds. The dissociation is thus direct. The total energy of ABC is $E = E_0 + h\nu$. The optical excitation is supposed not to excite the rotational motion. Within the framework of this reasonable approximation, the total angular momentum J is kept at 0 throughout the whole fragmentation process (see ref. 6, 19, 21, 23 and 24 for rigorous treatments of the possible rotational transitions implied by the optical excitation). $\boldsymbol{R}$ is the vector going from the center-of-mass G of AB to C and $\boldsymbol{r}$ is the one from A to B. V_g and V_e are the potential energies in the ground and excited electronic states, respectively. $\hat{V}_g$ and $\hat{V}_e$ are their corresponding operators and $\hat{\bar{H}}_e$ is the Hamiltonian in the excited electronic state. V_g and V_e both depend on the moduli R and r of $\boldsymbol{R}$ and $\boldsymbol{r}$ and the angle θ between them. P, p and P_θ are the momenta conjugate to R, r and θ, respectively. Far in the asymptotic channel, V_e reduces to the potential energy of the free AB diatom, denoted $v_e(r)$. The zero of energy is defined as the minimum of V_e, or $v_e(r)$, in the separated products. m and μ are, respectively, the reduced masses of AB and C with respect to AB. $\boldsymbol{d} \equiv \boldsymbol{d}(\boldsymbol{R},\boldsymbol{r})$ is the transition dipole vector responsible for the electronic transition,[6] and $\boldsymbol{e}$ is a unit vector in the direction of the polarization of the electric field of the photon. The final quantum state of AB is denoted (n,j), where n and j are the vibrational and rotational quantum numbers, respectively.

2. Quantum partial cross section and product state distribution. Within the electric dipole approximation, the (n,j) state-resolved, or partial, absorption cross section is shown in ref. 6 to be given by

$$\sigma_E^{nj} = \left| \langle \bar{\Psi}_E^{nj} | \boldsymbol{d} \cdot \boldsymbol{e} | \bar{\phi}_0 \rangle \right|^2. \tag{2}$$

$|\bar{\Psi}_E^{nj}\rangle$ is the state of inelastic scattering between AB and C at energy E, in the electronic excited state, and with unit outgoing flux in channel (n,j). $|\bar{\phi}_0\rangle$ is the rovibrational ground state in the electronic ground state. $|\bar{\phi}_0\rangle$ is supposed to be known. Final state populations are deduced from eqn (2) according to

$$P_E^{nj} = \frac{\sigma_E^{nj}}{\sum_{n,j} \sigma_E^{nj}}. \tag{3}$$

A very common approximation adopted here consists of replacing in eqn (2) $\boldsymbol{d}\cdot\boldsymbol{e}$ by the modulus d of $\boldsymbol{d}$, which amounts to suppose that $\boldsymbol{d}$ is parallel to $\boldsymbol{e}$ at the instant of the photon absorption. This approximation appears to be very satisfying provided that one is not interested in vector properties.[6,26,30,41–43] $\boldsymbol{d}$ is either parallel or perpendicular to the triatomic plane and d does only depend on the configuration of ABC, *i.e.*, $d \equiv d(R,r,\theta)$.

3. Quantum partial cross section in terms of the time-evolved initial state. Setting

$$\bar{\Phi}_0(\boldsymbol{R},\boldsymbol{r}) = d(R,r,\theta)\bar{\phi}_0(\boldsymbol{R},\boldsymbol{r}), \tag{4}$$

eqn (2) reads

$$\sigma_E^{nj} = \left| \int \mathbf{d}\boldsymbol{R}\, \mathbf{d}\boldsymbol{r}\; \bar{\Psi}_E^{nj*}(\boldsymbol{R},\boldsymbol{r})\bar{\Phi}_0(\boldsymbol{R},\boldsymbol{r}) \right|^2. \tag{5}$$

Writing the identity operator as

$$\hat{1} = e^{i\hat{\bar{H}}_e t/\hbar} e^{-i\hat{\bar{H}}_e t/\hbar} \tag{6}$$

where the optical excitation defines the origin of time, and inserting this operator between the two states in eqn (5) leads to

$$\sigma_E^{nj} = \left| \int \mathbf{d}\boldsymbol{R}\, \mathbf{d}\boldsymbol{r}\; \bar{\Psi}_E^{nj*}(\boldsymbol{R},\boldsymbol{r}) e^{iEt/\hbar} \bar{\Phi}_t(\boldsymbol{R},\boldsymbol{r}) \right|^2. \tag{7}$$

The phase factor $e^{iEt/\hbar}$ arises from the fact that $|\bar{\Psi}_E^{nj}\rangle$ is a stationary state of the system in the electronic excited state. This factor is only written for the sake of clarity, since its modulus is equal to one. $\bar{\Phi}_t(\boldsymbol{R},\boldsymbol{r})$ is the wave-packet obtained by propagating $\bar{\Phi}_0(\boldsymbol{R},\boldsymbol{r})$ in the electronic excited state during t.

It is shown in Appendix A that eqn (7) can be rewritten as

$$\sigma_E^{nj} = \left| \int \mathrm{d}R\,\mathrm{d}r\,\mathrm{d}\theta \sin\theta \Psi_E^{nj*}(R,r,\theta)\Phi_t(R,r,\theta) \right|^2 \quad (8)$$

where $\Psi_E^{nj}(R,r,\theta) = 8^{1/2}\pi R r \bar{\Psi}_E^{nj}(\boldsymbol{R},\boldsymbol{r})$ and $\Phi_t(R,r,\theta) = 8^{1/2}\pi R r \bar{\Phi}_t(\boldsymbol{R},\boldsymbol{r})$. $\Psi_E^{nj}(R,r,\theta)$ and $\Phi_t(R,r,\theta)$ are shown in the same appendix to satisfy the Schrödinger equations

$$\hat{H}_e \Psi_E^{nj} = [\hat{T} + \hat{V}_e]\Psi_E^{nj} = E\Psi_E^{nj} \quad (9)$$

and

$$i\hbar \frac{\mathrm{d}\Phi_t}{\mathrm{d}t} = \hat{H}_e \Phi_t, \quad (10)$$

with

$$\hat{T} = -\frac{\hbar^2}{2\mu}\frac{\partial^2}{\partial R^2} - \frac{\hbar^2}{2m}\frac{\partial^2}{\partial r^2} - \frac{\hbar^2}{2I\sin\theta}\frac{\partial}{\partial\theta}\sin\theta\frac{\partial}{\partial\theta}. \quad (11)$$

I is the reduced moment of inertia given by eqn (A.12).

$\Phi_t(R,r,\theta)$ is the wave-packet obtained by propagating $\Phi_0(R,r,\theta)$ during t. Setting $\phi_0(R,r,\theta) = 8^{1/2}\pi R r \bar{\phi}_0(\boldsymbol{R},\boldsymbol{r})$, we deduce from eqn (4) and (A.5) at $t = 0$, the identity

$$\Phi_0(R,r,\theta) = \mathrm{d}(R,r,\theta)\phi_0(R,r,\theta). \quad (12)$$

$\phi_0(R,r,\theta)$ is the solution of

$$\hat{H}_g\phi_0 = [\hat{T} + \hat{V}_g]\phi_0 = E_0\phi_0. \quad (13)$$

Far in the asymptotic channel, the general expression of $\Psi_E^{nj}(R,r,\theta)$ is

$$\Psi_E^{nj}(R,r,\theta) = \left[\frac{\mu}{2\pi\hbar^2 k_{nj}}\right]^{1/2} \mathrm{e}^{ik_{nj}R}\chi_n(r)\,Y_j^0(\theta) + \sum_{n'j'} S_{njn'j'}\left[\frac{\mu}{2\pi\hbar^2 k_{n'j'}}\right]^{1/2} \mathrm{e}^{-ik_{n'j'}R}\chi_{n'}(r)\,Y_{j'}^0(\theta). \quad (14)$$

This expression assumes that the vibrational and rotational motions of AB are uncoupled, a good approximation provided that too highly excited rovibrational states are not available. k_{nj} is defined by

$$k_{nj} = \frac{1}{\hbar}\left[2\mu\left(E - E_{nj}\right)\right]^{1/2} \quad (15)$$

where E_{nj} is the internal energy of AB in state (n,j). $\chi_n(r)$ is the nth excited vibrational state, and $Y_j^0(\theta)$ is the jth spherical harmonic defined by

$$Y_j^0(\theta) = \left[\frac{2j+1}{4\pi}\right]^{1/2} P_j(\cos\theta). \quad (16)$$

$P_j(x)$ is the jth Legendre polynomial. The S-matrix element $S_{njn'j'}$ is the probability amplitude to go from (n',j') to (n,j). The $\Psi_E^{nj}(R,r,\theta)$s satisfy the usual orthogonality relations.

For t tending to $+\infty$, $\Phi_t(R,r,\theta)$ entirely lies in the product channel and moves outwards. The overlap in eqn (8) between the incoming part of $\Psi_E^{nj}(R,r,\theta)$ (see eqn (14)) and $\Phi_t(R,r,\theta)$ is thus zero. Hence, eqn (8) becomes

$$\sigma_E^{nj} = \lim_{t\to+\infty}\left| \int \mathrm{d}R\mathrm{d}r\mathrm{d}\theta \sin\theta \left[\frac{\mu}{2\pi\hbar^2 k_{nj}}\right]^{1/2} \mathrm{e}^{-ik_{nj}R}\chi_n(r)\,Y_j^0(\theta)\Phi_t(R,r,\theta) \right|^2 \quad (17)$$

($\chi_n(r)$ and $Y_j^0(\theta)$ being real functions, they are equal to their complex conjugate). In principle, the partial cross section is thus straightforwardly deduced from the (infinite) time-evolved initial state.

4. Quantum partial cross section in terms of Wigner densities. It is shown in Appendix B that a strictly equivalent phase space integral expression of eqn (17) is

$$\sigma_E^{nj} = \lim_{t\to+\infty}(2\pi\hbar)^3 \int \mathbf{d}\boldsymbol{\Gamma}\rho_t(\boldsymbol{\Gamma})\rho_{\mathrm{tr}}(R,P)\rho_n(r,p)\rho_j(\theta,P_\theta) \quad (18)$$

with $\boldsymbol{\Gamma} = (R,r,\theta,P,p,P_\theta)$. $\rho_t(\boldsymbol{\Gamma})$ is the Wigner density related to $\Phi_t(R,r,\theta)$ through eqn (B.3). $\rho_{\mathrm{tr}}(R,P)$, $\rho_n(r,p)$ and $\rho_j(\theta,P_\theta)$, respectively, called translational, vibrational and rotational Wigner distributions, are given by

$$\rho_{\mathrm{tr}}(R,P) = \frac{1}{2\pi\hbar}\delta\left[\frac{P^2}{2\mu} - \frac{\hbar^2 k_{nj}^2}{2\mu}\right]\Theta(P), \quad (19)$$

$$\rho_n(r,p) = \frac{1}{\pi\hbar}\int \mathrm{d}s\ \mathrm{e}^{2ips/\hbar}\chi_n(r+s)\chi_n(r-s) \quad (20)$$

and

$$\rho_j(\theta,P_\theta) = \frac{1}{\pi\hbar}\int \mathrm{d}s\ \mathrm{e}^{2iP_\theta s/\hbar}\sin(\theta+s)\,Y_j^0(\theta+s) \times \sin(\theta-s)\,Y_j^0(\theta-s). \quad (21)$$

The present expression of $\rho_{\mathrm{tr}}(R,P)$ (eqn (19)) appears to be different from the one in ref. 9 and 10, due to different normalizations of translational states in eqn (14). $\rho_n(r,p)$ and $\rho_j(\theta,P_\theta)$ are discussed in Sections IIB and C. The argument of Y_j^0 being limited to the range $[0,\pi]$, the constraints on s in eqn (21) are $-\theta \le s \le \pi - \theta$ and $\theta - \pi \le s \le \theta$, or

$$\max[-\theta,\theta-\pi] \le s \le \min[\theta,\pi-\theta]. \quad (22)$$

5. Passage to the semiclassical description. We now introduce in the previous rigorous quantum formulation the following classical ingredient: we consider $\rho_\tau(\boldsymbol{\Gamma})$ as a solution of the Liouville equation,[40] *i.e.*, we classically propagate it from $\tau = 0$ to $\tau = t$. In the framework of this assumption, we have

$$\rho_t(\boldsymbol{\Gamma})\mathbf{d}\boldsymbol{\Gamma} = \rho_0(\boldsymbol{\Gamma}_0)\mathbf{d}\boldsymbol{\Gamma}_0. \quad (23)$$

In this identity, $\boldsymbol{\Gamma}$ should be understood as the dynamical state of ABC reached at time t when starting from state $\boldsymbol{\Gamma}_0$ at time 0. Eqn (23) expresses the fact that the probability to lie within $\mathbf{d}\boldsymbol{\Gamma}$ does not depend on t, a property due to the deterministic nature of classical mechanics. For the sake of

clarity, the components of $\boldsymbol{\Gamma}$ will be called $(R_t,r_t,\theta_t,P_t,p_t,P_{\theta_t})$ in the rest of this section. In practice, they are determined by solving the Hamilton equations given in chapter 5 of Schinke's book[6] (see eqn (5.3) and (5.4) where m, μ, V and γ are here denoted μ, m, V_e and θ, respectively; these equations are clearly the classical analogs of the present eqn (9) and (11)). Hamilton equations involve the classical Hamiltonian

$$H_e = \frac{P^2}{2\mu} + \frac{p^2}{2m} + \frac{P_\theta^2}{2I} + V_e(R,r,\theta) \tag{24}$$

needed in the following.

Eqn (18) and (23) finally lead to the semiclassical Wigner expression of Brown and Heller[9,10]

$$\sigma_E^{nj} = \lim_{t\to+\infty} (2\pi\hbar)^3 \int \mathbf{d}\boldsymbol{\Gamma_0}\, \rho_0(\boldsymbol{\Gamma_0})\rho_{tr}(R_t,P_t)\rho_n(r_t,p_t)\rho_j(\theta_t,P_{\theta_t}), \tag{25}$$

except that here, the rotational motion of AB is taken into account. We shall however see in Section IID that a slight formal modification of this expression strongly improves its accuracy.

A comment on θ_t is in order. As previously seen, $Y_j^0(\theta_t)$ is only defined for θ_t in the range $[0,\pi]$, and we shall see later below (Section IIC) that this is also the case of $\rho_j(\theta_t,P_{\theta_t})$. However, θ_t is a (roughly) linear function of time in the asymptotic channel (see Section IID) and thus, it eventually gets out of the previous interval. Replacing θ_t in eqn (25) by

$$\theta = \theta_t - \pi\,\mathrm{int}(\theta_t/\pi) \tag{26}$$

if $\mathrm{int}(\theta_t/\pi)$ is even, or

$$\theta = \pi - [\theta_t - \pi\,\mathrm{int}(\theta_t/\pi)] \tag{27}$$

if $\mathrm{int}(\theta_t/\pi)$ is odd, keeps the ABC configuration unchanged and constraints θ to belong to the range $[0,\pi]$.

A careful reading of Appendix B allows us to conclude that eqn (18) is still exact when $\rho_t(\boldsymbol{\Gamma})$ is the Wigner distribution associated with $(\sin\theta)^\lambda\Phi_t(R,r,\theta)$ (instead of $\Phi_t(R,r,\theta)$ alone) and $\rho_j(\theta,P_\theta)$ is the one corresponding to $(\sin\theta)^{1-\lambda}Y_j^0(\theta)$ (instead of $\sin\theta Y_j^0(\theta)$). But the only relevant choice is the one previously made, *i.e.* $\lambda = 0$, for the following reason. Eqn (25) assumes that $\rho_t(\boldsymbol{\Gamma})$ is well approximated by classically propagating $\rho_0(\boldsymbol{\Gamma}_0)$ during t. If $\rho_t(\boldsymbol{\Gamma})$ is taken to be the Wigner function associated with $\Phi_t(R,r,\theta)$, $\rho_0(\boldsymbol{\Gamma}_0)$ is then the Wigner function corresponding to the initial state $\Phi_0(R,r,\theta)$, supposed to be known. But if $\rho_t(\boldsymbol{\Gamma})$ is taken to be the Wigner function associated with $(\sin\theta)^\lambda\Phi_t(R,r,\theta)$, $\rho_0(\boldsymbol{\Gamma}_0)$ turns out to be the Wigner distribution corresponding to an unknown function (certainly not $(\sin\theta)^\lambda\Phi_0(R,r,\theta)$!). In such a case, $\rho_0(\boldsymbol{\Gamma}_0)$ is also unknown and $\rho_t(\boldsymbol{\Gamma}_0)$ cannot be estimated classical mechanically.

B. Vibrational Wigner densities

Vibrational Wigner densities have been discussed elsewhere, in particular for the harmonic and Morse oscillators.[6,37,38] Therefore, we only concentrate on those involved in the process studied later in this work in order to check the validity of the semiclassical Wigner method, *i.e.*, the triatomic-like model of methyl iodide photodissociation of Guo.[41]

In this model, the vibrational motion of the methyl radical CH_3 is reduced to its umbrella mode, treated as if this was the stretching mode of a pseudo diatomic molecule. The coordinate r is between the carbon atom and the center-of-mass of the three hydrogen atoms, assuming the C_{3v} symmetry of CH_3 is preserved throughout the whole process. This is illustrated in Fig. 1. The potential energy $v_e(r)$, corresponding to CH_3 far away from I, is represented in the same figure together with its second order expansion. r = 0 corresponds to the planar geometry of CH_3 and for an obvious reason of symmetry, $v_e(r)$ is even. $v_e(r)$ clearly appears to be strongly anharmonic with a significant contribution from a fourth order term.

The first vibrational states have been calculated by means of the Truhlar–Numerov algorithm[44] and perspective views of the resulting Wigner distributions, estimated from eqn (20) over a regular 100 × 100 grid, are displayed in Fig. 2 for the levels n = 0–5. The r and p axis are directed towards the right and left, respectively. r belongs to the range $[-1.2,1.2]$ and p to the range $[-12,12]$, both in atomic units. Despite the strong anharmonicity of $v_e(r)$, the shape similarity with the Wigner distributions of the harmonic oscillator is striking.[6,38]

While for n = 0, the Wigner density is always positive, it takes negative values for $n \geq 1$ in the crater-like areas. Craters are delimited by cones on the edge of which small summits are visible, particularly for $n \geq 3$. Contrary to the harmonic case, contour levels do not exactly correspond to classical orbits, especially in the vicinity of the edge.[45] This is at the origin of the degrading effect,[10,13] as discussed further below. This effect will however appear to be much stronger in the case of the rotational motion.

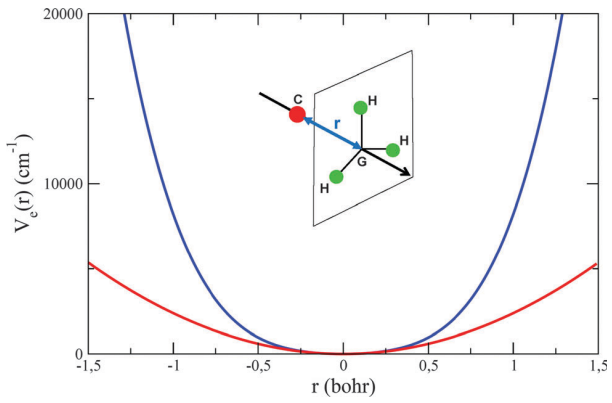

Fig. 1 The methyl radical is represented in C_{3v} symmetry. G is the center-of-mass of the three H atoms. The r coordinate represents the position of G with respect to the C atom along the symmetry axis of CH_3. Blue curve: r-dependence, in the $^1Q_1$ electronic state, of the potential energy in the separated products ($R \geq$ 12 bohr) for the reduced dimensionality model of methyl iodide photodissociation of Guo[41] which assumes that the C_{3v} symmetry of CH_3 is conserved throughout the fragmentation. Its shape is the same in the $^3Q_0$ electronic state, with the difference that the bottom of the well is 7603.92 cm^{-1} higher. Red curve: second order expansion of the previous potential.

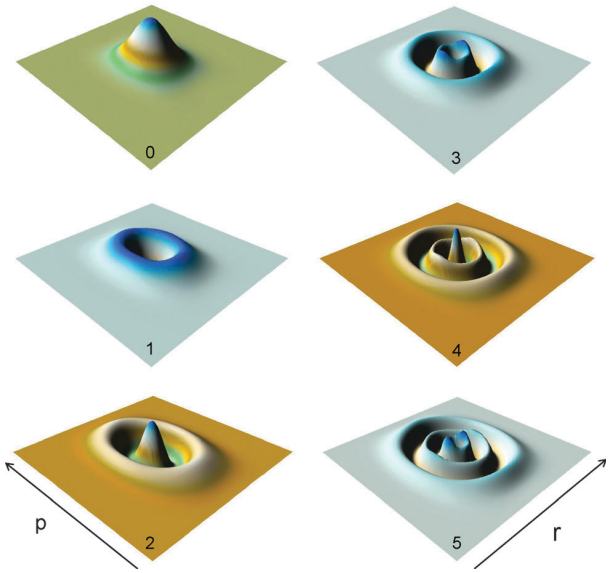

Fig. 2 Perspective views of the vibrational Wigner distributions for the levels n = 0–5 for the potential energy shown in Fig. 1 (blue curve). The r and p axis are directed towards the right and left, respectively. r belongs to the range [−1.2,1.2], and p to the range [−12,12], in atomic units.

C. Rotational Wigner densities

Perspective views of $\rho_j(\theta,P_\theta)$, estimated from eqn (21) over a regular 100 × 100 grid, are shown in Fig. 3 for j = 0–3, 6 and 10. The θ and P_θ axis are oriented towards the right and left, respectively. θ belongs to the range [0,π], and P_θ to the range $[-15\hbar,15\hbar]$.

At first sight, $\rho_j(\theta,P_\theta)$ appears to involve j narrow wells along the symmetry axis of the distribution defined by P_θ = 0,

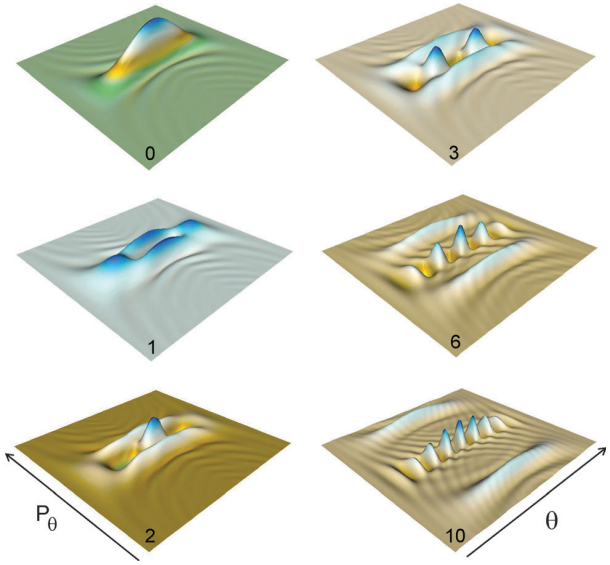

Fig. 3 Perspective views of the rotational Wigner distributions for the states j = 0–3, 6 and 10. The θ and P_θ axis are oriented towards the right and left, respectively. θ belongs to the range [0,π], and P_θ to the range $[-15\hbar,15\hbar]$.

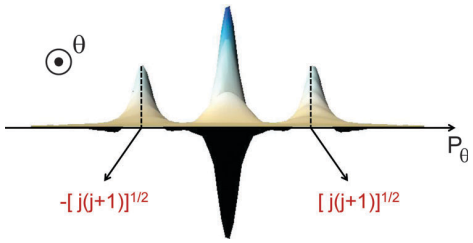

Fig. 4 Front view of $\rho_6(\theta,P_\theta)$ along the θ-axis, directed towards us. The wells along the symmetry axis of the distribution correspond to negative peaks, not visible in Fig. 3, having magnitudes comparable with those of the positive peaks. They form the black downward peak, resulting from the alignment of 6 peaks. The two lateral peaks, forming ridges along the θ-axis, have been found to be approximately centered at $\pm[j(j+1)]^{1/2}$ in $\hbar$ units.

separated by $j-1$ peaks (the second part of this statement is not true for j = 0). These wells are in fact negative peaks with magnitudes comparable with the ones of positive peaks. This is clearly seen in Fig. 4 where a front view of $\rho_6(\theta,P_\theta)$ along the θ-direction is displayed. In this complementary view where the previous peaks are aligned, positive ones are in the light while negative ones are in the shadow. We shall call this chain of alternatively positive and negative spikes central peaks. In addition, $\rho_j(\theta,P_\theta)$ for $j \neq 0$ involves two positive lateral ridges parallel to the θ-axis (note that for j = 0, the two lateral ridges have merged with the central peak). As indicated in Fig. 4, the summits of these ridges, located along the line $\theta = \pi/2$, appear to be roughly defined by $P_\theta \approx \pm\hbar[j(j+1)]^{1/2}$ in the upper and lower half plane, respectively. This is actually true only for large js, as illustrated in Fig. 5 where the difference between (i) the exact value of P_θ corresponding to the summit in the upper half plane and (ii) the quantum value $\hbar[j(j+1)]^{1/2}$ is seen to decrease to 0 in terms of j.

For completeness, the semiclassical limit of the rotational Wigner density is considered in Appendix C. The interest of this limit is that it clearly explains the main topological features of $\rho_j(\theta,P_\theta)$ outlined above. Moreover, it provides analytical

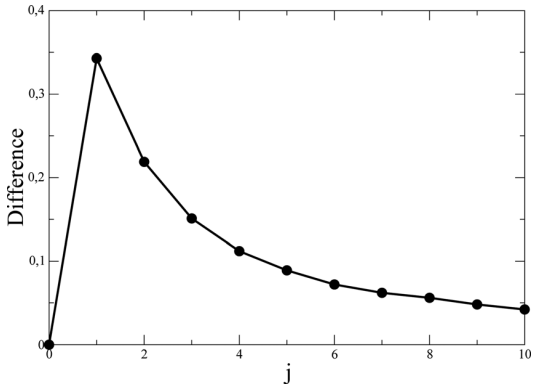

Fig. 5 The difference between (i) the exact value of P_θ corresponding to the summit of the rotational Wigner density in the upper half plane and (ii) the quantum value $\hbar[j(j+1)]^{1/2}$ tends to 0 as j takes large values. In the particular case where j = 0, the lateral ridges have merged with the central peak, and their top is rigorously at the expected quantum value, *i.e.*, 0.

expressions which prove to be useful to make the link between the semiclassical Wigner treatment and the method of Goursaud *et al.*[11] The study of this link will be published elsewhere.[46]

Due to the sign alternation of central peaks, their contribution to σ_E^{nj}, given by eqn (25), is expected to be negligible as compared to the one of lateral ridges provided that the distribution of the points (θ_t,P_{θ_t}) overlaps several central peaks. In the semiclassical limit of large js where the central peaks become very sharp (see $\rho_{10}(\theta,P_\theta)$ in Fig. 3), this will necessarily be the case. Consequently, one recovers the well known semiclassical rule stating that the values of P_θ close to $\pm\hbar[j(j+1)]^{1/2} \approx \pm\hbar(j+1/2)$ mostly contribute to the population of the jth rotational state. Conversely, the contribution of central peaks to σ_E^{nj} for j = 1–3 cannot be excluded and the semiclassical rule fails (in the case where $j = 0$, the semiclassical rule works for the trivial reason that there is only one central massif).

In the next two paragraphs where vibrational and rotational Wigner distributions are compared, we use the quantum number j for both densities (and for the vibrational eigenstate as well). The vibrational density $\rho_j(r,p)$ and its rotational analog $\rho_j(\theta,P_\theta)$ are then differentiated by their arguments only.

The functions $\sin\theta Y_0^0(\theta)$ and $\sin\theta Y_1^0(\theta)$ are proportional to $\sin\theta$ and $\sin\theta\cos\theta$, respectively. Topologically, these two functions are not very different from the ground and first excited vibrational states of a diatom. This is the reason why they result in densities $\rho_0(\theta,P_\theta)$ and $\rho_1(\theta,P_\theta)$ bearing strong similarities with $\rho_0(r,p)$ and $\rho_1(r,p)$, respectively. This is clearly seen when comparing Fig. 2 and 3. For the ground states, both densities are bell-shaped and for the first excited states, they both involve a crater with small summits lying on its edge (smaller for the vibrational density than for the rotational one).

On the other hand, $\sin\theta Y_j^0(\theta)$ is significantly different from $\chi_j(r)$ for $j \geq 2$, in particular because of the $\sin\theta$ term which makes the oscillation amplitude of $\sin\theta Y_j^0(\theta)$ decrease when going away from $\pi/2$ (see Appendix C) while the one of $\chi_j(r)$ tends to increase when going away from the equilibrium geometry (at least up to the classical turning points). Consequently, $\rho_j(\theta,P_\theta)$ appears to be very different from $\rho_j(r,p)$ for $j \geq 2$, as can be observed when comparing Fig. 2 and 3.

For the free rotor, P_θ is a constant of motion and classical orbits are defined by straight lines parallel to the θ-axis. It is thus clear from Fig. 3 that the rotational Wigner density strongly varies along a classical orbit, a fact responsible for the degrading effect, as shown in the next section. Note that the amplitude of the previous variation is much stronger than for the vibrational motion. On average, classical orbits may indeed be shown to be much closer to contour levels for the vibrational Wigner density than for the rotational one.

The Wigner distribution of a rigid rotator has already been discussed in ref. 47. However, the context is quite different, hence leading to a different mathematical definition of the distribution. In addition, it seems that the notion of rotational Wigner density has never been introduced in the reaction dynamics field to date (it is noted, however, that another type of rotational phase space distribution (a non-Wigner one) was previously used to represent the initial state of a system in the framework of photodissociation dynamics[48]). Lastly, we note the shape similarity between the present rotational Wigner distributions and those for a symmetric infinite square well potential (compare Fig. 1 in ref. 36 and Fig. 3 and 10 in the present work).

D. Franck–Condon process

1. System. We now assume that V_e is isotropic, *i.e.*, it does not depend on θ. Moreover, we freeze the AB vibrational motion for the sake of simplicity. AB is thus a rigid rotor the length of which is denoted r_e. In addition, the reduced moment of inertia I, given by eqn (A.12), is supposed to reduce to mr_e^2. This is a good approximation, since generally, R is already larger than r_e at time 0, and unless C is much lighter than both A and B, μ is also larger than m. Lastly, the transition dipole moment is kept at a constant value.

2. Degrading effect. Following the developments of Section IIA, the j state-resolved absorption cross section is proportional to

$$\sigma_E^j = \left| \int \mathrm{d}R\mathrm{d}\theta \ \sin\theta \Psi_E^{j*}(R,\theta)\Phi_0(R,\theta) \right|^2 \tag{28}$$

(see eqn (8) at time 0 without the r coordinate). Due to the isotropy of V_e which makes the radial and angular motions uncoupled, the scattering state $\Psi_E^j(R,\theta)$ can be written as

$$\Psi_E^j(R,\theta) = U_E(R)Y_j^0(\theta). \tag{29}$$

Asymptotically,

$$U_E(R) = \left[\frac{\mu}{2\pi\hbar^2 k_j}\right]^{1/2} \left(\mathrm{e}^{ik_jR} + \mathrm{e}^{i\eta - ik_jR}\right) \tag{30}$$

with

$$k_j = \frac{1}{\hbar}\left[2\mu\left(E - \frac{\hbar^2 j(j+1)}{2mr_e^2}\right)\right]^{1/2}. \tag{31}$$

η is the phase shift. We shall suppose that V_e is sufficiently repulsive for the final translational energy to be much larger than the rotational energy $\hbar^2 j(j+1)/(2mr_e^2)$. In other words, the product energy E is mainly deposited into the translation motion and the rotational energy is negligible as compared to E. Hence, k_j, and consequently $U_E(R)$, do not depend on j in practice. Using eqn (29) and following the developments of Appendix B, we can rewrite eqn (28) as

$$\sigma_E^j = (2\pi\hbar)^2 \int \mathrm{d}R\mathrm{d}\theta\mathrm{d}P\mathrm{d}P_\theta \ \rho_0(R,\theta,P,P_\theta)\rho_U(R,P)\rho_j(\theta,P_\theta). \tag{32}$$

$\rho_0(R,\theta,P,P_\theta)$ and $\rho_U(R,P)$ are the Wigner distributions associated with $\Phi_0(R,\theta)$ and $U_E(R)$, respectively, and $\rho_j(\theta,P_\theta)$ has already been introduced.

Within the harmonic approximation of V_g, $\rho_0(R,\theta,P,P_\theta)$ is found from eqn (5.20) of ref. 6 to have the form

$$\rho_0(R,\theta,P,P_\theta) = \frac{1}{(\pi\hbar)^2} e^{-2\alpha_R(R-R_e)^2/\hbar} e^{-P^2/(2\alpha_R\hbar)^2} \times e^{-2\alpha_\theta(\theta-\theta_e)^2/\hbar} e^{-P_\theta^2/(2\alpha_\theta\hbar)^2}, \quad (33)$$

where R_e and θ_e define the equilibrium geometry of the system in the electronic ground state. Consequently, σ_E^j becomes

$$\sigma_E^j \propto I_1 I_2 \quad (34)$$

with

$$I_1 = \int dR dP\, e^{-2\alpha_R(R-R_e)^2/\hbar} e^{-P^2/(2\alpha_R\hbar)^2} \rho_U(R,P) \quad (35)$$

and

$$I_2 = \int d\theta dP_\theta\, e^{-2\alpha_\theta(\theta-\theta_e)^2/\hbar} e^{-P_\theta^2/(2\alpha_\theta\hbar)^2} \rho_j(\theta,P_\theta). \quad (36)$$

I_2 is the equivalent, within the Wigner formalism, of a rotational Franck–Condon factor.

Since $U_E(R)$, and consequently $\rho_U(R,P)$, do not depend on j, the j dependence of σ_E^j is only due to I_2. Therefore, I_1 can be transferred into the proportionality factor of eqn (34), hence leading to

$$\sigma_E^j \propto I_2. \quad (37)$$

With $\alpha_\theta = 5$, corresponding to an initial angular distribution spreading over $\sim$20 degrees, and $\theta_e = 0$, we arrive at the distribution P_j represented by the black curve in Fig. 6. This distribution is "exact" within the assumptions of the present Franck–Condon model.

Besides, σ_E^j is equally well given by

$$\sigma_E^j = \left| \int dR d\theta\, \sin\theta\, \Psi_E^{j*}(R,\theta) \Phi_t(R,\theta) \right|^2 \quad (38)$$

(see eqn (8)), which is eqn (28) at time t instead of time 0. Using eqn (29) and following the developments of Appendix B, we can rewrite eqn (38) as

$$\sigma_E^j = (2\pi\hbar)^2 \int \mathbf{d\Gamma}\, \rho_t(\boldsymbol{\Gamma}) \rho_U(R,P) \rho_j(\theta,P_\theta) \quad (39)$$

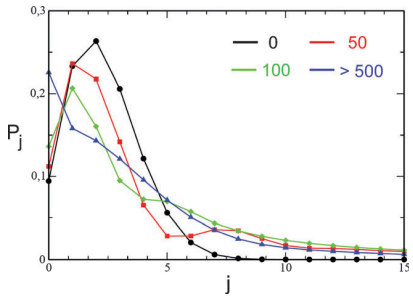

Fig. 6 Time dependence of the rotational state distribution for the Franck–Condon process. Time is given in fs.

where $\boldsymbol{\Gamma} = (R,\theta,P,P_\theta)$. Just as eqn (18) and (23) lead to eqn (25), (23) and (39) lead to

$$\sigma_E^j = (2\pi\hbar)^2 \int \mathbf{d\Gamma_0}\, \rho_0(\boldsymbol{\Gamma_0}) \rho_U(R_t,P_t) \rho_j(\theta_t,P_{\theta_t}), \quad (40)$$

$\boldsymbol{\Gamma_0}$ being the value of $\boldsymbol{\Gamma} = (R,\theta,P,P_\theta)$ at time 0. When making t tend to infinity, one recovers the semiclassical Wigner expression analogous to eqn (25) in the present case where the vibrational motion is frozen.

Since the radial motion is uncoupled with the angular motion, R_t and P_t are functions of R_0, P_0 and t, while θ_t and P_{θ_t} are functions of θ_0, P_{θ_0} and t. Using eqn (33), eqn (40) can thus be rewritten as

$$\sigma_E^j \propto I_1(t) I_2(t) \quad (41)$$

with

$$I_1(t) = \int dR_0 dP_0\, e^{-2\alpha_R(R_0-R_e)^2/\hbar} e^{-P_0^2/(2\alpha_R\hbar)^2} \rho_U(R_t,P_t) \quad (42)$$

and

$$I_2(t) = \int d\theta_0 dP_{\theta_0}\, e^{-2\alpha_\theta(\theta_0-\theta_e)^2/\hbar} e^{-P_{\theta_0}^2/(2\alpha_\theta\hbar)^2} \rho_j(\theta_t,P_{\theta_t}). \quad (43)$$

Since $\rho_U(R_t,P_t)$ does not depend on j, the j dependence of σ_E^j is only due to $I_2(t)$. Therefore, $I_1(t)$ can be transferred into the proportionality factor of eqn (41), leading thereby to

$$\sigma_E^j \propto I_2(t). \quad (44)$$

AB rotating freely after the photon absorption, θ_t and P_{θ_t} are given by

$$\theta_t = \theta_0 + \frac{P_{\theta_0}}{m r_e^2} t \quad (45)$$

and

$$P_{\theta_t} = P_{\theta_0}. \quad (46)$$

Eqn (45) is the solution of eqn (5.4c) of ref. 6, remembering that the reduced moment of inertia I (see eqn (12)) reduces here to mr_e^2, as stated at the beginning of this section. Therefore, we finally arrive at

$$\sigma_E^j \propto \int d\theta_0 dP_{\theta_0}\, e^{-2\alpha_\theta(\theta_0-\theta_e)^2/\hbar}\, e^{-P_{\theta_0}^2/(2\alpha_\theta\hbar)^2} \rho_j\left[\theta_0 + \frac{P_{\theta_0}}{m r_e^2} t, P_{\theta_0}\right]. \quad (47)$$

Note that eqn (36) and (37) are recovered from eqn (47) at time 0.

With the hypothetical values $m = 5$ g mol^{-1} and $r_e = 1$ Å, eqn (47) applied at $t = 50$, 100 and 500 fs leads to the rotational state distributions displayed in Fig. 6, in addition to the "exact" one at time 0. Beyond 500 fs, the distribution does not evolve. The degrading effect previously outlined is patent, the distribution getting strongly altered after only 50 fs. This is a clear illustration of the inability of eqn (25), as such, to correctly describe partial cross sections.

We note from eqn (47) that the degrading effect is due to the strong variation of the rotational Wigner distribution along

classical orbits, as previously outlined. The analogous variation being much weaker for the vibrational motion, so is the corresponding degrading effect.

3. Using Brown and Heller expression at the boundary of the interaction region rather than at a large time. For the previous Franck–Condon process, it is equivalent to state that the distribution is exact at time 0, or at the time beyond which P_θ ceases to vary. For a general process, the latter corresponds to the instant where the system crosses the frontier separating the interaction region from the free products. This frontier being well defined by a given value R_f of R, we shall use instead of Brown and Heller expression (25),

$$\sigma_E^{nj} = (2\pi\hbar)^3 \int \mathbf{d\Gamma_0}\ \rho_0(\mathbf{\Gamma_0})\rho_{\rm tr}(R_f, P_f)\rho_n(r_f, p_f)\rho_j(\theta_f, P_{\theta_f}), \tag{48}$$

where P_f is the value of P at R_f when starting from $\mathbf{\Gamma_0}$, with a similar definition for r_f, p_f, θ_f and P_{θ_f}. One will not forget to substitute θ for θ_f according to eqn (26) and (27) (with θ_f instead of θ_t). The above expression is assumed to minimize the degrading effect, and is exact in the Franck–Condon limit.

In practice, the delta function in $\rho_{\rm tr}(R_f,P_f)$ (see eqn (19)) may be replaced by a bin centered at $\hbar^2 k_{nj}^{\ 2}/(2\mu)$, much narrower than the distribution of $P_f^2/(2\mu)$. In this work, the bin width is taken at five percent of the full-width-at-half-maximum (FWHM) of the previous distribution.

As stated in the introduction, we call the present method forward I and apply it to the photodissociation of methyl iodide in Section V.

E. Approximate formulation

Eqn (48) contains a delta distribution through the translational Wigner function $\rho_{\rm tr}(R_f,P_f)$, given by eqn (19). This term, replaced by a narrow Gaussian or a thin box in practical calculations,[9,10] makes them heavy. However, at the exit of the interaction region, the classical Hamiltonian (24) reads

$$H_{\rm e} = \frac{P^2}{2\mu} + E_{int}(r, p, P_\theta) \tag{49}$$

with

$$E_{\rm int}(r, p, P_\theta) = \frac{p^2}{2m} + v_{\rm e}(r) + \frac{P_\theta^{\ 2}}{2mr^2} \tag{50}$$

(R_f being much larger than r, I in eqn (24) reduces to mr^2 (see eqn (A.12))). $E_{\rm int}(r,p,P_\theta)$ represents the internal energy of AB. From eqn (15) and (49), one may thus rewrite $\rho_{\rm tr}(R_f,P_f)$ as

$$\rho_{\rm tr}(R_f, P_f) = \frac{1}{2\pi\hbar}\delta[H_{\rm e} - E + E_{nj} - E_{\rm int}(r_f, p_f, P_{\theta_f})]. \tag{51}$$

Note the disappearance of the term $\Theta(P_f)$ as compared to eqn (19), for P_f is necessarily positive.

For not too excited rovibrational states, E_{nj} is very well approximated by the sum of E_n^v, the vibrational energy corresponding to the nth state of the non-rotating AB diatom, and the rotational energy $E_j^r = \hbar^2 j(j+1)/(2mr_{\rm e}^{\ 2})$. The values of r_f and p_f corresponding to E_n^v define an elliptic-like curve in the (r,p) plane (a true ellipse for a purely harmonic oscillator) while the values of P_{θ_f} corresponding to E_j^r are $\sim\pm\hbar(j+1/2)$. However, r_f, p_f and P_{θ_f} are weighted in eqn (48) by $\rho_n(r_f,p_f)$ and $\rho_j(\theta_f,P_{\theta_f})$ which broadly extend around the previous values. Consequently, one expects $E_{\rm int}(r_f,p_f,P_{\theta_f})$ to have roughly the same chance to be larger or smaller than E_{nj}. In other words, their average difference should be negligible as compared to E, so the partial cross sections obtained by means of eqn (51) or

$$\rho_{\rm tr}(R_f, P_f) = \frac{1}{2\pi\hbar}\delta(H_{\rm e} - E) \tag{52}$$

should not be very different.

The interest of this approximation is that $H_{\rm e}$, as a constant of motion, can be expressed in terms of $\mathbf{\Gamma_0}$. One can use this fact to analytically integrate with respect to P_0 and p_0 as follows. Setting

$$P_0 = \mu^{1/2}\eta\cos\beta \tag{53}$$

and

$$p_0 = m^{1/2}\eta\sin\beta \tag{54}$$

with β in the range $[0,2\pi]$, eqn (24) becomes

$$H_{\rm e} = \frac{\eta^2}{2} + \frac{{P_{\theta_0}}^2}{2I} + V_{\rm e}(R_0, r_0, \theta_0). \tag{55}$$

From eqn (48) and (52)–(55), the partial cross section σ_E^{nj} reads

$$\sigma_E^{nj} \propto \int \eta\,{\rm d}\eta{\rm d}\beta{\rm d}R_0{\rm d}r_0{\rm d}\theta_0{\rm d}P_{\theta_0}\rho_0(\mathbf{\Gamma_0})\delta\left[\frac{\eta^2}{2} - Q\right]\rho_n(r_f,p_f)\rho_j(\theta_f,P_{\theta_f}) \tag{56}$$

with

$$Q = E - \frac{{P_{\theta_0}}^2}{2I} - V_{\rm e}(R_0, r_0, \theta_0). \tag{57}$$

Replacing $\eta{\rm d}\eta$ in eqn (56) by ${\rm d}\eta^2/2$ makes the delta function disappear and we finally arrive at the useful expression

$$\sigma_E^{nj} \propto \int {\rm d}\beta{\rm d}R_0{\rm d}r_0{\rm d}\theta_0{\rm d}P_{\theta_0}\ \rho_0(\mathbf{\Gamma_0})\rho_n(r_f,p_f)\rho_j(\theta_f,P_{\theta_f}). \tag{58}$$

The values of R_0, r_0, θ_0 and P_{θ_0} contributing to the integral are those making Q positive or zero. P_0 and p_0, which complete the set of initial conditions, are determined by means of eqn (53) and (54) with

$$\eta = (2Q)^{1/2}. \tag{59}$$

We call the present method forward II.

Another possibility would have been to follow Goursaud *et al.*[11] and integrate over one of the two momenta P_0 or p_0. But a term diverging at the boundaries of the available phase space volume would have appeared in the integrand, rendering thereby the numerical calculation of σ_E^{nj} more tricky.

III. Backward semiclassical Wigner approach

From eqn (48) and (51), we have

$$\sigma_E^{nj} = (2\pi\hbar)^2 \int \mathbf{d}\boldsymbol{\Gamma_0}\ \rho_0(\boldsymbol{\Gamma_0})\delta[H_e - E + E_{nj} - E_{int}(r_f, p_f, P_{\theta_f})] \times \rho_n(r_f, p_f)\rho_j(\theta_f, P_{\theta_f}). \quad (60)$$

In ref. 16–18 and 50–52, it is shown that an alternative set of coordinates to $\boldsymbol{\Gamma}_0$ is $(t,H_e,r_f,p_f,\theta_f,P_{\theta_f})$. The origin of time corresponds to the instant where the system is at R_f. The quadruplet $(r_f,p_f,\theta_f,P_{\theta_f})$ specifies the internal state of AB at time 0 and H_e forces P_f to take the value

$$P_f = [2\mu(H_e - E_{int}(r_f,p_f,P_{\theta_f}))]^{1/2} \quad (61)$$

(see eqn (49)). $\boldsymbol{\Gamma}_f = (R_f,P_f,r_f,p_f,\theta_f,P_{\theta_f})$ lies along a given trajectory. Now, any point along this trajectory can be reached from $\boldsymbol{\Gamma}_f$ by moving along the trajectory a given period of time $|t|$ either forward ($t > 0$) or backward ($t < 0$). In other words, for a given R_f, $(H_e,r_f,p_f,\theta_f,P_{\theta_f})$ imposes the classical path, and t the location along it. Consequently, $(t,H_e,r_f,p_f,\theta_f,P_{\theta_f})$ allows to span the whole phase space.

In addition to that, one may show the important property[16–18,50–52]

$$\mathbf{d}\boldsymbol{\Gamma}_0 = \mathrm{d}t\mathrm{d}H_e\mathrm{d}r_f\mathrm{d}p_f\mathrm{d}\theta_f\mathrm{d}P_{\theta_f}. \quad (62)$$

The exact demonstration of the above identity is not given in the previous references, but it closely follows, for example, the developments in Appendix C of ref. 18 for different (though partly related) coordinates. From eqn (60) and (62) and the straightforward integration over H_e, we finally arrive at

$$\sigma_E^{nj} = (2\pi\hbar)^2 \int \mathrm{d}r_f\mathrm{d}p_f\mathrm{d}\theta_f\mathrm{d}P_{\theta_f}\ \rho_n(r_f,p_f)\rho_j(\theta_f,P_{\theta_f}) \int_{-\infty}^{0} \mathrm{d}t\ \rho_0(\boldsymbol{\Gamma}_t). \quad (63)$$

Integration over H_e forces the latter to be equal to $E - E_{nj} + E_{int}(r_f,p_f,P_{\theta_f})$. From eqn (15) and (61), we thus have

$$P_f = \hbar k_{nj}. \quad (64)$$

At last, $\boldsymbol{\Gamma}_t$ in eqn (63) is the value of $\boldsymbol{\Gamma}$ at time t when starting from $\boldsymbol{\Gamma}_f$ at time 0 (the meaning of $\boldsymbol{\Gamma}_t$ is thus different here and in Section IIA).

To summarize, the internal state $(r_f,p_f,\theta_f,P_{\theta_f})$ of AB is randomly chosen within appropriate boundaries. Together with eqn (64), they allow to generate a trajectory from R_f at time 0. The trajectory is then propagated backward in time, *i.e.*, in the direction of the reagent molecule, and $\rho_0(\boldsymbol{\Gamma}_t)$ is time-integrated until the trajectory recrosses R_f towards the products. The result is multiplied by the statistical weight $\rho_n(r_f,p_f)\rho_j(\theta_f,P_{\theta_f})$ in order to get the integrand of eqn (63). A simple Monte-Carlo procedure can then be used to estimate σ_E^{nj}.

In practice, the power of the backward approach is limited by the fact that one cannot *a priori* guess which values of r_f, p_f, θ_f and P_{θ_f} lead to trajectories crossing the Wigner region, corresponding to the phase space volume where Wigner distribution $\rho_0(\boldsymbol{\Gamma})$ takes significant values (there is some arbitrariness in this definition). Therefore, a straightforward application of eqn (63) may require running a large amount of useless trajectories that do not contribute to σ_E^{nj}. To go round this difficulty, one may first apply the forward approach in order to determine the boundaries of r_f, p_f, θ_f and P_{θ_f} contributing to σ_E^{nj}, and then apply the backward method with these variables selected within the previous boundaries.

The practical method used here to perform this selection is as follows. First, one runs a few thousand trajectories, say N, within the forward I method, leading to the same number of final points $(r_k,p_k,\theta_k,P_{\theta_k})$, $k = 1,\ldots,N$, at $R = R_f$. Next, one randomly generates a point $(r_f,p_f,\theta_f,P_{\theta_f})$ and checks whether it lies within at least one of the small rectangular cuboids defined by $|r_f - r_k| \leq \eta_r$, $|p_f - p_k| \leq \eta_p$, $|\theta_f - \theta_k| \leq \eta_\theta$, $|P_{\theta_f} - P_{\theta_k}| \leq \eta_{P_\theta}$, $k = 1,\ldots,N$. If so, this point serves as initial conditions together with $R = R_f$ and eqn (64). Otherwise, one randomly generates another point and so on. The parameters η_r, η_p, η_θ and η_{P_θ} have to be chosen from a visual inspection of the domain covered by the rectangular projections of the cuboids in the planes (r,p) and (θ,P_θ), separately. The parameters must be large enough for the domains to be compact, as they appear to be when running millions of trajectories within the forward I method.

Finally, we have found that for the model of methyl iodide photodissociation considered in Section V, the values of k_{nj} appear to be almost independent on j (see Section IID for an explanation), a bit less on n. In such a case, a single batch of trajectory can be run with $P_f = k_{n0}$ for calculating all the σ_E^{nj}s corresponding to n.

IV. The standard method of Goursaud *et al.*

The method of Goursaud *et al.* was initially applied to a bi-dimensional model of triatomic ion fragmentation with frozen valence angle. The method was later extended by Schinke to realistic three-dimensional triatomic photodissociations.[49] Within this approach, which is detailed in Chapter 5 of Schinke's book,[6] σ_E^{nj} is given by

$$\sigma_E^{nj} = (1+\delta_{j0}) \int \mathbf{d}\boldsymbol{\Gamma}_0\ \rho_0(\boldsymbol{\Gamma}_0)\sin\theta_0\delta(H_e - E) \times \delta(n(r_f,p_f) - n)\delta(|P_{\theta_f}| - j) \quad (65)$$

where the only quantity not defined until now is the final vibrational action $n(r_f,p_f)$ of AB, given by

$$n(r_f,p_f) = \frac{2}{h}\int_{r_{in}}^{r_{out}} \mathrm{d}r\ p(r) - \frac{1}{2} \quad (66)$$

with

$$p(r) = \left(2m\left[E_{int}(r_f,p_f,P_{\theta_f}) - \frac{{P_{\theta_f}}^2}{2mr^2} - v_e(r)\right]\right)^{1/2}. \quad (67)$$

r_{in} and r_{out} are the values of r at the inner and outer turning points. The internal energy $E_{int}(r_f,p_f,P_{\theta_f})$ is given by eqn (50).

In practice, the delta functions are replaced by standard bins (SB) of unit height and width, or Gaussians the FWHM of which

is usually taken at 10%. The second procedure is called Gaussian binning (GB).[53–59] These procedures are discussed at length in ref. 18. Since no Wigner distributions are used to weight the final dynamical states, the present method is more classical than the previous ones.

The transition moment being absorbed in $\rho_0(\boldsymbol{\Gamma_0})$, eqn (65) is similar to eqn (5.23) in ref. 6 (see also eqn (5.22)). The main difference is that the degeneracy factor $(1 + \delta_{j0})$ has been added in the present work. Note that Schinke and co-workers also include this factor in practice.[60]

The degeneracy factor doubles the integral in eqn (65) for $j = 0$. This counterbalances the fact that due to the $\delta(|P_{\theta_f}| - j)$ term, two values of P_{θ_f} contribute to the integral for $j > 0$ ($\pm j$), against only one for $j = 0$. The interest of this factor clearly appears in the purely statistical limit where $n(r_f,p_f)$ and P_{θ_f} are random variables. σ_E^{nj} being proportional to the density of probability to get $n(r_f,p_f) = n$ and $|P_{\theta_f}| = j$ (see eqn (65)), all the σ_E^{nj}s are equal (without the degeneracy factor, σ_E^{n0} would be half $\sigma_E^{nj\neq 0}$), a result in conformity with the quantum phase space theory expectations of equal final state populations.[61,62]

V. Photodissociation of methyl iodide

We briefly summarize the main features of the triatomic-like model of methyl iodide photodissociation and the quantum dynamical method used to check the validity of the semiclassical Wigner method. More details can be found in the references mentioned below.

A. Model

The CH_3I molecule is considered as a CXI pseudotriatomic molecule,[41,63,64] the pseudoatom X = H_3 being located at the center-of-mass (CM) of the three H atoms. $\boldsymbol{R}$ is the vector between the CH_3 (or C–X) CM and I and $\boldsymbol{r}$ is the one between X and C. r represents the umbrella bend of the C–H_3 group. It is assumed that the C_{3v} symmetry of CH_3 is preserved throughout the whole process (see also Fig. 1).

Photodissociation of CH_3I is assumed to take place upon optical excitation at 266 nm (A band) from the $\tilde{X}^1A_1$ ground electronic state to the $^3Q_0$, $^1Q_1$ and $^3Q_1$ excited electronic states. Taking however into account that absorption to the $^3Q_1$ state is relatively small at 266 nm, the present simulations only involve the $^3Q_0$, and $^1Q_1$ excited electronic states, in addition to the ground state $\tilde{X}^1A_1$. The $\tilde{X}^1A_1$ and $^1Q_1$ electronic surfaces correlate asymptotically with the $CH_3 + I(^2P_{3/2})$ products, while the $^3Q_0$ surface correlates with the $CH_3 + I^*(^2P_{1/2})$ products. In addition to the coupling of $\tilde{X}^1A_1$ to the excited electronic states through electric-dipole moments, the $^3Q_0$ and $^1Q_1$ states are non-adiabatically coupled. Taking into account the transitions between these states in the semiclassical Wigner method would require treating these by means of a semiclassical approach of non-adiabatic transitions such as, for instance, the Landau–Zener model,[65] the Zhu–Nakamura model,[66] or the surface hopping method of Tully.[67,68] For the sake of clarity, however, we artificially take at zero the coupling between the $^3Q_0$ and $^1Q_1$ states, focusing our attention in a first step on the semiclassical Wigner method for fragmentations taking place on a single excited electronic state. However, we plan to extend this method to processes involving non-adiabatic transitions in a near future, for we are aware of their importance in photochemistry.

Upon optical excitation at 266 nm, the energies available to the final products in the $^3Q_0$ and $^1Q_1$ states are 11258.53 cm^{-1} and 18862.09 cm^{-1}, respectively.

High-quality *ab initio* calculations have been used to model the three electronic potential energy surfaces (PESs) involved in the calculations. In the case of the $\tilde{X}^1A_1$ ground state, the PES ($V_g(R,r,\theta)$) is represented as a sum of three potential interactions in the R_{C-I} (the C–I nuclear distance), r and θ coordinates, respectively. The interaction potential in the R_{C-I} coordinate is taken from the recently reported 2D ground-state potential for CH_3I, obtained by means of multireference spin–orbit configuration interaction *ab initio* calculations.[69,70] The potential interactions in the r and θ coordinates are represented by harmonic oscillator functions.[26,41]

The PESs for the excited electronic states $^3Q_0$ and $^1Q_1$ ($V_e(R,r,\theta)$) are the *ab initio* PES constructed by Xie *et al.*[71] These are improved versions of the previous nine-dimensional surfaces of Amatatsu *et al.*,[72] where the spin–orbit configuration interaction method was used with a better basis by changing the valence double-ζ level to the triple-ζ one. Out of the nine coordinates of the surfaces, the six coordinates which are neglected in the simulations were fixed at their equilibrium values.[63]

The electric-dipole moment functions ($d(R,r,\theta)$) coupling radiatively the $\tilde{X}^1A_1$ ground state with $^3Q_0$ and $^1Q_1$ were obtained from the *ab initio* calculations of Alekseyev *et al.*,[70,73] subsequently fitted to analytical forms used in the simulations.[63]

B. Time-dependent quantum calculations

CH_3I is initially in the rovibrational ground state $\phi_0(R,r,\theta)$, variationally obtained from eqn (13) within the framework of an adiabatic approximation detailed in ref. 26. CH_3I is then excited to one of the $^3Q_0$ and $^1Q_1$ electronic states, creating a wave packet $\Phi_0(R,r,\theta)$ (see eqn (12)) undergoing dynamical evolution according to eqn (10). In order to solve this equation, the wave packet $\Phi_t(R,r,\theta)$ is represented in a basis set consisting of a two-dimensional rectangular grid for the radial coordinates and an angular basis including 24 Legendre polynomials for the θ coordinate. The rectangular grid consists of 450 equidistant points in the R coordinate in the range $3.5a_0 \leq R \leq 16.0a_0$, and 32 equidistant points in the r coordinate in the range $-1.6a_0 \leq r \leq 1.6a_0$. Propagation of the wave packet is performed by representing the evolution operator by means of a Chebyshev polynomial expansion. The wave packet was propagated for 200 fs with a time step $\Delta t = 0.4$ fs, and was absorbed at the edge of the grid in the R coordinate after each propagation time step by multiplying it by the function $\exp[-\alpha(R - R_{abs})^2]$, with $\alpha = 0.9a_0^{-2}$ and $R_{abs} = 13.0a_0$. In order to obtain the product fragment distributions of interest, the wave packet was projected out in the asymptotic region onto the fragment states. Details of the projection procedure are given in ref. 26.

C. Comparison between semiclassical and quantum results

$\Phi_0(R,r,\theta)$ was expressed as a product of three independent Gaussians, respectively, depending on R, r and θ, a very good approximation in the present case. As in Section IID, the density $\rho_0(\boldsymbol{\Gamma}_0)$ was then deduced from eqn (5.20) of ref. 6.

The results obtained by means of the forward I, forward II and Goursaud *et al.* methods involved 5 million, 100 thousand and 1 million trajectories, respectively. The results obtained by means of the backward method involved 60 thousand trajectories per vibrational level (see end of Section III). These numbers are for each electronic state, $^3Q_0$ and $^1Q_1$. For the backward approach, η_r and η_θ were kept at 0.02 while η_p and η_{P_θ} were taken at 0.2 (in atomic units for η_r, η_p and η_{P_θ} and in radian for η_θ). R_f was found to be equal to 13 and 10 bohr for the $^3Q_0$ and $^1Q_1$ states, respectively.

The vibrational state populations P_n, deduced from eqn (3) by summing over j, are given in Fig. 7. The vibrationally resolved rotational state distributions are displayed in Fig. 8 and 9. The latter are simply denoted P_j, but the value of n to which they refer is indicated.

The agreement between backward and quantum mechanical (QM) results is quantitative for all the distributions but P_n in the $^1Q_1$ state, for which it is nevertheless very good.

These conclusions hold between forward I and QM results, apart from P_j, n = 1,2, in the $^1Q_1$ state for which the quality of the agreement decreases. The reason seems to be the following. As seen at the end of Section IID, the partial cross section involves a delta function through $\rho_{tr}(R_f,P_f)$ (see eqn (48) and (19)) which is replaced by a narrow bin. However, the bin cannot be too narrow, for a negligible amount of trajectories would contribute to the partial cross sections. With a true delta function, P would be strictly equal to $\hbar k_{nj}$. With a bin, however, there is an uncertainty on the value of P around $\hbar k_{nj}$, which seems to cause the differences observed between the forward I results and the backward and quantum ones. By dividing the width of the bin by two, we indeed reduced the differences. We tried to reduce even more the width of the bin, but this prevented from converging the partial cross sections.

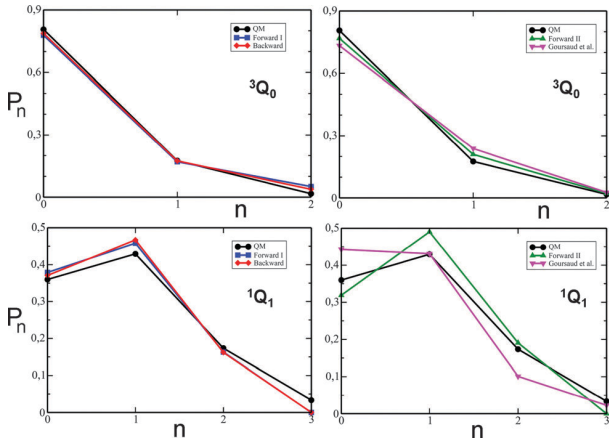

Fig. 7 Vibrational state distributions in the $^3Q_0$ and $^1Q_1$ states found by means of the QM, forward I, forward II, backward and Goursaud *et al.* methods.

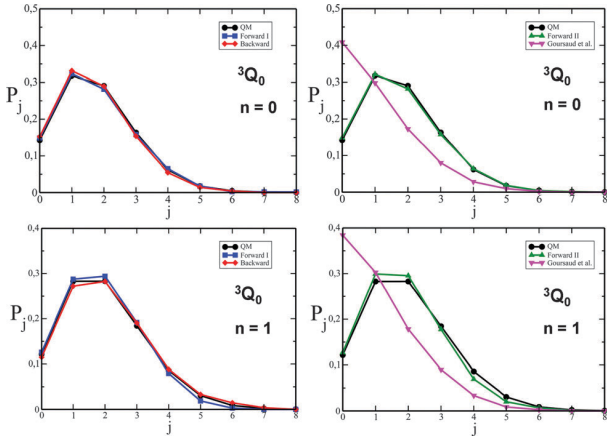

Fig. 8 Vibrationally resolved rotational state distributions in the $^3Q_0$ state found by means of the QM, forward I, forward II, backward and Goursaud *et al.* methods.

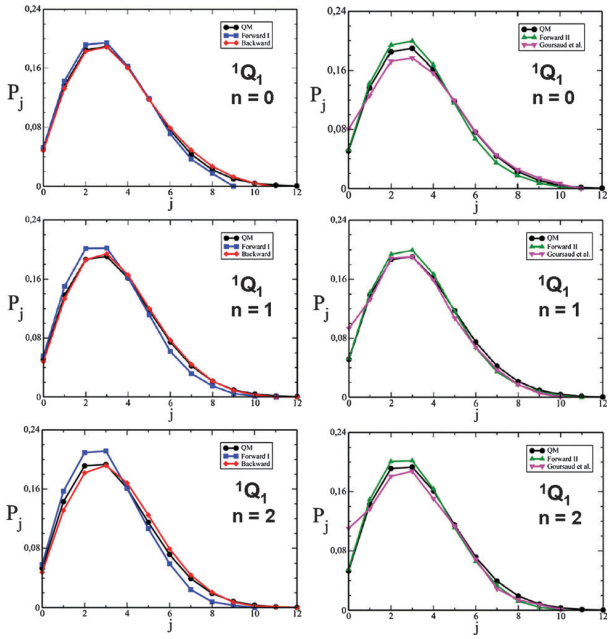

Fig. 9 Vibrationally resolved rotational state distributions in the $^1Q_1$ state found by means of the QM, forward I, forward II, backward and Goursaud *et al.* methods.

The minimum number of trajectories necessary to converge the calculations was found to be 800 thousand for the forward I method in both electronic states, against 10 thousand for n = 0 in the $^3Q_0$ state, 20 thousand for n = 1 in the $^3Q_0$ state, 8 thousand for n = 0 in the $^1Q_1$ state, 10 thousand for n = 1 in the $^1Q_1$ state and 30 thousand for n = 2 in the $^1Q_1$ state. As a matter of fact, the backward method is at the same time more efficient and more accurate than the forward I method.

The agreement between forward II and QM results is very good for all the rotational distributions, a bit less for the vibrational ones, especially in the $^1Q_1$ state. Like the forward I and backward methods, the forward II method accounts for the vibrational

inversion in the $^1Q_1$ state. The quality of the forward II predictions gives credit to the approximation on which they are based.

The agreement between Goursaud *et al.* and QM results is very satisfying for the rotational distributions in the $^1Q_1$ state, except for $j = 0$, and for the vibrational distribution in the $^3Q_0$ state. On the other hand, the method of Goursaud *et al.* fails at reproducing the vibrational inversion in the $^1Q_1$ state, and badly describes the rotational distributions in the $^3Q_0$ state, even qualitatively. Overall, this method is only semi-quantitative.

As previously stated, the energy available to the final products is larger in the $^1Q_1$ than in the $^3Q_0$ state. This explains in part why there is more vibrational and rotational excitation in $^1Q_1$ than in $^3Q_0$. The system is thus less quantum-like in $^1Q_1$ than in $^3Q_0$, justifying thereby to some extent why the method of Goursaud *et al.*, the more classical of the four semiclassical approaches considered in this work, is able to reproduce the energy partitioning in $^1Q_1$ and not in $^3Q_0$.

VI. Conclusion

In their concluding remarks, Brown and Heller[9] raised the basic issue of including rotations in their semiclassical Wigner description of photodissociation dynamics so as to make it full-dimensional and thus, realistic. This issue has been solved in the present work in the case of triatomic, or triatomic-like polyatomic fragmentations.

Three methods have been proposed, respectively, called forward I, forward II and backward. While forward approaches involve trajectories run from the reagent molecule onto the products, the backward one deals with trajectories run in the reverse direction. This makes the backward method state-selective, and thus, ideally suited to the description of state-correlated distributions measured in velocity imaging experiments.

The forward I and backward methods are exact applications of the semiclassical Wigner treatment. They closely parallel the quantum description as far as possible. The forward II approach involves an approximation strongly increasing the numerical efficiency of the semiclassical Wigner treatment as compared to the forward I method.

In addition to the usual vibrational Wigner distributions, these three approaches include rotational Wigner distributions which seem to be introduced for the first time in the present context. These densities have remarkable structures clearly showing that classical trajectories most contributing to rotational state j are those reaching the products with a rotational angular momentum close to $[j(j+1)]^{1/2}$ (in $\hbar$ units).

The results obtained by means of these methods are compared with rigorous quantum results in the case of Guo's triatomic-like model of methyl iodide photodissociation[41] and very good – often quantitative – agreement is found, especially with the forward I and backward methods. In comparison, the standard and more classical method of Goursaud *et al.*[11] is only semi-quantitative. Last but not least, the backward approach appears to be much more powerful, and even more accurate than the forward I method which requires far more trajectories than the former approach to provide converged results.

This study demonstrates the applicability of the semiclassical Wigner treatment to realistic triatomic or triatomic-like photodissociations and confirms its level of accuracy as compared to the initial work of Brown and Heller.[9] Important next steps are the extension of the method to processes involving non-adiabatic transitions and/or polyatomic species that cannot be treated as a triatom.

Appendix A: derivation of eqn (8)

Consider a given state $\bar{\Psi}^{JM\varepsilon}(\boldsymbol{R},\boldsymbol{r})$ of ABC for the value J of the total angular momentum quantum number, the value M of its projection on the Z-axis of the laboratory reference frame, and the parity ε under inversion of $\boldsymbol{R}$ and $\boldsymbol{r}$. This state can generally be expanded as[23,24]

$$\bar{\Psi}^{JM\varepsilon}(\boldsymbol{R},\boldsymbol{r}) = \sum_{\Omega} W^{J\varepsilon}_{M\Omega}(\alpha,\beta,\gamma)\frac{\Psi^{J\varepsilon}_{M\Omega}(R,r,\theta)}{Rr} \tag{A.1}$$

with

$$W^{J\varepsilon}_{M\Omega}(\alpha,\beta,\gamma) = \left[\frac{2J+1}{16\pi^2(1+\delta_{\Omega 0})}\right]^{1/2} \times \left[D^J_{M,\Omega}(\alpha,\beta,\gamma) + \varepsilon(-1)^{(J+\Omega)}D^J_{M,-\Omega}(\alpha,\beta,\gamma)\right]. \tag{A.2}$$

α, β and γ are the Euler angles orienting ABC in the laboratory reference frame.[75] The helicity quantum number Ω is the projection of the total angular momentum on $\boldsymbol{R}$, chosen as the Z-axis of the body-fixed frame. $D^J_{M,\Omega}(\alpha,\beta,\gamma)$ and $D^J_{M,-\Omega}(\alpha,\beta,\gamma)$ are Wigner D-matrix elements.[75]

When $J = 0$, $M = \Omega = 0$ and ε is necessarily equal to 1 for $W^{J\varepsilon}_{M\Omega}(\alpha,\beta,\gamma)$ not to be 0. Given that $D^0_{0,0}(\alpha,\beta,\gamma) = 1$ (see eqn (4.1.26) of ref. 75), eqn (A.1) reduces to

$$\bar{\Psi}^{001}(\boldsymbol{R},\boldsymbol{r}) = \frac{\Psi^{01}_{00}(R,r,\theta)}{8^{1/2}\pi Rr}. \tag{A.3}$$

We can thus rewrite $\bar{\Psi}^{nj}_E(\boldsymbol{R},\boldsymbol{r})$ and $\bar{\Phi}_t(\boldsymbol{R},\boldsymbol{r})$ in eqn (7) as

$$\bar{\Psi}^{nj}_E(\boldsymbol{R},\boldsymbol{r}) = \frac{\Psi^{nj}_E(R,r,\theta)}{8^{1/2}\pi Rr} \tag{A.4}$$

and

$$\bar{\Phi}_t(\boldsymbol{R},\boldsymbol{r}) = \frac{\Phi_t(R,r,\theta)}{8^{1/2}\pi Rr} \tag{A.5}$$

where for the sake of convenience, subscripts and indices relative to angular momentum quantum numbers and parity have been dropped.

Eqn (7), (A.4) and (A.5) lead to

$$\sigma^{nj}_E = \left|\int \frac{\mathbf{d}\boldsymbol{R}\mathbf{d}\boldsymbol{r}}{8\pi^2R^2r^2}\,\Psi^{nj*}_E(R,r,\theta)\Phi_t(R,r,\theta)\right|^2. \tag{A.6}$$

Moreover, some steps of algebra allow us to prove the two identities

$$\mathbf{d}\boldsymbol{R}\mathbf{d}\boldsymbol{r} = R^2r^2\mathrm{d}R\mathrm{d}r\sin\theta\mathrm{d}\theta\mathrm{d}\alpha\sin\beta\mathrm{d}\beta\mathrm{d}\gamma \tag{A.7}$$

and

$$\int \mathrm{d}\alpha \sin\beta \mathrm{d}\beta \mathrm{d}\gamma = 8\pi^2. \tag{A.8}$$

Eqn (A.6)–(A.8) finally lead to eqn (8).

For $J = 0$, $\bar{\Psi}_E^{nj}(\boldsymbol{R},\boldsymbol{r})$ and $\bar{\Phi}_t(\boldsymbol{R},\boldsymbol{r})$ are shown to satisfy the Schrödinger equations,[76,77]

$$\hat{\bar{H}}_\mathrm{e} = \left[\hat{\bar{T}} + \hat{V}_\mathrm{e}\right]\bar{\Psi}_E^{nj} = E\bar{\Psi}_E^{nj} \tag{A.9}$$

and

$$i\hbar\frac{\mathrm{d}\bar{\Phi}_t}{\mathrm{d}t} = \hat{\bar{H}}_\mathrm{e}\bar{\Phi}_t, \tag{A.10}$$

with

$$\hat{\bar{T}} = -\frac{\hbar^2}{2\mu R^2}\frac{\partial}{\partial R}R^2\frac{\partial}{\partial R} - \frac{\hbar^2}{2mr^2}\frac{\partial}{\partial r}r^2\frac{\partial}{\partial r} - \frac{\hbar^2}{2I\sin\theta}\frac{\partial}{\partial\theta}\sin\theta\frac{\partial}{\partial\theta}. \tag{A.11}$$

The reduced moment of inertia I satisfies the identity

$$\frac{1}{I} = \frac{1}{\mu R^2} + \frac{1}{mr^2}. \tag{A.12}$$

From eqn (A.4), (A.5), (A.9)–(A.11), $\Psi_E^{nj}(R,r,\theta)$ and $\Phi_t(R,r,\theta)$ are shown to satisfy eqn (9)–(11).

Appendix B: derivation of eqn (18)

Any quantity σ defined by

$$\sigma = \left|\int \mathrm{d}R\mathrm{d}r\mathrm{d}\theta\ \Psi_1^*(R,r,\theta)\Psi_2(R,r,\theta)\right|^2 \tag{B.1}$$

can be rewritten as[9,10,12]

$$\sigma = (2\pi\hbar)^3\int \mathrm{d}R\mathrm{d}r\mathrm{d}\theta\mathrm{d}P\mathrm{d}p\mathrm{d}P_\theta\ \rho_1(R,r,\theta,P,p,P_\theta)\rho_2(R,r,\theta,P,p,P_\theta) \tag{B.2}$$

where $\rho_l(R,r,\theta,P,p,P_\theta)$, $l = 1$ or 2, is the Wigner density defined by

$$\begin{aligned}\rho_l(R,r,\theta,P,p,P_\theta) = \frac{1}{(\pi\hbar)^3}\int \mathrm{d}s_R\mathrm{d}s_r\mathrm{d}s_\theta\ \mathrm{e}^{2i(Ps_R+ps_r+P_\theta s_\theta)/\hbar}\\ \times\ \Psi_l^*(R+s_R, r+s_r, \theta+s_\theta)\\ \times\ \Psi_l(R-s_R, r-s_r, \theta-s_\theta).\end{aligned} \tag{B.3}$$

This expression is a generalization of eqn (1) to three dimensions.

A pedestrian demonstration of the strict equivalence between eqn (B.1) and (B.2) for one configuration space coordinate is given in Appendix B of ref. 18. In the present case of three coordinates, the developments are more tedious, but present no difficulty.

Setting

$$\Psi_1(R,r,\theta) = \left[\frac{\mu}{2\pi\hbar^2 k_{nj}}\right]^{1/2}\mathrm{e}^{ik_{nj}R}\chi_n(r)\sin\theta Y_j^0(\theta) \tag{B.4}$$

and

$$\Psi_2(R,r,\theta) = \Phi_t(R,r,\theta), \tag{B.5}$$

we arrive from eqn (B.2) and (B.3) at

$$\begin{aligned}\sigma_E^{nj} = (2\pi\hbar)^3\lim_{t\to+\infty}\int \mathrm{d}R\mathrm{d}r\mathrm{d}\theta\mathrm{d}P\mathrm{d}p\mathrm{d}P_\theta\ \rho_t(R,r,\theta,P,p,P_\theta)\\ \times\ \rho_\mathrm{tr}(R,P)\rho_n(r,p)\rho_j(\theta,P_\theta).\end{aligned} \tag{B.6}$$

$\rho_t(R,r,\theta,P,p,P_\theta)$ is related to $\Phi_t(R,r,\theta)$ by eqn (B.3). The translational Wigner distribution $\rho_\mathrm{tr}(R,P)$ is given by

$$\rho_\mathrm{tr}(R,P) = \frac{1}{\pi\hbar}\int \mathrm{d}s\ \mathrm{e}^{2iPs/\hbar}\left[\frac{\mu}{2\pi\hbar^2 k_{nj}}\right]\mathrm{e}^{-ik_{nj}(R+s)}\mathrm{e}^{ik_{nj}(R-s)} \tag{B.7}$$

while the vibrational and rotational Wigner distributions $\rho_n(r,p)$ and $\rho_j(\theta,P_\theta)$ are given by eqn (20) and (21). Eqn (B.7) gives

$$\rho_\mathrm{tr}(R,P) = \left[\frac{\mu}{2\pi\hbar^2 k_{nj}}\right]\frac{1}{\pi\hbar}\int \mathrm{d}s\ \mathrm{e}^{2i(P-\hbar k_{nj})s/\hbar} \tag{B.8}$$

which, using

$$\delta(x) = \frac{1}{2\pi}\int \mathrm{d}s\ \mathrm{e}^{isx}, \tag{B.9}$$

leads to

$$\rho_\mathrm{tr}(R,P) = \left[\frac{\mu}{2\pi\hbar^2 k_{nj}}\right]\frac{2}{\hbar}\delta[2(P-\hbar k_{nj})/\hbar] \tag{B.10}$$

or equivalently, eqn (19). Eqn (B.10) is indeed readily obtained from eqn (19) by means of the following theorem

$$\delta[f(x)] = \sum_k \frac{1}{|f'(x_k)|}\delta(x-x_k) \tag{B.11}$$

where the x_ks are solutions of $f(x) = 0$.[74]

Appendix C: semiclassical limit of the rotational Wigner distribution

Our goal here is to derive an analytical expression of $\rho_j(\theta,P_\theta)$ within the semiclassical approximation along the relevant axis defined by $\theta = \pi/2$ and $P_\theta = 0$, $\pm(j+1/2)$. P_θ is expressed in $\hbar$ units throughout this appendix. These four axis are represented in Fig. 10 for $j = 10$. D_1 and D_2 are the two orthogonal symmetry axis of $\rho_j(\theta,P_\theta)$. D_3 and D_4 are not exact symmetry axes, but they can be considered as local symmetry axes of the lateral ridges for sufficiently large js, as shown further below.

The semiclassical (WKB) limit of the Legendre polynomial $P_j(\cos\theta)$ is given by[78]

$$P_j(\cos\theta) = \frac{2\cos[(j+1/2)\theta - \pi/4]}{[2\pi(j+1/2)\sin\theta]^{1/2}}. \tag{C.1}$$

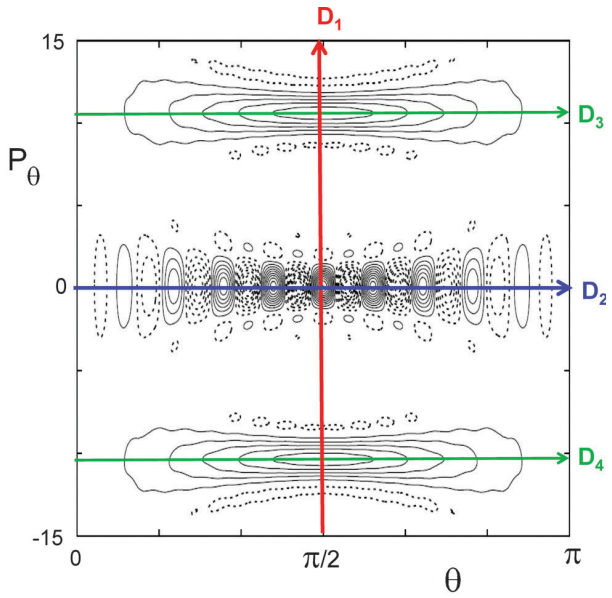

Fig. 10 Contour plot representation of $\rho_{10}(\theta,P_\theta)$ and axis D_i, I = 1–4, along which semiclassical expressions of the rotational Wigner distribution are derived in Appendix C. P_θ is in $\hbar$ units. Solid and dashed contours correspond to positive and negative densities, respectively.

From eqn (16), (21) and (C.1), we have

$$\rho_j(\theta,P_\theta)=\frac{1}{\pi^3}\int \mathrm{d}s\,\mathrm{e}^{2iP_\theta s}[\sin(\theta+s)\sin(\theta-s)]^{1/2}\times\cos[(j+1/2)(\theta+s)-\pi/4]\times\cos[(j+1/2)(\theta-s)-\pi/4]. \tag{C.2}$$

Using the fact that

$$\cos x=\frac{\mathrm{e}^{ix}+\mathrm{e}^{-ix}}{2}, \tag{C.3}$$

we arrive after some steps of simple algebra at

$$\rho_j(\theta,P_\theta)=\frac{1}{2\pi^3}\int \mathrm{d}s\,\mathrm{e}^{2iP_\theta s}[\sin(\theta+s)\sin(\theta-s)]^{1/2}\times[\cos[(2j+1)s]+\sin[(2j+1)\theta]]. \tag{C.4}$$

Along D_1, defined by $\theta=\pi/2$, we have

$$\rho_j(\pi/2,P_\theta)=\frac{1}{2\pi^3}\int_{-\pi/2}^{\pi/2}\mathrm{d}s\,\mathrm{e}^{2iP_\theta s}\cos s[\cos[(2j+1)s]+(-1)^j]. \tag{C.5}$$

The boundaries of the integral are determined by eqn (22). From eqn (C.3) and given that

$$\int_{-\pi/2}^{\pi/2}\mathrm{d}s\,\mathrm{e}^{2ias}=\frac{\sin(\pi a)}{a}=\pi\,\mathrm{sinc}(\pi a), \tag{C.6}$$

we finally obtain

$$\rho_j(\pi/2,P_\theta)=\frac{1}{4\pi^2}(-1)^j[\mathrm{sinc}[\pi(P_\theta+1/2)]+\mathrm{sinc}[\pi(P_\theta-1/2)]]+\frac{1}{8\pi^2}[\mathrm{sinc}[\pi(P_\theta+j+1)]+\mathrm{sinc}[\pi(P_\theta+j)]+\mathrm{sinc}[\pi(P_\theta-j)]+\mathrm{sinc}[\pi(P_\theta-j-1)]]. \tag{C.7}$$

This expression is represented in Fig. 11 for j = 0, 1, 2 and 6 and is compared with the exact Wigner distribution. For j = 0, the agreement is already satisfying. For j = 1 and 2, it is very good and for j = 6, there is virtually no difference between both results.

For large js, the central peak is due to the first pair of sinc functions in eqn (C.7) and its sign is thus given by $(-1)^j$. The lateral peaks, or cuts of ridges, centered at $-(j+1/2)$ and $(j+1/2)$ are due to the second and third pairs of sinc functions, respectively. They are always positive. Each of these three peaks

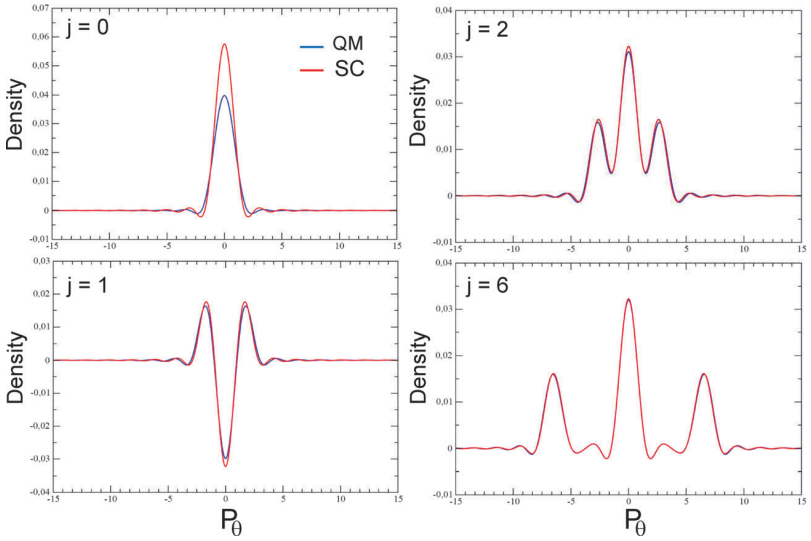

Fig. 11 Comparison between the semiclassical value of $\rho_j(\pi/2,P_\theta)$ along the D_1 axis (see Fig. 10), obtained from eqn (C.7), and its exact quantum value for j = 0, 1, 2 and 6. P_θ is in $\hbar$ units.

is thus made of two narrower peaks sufficiently close to each other for resulting in a single peak. The full width at half maximum is 1.2 for the sinc function and 1.64 for the central and lateral peaks.

For small js, the situation is a bit more complex, since the three peaks overlap. Consequently, the lateral peaks are not exactly centered at $-(j + 1/2)$ and $(j + 1/2)$. For $j = 0$, the lateral peaks have merged with the central peak, and their top is rigorously at 0.

Along D_2, defined by $P_\theta = 0$, we have from eqn (C.4)

$$\rho_j(\theta,0) = \frac{1}{2\pi^3}\int_{s_-}^{s_+} \mathrm{d}s\, [\sin(\theta+s)\sin(\theta-s)]^{1/2} \times [\cos[(2j+1)s] + \sin[(2j+1)\theta]] \quad \text{(C.8)}$$

where the boundaries are found from eqn (22) to be given by $s_\pm = \pm\theta$ if $\theta \leq \pi/2$ and $s_\pm = \pm(\pi - \theta)$ if $\theta > \pi/2$. It is thus clear that the angular range around $\pi/2$ mostly contributes to $\rho_j(\theta,0)$.

For significantly large js, $\cos[(2j + 1)s]$ strongly varies within the previous range and can thus be neglected with respect to $\sin[(2j + 1)\theta]$. We thus arrive at

$$\rho_j(\theta,0) = \frac{1}{2\pi^3}\sin[(2j+1)\theta]\int_{s_-}^{s_+} \mathrm{d}s\, [\sin(\theta+s)\sin(\theta-s)]^{1/2}. \quad \text{(C.9)}$$

The integral seems not to be analytically calculable, but it appears that a good approximation of it is $2\sin\theta^{5/2}$. Therefore, $\rho_j(\theta,0)$ reads

$$\rho_j(\theta,0) \approx \frac{1}{\pi^3}\sin\theta^{5/2}\sin[(2j+1)\theta]. \quad \text{(C.10)}$$

This expression is represented in Fig. 12 for $j = 0$, 1, 2 and 6 and is compared with the exact Wigner distribution. The agreement is correct for $j = 0$ and 1, good for $j = 2$ and very good for $j = 6$.

Along D_3, defined by $P_\theta = j + 1/2$ for sufficiently large js, we obtain from eqn (C.3) and (C.4)

$$\begin{aligned}\rho_j(\theta,j+1/2) &= \frac{1}{4\pi^3}\int \mathrm{d}s\, [\sin(\theta+s)\sin(\theta-s)]^{1/2} \\ &+ \frac{1}{4\pi^3}\int \mathrm{d}s\, \mathrm{e}^{2i(2j+1)s}[\sin(\theta+s)\sin(\theta-s)]^{1/2} \\ &+ \frac{1}{2\pi^3}\int \mathrm{d}s\, \mathrm{e}^{i(2j+1)s}[\sin(\theta+s)\sin(\theta-s)]^{1/2} \\ &\times \sin[(2j+1)\theta].\end{aligned} \quad \text{(C.11)}$$

Since the second and third integrands strongly oscillate as compared to the first one, the above expression is well approximated by its first line. Using the previous approximation for the integral of the first line, we then arrive at

$$\rho_j(\theta,j+1/2) \approx \frac{1}{2\pi^3}\sin\theta^{5/2}. \quad \text{(C.12)}$$

The quality of the agreement between this expression and the exact Wigner distribution is shown in Fig. 13 for $j = 10$.

Finally, the semiclassical expression of the rotational Wigner distribution along D_4, defined by $P_\theta = -(j + 1/2)$, is also given by the right-hand-side of eqn (12), due to the symmetry of the density with respect to D_2.

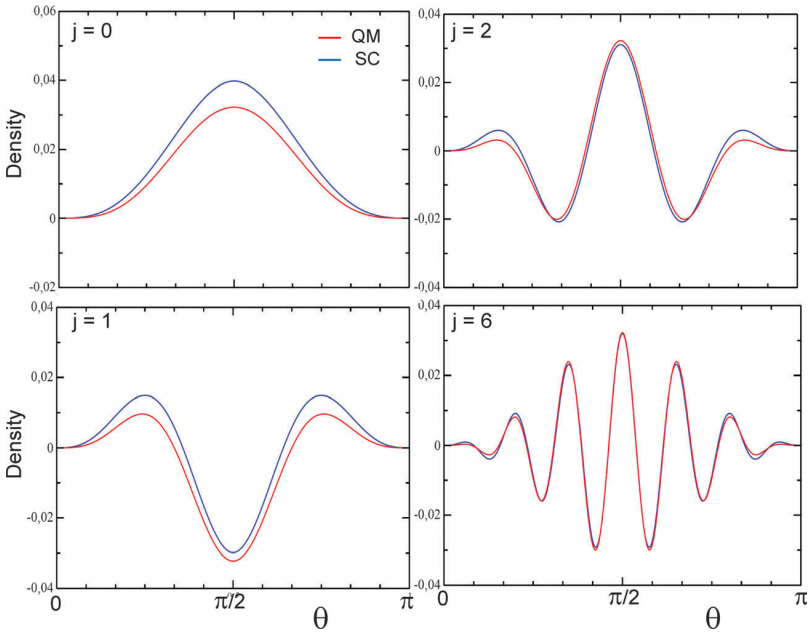

Fig. 12 Comparison between the semiclassical value of $\rho_j(\theta,0)$ along the D_2 axis (see Fig. 10), obtained from eqn (C.10), and its exact quantum value for $j = 0$, 1, 2 and 6.

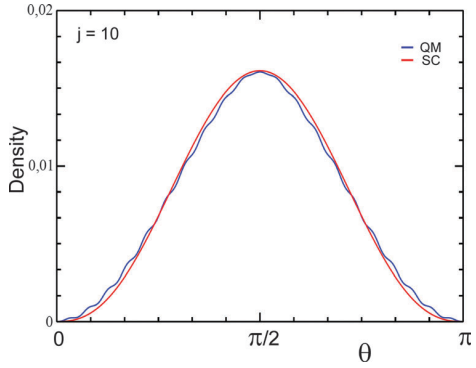

Fig. 13 Comparison between the semiclassical value of $\rho_j(\theta_j j + 1/2)$ along the D_3 axis (see Fig. 10), obtained from eqn (C.12), and its exact quantum value for $j = 10$.

Acknowledgements

L.B. is grateful to Profs G. G. Balint-Kurti, A. Beswick and O. Roncero for valuable help regarding the derivations of Appendix A. A.G.-V. acknowledges support from the Ministerio de Economía y Competitividad, Spain, Grant No. FIS2011-29596-CO2, Consolider program, "Science and Applications of Ultrafast Ultraintense Lasers", Grant No. CSD2007-00013, and COST Action program CODECS, Grant No. CM1002. The Centro de Supercomputación de Galicia (CESGA), Spain, is acknowledged for the use of their resources.

References

1 D. Townsend, W. Li, S. K. Lee, R. L. Gross and A. G. Suits, *J. Phys. Chem. A*, 2005, **109**, 8661.
2 A. G. Suits and O. S. Vasyutinskii, *Chem. Rev.*, 2008, **108**, 3706.
3 A. I. Chichinin, K.-H. Gericke, S. Kauczok and C. Maul, *Int. Rev. Phys. Chem.*, 2009, **28**, 607.
4 Z. Chen, A. T. Eppink, B. Jiang, G. C. Groenenboom, X. Yang and D. H. Parker, *Phys. Chem. Chem. Phys.*, 2011, **13**, 2350.
5 Z. Chen, Q. Shuai, A. T. Eppink, B. Jiang, D. Dai, X. Yang and D. H. Parker, *Phys. Chem. Chem. Phys.*, 2011, **13**, 8531.
6 R. Schinke, *Photodissociation Dynamics*, Cambridge University Press, Cambridge, 1993.
7 Y. L. Yung and W. B. De More, *Photo-chemistry of Planetary Atmospheres*, Oxford University Press, Oxford, 1999.
8 P. Pilling, D. P. P. Andrade, R. Neves, A. M. Ferreira-Rodrigues, A. C. F. Santos and H. M. Boechat-Roberty, *Mon. Not. R. Astron. Soc.*, 2007, **375**, 1488.
9 R. C. Brown and E. J. Heller, *J. Chem. Phys.*, 1981, **75**, 186.
10 N. E. Henriksen, V. Engel and R. Schinke, *J. Chem. Phys.*, 1987, **86**, 6862.
11 S. Goursaud, M. Sizun and F. Fiquet-Fayard, *J. Chem. Phys.*, 1976, **65**, 5453.
12 E. J. Heller, *J. Chem. Phys.*, 1978, **68**, 2066.
13 J. C. Gray and D. G. Truhlar, *J. Chem. Phys.*, 1982, **76**, 5350.
14 M. G. Sheppard and R. B. Walker, *J. Chem. Phys.*, 1983, **78**, 7191.
15 J. G. López and A. B. McCoy, *Chem. Phys.*, 2005, **308**, 267.
16 L. Bonnet, *J. Chem. Phys.*, 2010, **133**, 174108.
17 W. Arbelo-González, L. Bonnet, P. Larrégaray, J.-C. Rayez and J. Rubayo-Soneira, *Chem. Phys.*, 2012, **399**, 117.
18 L. Bonnet, *Int. Rev. Phys. Chem.*, 2013, **32**, 171.
19 G. G. Balint-Kurti and M. Shapiro, *Chem. Phys.*, 1981, **61**, 137.
20 G. G. Balint-Kurti, R. N. Dixon and C. C. Marston, *J. Chem. Soc., Faraday Trans.*, 1990, **86**, 1741.
21 O. Roncero, J. A. Beswick, N. Halberstadt, P. Villarreal and G. Delgado-Barrio, *J. Chem. Phys.*, 1990, **92**, 3348.
22 M. Monnerville and B. Pouilly, *Chem. Phys. Lett.*, 1998, **294**, 473.
23 M. Paniagua, A. Aguado, M. Lara and O. Roncero, *J. Chem. Phys.*, 1999, **111**, 6712.
24 G. G. Balint-Kurti, L. Füsti-Molnár and A. Brown, *Phys. Chem. Chem. Phys.*, 2001, **3**, 702.
25 G. G. Balint-Kurti, *Int. Rev. Phys. Chem.*, 2008, **27**, 507.
26 R. de Nalda, J. Durá, A. García-Vela, J. G. Izquierdo, J. González-Vázquez and L. Bañares, *J. Chem. Phys.*, 2008, **128**, 244309.
27 S. Woittequand, C. Toubin, M. Monnerville, S. Briquez, B. Pouilly and H.-D. Meyer, *J. Chem. Phys.*, 2009, **131**, 194303.
28 X.-G. Wang and T. Carrington Jr., *Comput. Phys. Commun.*, 2010, **181**, 455.
29 C. R. Evenhuis and U. Manthe, *J. Phys. Chem. A*, 2011, **115**, 5992.
30 A. García-Vela, R. de Nalda, J. Durá, J. González-Vázquez and L. Bañares, *J. Chem. Phys.*, 2011, **135**, 154306.
31 B. Jiang, D. Xie and H. Guo, *J. Chem. Phys.*, 2012, **136**, 034302.
32 E. J. Wigner, *Phys. Rev.*, 1932, **40**, 749.
33 E. J. Heller, *J. Chem. Phys.*, 1976, **65**, 1289.
34 M. V. Berry, *Philos. Trans. R. Soc. London, Ser. A*, 1977, **287**, 237.
35 H.-W. Lee and M. O. Scully, *Found. Phys.*, 1983, **13**, 61.
36 H.-W. Lee, *Phys. Rep.*, 1995, **259**, 147.
37 J. Stanek and J. Konarski, *Int. J. Quantum Chem.*, 2005, **103**, 10.
38 W. B. Case, *Am. J. Phys.*, 2008, **76**, 937.
39 T. Dittrich, E. A. Gómez and L. A. Pachón, *J. Chem. Phys.*, 2010, **132**, 214102.
40 H. Goldstein, *Classical Mechanics*, Addison-Wesley, MA, 2nd edn, 1980.
41 H. Guo, *J. Chem. Phys.*, 1992, **96**, 6629.
42 S. López-López, R. Prosmiti and A. García-Vela, *J. Chem. Phys.*, 2007, **127**, 184307.
43 Y.-C. Han, K.-J. Yuan, W.-H. Hu, T.-M. Yan and S.-L. Cong, *J. Chem. Phys.*, 2008, **128**, 134303.
44 G. Delgado-Barrio, A. M. Cortina, A. Varad, P. Mareca, P. Villarreal and S. Miret-Arts, *J. Comput. Chem.*, 1986, **7**, 208.
45 Eqn (5.13) and (5.14) in ref. 6 prove that for the harmonic oscillator, contour levels correspond to classical orbits.
46 W. Arbelo-González and L. Bonnet, in preparation.

47 C. P. Malta, T. S. Marshall and E. Santos, *Phys. Rev. C: Nucl. Phys.*, 1997, **55**, 2551.
48 A. García-Vela, *J. Chem. Phys.*, 2000, **112**, 8302.
49 R. Schinke, *J. Phys. Chem.*, 1988, **92**, 3195.
50 M. C. Gutzwiller, *Chaos in Classical and Quantum Mechanics*, Springer, 1990, ch. 7.5.
51 Y. Elran and K. G. Kay, *J. Chem. Phys.*, 1999, **110**, 8912.
52 K. G. Kay, *J. Chem. Phys.*, 2010, **132**, 244110.
53 L. Bonnet and J.-C. Rayez, *Chem. Phys. Lett.*, 1997, **277**, 183.
54 L. Bañares, F. J. Aoiz, P. Honvault, B. Bussery-Honvault and J.-M. Launay, *J. Chem. Phys.*, 2003, **118**, 565.
55 L. Bonnet and J.-C. Rayez, *Chem. Phys. Lett.*, 2004, **397**, 106.
56 L. Bonnet, *Chin. J. Chem. Phys.*, 2009, **22**, 210.
57 L. Bonnet, P. Larrégaray, W. Arbelo-González and M. de Castro-Vítores, *Comput. Theor. Chem.*, 2012, **990**, 30.
58 G. Czakó and J. M. Bowman, *J. Chem. Phys.*, 2009, **131**, 244302.
59 L. Bonnet and J. Espinosa-García, *J. Chem. Phys.*, 2010, **133**, 164108.
60 A. J. Dobbyn, M. Stumpf, H.-M. Keller and R. Schinke, *J. Chem. Phys.*, 1996, **104**, 8357.
61 T. González-Lezana, *Int. Rev. Phys. Chem.*, 2007, **26**, 29.
62 L. Bonnet, P. Larregaray and J.-C. Rayez, *Phys. Chem. Chem. Phys.*, 2007, **9**, 3228.
63 L. Rubio-Lago, A. García-Vela, A. Arregui, G. A. Amaral and L. Bañares, *J. Chem. Phys.*, 2009, **131**, 174309.
64 H. Guo, *Chem. Phys. Lett.*, 1991, **187**, 360.
65 E. E. Nikitin, *Annu. Rev. Phys. Chem.*, 1999, **50**, 1.
66 H. Nakamura, *Adv. Chem. Phys.*, 2008, **138**, 95.
67 J. C. Tully, *J. Chem. Phys.*, 2012, **137**, 22A301.
68 M. Barbatti, *Wiley Interdiscip. Rev.: Comput. Mol. Sci.*, 2011, **1**, 620.
69 A. B. Alekseyev, H.-P. Liebermann, R. J. Buenker and S. N. Yurchenko, *J. Chem. Phys.*, 2007, **126**, 234102.
70 A. B. Alekseyev, private communication.
71 D. Xie, H. Guo, Y. Amatatsu and R. Kosloff, *J. Phys. Chem. A*, 2000, **104**, 1009.
72 Y. Amatatsu, S. Yabushita and K. Morokuma, *J. Chem. Phys.*, 1996, **104**, 9783.
73 A. B. Alekseyev, H.-P. Liebermann and R. J. Buenker, *J. Chem. Phys.*, 2007, **126**, 234103.
74 C. Cohen-Tannoudji, B. Diu and F. Laloë, *Quantum Mechanics*, Hermann, Paris, 1977, see Appendix II.
75 A. R. Edmonds, *Angular Momentum in Quantum Mechanics*, Princeton University Press, Princeton, New Jersey, 1960.
76 G. C. Schatz and A. Kuppermann, *J. Chem. Phys.*, 1976, **65**, 4642.
77 J. Tennyson and B. T. Sutcliffe, *J. Chem. Phys.*, 1982, **77**, 4061.
78 R. M. More, *J. Phys. II*, 1991, **1**, 97.

Summary

As numerous studies have already shown [64], taking into account in the quasi-classical trajectory (QCT) simulation of chemical reactions the quantization of vibrational motions of reagent and product species may strongly improve the quality of final state distributions in the quantum regime where only a small number of vibrational states are available to the final fragments.

A first type of approach consists in assigning statistical weights to trajectories such as respecting the Bohr quantization principle. According to it, the relevant trajectories are, for bimolecular processes, those starting with integer vibrational actions in the reagents, and ending with integer vibrational actions in the products. For photodissociations, these trajectories are those reaching the products with integer vibrational actions.

Two rather natural procedures can be used, called Gaussian binning (GB) and 1GB. Within the GB procedure, trajectories are assigned Gaussian statistical weights such that the closer the final vibrational actions to integer values, the larger the weights. However, the number of trajectories required to converge the calculations scales in general as 10^N, where N is the number of product (or re-formed reagent) vibrational modes. Consequently, QCT-GB can hardly be applied to more than four-atom processes. Within the 1GB procedure, Gaussian statistical weights depend on how close is the final vibrational energy to its quantized value. Only one Gaussian is used, so the previous scaling issue is avoided. However, 1GB is generally not justified from first principles, contrary to GB, which is a practical implementation of classical S matrix theory (CSMT) in the limit of quenching of interference effects [64].

As far as photodissociations are concerned, an alternative to QCT-GB is the backward description of molecular collisions [71]. This method may be used to

perform calculations rigorously equivalent to QCT-GB ones, with the decisive advantage that the backward method can in principle be applied to polyatomic reactions.

A second type of approach to photofragmentation, more sophisticated than QCT-GB in the hierarchy of semiclassical theories, is the semiclassical Wigner method (SWM) of Heller [73, 74]. Like QCT-GB, SWM takes into account the quantization of reagent and product species, but neither the possible interference effects occurring during the process, nor tunneling. It must thus be applied to fast fragmentations such that the nature of the wave-packet is not too altered en route to the products and tunneling is negligible. Fragmentations involving a long-lived complex are thus not expected to be accurately described by the SWM.

During this thesis, we carried out four different works:

First, we considered the normalization issue in QCT-GB and showed that normalizing may significantly improve the reaction cross section, as well as the state-resolved ones. In addition, we analyzed the reason why this is so within the framework of a statistical treatment.

Second, we checked the ability of QCT-GB to describe the fragmentation of the tetratomic van der Waals complex $Ne_2Br_2(B)$, involving vibrational predissociation. We confirmed the conclusions of previous studies on triatomic systems, *i.e.*, QCT-GB is unable to correctly reproduce the experimental vibrational state distributions of the final diatom $Br_2(B)$.

Third, we tested for the first time the backward method on a realistic three-dimensional photodissociation, namely, the one following excitation from the linear isomer of the van der Waals complex $NeBr_2(B)$. The results obtained were found to be in excellent agreement with QCT-GB ones, despite the fact that 10 times less trajectories are needed to converge the results.

Fourth, we extended the applicability of the SWM to three-dimensional realistic processes by including rotational motions in its formulation, and we strongly improved its numerical efficiency by recasting it within the backward description. The previous developments were a good opportunity to introduce rotational Wigner distributions for the first time in reaction dynamics, and the results obtained by means of the previous method were found to be in close agreement with rigorous quantum results in the case of Guo's triatomic-like model of methyl iodide photodissociation. In comparison, QCT-GB is only semi-quantitative.

Some perspectives

Most QCT-GB calculations have been performed without normalization to date [64]. Though they lead to final state distributions the shapes of which are satisfying, the values of the reaction cross sections are generally not very accurate. It would be interesting to check if normalizing could improve the cross sections. This work could be done in collaboration with the various groups performing QCT-GB calculations

As shown in chapters III and IV, the backward description of molecular collisions strongly improves the numerical efficiency of classical methods dealing with the Bohr quantization of final vibration motions or the more sophisticated semiclassical Wigner method. It is thus hoped that accurate descriptions of the dynamics of polyatomic photodissociations are now feasible. In particular, we should be able to reproduce the state-correlated translational energy distributions measured by means of the velocity imaging techniques, which are among the most refined data available on chemical reactivity.

Last but not least, coupling the previous methods with surface hopping methods is possible, as preliminary studies in our group have shown. Hence, the theoretical tools developed in the present thesis should contribute to accurately describe and rationalize the photodynamics of polyatomic species, provided that their electronic structure is well characterized.

Bibliography

[1] F. F. Crim; *Proc. Natl. Acad. Sci.* **105**, 12647 (2008)

[2] D. J. Tannor; *Introduction to Quantum Mechanics: A time-dependent perspective* (University Science Books, Sausalito, California, 2007)

[3] Y. L. Yung and W. B. D. More; *Photo-chemistry of Planetary Atmospheres* (Oxford University Press, 1999)

[4] P. Pilling, D. P. P. Andrade, R. Neves, A. M. Ferreira-Rodrigues, A. C. F. Santos and H. M. Boechat-Roberty; *Mon. Not. R. Astron. Soc.* **375**, 1488 (2007)

[5] K. Liu and A. Wagner; *The chemical Kinetics and Dynamics of Small Radicals* (Advanced Series in Physical Chemistry 6, World Scientific, 1995)

[6] P. Casavecchia; *Rep. Prog. Phys.* **63**, 355 (2000)

[7] M. Kawasaki and R. Bersohn; *Bull. Chem. Soc. Jpn.* **75**, 1885 (2002)

[8] X. Yang and K. Liu; *Modern Trends in Chemical Reaction Dynamics* (Advanced Series in Physical Chemistry 14, World Scientific, 2004)

[9] K. Liu; *J. Chem. Phys.* **125**, 132307 (2006)

[10] N. Balucani, G. Capozza, F. Leonori, E. Segoloni and P. Casavecchia; *Int. Rev. Phys. Chem.* **25**, 109 (2006)

[11] J. H. Choi; *Int. Rev. Phys. Chem.* **25**, 613 (2006)

[12] A. G. Suits; *Acc. Chem. Res.* **41**, 873 (2008)

[13] S. Greaves, R. Rose and A. Orr-Ewing; *Phys. Chem. Chem. Phys.* **12**, 9129 (2010)

[14] C. Berteloite, M. Lara, A. Bergeat, S. D. L. Picard, F. Dayou, K. M. Hickson, A. Canosa, C. Naulin, J. M. Launay, I. R. Sims and M. Costes; *Phys. Rev. Lett.* **105**, 203201 (2010)

[15] X. Yang; *Phys. Chem. Chem. Phys.* **13**, 8112 (2011)

[16] C. Xiao, X. Xu, S. Liu, T. Wang, W. Dong, T. Yang, Z. Sun, D. Dai, X. Xu, D. H. Zhang and X. Yang; *Science* **333**, 440 (2011)

[17] P. Casavecchia, M. Brouard, M. Costes, D. Nesbitt, E. Bieske and S. Kable; *Phys. Chem. Chem. Phys.* **13**, 8073 (2011)

[18] E. Garand, J. Zhou, D. E. Manolopoulos, M. H. Alexander and D. M. Neumark; *Science* **319**, 72 (2008)

[19] N. T. Goldberg, J. Zhang, K. Koszinowski, F. Bouakline, S. C. Althorpe and R. N. Zare; *Proc. Natl. Acad. Sci.* **105**, 18194 (2008)

[20] B. R. Strazisar, C. Lin and H. F. Davis; *Science* **290**, 958 (2000)

[21] A. Stolow; *Int. Rev. Phys. Chem.* **22**, 377 (2003)

[22] T. Suzuki; *Ann. Rev. Phys. Chem.* **57**, 555 (2006)

[23] H. J. Wörner, J. B. Bertrand, B. Fabre, J. Higuet, H. Ruf, A. Dubrouil, S. Patchkovskii, M. Spanner, Y. Mairesse, V. Blanchet, E. Mével, E. Constant, P. B. Corkum and D. M. Villeneuve; *Science* **334**, 208 (2011)

[24] G. Nyman and H.-G. Yu; *Int. Rev. Phys. Chem.* **32**, 39 (2013)

[25] P. Honvault and J.-M. Launay; *Theory of Chemical Reaction Dynamics* (Kluwer Academic, Dordrecht, The Netherlands, 2004)

[26] S. C. Althorpe; *Int. Rev. Phys. Chem.* **23**, 219 (2004)

[27] W. Hu and G. C. Schatz; *J. Chem. Phys.* **125**, 132301 (2006)

[28] B. Lepetit, D. Wang and A. Kuppermann; *J. Chem. Phys.* **125**, 133505 (2006)

[29] X. Q. Zhang, Q. Cui, J. Z. H. Zhang and K. L. Han; *J. Chem. Phys.* **126**, 234304 (2007)

[30] D. D. Fazio, J. M. Lucas, V. Aquilanti and S. Cavalli; *Phys. Chem. Chem. Phys.* **13**, 8571 (2011)

[31] A. Kuppermann; *Phys. Chem. Chem. Phys.* **13**, 8259 (2011)

[32] C. R. Evenhuis and U. Manthe; *J. Phys. Chem. A* **115**, 5992 (2011)

[33] S. Liu, X. Xu and D. H. Zhang; *J. Chem. Phys.* **136**, 144302 (2012)

[34] I. N. Levine; *Quantum Chemistry*; 6th edition (Prentice-Hall, Englewood Cliffs, NJ, 2008)

[35] T. Helgaker, P. Jorgensen and J. Olsen; *Molecular Electronic Structure Theory* (Wiley, New York, 2000)

[36] R. N. Porter and L. M. Rafi; *Dynamics of Molecular Collisions* (ed. by W. H. Miller, Plenum, New York, Part B, 1976)

[37] T. D. Sewell and D. L. Thomson; *Int. J. Mod. Phys. B* **11**, 1067 (1997)

[38] F. J. Aoiz, L. Bañares and V. J. Herrero; *J. Chem. Soc. Faraday Trans.* **94**, 2483 (1998)

[39] R. Schinke; *Photodissociation Dynamics* (Cambridge University Press, Cambridge, 1993)

[40] J. Espinosa-García, L. Bonnet and J. Corchado; *Phys. Chem. Chem. Phys.* **12**, 3873 (2010)

[41] J. D. Sierra, L. Bonnet and M. González; *J. Phys. Chem. A* **115**, 7413 (2011)

[42] G. Czakó, Y. Wang and J. M. Bowman; *J. Chem. Phys.* **135**, 151102 (2011)

[43] G. Czakó; *J. Phys. Chem. A* **116**, 7467 (2012)

[44] J. Polanyi; *Science* **236**, 680 (1987)

[45] J. C. Tully; *Faraday Disc.* **110**, 407 (1998)

[46] C. Y. Zhu, Y. Teranishi and H. Nakamura; *Adv. Chem. Phys.* **117**, 127 (2001)

[47] W. Domcke, D. R. Yarkoni and H. Köppel; *Conical Intersections: Electronic Structure, Dynamics and Spectroscopy* (World Scientific, 2004)

[48] G. Stock and M. Thoss; *Adv. Chem. Phys.* **131**, 243 (2005)

[49] A. Fernández-Ramos, J. A. Miller, S. J. Klippenstein and D. G. Truhlar; *Chem. Rev.* **106**, 4518 (2006)

[50] H. Nakamura; *Adv. Chem. Phys.* **138**, 95 (2008)

[51] M. Barbatti; *Comp. Mol. Science* **1**, 620 (2011)

[52] D. R. Yarkony; *Chem. Rev.* **112**, 481 (2012)

[53] T. Yonehara, K. Hanasaki and K. Takatsuka; *Chem. Rev.* **112**, 499 (2012)

[54] G. C. Schatz; *Chem. Rev.* **87**, 81 (1987)

[55] N. Makri and W. H. Miller; *J. Chem. Phys.* **91**, 4026 (1989)

[56] S. Keshavamurthy and W. H. Miller; *Chem. Phys. Lett.* **205**, 96 (1993)

[57] Y. Guo and D. L. Thompson; *J. Chem. Phys.* **105**, 7480 (1996)

[58] H. Ushiyama and K. Takatsuka; *J. Chem. Phys.* **109**, 9664 (1998)

[59] G. V. Mil'nikov and A. J. C. Varandas; *Phys. Chem. Chem. Phys.* **1**, 1071 (1999)

[60] K. Takatsuka, H. Ushiyama and A. Inoue-Ushiyama; *Phys. Rep.* **322**, 347 (1999)

[61] J. Xing, E. A. Coronado and W. H. Miller; *J. Phys. Chem. B* **105**, 6574 (2001)

[62] P. Larrégaray, L. Bonnet and J.-C. Rayez; *Phys. Chem. Chem. Phys.* **4**, 1571 (2002)

[63] C. Rosa and J. Brandão; *Chem. Phys. Lett.* **461**, 150 (2008)

[64] L. Bonnet; *International Reviews in Physical Chemistry* **32**, 171 (2013)

[65] W. H. Miller; *Adv. Chem. Phys.* **25**, 69 (1974)

[66] W. H. Miller; *Adv. Chem. Phys.* **30**, 77 (1975)

[67] J. R. Stine and R. A. Marcus; *Chem. Phys. Lett.* **29**, 575 (1974)

[68] K. Liu; *Phys. Chem. Chem. Phys.* **9**, 17 (2007)

[69] G. Czakó and J. M. Bowman; *J. Chem. Phys.* **131**, 244302 (2009)

[70] L. Bonnet and J. Espinosa-García; *J. Chem. Phys.* **133**, 164108 (2010)

[71] L. Bonnet; *J. Chem. Phys.* **133**, 174108 (2010)

[72] H. Guo; *J. Chem. Phys.* **96**, 6629 (1992)

[73] E. J. Heller; *J. Chem. Phys.* **65**, 1289 (1976)

[74] R. C. Brown and E. J. Heller; *J. Chem. Phys.* **75**, 186 (1981)

[75] E. Wigner; *Physical Review* **40**, 749 (1932)

[76] H.-W. Lee and M. O. Scully; *Foundations of Physics* **13**, 61 (1983)

[77] W. H. Miller; *J. Chem. Phys.* **50**, 407 (1969)

[78] M. S. Child; *Molecular Collision Theory* (Academic Press, New York, 1974)

[79] P. Pechukas and J. Light; *J. Chem. Phys.* **42**, 3281 (1965)

[80] E. E. Nikitin; *Theory of Elementary Atomic and Molecular Process in Gases* (Clarendon Press, Oxford, USA, 1974)

[81] L. Bonnet and J. C. Rayez; *Chem. Phys.* **201**, 203 (1995)

[82] L. Bonnet and J. C. Rayez; *J. Phys. Chem. A* **101**, 9318 (1997)

[83] P. Larrégaray, L. Bonnet and J. C. Rayez; *J. Phys. Chem. A* **110**, 1552 (2006)

[84] P. Larrégaray, L. Bonnet and J. C. Rayez; *J. Chem. Phys.* **127**, 084308 (2007)

[85] A. A. Buchachenko, R. Prosmiti, C. Cunha, G. Delgado-Barrio and P. Villarreal; *Journal of Chemical Physics* **117**, 6117 (2002)

[86] J. M. Pio, W. E. van der Veer, C. R. Bieler and K. C. Janda; *J. Chem. Phys.* **128**, 134311 (2008)

[87] G. Kubiak, P. S. H. Fitch, L. Wharton and D. H. Levy; *J. Chem. Phys.* **68**, 4477 (1978)

[88] K. E. Johnson, W. Sharfin and D. H. Levy; *J. Phys. Chem.* **74**, 163 (1981)

[89] M. A. Taylor, J. M. Pio, W. E. van der Veer and K. C. Janda; *J. Chem. Phys.* **132**, 104309 (2010)

[90] C. Sanz-Sanz, O. Roncero, R. Hernández-Lamoneda, J. M. Pio, M. A. Taylor and K. C. Janda; *J. Chem. Phys.* **132**, 221103 (2010)

[91] D. D. Evard, C. R. Bieler, J. I. Cline, N. Sivakumar and K. C. Janda; *J. Chem. Phys.* **89**, 2829 (1988)

[92] N. Halberstadt, S. Serna, O. Roncero and K. C. Janda; *Journal of Chemical Physics* **97**, 341 (1992)

[93] T. González-Lezana, M. I. Hernández, G. Delgado-Barrio and P. Villarreal; *Journal of Chemical Physics* **106**, 3216 (1997)

[94] M. Nejad-Sattari and T. A. Stephenson; *J. Chem. Phys.* **106**, 5454 (1997)

[95] T. González-Lezana, M. I. Hernandez, G. Delgado-Barrio, A. A. Buchachenko and P. Villarreal; *J. Chem. Phys.* **105**, 7454 (1996)

[96] T. A. Stephenson and N. Halberstadt; *J. Chem. Phys.* **112**, 2265 (2000)

[97] O. Roncero, J. Campos-Martínez, M. I. Hernández, G. Delgado-Barrio, P. Villarreal and J. Rubayo-Soneira; *J. Chem. Phys.* **115**, 2566 (2001)

[98] A. García-Vela and K. C. Janda; *J. Chem. Phys.* **124**, 034305 (2006)

[99] A. García-Vela; *J. Chem. Phys.* **126**, 124306 (2007)

[100] A. García-Vela; *J. Chem. Phys.* **129**, 094307 (2008)

[101] C. Meier and U. Manthe; *J. Chem. Phys.* **115**, 5477 (2001)

[102] A. García-Vela; *J. Chem. Phys.* **122**, 014312 (2005)

[103] A. García-Vela; *Phys. Chem. Chem. Phys.* **130**, 12075 (2011)

[104] B. Miguel, A. Bastida, J. Zúñiga, A. Requena and N. Halberstadt; *J. Chem. Phys.* **113**, 10130 (2000)

[105] B. Miguel, A. Bastida, J. Zúñiga, A. Requena and N. Halberstadt; *Faraday Discuss.* **118**, 257 (2001)

[106] A. Bastida, J. Zúñiga, A. Requena, N. Halberstadt and J. A. Beswick; *J. Chem. Phys.* **109**, 6320 (1998)

[107] S. Fernández-Alberti, N. Halberstadt, J. A. Beswick, A. Bastida, J. Zúñiga and A. Requena; *J. Chem. Phys.* **111**, 4577 (1999)

[108] A. Bastida, B. Miguel, J. Zúñiga, A. Requena, N. Halberstadt and K. C. Janda; *J. Chem. Phys.* **111**, 4577 (1999)

[109] J. Rubayo-Soneira; Ph.D. thesis; Madrid (1995)

[110] M. L. González-Martínez, W. Arbelo-González, J. Rubayo-Soneira, L. Bonnet and J. -C. Rayez; *Chem. Phys. Lett.* **463**, 65 (2008)

[111] L. Bonnet and J. -C. Rayez; *Chem. Phys. Lett.* **227**, 183 (1997)

[112] L. Bañares, F. J. Aoiz, P. Honvault, B. Bussery-Honvault and J.-M. Launay; *J. Chem. Phys.* **118**, 565 (2003)

[113] L. Bonnet and J.-C. Rayez; *Chem. Phys. Lett.* **397**, 106 (2004)

[114] M. L. González-Martínez, J. Rubayo-Soneira and K. C. Janda; *Phys. Chem. Chem. Phys.* **8**, 4550 (2006)

[115] M. C. Gutzwiller; *Chaos in Classical and Quantum Mechanics* (Springer, 1990)

[116] Y. Elran and K. G. Kay; *J. Chem. Phys.* **110**, 8912 (1999)

[117] K. G. Kay; *J. Chem. Phys.* **132**, 244110 (2010)